

Site U1374¹

Expedition 330 Scientists²

Chapter contents

Background and objectives	1
Operations	3
Sedimentology	4
Paleontology	14
Igneous petrology and volcanology	17
Alteration petrology	25
Structural geology	29
Geochemistry	31
Physical properties	33
Paleomagnetism	37
Downhole logging	39
Microbiology	45
References	47
Figures	51
Tables	163

Background and objectives

Site U1374 (alternate Site LOUI-6B) was the third site completed during Integrated Ocean Drilling Program (IODP) Expedition 330 (Fig. F1) and the second of two sites (U1373 and U1374) drilled on Rigil Guyot. At a predicted age of ~73 Ma, this site is one of the older seamount targets and is only a few million years younger than Site U1372 on Canopus Guyot to the northwest. If the Louisville hotspot experienced a paleolatitude shift similar to the recorded ~15° southern motion of the Hawaiian hotspot during the Late Cretaceous and early Cenozoic, this shift is expected to be largest for the oldest seamounts in the Louisville Seamount Trail. Because Sites U1373 and U1374 target two separate sequences of ancient lava flows on the same volcanic edifice and because Rigil Guyot is only slightly younger than Canopus Guyot, these three sites together are expected to significantly strengthen our determinations of the Louisville paleolatitude at the old end of the trail. Rigil Guyot shows no evidence of tilting and is part of a small cluster of two guyots (oriented east–west at 28.6°S and 28.7°S) and one small seamount to the south (28.8°S) (Fig. F2). Rigil Guyot itself consists of a single volcanic center that is 40 km long and 36 km wide; however, two small (perhaps posterosional) topographic highs remain on the western portion of its summit plain along with a third, more obvious topographic high on the eastern part of the summit plain. Site U1374 was placed west of these two small topographic highs and near its western rift zone at ~1559 m water depth (Fig. F2). Side-scan sonar reflectivity and 3.5 kHz subbottom profiling data indicate that Site U1374 is covered with <10 m of pelagic sediment, and seismic reflection profiles suggest that this site is characterized by a 110 m thick section of volcanoclastics dipping toward the west and overlying igneous basement.

Site U1374 was an alternate site requested during Expedition 330 to allow more flexibility while drilling Rigil Guyot. It was argued that if we encountered borehole instabilities comparable to those at Site U1372 on Canopus Guyot (see “Operations” in the “Site U1372” chapter [Expedition 330 Scientists, 2012b]) or if drilling at Site U1373 had to be abandoned for other unforeseen reasons, then we could divert to Site U1374 to continue drilling Rigil Guyot and still complete our most important scientific objective. Because reentry using a free-fall funnel failed for Hole U1373A and the first site at Rigil Guyot did in fact need to be abandoned,

¹Expedition 330 Scientists, 2012. Site U1374. In Koppers, A.A.P., Yamazaki, T., Geldmacher, J., and the Expedition 330 Scientists, *Proc. IODP, 330*: Tokyo (Integrated Ocean Drilling Program Management International, Inc.).
doi:10.2204/iodp.proc.330.105.2012

²Expedition 330 Scientists’ addresses.



Hole U1374A was spudded about 5.6 nmi away on the western portion of its summit plain.

The original drilling plan was to recover soft sediment using a gravity-push approach with little or no rotation of the rotary core barrel assembly, followed by standard coring into the volcanoclastic material and 350 m into igneous basement. A full downhole logging series was planned, including the standard triple combination and Formation MicroScanner-sonic tool strings, the Ultrasonic Borehole Imager tool, and the third-party Göttingen Borehole Magnetometer tool. After successful drilling to 522 meters below seafloor (mbsf), the full logging program was carried out. Coring was particularly successful, with a record-breaking 88% average recovery in igneous basement.

Objectives

Drilling during Ocean Drilling Program (ODP) Leg 197 provided compelling evidence for the motion of mantle plumes by documenting a large $\sim 15^\circ$ shift in paleolatitude for the Hawaiian hotspot (Tarduno et al., 2003; Duncan et al., 2006). This evidence led to testing two geodynamic end-member models during Expedition 330, namely that the Louisville and Hawaiian hotspots moved coherently over geological time (Courillot et al., 2003; Wessel and Kroenke, 1997) or, quite the opposite, that these hotspots show considerable interhotspot motion, as predicted by mantle flow models (Steinberger, 2002; Steinberger et al., 2004; Koppers et al., 2004; Steinberger and Antretter, 2006; Steinberger and Calderwood, 2006). The most important objective of Expedition 330, therefore, was to core deep into the igneous basement of four seamounts in the Louisville Seamount Trail in order to sample a large number of in situ lava flows ranging in age between 80 and 50 Ma. With a sufficiently large number of these independent cooling units, high-quality estimates of their paleolatitude can be determined, and any paleolatitude shift (or lack thereof) can be compared with seamounts in the Hawaiian-Emperor Seamounts Trail. For this reason, Expedition 330 mimicked the drilling strategy of Leg 197 by drilling seamounts equivalent in age to Detroit (76–81 Ma), Suiko (61 Ma), Nintoku (56 Ma), and Koko (49 Ma) Seamounts in the Emperor Seamount Trail. Accurate paleomagnetic inclination data are required for the drilled seamounts in order to establish a record of past Louisville hotspot motion, and, together with high-resolution $^{40}\text{Ar}/^{39}\text{Ar}$ age dating of the cored lava flows, these data will help us constrain the paleolatitude of the Louisville hotspot between 80 and 50 Ma. These comparisons are of fundamental importance in determining whether these two primary

hotspots have moved coherently or not and in understanding the nature of hotspots and convection in the Earth's mantle.

Expedition 330 also aimed to provide important insights into the magmatic evolution and melting processes that produced and constructed Louisville volcanoes as they progressed from shield to postshield, and perhaps posterosional, volcanic stages. Existing data from dredged lava suggest that the mantle source of the Louisville hotspot has been remarkably homogeneous for as long as 80 m.y. (Cheng et al., 1987; Hawkins et al., 1987; Vanderkluysen et al., 2007; Beier et al., 2011). In addition, all dredged basalt is predominantly alkalic and possibly represents a mostly alkalic shield-building stage, which contrasts with the tholeiitic shield-building stage of volcanoes in the Hawaiian-Emperor Seamount Trail (Hawkins et al., 1987; Vanderkluysen et al., 2007; Beier et al., 2011). Therefore, the successions of lava flows cored during Expedition 330 will help us characterize the Louisville Seamount Trail as the product of a primary hotspot and test the long-lived homogeneous geochemical character of its mantle source. Analyses of melt inclusions, volcanic glass samples, high-Mg olivine, and clinopyroxene phenocrysts will provide further constraints on the asserted homogeneity of the Louisville plume source, its compositional evolution between 80 and 50 Ma, its potential mantle plume temperatures, and its magma genesis, volatile outgassing, and differentiation. Incremental heating $^{40}\text{Ar}/^{39}\text{Ar}$ age dating will allow us to establish age histories within each drill core, delineating any transitions from the shield-building phase to the postshield capping and posterosional stages.

Another important objective of Expedition 330 at Site U1374 was to use new paleolatitude estimates, $^{40}\text{Ar}/^{39}\text{Ar}$ ages, and geochemical data to decide whether the oldest seamounts in the Louisville Seamount Trail were formed close to the 18° – 28°S paleolatitude determined from ODP Leg 192 basalt for the Ontong Java Plateau (Riisager et al., 2003) and whether this large igneous province was genetically linked to the Louisville hotspot or not. Such a determination would prove or disprove the hypothesis that the Ontong Java Plateau formed from massive large igneous province volcanism at ~ 120 Ma, when the preceding plume head of the Louisville mantle upwelling reached the base of the Pacific lithosphere and started extensive partial melting (e.g., Richards and Griffiths, 1989; Mahoney and Spencer, 1991).

Finally, basalt and sediment cored at Site U1374 were planned for use in a range of secondary objectives, such as searching for active microbial life in the old seamount basement and determining whether fossil

traces of microbes were left behind in volcanic glass or rock biofilms. We also planned to determine $^3\text{He}/^4\text{He}$ and $^{186}\text{Os}/^{187}\text{Os}$ signatures of the Louisville mantle plume to evaluate its potential deep-mantle origin, to use oxygen and strontium isotope measurements on carbonates and zeolites in order to assess the magnitude of carbonate vein formation in aging seamounts and its role as a global CO_2 sink, to age date celadonite alteration minerals for estimating the total duration of low-temperature alteration following seamount emplacement, and to determine the hydrogeological and seismological character of the seamount basement.

Operations

After Hole U1373A, on the eastern side of the summit plain of Rigil Guyot, had to be abandoned, the vessel was offset in dynamic positioning mode to Site U1374, on the western side of the summit plain. The 5.6 nmi offset was accomplished in 3.25 h, and by 1630 h on 5 January 2011 the ship was positioning at the new location (all times are New Zealand Daylight Time, Universal Time Coordinated [UTC] + 13 h). The vibration-isolated television (VIT) frame was deployed and used to monitor the bit tagging the seafloor at 1570.0 meters below rig floor (mbrf) (1559.0 meters below sea level [mbsl]), 2.6 m shallower than the corrected precision depth recorder depth.

Hole U1374A was spudded with a Type C-4 rotary core barrel bit at 2035 h on 5 January (Fig. F3; Table T1). After penetrating a thin sedimentary cover, the bit penetrated igneous basement at 16.7 mbsf. By 0345 h on 10 January, rotary coring had slowly advanced to 130.4 mbsf, with an average recovery of 84%. At this time, the bit had acquired 81.3 rotating hours, and preparations were made to recover the drill string and replace the bit with a fresh unit. Penetration into basement was 113.7 m, with an average recovery of 85%. The average rate of penetration while coring basement was 1.6 m/h.

A free-fall funnel (FFF) was made up and deployed at 0550 h on 10 January. The VIT frame was launched, and the bit extraction from the hole was monitored with the VIT system to ensure that the FFF was not dislodged during the process. The used bit was at the rotary table at 1145 h and was replaced with a new Type C-4 bit. The latch sleeve was also inspected, and the mechanical bit release (MBR) was replaced with a rebuilt unit. The used bit was found to be in excellent condition and only $\frac{1}{16}$ inch undergauge, with all inserts intact and very minor wear across all rows. The bearings were also still moderately tight.

The FFF was reentered at 1635 h. The bottom-hole assembly (BHA) was run in the hole without incident while the driller maintained slow rotation and a low pump rate. There was no fill at the bottom of the hole. Coring resumed at 1900 h on 10 January. During the course of the week the scientific party decided to core with the present bit until its destruction and to forego a second bit trip at this site. Rotary coring continued until 0545 h on 18 January, when erratic pump pressure indicated that there was a problem at the bottom of the drill string. Instead of continuing to core with a bit that had far outlasted its expected life at 133.4 rotating hours, it was decided to end coring at a final depth of 522.0 mbsf. Penetration into basement was 505.3 m, with an average recovery and rate of penetration of 88.0% and 2.5 m/h, respectively. The average recovery for the entire hole was 87.8%, with an average penetration rate of 2.4 m/h.

After a routine wiper trip, which suggested that the hole was in good condition, an attempt was made to release the bit with the rotary shifting tool (RST). There was no positive indication that the window sleeve in the MBR was shifted, and it was initially thought that an obstruction in the throat of the bit was preventing the tool from engaging the window latch. To possibly remedy this, a bit deplugger was pumped down, but there was no indication by a change in pump pressure that it had landed. The deplugger had to be jarred free and was recovered on the coring line. Multiple abrasions on the deplugger indicated that it was mechanically prevented from landing in the throat of the bit. Because downhole logging in this particular deep hole was considered important, it was decided to trip the drill pipe, remove the bit and MBR, and make up a shorter logging BHA with a $9\frac{1}{4}$ inch diameter logging/clean-out bit that would allow more of the open hole to be logged.

As the drill pipe was recovered, sepiolite-laden mud was discharged under pressure on the rig floor with each connection. In order to remedy this, the circulating head was made up and the pipe was flushed out. It is possible that during this process the bit may have been released and fallen to the seafloor, because no further mud was discharged as the remaining pipe was recovered. The exact time and position of the bit release can only be speculated.

The end of pipe cleared the rotary table at 2015 h on 18 January. A shorter logging BHA was made up with the cleanout bit and deployed at 0145 h. The bit entered the FFF at 0430 h and was positioned at a logging depth of 101.2 mbsf. The standard triple combination (triple combo) suite was made up and run in

at 1045 h. The tool was not able to advance into the open hole because of a bridge ~7 m below the end of the drill pipe. The tool was recovered, and the bit was lowered to 143.6 mbsf to clear the bridge. The bit was then pulled back and placed at 110.8 mbsf. When the triple combo tool string was unable to advance below 138.0 mbsf, the tool string was again recovered and reconfigured to a shorter assembly using only the density and gamma ray sensors in the hope that this tool string would more easily negotiate hole entry. After this attempt was unsuccessful, the drill pipe was recovered with the bit, clearing the rotary table at 1115 h.

A four-stand rotary core barrel coring assembly was made up with a new MBR and a used Type C-4 bit (recovered from Hole U1373A). The drill string entered the FFF at 1540 h on 20 January. From 1730 to 2315 h the hole was washed and reamed to bottom (522 mbsf), flushed with mud, and then displaced with 165 bbl of heavy (10.5 ppg) mud. The bit was dropped at the bottom of the hole, and the end of pipe was placed at a logging depth of 128.1 mbsf, ~18 m deeper than the previous logging attempt and below a potentially unstable zone in the formation. An extra stand of drill collars was added to the BHA to keep the tapered drill collar as close to the seafloor as possible, as that is the usual choke point at which a BHA becomes stuck.

The triple combo logging tool string was made up (in its standard extended version) and deployed again at 0540 h on 21 January and succeeded in logging the hole up from 520 mbsf. The tool suite was recovered and laid out. The second instrument deployed was the Göttingen Borehole Magnetometer (GBM), which made one full pass down from the rig floor to 520 mbsf and back up. Communication with the GBM was lost while it was being retrieved in the pipe; however, because a sighting of the tool was carried out at the start of deployment, the rotation history of the GBM may still be obtainable. The third logging run was performed with the Formation MicroScanner-sonic tool string, which also successfully came within 2 m of the bottom of the hole. The fourth log was conducted with the Ultrasonic Borehole Imager. The fifth log was a redeployment of the GBM tool. All runs were successful.

While the GBM was being deployed for the second time, the driller noticed that the suspended string weight was decreasing slightly, indicating that the formation was starting to squeeze the BHA. In order to compensate for this, the driller picked up the string an additional 3 m. While the logging tool was being retrieved the vessel had to be offset 75 m in order to lower the pipe connection the additional 3 m so that the slips could be set. From 2215 h on 22 Jan-

uary to 0930 h on 23 January the driller attempted to free the drill string. Although circulation was maintained, there was no rotation and the drill pipe could not be raised or lowered. Realizing that further efforts would be fruitless, the crew made the necessary preparations to sever the drill string directly above the tapered drill collar. The top of the tapered drill collar was at ~13 mbsf. The drill pipe was severed at 1500 h on 23 January.

Once the drill pipe was recovered and the beacon was retrieved, the vessel was secured for sea. The vessel departed for Site U1375 at 1945 h on 23 January, with an estimated time of arrival of 0500 h on 25 January.

Sedimentology

At Site U1374 on Rigel Guyot sediment occurs in (1) the uppermost sedimentary cover of the seamount, (2) three intervals within the top of the volcanic basement, and (3) finer grained interclast infill deposits, thin-bedded sedimentary layers, or peperitic intervals deeper in the volcanic basement in intervals mainly consisting of basalt breccia (volcanic or sedimentary in origin). Five stratigraphic units were defined on the basis of stratigraphic relationships and the compositional and textural characteristics of the sediment at macroscopic and microscopic scales (Fig. F4):

- Unit I (0–6.64 mbsf; lower boundary = Section 330-U1374A-1R-5, 63.5 cm): youngest sedimentary cover, predominantly composed of brownish-yellow sandy foraminiferal ooze.
- Unit II (6.64–16.70 mbsf; lower boundary = Section 330-U1374A-3R-2, 87 cm): older sedimentary cover composed of an assemblage of volcanic sandstone, foraminiferal bioclast limestone with ferromanganese encrustations, and grain-supported basalt conglomerate with bioclasts. Unit II was deposited on top of a volcanic interval (Units III–VI) that includes only a single thin-bedded sedimentary layer and rare interclast infill deposits. Unit II was divided into five subunits (see below).
- Unit VII (37.60–41.84 mbsf; upper boundary = Section 330-U1374A-7R-3, 72 cm; lower boundary = Section 8R-3, 52 cm): volcanic sandstone and grain-supported basalt breccia with few bioclasts. Unit VII was divided into three subunits (see below). This unit was deposited on top of a volcanic sequence (Unit VIII) composed of grain-supported monolithic basalt breccia mostly devoid of infill sediment.
- Unit IX (63.67–84.70 mbsf; upper boundary = Section 330-U1374A-12R-4, 100 cm; lower boundary

= Section 16R-1, 10 cm): sedimentary interval emplaced on top of volcanic deposits (Unit X) and composed of grain-supported heterolithic basalt breccia and volcanic sandstone devoid of fossils. This unit was divided into three subunits (see below). Underlying Unit X includes a peperite with enclaves of bioclast-bearing sediment and extended sequences of basalt breccia with frequent bioclast-bearing interclast infill deposits.

- Unit XI (109.87–116.45 mbsf; upper boundary = Section 330-U1374A-21R-3, 59.5 cm; lower boundary = Section 22R-5, 24 cm): lowermost extended sedimentary interval composed of volcanic sandstone and grain-supported basalt conglomerate with bioclasts. This unit was divided into two subunits (see below). Unit XI was deposited on top of an extended volcanic sequence (Units XII–XIX) observed from 116.45 mbsf to the bottom of Hole U1374A at 522 mbsf. This underlying volcanic sequence includes basalt lava flows and abundant grain-supported monolithic basalt breccia with frequent fossil-free interclast infill deposits and a few thin-bedded sedimentary intervals essentially devoid of bioclasts.

Unit I

Interval: Sections 330-U1374A-1R-1, 0 cm, to 1R-5, 63.5 cm

Depth: 0–6.64 mbsf

Age: Pleistocene to Holocene

Stratigraphic Unit I represents the youngest sedimentary cover found at Site U1374 and extends downhole from the seafloor to the older sediment cover of underlying Unit II at 6.64 mbsf (Fig. F4). This unit's lower boundary was defined by the occurrence of ferromanganese encrustations on top of underlying Unit II (see below). Its age was constrained by foraminiferal and nannofossil assemblages (see "Paleontology"). Unit I is composed of sandy foraminiferal ooze with local occurrences of reworked glass fragments and pumice (Fig. F5A). Although this unit shows severe drilling disturbance (possible entire loss of original beddings), paleontological observations (see "Paleontology") indicate that the ooze likely represents a recent winnowing residue of sediment originally richer in finer grained particles and nannofossils. The lowermost part of Unit I (6.49–6.64 mbsf) is composed of drilling breccia that includes pumiceous gravel and poorly consolidated sandy foraminiferal ooze similar in composition to the overlying ooze. Smear slide observations (Samples 330-U1374-1R-1, 75 cm; 1R-2, 75 cm; 1R-3, 75 cm; 1R-4, 75 cm; 1R-5, 15 cm; and 1R-5, 50 cm) showed that the foraminiferal ooze includes some

fresh glass, clinopyroxene, plagioclase, and lithic fragments.

Unit II

Interval: Sections 330-U1374A-1R-5, 63.5 cm, to 3R-2, 87 cm

Depth: 6.64–16.70 mbsf

Age: between late Maastrichtian and Pleistocene (Subunit IIA), late Maastrichtian (Subunits IIB and IIC), late Campanian (Subunit IID), and late Campanian or older (Subunit IIE)

Stratigraphic Unit II represents an older 10.06 m thick sediment cover that extends between 6.64 and 16.70 mbsf. Its lower boundary is defined by the first occurrence downhole of a basalt lava flow in underlying Unit III. Unit II includes a complicated sediment assemblage that ranges in composition from vitric sandstone to foraminiferal bioclast limestone to basalt conglomerate with bioclasts. Distinct sediment compositions, textures, and ages (see "Paleontology") allowed this unit to be divided into five subunits (Fig. F4). The basalt clast compositions in Units II, IX, and XI indicate that Unit II is distinct from other sediments downhole; Unit II includes basalt clast Types 1–3, whereas Units IX and XI generally lack Type 2 and contain local occurrences of Types 4–11 (Table T2; see also U1374A.DOC in CHAR in SEDIMENT in "Supplementary material"). Estimates of grain size and roundness with depth in Units II, VII, IX, and XI (see "Sedimentology" in the "Methods" chapter [Expedition 330 Scientists, 2012a]) are illustrated in Figure F4 and provided in a supplementary table (see U1374A.XLS in SIZE in SEDIMENT in "Supplementary material").

Subunit IIA

Interval: Sections 330-U1374A-1R-5, 63.5 cm, to 2R-4, 15.5 cm

Depth: 6.64–13.59 mbsf

Age: between late Maastrichtian and Pleistocene

Stratigraphic Subunit IIA is 6.95 m thick and extends between 6.64 and 13.59 mbsf (Fig. F4). Its lower boundary was not recovered, and the Subunit IIA/IIB boundary was defined on the basis of the appearance of bioturbation and bioclasts in underlying Subunit IIB (see below). Subunit IIA is composed of fossil-barren multicolor volcanic sandstone (Fig. F5B). An age of deposition between late Maastrichtian and Pleistocene was based on stratigraphic relationships and paleontological dating of overlying and underlying sediments (see "Paleontology"). The occurrence of ferromanganese encrustations at the top of Subunit IIA indicates existence of a hardground surface. The sandstone of Subunit IIA is essentially composed of

altered glass fragments with rare occurrences of fresh glass. It is very well sorted and is characterized by several thin-bedded intervals with subhorizontal layering, normal grading, and cross-bedding structures. The size of the largest volcanic clasts (observed over 10 cm intervals) ranges between very coarse sand and granule size. A fining-upward sequence may occur in the lowermost part of Subunit IIA (Fig. F4). The average roundness of volcanic clasts per 10 cm interval is very angular.

Microscopic observations of four thin sections (Samples 330-U1374A-2R-1, 35–38 cm [Thin Section 107]; 2R-2, 106–109 cm [Thin Section 108]; 2R-3, 70–73 cm [Thin Section 109]; and 2R-4, 10–13 cm [Thin Section 110]) indicated that the glass fragments in the sandstone are highly vesiculated. Some are pumiceous and most contain euhedral olivine crystals. The very high angularity of the glass suggests absent, or very limited, reworking. Sample 330-U1374A-2R-2, 106–109 cm (Thin Section 108), includes remnants of fresh glass and olivine, some of which contain fresh, small (<10 μm) melt inclusions. At least two generations of cement (possible zeolite and later calcite) were observed.

Subunit IIB

Interval: Sections 330-U1374A-2R-4, 15.5 cm, to 2R-4, 35 cm

Depth: 13.59–13.78 mbsf

Age: late Maastrichtian

Stratigraphic Subunit IIB is 0.19 m thick and extends between 13.59 and 13.78 mbsf (Fig. F4). Its lower boundary was not recovered, and the Subunit IIB/IIC boundary was based on the lower bioclast content and distinct sedimentary structures in underlying Subunit IIC (see below). Subunit IIB is composed of multicolor volcanic sandstone with common bioclasts. It contains two distinct lithologies. The first consists of cemented darker volcanic sandstone with abundant vesiculated glass fragments devoid of phenocrysts. The second is a micrite-bearing lighter volcanic sandstone with abundant calcitized subeuhedral olivine, minor vesiculated glass fragments devoid of phenocrysts, and rare subrounded basalt grains (Fig. F5C). The lighter micrite-bearing sandstone is abundantly bioturbated, whereas the darker cemented sandstone contains only few boreholes. Because of the limited extension or recovery of Subunit IIB, the stratigraphic relationship between the two sandstones is unclear. However, the composition of burrow infills in the darker sandstone suggests that the olivine-rich sandstone may represent a younger phase of sedimentation. The uppermost part of Subunit IIB composed of darker sandstone possibly represents an intraclast. Both sandstones in-

clude shallow-marine bioclasts (gastropods, shell fragments, and echinoderms). The age of Subunit IIB was restricted to the late Maastrichtian on the basis of fossil ages in the darker and lighter sandstones (see “Paleontology”) and inferred stratigraphic relationships with underlying Subunits IIC and IID.

Thin section observations (Sample 330-U1374A-2R-4, 27–32 cm [Thin Sections 111, 134, and 134A]) showed that the micrite in the olivine-rich sandstone contains abundant recrystallized radiolarians and foraminifers. Glass fragments in Subunit IIB are entirely altered and very angular, but they exhibit a slightly more rounded habit than the glass fragments of overlying Subunit IIA. Geopetal structures found in gastropods are consistent with the undisturbed (horizontal) orientation of the lower occurrence of darker volcanic sandstone. Pores in this sediment were filled with granular sparite.

Subunit IIC

Interval: Sections 330-U1374A-2R-4, 35 cm, to 3R-1, 64.5 cm

Depth: 13.78–15.05 mbsf

Age: late Maastrichtian

Stratigraphic Subunit IIC is 1.27 m thick and extends from 13.78 to 15.05 mbsf (Fig. F4). Its lower boundary corresponds to an erosional contact (possibly an angular unconformity) with the underlying foraminiferal bioclast limestone of Subunit IID. Subunit IIC is composed of multicolor volcanic sandstone with few shallow-marine and hemipelagic bioclasts (Fig. F5D). The sandstone resembles that of Subunit IIA and is essentially composed of highly vesicular glass fragments with few euhedral olivines. On the other hand, the sedimentary textures in Subunit IIC are distinct from those of Subunit IIA, with the occurrence of poor, diffuse subhorizontal layering and cross-bedding structures. Bioclasts in Subunit IIC are predominantly composed of shell fragments and gastropods, with rare ammonite fragments (see inset in Fig. F5D; see also “Paleontology”). Maximum clast size (very coarse sand to granule size) and clast roundness (angular to very angular) are similar to those of Subunit IIA. The late Maastrichtian age of deposition of Subunit IIC was constrained by nannofossil assemblages found in a burrow infill of underlying Subunit IID (Fig. F6; see also “Paleontology”).

Observation of one thin section (Sample 330-U1374A-2R-4, 88–91 cm [Thin Section 112]) showed that the pores of the sandstone in Subunit IIC include three generations of cement, with two fringing fibrous cements (zeolite and calcite) and a later granular cement filling the center of the interstitial spaces. Fossil fragments are entirely replaced by

granular cement. Pervasive alteration of glass fragments and olivine was observed.

Subunit IID

Interval: Sections 330-U1374A-3R-1, 64.5 cm, to 3R-1, 91 cm

Depth: 15.05–15.31 mbsf

Age: late Campanian

Stratigraphic Subunit IID is composed of a 0.26 m thick foraminiferal bioclast limestone that extends from 15.05 to 15.31 mbsf (Figs. F4, F5E). Although the contact between Subunits IID and IIE was not observed, the lower boundary of Subunit IID was defined on the basis of the increased occurrence of basalt clasts and the reduced abundance of foraminifers in underlying Subunit IIE (see below). Fossils in Subunit IID are composed of abundant shallow-marine bioclasts (shell fragments, red algae, gastropods, echinoderms, and bryozoans), benthic and planktonic foraminifers, and small ammonite fragments. Most of the larger bioclasts are broken and rounded, whereas the foraminifers do not display evidence of substantial reworking. Well-rounded basalt pebbles were observed to have a maximal size larger than that of volcanoclasts in Subunits IIA, IIB, and IIC and similar to that of basalt clasts in underlying Subunit IIE (Fig. F4). The uppermost part of Subunit IID includes a condensed interval composed of a complicated assemblage of basalt clasts, different types of bioclast-rich limestone, and ferromanganese-phosphate encrustations (Fig. F6). Also, the interval contains burrows filled with the late Maastrichtian glass-rich sandstone of overlying Subunit IIC (“Snd” in Fig. F6). A foraminiferal assemblage found in a limestone sample (“Lm3” in Fig. F6) provided a late Campanian (~75.7–75.2 Ma) age of deposition (see “Paleontology”). Also, preliminary observations of the foraminiferal assemblage indicated that the sediment of Subunit IID was deposited at hemipelagic depths. Sedimentologic and paleontological observations indicate a significant time gap (~6–11 Ma) between emplacement of the volcano-sedimentary sequences below and above Subunit IID.

The chemical composition of limestone Sample 330-U1374A-3R-1W, 66.5–70.5 cm (Fig. F6), was measured by qualitative X-ray fluorescence (XRF) analyses using the shipboard Thermo Scientific Niton XL3 Analyzer. XRF analyses showed that Horizons 2 and 3 are characterized by high iron, manganese, and phosphorous contents. These data indicate the occurrence of several ferromanganese-phosphate encrustations, suggesting several hiatuses in the uppermost interval of Subunit IID (Fig. F6).

Lm2 in Figure F6 contains high iron, manganese, and phosphorus, which likely reflects phosphatization of the sediment and suggests the presence of phosphatic hardground(s) in Subunit IID (see XL3_EVAL.PDF in XRF in “Supplementary material”).

Thin section observations (Sample 330-U1374A-3R-1, 70–72 cm [Thin Sections 113, 128, 128A, and 128B]) showed that the sediment matrix of Subunit IID is predominantly composed of micrite. However, granular, syntaxial, and dogtooth cement as well as vadose silt encountered in interstitial pores or dissolved shell fragments indicate a vadose environment of cementation (Fig. F7A) (Flügel, 1982).

Subunit IIE

Interval: Sections 330-U1374A-3R-1, 91 cm, to 3R-2, 87 cm

Depth: 15.31–16.70 mbsf

Age: late Campanian or older

Stratigraphic Subunit IIE is 1.39 m thick and extends from 15.31 to 16.70 mbsf (Fig. F4). Its lower boundary corresponds to the top of an underlying basalt lava flow in Unit III (see “Igneous petrology and volcanology”). Subunit IIE is composed of grain-supported, poorly sorted grayish basalt conglomerate with bioclasts (Fig. F5F). The intercobble and interboulder spaces, as well as cracks in the underlying basalt lava flow, are filled with finer grained basalt sandstone-conglomerate with abundant shallow-marine bioclasts (e.g., red algae, shell fragments, and annelids), light gray micrite, and cement. The orientation of the shell fragments defines subhorizontal layering throughout Subunit IIE. Volcanoclasts include altered vesicular to nonvesicular glass fragments with plagioclase. These fragments were not observed in overlying Subunits IIA, IIB, or IIC and suggest a distinct volcanic source for the Subunit IIE fragments in the volcanic basement. The maximum clast size in Subunit IIE is slightly larger than that in overlying Subunit IID. The average roundness of clasts in Subunit IIE ranges between very angular and subrounded. A late Campanian or older age of deposition for this subunit was defined on the basis of paleontological determinations in Subunit IID and inferred stratigraphic relationships.

Similar to Subunit IID, thin section observations (Sample 330-U1374A-3R-2, 65–68 cm [Thin Section 117]) indicated the occurrence of dripstone cement and geopetal structures defined by vadose silt and sparry calcite cement (Fig. F7B, F7C). These observations suggest that cementation of Subunit IIE occurred in a vadose environment (Flügel, 1982).

Unit VII

Interval: Sections 330-U1374A-7R-3, 72 cm, to 8R-3, 52 cm

Depth: 37.60–41.84 mbsf

Age: late Campanian or older

Stratigraphic Unit VII is a 4.24 m thick sedimentary interval that extends from 37.60 to 41.84 mbsf within a predominantly volcanic sequence. Its upper boundary is defined by a transitional contact with the volcanic basalt breccia of Unit VI. Its lower boundary is defined by the occurrence of volcanic basalt breccia in underlying Unit VIII. Unit VII is composed of volcanoclastic deposits with few bioclasts. A high content of vitric fragments, the occurrence of bioclasts, and a lack of micrite are characteristic features of Unit VII. This unit was divided into three subunits on the basis of distinct sediment compositions and textures (Fig. F4). A late Campanian or older age of deposition was determined on the basis of faunal assemblages found in the sediment above and stratigraphic relationships.

Subunit VIIA

Interval: Sections 330-U1374A-7R-3, 72 cm, to 7R-4, 55 cm

Depth: 37.60–38.79 mbsf

Age: late Campanian or older

Stratigraphic Subunit VIIA is 1.19 m thick and extends from 37.60 to 38.79 mbsf (Fig. F4). Its lower boundary was not recovered, and the Subunit VIIA/VIIIB boundary was based on the distinct sedimentary structures and sediment composition of underlying Subunit VIIB (see below). Subunit VIIA is composed of grain-supported, very well sorted multicolor basalt sandstone with few shallow-marine bioclasts (e.g., red algae, shell fragments, annelids, gastropods, and echinoderms) (Fig. F5G). The sediment is predominantly composed of vitric and basalt grains. It is entirely cemented and characterized by pervasive steep layering with possible large-amplitude cross-beds. The maximal clast size of Subunit VIIA ranges from very coarse sand to granule size, smaller than that of the volcanic breccia above and below (Units VI and VIII, respectively). The average clast roundness ranges between very angular and angular.

Thin section observations (Sample 330-U1374A-7R-4, 26–30 cm [Thin Section 125]) indicated that the sediment includes at least three generations of cement, with (in order of formation) fibrous zeolite, fibrous calcite, and sparry calcite.

Subunit VIIB

Interval: 330-U1374A-7R-4, 55 cm, to 8R-3, 16 cm

Depth: 38.79–41.48 mbsf

Age: late Campanian or older

Stratigraphic Subunit VIIB is 2.69 m thick and extends from 38.79 to 41.48 mbsf (Fig. F4). Its lower boundary was not recovered, and the Subunit VIIB/VIIIC boundary was constrained by the appearance of multicolor basalt breccia with bioclasts in underlying Subunit VIIIC (see below). Subunit VIIB is composed of grain-supported cemented multicolor volcanic sandstone with few large basalt clasts (Fig. F5H). The sandstone is predominantly composed of fragments of poorly to moderately vesicular altered glass with abundant plagioclase. A shallow-marine bioclast component occurs in the lower part of Subunit VIIB. The sandstone of Subunit VIIB is characterized by a steeply inclined, consistently layered structure without evidence of large-amplitude cross-beds. The size of the grains is bimodal, with few basalt pebbles embedded in a very well sorted, very coarse sandstone (Fig. F4). The average roundness of the clasts ranges from very angular to subrounded.

Thin section observations (Samples 330-U1374A-7R-4, 112–114 cm [Thin Section 126]; 7R-5, 14–18 cm [Thin Section 127]; 8R-1, 53–57 cm [Thin Section 129]; and 8R-2, 111–115 cm [Thin Section 130]) showed that the cement of the sandstone resembles that of the overlying basalt breccia (Subunit VIIA), with occurrences of fibrous zeolite, fibrous calcite, and sparry calcite.

Subunit VIIIC

Interval: Sections 330-U1374A-8R-3, 16 cm, to 8R-3, 52 cm

Depth: 41.48–41.84 mbsf

Age: late Campanian or older

Stratigraphic Subunit VIIIC is 0.36 m thick and extends from 41.48 to 41.84 mbsf (Fig. F4). Its lower boundary corresponds to a transitional change to the underlying volcanic interval composed of basalt breccia (Unit VIII). Subunit VIIIC consists of cemented grain-supported multicolor basalt breccia with bioclasts (Fig. F5I). The bioclasts include a shallow-marine fauna similar in composition to that observed in sediments above (Subunits IIB–IID and VIIA–VIIIB). The larger clasts are composed of basalt cobbles, and the average clast roundness is angular to subangular.

Thin section observations (Sample 330-U1374A-8R-3, 19–22 cm [Thin Section 13]) showed that the breccia includes rare foraminifers. Interstitial cement is composed of granular calcite.

Unit IX

Interval: Sections 330-U1374A-12R-4, 100 cm, to 16R-1, 10 cm

Depth: 63.67–84.70 mbsf

Age: late Campanian or older

Stratigraphic Unit IX is a 21.03 m thick sedimentary interval that extends between 63.67 and 84.70 mbsf within a predominantly volcanic sequence. Although the upper boundary of Unit IX was not recovered, it is believed to correspond to a lithologic change from reddish monolithic basalt breccia (Unit VIII) to multicolor heterolithic basalt breccia (Unit IX). The lower boundary of Unit IX was defined by the occurrence of a basalt lava flow at the top of underlying Unit X (see “[Igneous petrology and volcanology](#)”). Unit IX is essentially composed of volcaniclastic deposits, and its characteristic features include a lack of micrite and fossils and rare occurrences of sediment clasts (vitric sandstone). Late-stage sedimentary infills are common within the coarser breccia deposits (Fig. F8). Distinct sediment compositions and textures allowed Unit IX to be divided into three subunits (Fig. F4; Table T2).

Subunit IXA

Interval: Sections 330-U1374A-12R-4, 100 cm, to 14R-2, 112 cm

Depth: 63.67–74.78 mbsf

Age: late Campanian or older

Stratigraphic Subunit IXA is 11.11 m thick and extends from 63.67 to 74.78 mbsf (Fig. F4). Its lower boundary is marked by a sharp change downhole to the multicolor volcanic sandstone of Subunit IXB (see below). Subunit IXA is composed of heterolithic cemented multicolor volcanic breccia with few altered volcanic fragments (Fig. F5J). The compositional range of the larger basalt clasts is wider than that observed in Unit II (Table T2). The breccia is grain supported, poorly sorted, and devoid of fossils. Its maximal clast size ranges between pebble and cobble size, with very angular to subrounded clasts (Fig. F4). Local changes in grain sorting and the orientation of contact with the underlying finer grained sediment of Subunit IXB outline the occurrence of steep layering throughout Subunit IXA (Fig. F5J).

Microscope observations (Samples 330-U1374A-13R-1, 50–53 cm [Thin Section 137]; 14R-1, 8–10 cm [Thin Section 138]; and 14R-1, 57–60 cm [Thin Section 139]) indicated that the breccia includes several generations of cement (fibrous zeolite, fibrous calcite, and sparry calcite).

Subunit IXB

Interval: Sections 330-U1374A-14R-2, 112 cm, to 15R-1, 59.5 cm

Depth: 74.78–78.20 mbsf

Age: late Campanian or older

Stratigraphic Subunit IXB is 3.42 m thick and extends from 74.78 to 78.20 mbsf (Fig. F4). Although not recovered, its lower boundary was defined on the basis of the occurrence in Subunit IXC of basalt breccia (see below). Subunit IXB is composed of fossil-barren multicolor volcanic sandstone with few larger basalt clasts (Fig. F5K). The sandstone is predominantly composed of fragments of plagioclase-bearing variously vesiculated altered glass. The basalt clasts have a clast type composition distinct from those of overlying Unit II and Subunit IXA (Table T2). Subunit IXB has a bimodal grain size distribution with pebbly, cobbly basalt clasts embedded in a coarse sandstone. The size of the largest basalt clasts is similar to that of other sediments in Unit IX (Fig. F4). Clast roundness in Subunit IXB ranges between very angular and angular. Subunit IXB is characterized by a diffuse, steep layering in the finer grained sediment, which is locally enhanced by a higher concentration of basalt pebbles (Fig. F5K).

Thin section observation (Sample 330-U1374A-14R-3, 59–63 cm [Thin Section 140]) suggested that Subunit IXB shares a cementation pattern similar to that of overlying Subunit IXA, with occurrences of at least three types of cement (fibrous zeolite, fibrous calcite, and sparry calcite).

Subunit IXC

Interval: Sections 330-U1374A-15R-1, 59.5 cm, to 16R-1, 10 cm

Depth: 78.20–84.70 mbsf

Age: late Campanian or older

Stratigraphic Subunit IXC is 6.50 m thick and extends from 78.20 to 84.70 mbsf (Fig. F4). Its lower boundary corresponds to a contact with a basalt lava flow in the upper part of Unit X (see “[Igneous petrology and volcanology](#)”). Subunit IXC is composed of multicolor basalt breccia very similar in terms of composition and texture to the sediment observed in Subunit IXA (Fig. F5L).

Unit XI

Interval: Sections 330-U1374A-21R-3, 59.5 cm, to 22R-5, 24 cm

Depth: 109.87–116.45 mbsf

Age: late Campanian or older

Stratigraphic Unit XI is the last downhole occurrence of a thick (>1 m) sedimentary interval at Site U1374. The unit is 6.58 m thick and extends from 109.87 to 116.45 mbsf. Its upper boundary is gradational with the basalt breccia of Unit X. Its lower boundary is defined by the occurrence of a peperitic basalt in underlying Unit XII (see “[Igneous petrology and volcanology](#)”). The composition of basalt clasts found

in Unit XI is slightly distinct from those of other sedimentary intervals above (Table T2). Distinct sediment compositions and textures allowed Unit XI to be divided into two subunits (Fig. F4).

Subunit XIA

Interval: Sections 330-U1374A-21R-3, 59.5 cm, to 21R-3, 101 cm

Depth: 109.87–110.28 mbsf

Age: late Campanian or older

Stratigraphic Subunit XIA is 0.41 m thick and extends from 109.87 to 110.28 mbsf (Fig. F4). Its lower boundary corresponds to a sharp, steep contact with underlying multicolor basalt conglomerate with bioclasts (Subunit XIB; see below). Subunit XIA includes multicolor volcanic sandstone similar in terms of composition and texture to the volcanic sandstone found in Subunit IXB (Fig. F5M). However, the lower part of the sandstone in Subunit XIA includes minor amounts of shallow-marine bioclasts.

Microscope observations in Subunit XIA (Sample 330-U1374A-21R-3, 80–84 cm [Thin Section 151]) showed that the sediment is predominantly composed of poorly to moderately vesicular altered glass fragments with plagioclase. Cement precipitated in interstitial pores comprises fibrous zeolite, fibrous calcite, and sparry calcite. These observations further support the high compositional and textural similarity of Subunits XIA and IXB.

Subunit XIB

Interval: Sections 330-U1374A-21R-3, 101 cm, to 22R-5, 24 cm

Depth: 110.28–116.45 mbsf

Age: late Campanian or older

Stratigraphic Subunit XIB is 6.17 m thick and extends from 110.28 to 116.45 mbsf (Fig. F4). Its lower boundary was defined on the basis of the occurrence of a peperitic basalt lava flow in the uppermost part of underlying Unit XII (see “[Igneous petrology and volcanology](#)”). Subunit XIB is composed of grayish basalt conglomerate with bioclasts. It is compositionally and texturally similar to the conglomerate found in Subunit IIE (Fig. F5N). However, the occurrence of larger shallow-marine bioclasts in Subunit XIB is indicative of very limited reworking of some of the fossils prior to final deposition.

Thin section observations (Samples 330-U1374A-21R-4, 76–80 cm [Thin Section 152]; 22R-1, 2–6 cm [Thin Sections 153 and 165]; 22R-2, 1–5 cm [Thin Section 154]; and 22R-3, 21–25 cm [Thin Section 155]) indicated that the conglomerate includes a bioclast faunal assemblage similar to that of Subunit IIE, with abundant shell fragments and red algae; com-

mon bryozoans, annelids, and echinoderms; and rare foraminifers. The sediment in Subunit XIB also includes pendant, meniscus, and dogtooth cement, as well as horizontal geopetal structures (Fig. F7D). Similar to cement patterns found in Subunit IIE, these observations are indicative of a vadose environment of cementation for Subunit XIB.

Sediments in volcanic sequences

Apart from Stratigraphic Units I, II, VII, IX, and XI, defined above, additional occurrences of sediment were encountered at Site U1374 in peperitic intervals, thin-bedded sedimentary intervals, or interclast infill deposits in the predominantly volcanic sequences. It is important to note that distinguishing between sedimentary and volcanic deposits was very difficult in large intervals of basalt breccia because both types of deposit can have similar compositional and textural characteristics. We present below only the most obvious sediment occurrences that were identified in predominantly volcanic sequences on the basis of their matrix-supported texture and/or finer matrix grain size.

Three peperitic intervals were observed at Site U1374:

- Unit V: interval 330-U1374A-5R-4, 99 cm, to 6R-1, 91 cm (29.69–30.31 mbsf), is a 62 cm thick peperitic interval with bioclast- and micrite-bearing volcanoclastic limestone (Fig. F8B). The bioclasts consist of shell fragments and red algae. Thin section observations (Sample 330-U1374A-5R-4, 102–106 cm [Thin Section 121]) indicated that the sediment is characterized by a cementation pattern similar to that found in the basalt breccia and volcanic sandstone of Units VII, IX, and XI, with occurrences of fringing zeolite cement, fringing calcite cement, and sparry calcite cement.
- Unit X: interval 330-U1374A-16R-2, 130 cm, to 17R-3, 84 cm (87.32–90.62 mbsf), is a 3.30 m thick predominantly peperitic interval with cemented bioclast-bearing basalt sandstone. The bioclasts consist mostly of shell fragments, red algae, and annelids. Microscope observations (Samples 330-U1374A-17R-1, 9–12 cm [Thin Section 142], and 17R-3, 78–81 cm [Thin Section 144]) indicated that the sandstone is characterized by a cementation pattern similar to that found in the basalt breccia and volcanic sandstone of Units VII, IX, and XI and the peperitic interval of Unit V.
- Unit XII: interval 330-U1374A-22R-5, 24 cm, to 24R-4, 48 cm (116.45–124.59 mbsf), is an 8.14 m thick predominantly peperitic interval with bioclast-bearing basalt sandstone and volcanoclastic limestone with bioclasts. The bioclasts include

shell fragments, red algae, and annelids. The peperitic interval grades transitionally into the overlying grayish basalt conglomerate with bioclasts of Subunit XIB.

In addition, several thin-bedded sedimentary intervals were observed in the volcanic basement:

- Unit XII: interval 330-U1374A-27R-2, 10–45 cm (136.66–137.01 mbsf), contains a 35 cm thick monolithic, grain-supported grayish basalt breccia with a matrix composed of cemented coarse basalt sandstone.
- Unit XII: interval 330-U1374A-29R-2, 10–107 cm (146.19–146.98 mbsf), contains a 97 cm thick monolithic, matrix-supported grayish basalt breccia with a matrix composed of cemented coarse basalt sandstone without fossils. Thin section observations (Sample 330-U1374A-29R-2, 41–45 cm [Thin Section 168]) showed that the finer grained sediment is composed of basalt and altered glass fragments with plagioclase.
- Unit XIII: interval 330-U1374A-31R-5, 8–43 cm (168.67–169.02 mbsf), is a 35 cm thick monolithic, matrix-supported grayish basalt breccia with a matrix composed of cemented coarse basalt sandstone without fossils. Thin section observation (Sample 330-U1374A-31R-5, 28–32 cm [Thin Section 174]) showed that the finer grained sediment is composed of basalt and altered highly vesicular glass fragments with plagioclase.
- Unit XIII: interval 330-U1374A-31R-6, 56–67 cm (170.64–170.75 mbsf), is an 11 cm thick sedimentary interval that is texturally and compositionally similar to the interval of grayish matrix-supported basalt breccia above.
- Unit XIII: interval 330-U1374A-32R-1, 0–8 cm (172.70–172.78 mbsf), is an 8 cm thick sedimentary interval that is texturally and compositionally similar to the interval of grayish matrix-supported basalt breccia above.
- Unit XIII: interval 330-U1374A-32R-1, 79–106 cm (173.49–173.76 mbsf), is a 27 cm thick sedimentary interval that is texturally and compositionally similar to the interval of grayish matrix-supported basalt breccia above.
- Unit XIII: interval 330-U1374A-32R-3, 35–60 cm (175.92–176.17 mbsf), is a 25 cm thick sedimentary interval that is texturally and compositionally similar to the interval of grayish matrix-supported basalt breccia above (Fig. F8A).
- Unit XIII: interval 330-U1374A-36R-3, 43–47 cm (195.09–195.13 mbsf), is a 4 cm thick grayish basalt sandstone.
- Unit XIV: interval 330-U1374A-43R-6, 7.5–82 cm (256.75–257.49 mbsf), is a 74.5 cm thick grain-supported micrite-bearing greenish-black basalt breccia with few bioclasts. Thin section observations (Samples 330-U1374A-43R-6, 33–36 cm [Thin Section 193], and 43R-6, 70–74 cm [Thin Section 194]) showed that the sediment contains abundant angular red algae, common shell fragments, minor foraminifers, and altered vesicular glass fragments. The occurrence of this sedimentary interval corresponds to the appearance downhole of a distinct sequence of aphyric basalt breccia (see “[Igneous petrology and volcanology](#)”).
- Unit XVI: interval 330-U1374A-47R-3, 5–100 cm (290.32–291.27 mbsf), is a 95 cm thick grain-supported micrite-bearing greenish-black basalt breccia with few bioclasts. Thin section observations (Sample 330-U1374A-47R-3, 20–80 cm [Thin Section 201]) showed that the sediment contains abundant variously preserved glass fragments, few shallow-marine bioclasts (e.g., echinoderms, red algae, and bryozoans), and rare foraminifers. The occurrence of this sedimentary interval corresponds to the appearance downhole of an extended sequence of moderately plagioclase-augite-olivine-phyric and plagioclase-phyric basalt breccia with abundant aphyric intrusive sheets of basaltic composition (see “[Igneous petrology and volcanology](#)”).

Fine-grained sediments consisting mostly of basalt and vitric sandstones were observed throughout the predominantly volcanic sequence of Hole U1374A as infill deposits between larger clasts of basalt breccia (Fig. F8C–F8E). Locally, geopetal structures were formed by the infill of sediment and later calcite cement (see point 2 in Fig. F8C). Rare shallow-marine bioclasts and micrite were locally found in infill deposits down to 121.28 mbsf (Fig. F4).

Interpretation of lithologies and lithofacies at Site U1374

Eight lithofacies were defined in Units I, II, VII, IX, and XI, permitting overall characterization of the environment of deposition of the sediment and stratigraphic development at Site U1374 on Rigil Guyot (Figs. F4, F5).

Lithofacies 1 corresponds to the grain-supported grayish basalt conglomerate with bioclasts of Subunits IIE and XIB. It is characterized by the occurrence of (1) rounded basalt clasts and bioclasts, (2) abundant shallow-marine bioclasts, and (3) cement textures indicative of a vadose environment. These observations are strong indications that the

sediment of Lithofacies 1 was deposited in a shallow-marine, subtidal to intertidal environment.

Lithofacies 2 comprises the multicolor basalt breccia of Subunits VIIA and VIIC. This lithofacies is characterized by the occurrence of shallow-marine fossils and fibrous zeolite-calcite cements and the lack of micrite content. These characteristics suggest that Lithofacies 2 reflects emplacement of debris flows in a shallow-marine environment.

Lithofacies 3 includes the multicolor volcanic sandstone of Subunits IIB and IIC. It is characterized by (1) the occurrence of hemipelagic to shallow-water fossils; (2) an essentially monomict composition with highly vesicular, partly reworked vitric fragments with olivine; (3) extensive bioturbation; (4) diffuse layering with large-amplitude cross-bedding structures (Subunit IIC only); and (5) fibrous cement. These observations suggest that Lithofacies 3 represents subaerial to shallow-marine volcanic products deposited or reworked in a shallow-marine to hemipelagic environment. More abundant bioclasts and burrows as well as occurrences of micrite were observed in Subunit IIB, which suggests deposition in a low-energy, possibly hemipelagic environment.

Lithofacies 4 corresponds to Subunits VIIB and XIA and is characterized by the occurrence of multicolor volcanic sandstone with few bioclasts. The volcanic sandstone of Lithofacies 4 is compositionally and texturally distinct from that of Lithofacies 3 in that (1) it is mostly composed of poorly to moderately vesicular vitric fragments with abundant plagioclase, and (2) its texture is characterized by strong to diffuse layering with few basalt pebbles. The consistency of layering and the absence of cross-beds and scour structures, as well as gradational transitions between well-layered and poorly layered intervals, suggest that sediment in Lithofacies 4 was deposited in a hyperconcentrated flow(s), a process hydrodynamically intermediate between a dilute stream flow (such as turbidites) and a debris flow (Smith and Lowe, 1991). This mode of emplacement possibly reflects dilution of a debris flow progressing in a submarine environment (e.g., Kataoka, 2005).

Lithofacies 5 includes Unit IX and is composed of fossil-barren heterolithic basalt breccia and volcanic sandstone. Textural and compositional characteristics of these sediments, as well as the nature of underlying and overlying sedimentary and volcanic intervals (see [“Igneous petrology and volcanology”](#)) likely indicate that Lithofacies 5 reflects emplacement of debris flows into a shallow-marine or subaerial environment.

Lithofacies 6 includes the foraminiferal bioclast limestone of Subunit IID and corresponds to a condensed section with possibly several hardground surfaces that developed between the late Campanian and late Maastrichtian (see [“Paleontology”](#)). Occurrences of keeled forms of planktonic foraminifers suggest that the sediment originally was deposited at hemipelagic depth (see [“Paleontology”](#)). On the other hand, the sediment contains abundant shallow-marine bioclasts and rounded basalt pebbles, as well as cement and dissolution textures characteristic of diagenesis in a subtidal to intertidal environment. Also, the upper boundary of Subunit IID corresponds to an erosional surface, and this subunit includes burrows filled with the volcanic sandstone of Subunit IIC (Lithofacies 3). On the basis of these observations, Lithofacies 6 was interpreted to record (1) the initial drowning of a formerly oceanic island at Site U1374, which allowed formation of a condensed interval with several ferromanganese-phosphate encrustations of Subunit IID, and (2) the emergence in a later stage of the previously deposited condensed interval, which is recorded by cement and dissolution textures, an erosional upper boundary, and burrows filled with substantially younger volcanic sandstone.

Lithofacies 7 includes the multicolor volcanic sandstone of Subunit IIA. Characteristic features of Lithofacies 7 are occurrences of (1) very angular glass fragments forming the bulk of the sediment, (2) high vesicularity and pumiceous texture of the glass, and (3) several layers with subhorizontal normal grading. On the basis of these observations, we interpret Lithofacies 7 to reflect deposition of possibly air fall or shallow-water volcanic products in a submarine environment with limited postdepositional reworking.

Lithofacies 8 includes Unit I and is predominantly composed of sandy foraminiferal ooze. This lithofacies corresponds to the youngest deposit found at Site U1374 (see [“Paleontology”](#)) and reflects pelagic sedimentation on the flat-topped Rigil Guyot.

Another lithofacies corresponds to the deepest fossil-bearing sedimentary intervals found at Site U1374 (Unit XIV [256.75–257.49 mbsf] and Unit XVI [290.32–291.27 mbsf]). This lithofacies is characterized by the occurrence of micrite-bearing basalt conglomerate with angular fragments of red algae and other shallow-marine biota. It was interpreted to represent shallow-marine sediment deposition on the flank of a former oceanic island.

The stratigraphic distribution of the above-described lithofacies and lithologies provides some significant

constraints on the development and evolution of Rigil Guyot at Site U1374 (Fig. F9). Although the deepest occurrence of sediment observed in volcanic basement (Unit XVI; 290.32–291.27 mbsf) was deposited in submarine conditions, the fossil content provides clear evidence for the occurrence of nearby subaerial conditions at the time of deposition. Similarly, sediments found in Subunits IIE–XIB (Lithofacies 1, 2, 4, and 5) indicate a nearby subaerial to shallow-marine environment of deposition between 116.45 and 15.31 mbsf. On the basis of these observations and the nature of the volcanic sequences (see [“Igneous petrology and volcanology”](#)), we propose that the entire interval from 290.32 to 15.31 mbsf (Units XVI–IIE) records growth of the drilled volcano in subaerial to shallow-submarine conditions. Possibly, the first occurrence of fossil-bearing sediment at 291.27 mbsf may correspond to an unconformity indicative of the shoaling of the island away from Site U1374 and toward the center of this volcanic edifice (see [“Igneous petrology and volcanology”](#)). The deepest clear occurrence of subaerial conditions at Site U1374 was found in Subunit XIB (110.28–116.45 mbsf; Lithofacies 1) and possibly records the first emergence of the drilled volcano at Site U1374. Coeval occurrences of shallow-marine bioclasts and volcanic deposits above Subunit XIB uphole to 29.69 mbsf (including the fossil-bearing peperitic interval of Unit III) define an ~87 m thick interval (116.45–29.69 mbsf) that was deposited under more consistent subaerial (and still shallow submarine) conditions. This interval may have resulted from (1) occasional subsidence of the oceanic island during discontinuous supply of sedimentary and volcanic materials at Site U1374, (2) significant eustatic changes, and (3) occurrence of unrecovered or unrecognized erosional surface(s).

Significantly, bedding and layering structures below 16.70 mbsf (Unit III and below) at Site U1374 dip consistently with a moderate angle, whereas dips above 16.70 mbsf (Unit II) are mostly subhorizontal (see [“Structural geology”](#)). This observation and the deposition of the basalt conglomerate of Subunit IIE in a subtidal to intertidal environment suggest that the Unit II/III boundary at 16.70 mbsf corresponds to a major erosional surface. We interpret this surface to record wave-induced flattening of the drilled volcano at Site U1374. In this interpretation, a thick volcanic sequence was possibly deposited on top of Unit III but completely eroded before emplacement of Subunit IIE.

Deposition of Subunit IIE was followed by sedimentation of Subunit IID (Lithofacies 6), which was deposited in a hemipelagic environment between the late Campanian and late Maastrichtian and was

probably subjected to subtidal to intertidal conditions in the late Maastrichtian (see above). Although occurrence of a condensed interval in Subunit IID most likely reflects initial drowning of the drilled seamount at Site U1374, the exact cause of possible later emergence in Subunits IIC, IIB, and IIA needs to be constrained by additional dating and correlation with possible similar events elsewhere in the Pacific. Possibly, these repeated emergence/drowning events in Subunit IID occurred in response to some significant eustatic changes in the latest Cretaceous (see [“Paleontology”](#)).

A second drowning event of the former island is recorded by the volcanic sandstone of Subunits IIB and IIC (Lithofacies 3) that contains shallow-marine fossils, foraminifers, radiolarians, and ammonite fragments. The volcanic sandstone of Subunits IIA–IIC (Lithofacies 3 and 7) is interpreted as a possible record of rejuvenated volcanism on Rigil Guyot on the basis of (1) a significant age span (at least ~6–11 m.y.) between emplacement of lava flows in Unit III (late Campanian or older) and volcanic sandstone in Subunits IIA–IIC (late Maastrichtian); (2) the occurrence of highly vesicular olivine-rich glass fragments in Subunits IIA–IIC, which are clearly distinct from moderately vesicular plagioclase-rich glass fragments found in volcanoclastic deposits in Unit III and below; and (3) the pristine habit of vitric fragments and the occurrence of graded, subhorizontal beds found in Subunit IIA (Lithofacies 7), which possibly indicate the occurrence of volcanic material initially produced in a shallow-marine to subaerial environment. Deposition of Unit II was followed by a condensed interval with ferromanganese-phosphate encrustations at 6.64 mbsf. Finally, deposition of sandy foraminiferal ooze (Lithofacies 8) represents the last record of sedimentation on top of Rigil Guyot, which occurred in a pelagic environment during the Pleistocene to Holocene (see [“Paleontology”](#)).

In summary, the volcano-sedimentary sequences recovered at Site U1374 (Units I, II, VII, IX, XI, and other sedimentary intervals and infill deposits) represent an extended record of the stratigraphic development of Rigil Guyot. Our preliminary interpretation suggests the following, from oldest to youngest:

1. Submarine volcanic development on the flank of a former oceanic island with input from a nearby subaerial environment likely toward the (higher) center of the volcanic island (Unit XII and deeper; 522.00–116.45 mbsf), indicative of shoaling of the island, first at its center and later at Site U1374 toward its western flank;
2. Shallow-marine to subaerial emplacement of volcanoclastics on the slope of a former oceanic island (Units XI–III; 116.45–16.70 mbsf);

3. Formation of a major erosional surface on top of Unit III at 16.70 mbsf, indicating true subaerial conditions;
4. Onset of deposition of the sedimentary cover in a subtidal to intertidal environment (Subunit IIE; 16.70–15.31 mbsf);
5. Initial drowning of the former volcanic island at Site U1374 with deposition of a condensed section with ferromanganese-phosphate encrustations in the late Campanian (Subunit IID; 15.31–15.05 mbsf);
6. Reemergence of this former island at Site U1374 prior to or during the late Maastrichtian, with formation of another erosional surface at 15.05 mbsf;
7. Second drowning of the island and rejuvenated volcanism in the late Maastrichtian and possibly younger times (Subunits IIA–IIC; 15.05–6.64 mbsf);
8. Formation of a second condensed interval with ferromanganese-phosphate encrustations at 6.64 mbsf (top of Unit II, undated); and
9. Deposition of pelagic sediment on top of the guyot in the Pleistocene to Holocene (Unit I; 6.64 mbsf to seafloor).

Paleontology

The first core of Hole U1374A contained 6.64 m of unconsolidated pelagic sediment (Unit I), with an additional 0.62 m of volcanic sandstone at the bottom (upper portion of Subunit IIA). The unconsolidated sediment is composed of tan winnowed foraminiferal ooze with a small amount of fine fraction, suggesting deposition under relatively strong ocean-bottom currents. Low natural gamma radiation also indicates a paucity of clay minerals throughout the pelagic sedimentary interval of Unit I (see “[Physical properties](#)”). The sediment recovered in Unit I contains abundant planktonic foraminifers together with calcareous nannofossils in the fine fraction. Shipboard examination of the microfossils from Core 330-U1374-1R was conducted on samples recovered from section halves. Preliminary age estimations are summarized in Figure [F10](#) and Tables [T3](#) and [T4](#).

Beneath the Pleistocene–Holocene unconsolidated sediment of Unit I, consolidated sequences of igneous and sedimentary rocks were recovered, including Units II, VII, IX, and XI. Smear slides and thin sections prepared from these sedimentary units and additional thin sections containing sediment recovered from igneous sequences were examined for microfossil biostratigraphy. Preliminary age estimations are summarized in Figure [F10](#) and Tables [T5](#) and [T6](#). Al-

though age-diagnostic microfossils were not observed in the barren Units III–XIX, the preliminary ages of Subunits IIB–IIC and IID were estimated to be late Maastrichtian and late Campanian, respectively.

Calcareous nannofossils

Unit I

Initial examination of the pelagic sediment of Unit I at Rigil Guyot revealed a fairly homogeneous assemblage, likely the result of the soupy character of the sediment, the sloshing of the unconsolidated material in the core liner, as well as some degree of mechanical disturbance caused by rotary coring, which together allowed for movement of the nannofossils through the length of the core. In general, the pelagic cap recovered in Hole U1374A contains calcareous nannofossil assemblages of Pleistocene to Holocene age (Zones CN13–CN15).

Samples of pelagic sediment (Unit I) were taken from the 99–100 cm intervals of Sections 330-U1374A-1R-1 through 1R-4, with an additional sample from Section 1R-5 at 30–31 cm. All nannofossil samples exhibit moderate preservation. Small geophyrocapsids are abundant in all samples and compose the majority of the assemblage relative to all other species. Because of their extremely small size, definite determination of individual species is best done with onshore scanning electron microscopy. The Pleistocene species *Ceratolithus cristatus* (Zones CN13–CN15) appears in all samples, though its occurrence is rare. The late Pleistocene form *Ceratolithus telesmus* (first occurrence in Subzone CN14b) was found in rare abundance in most samples (Table [T3](#)). In Sample 1R-5, 30–31 cm, it occurs with *Helicosphaera sellii* (last occurrence in Subzone CN13b). The nonconcurrent intervals of these two species support an interpretation of mechanical disturbance or reworking. Neogene background species *Helicosphaera kamptneri* and *Calcidiscus leptoporus* occur frequently throughout Unit I. Sediment that settled through the core liner into the core catcher of Section 1R-5 was examined for calcareous nannofossil content. Small *Gephyrocapsa* and *Pseudoemiliania lacunosa* compose the majority of the calcareous nannofossils present. Given this, the sediment of Unit I was preliminarily assigned to Zones CN13–CN15 (Pleistocene–Holocene).

Unit II

In addition to the uncemented pelagic sedimentary samples taken for shipboard analysis, samples of consolidated sediment from Cores 330-U1374A-2R and 3R in Unit II, obtained from razor blade scrapings, were examined. A sample of dark brownish

fine-grained sandstone from Subunit IIC (Section 2R-4, 32 cm) was found to be nearly barren; two specimens of *Micula concava* were found. A sample obtained from volcanoclastic sandstone of Subunit IIC, which is interpreted to be burrow infilling in Subunit IID (Sample 3R-1, 70 cm; see below), contains other Cretaceous species in rare abundances. Preliminary investigation revealed the presence of *Nephrolithus frequens*, indicative of Zone CC26, among other Late Cretaceous species; therefore, the preliminary age of this sediment within Subunit IIC was assigned as latest Cretaceous (late Maastrichtian) (Table T5). Additional samples from this interval were taken for detailed postexpedition study in order to refine these biostratigraphic age assignments.

Planktonic foraminifers

Unit I

The planktonic foraminiferal biostratigraphy of Unit I was based on analysis of five samples from Sections 330-U1374A-1R-1, 1R-2, 1R-4, and 1R-5 that consist of sandy foraminiferal ooze (see “Sedimentology”). Only a small amount of fine fraction was washed away during the washing procedure, indicating that this sediment is composed mainly of foraminiferal tests. Indeed >50% of the washed sediment was composed of foraminiferal tests. Although Sample 1R-5, 60–62 cm (6.60 mbsf), is slightly consolidated and dark grayish brown, all other samples are unconsolidated and pale brown. Some foraminiferal tests in Sample 1R-5, 60–62 cm, display moderate preservation, with calcite overgrowth on test surfaces. With the exception of this sample, all others contain relatively well preserved foraminifers. Although foraminiferal specimens with glassy preservation are present, most tests are brownish in appearance. The chambers of all specimens are not filled with calcite, but the sutures of a few are. Foraminiferal preservation and abundance are shown in Table T4. Zonal assignments summarized in Figure F10 show correlation of Unit I to the Pleistocene–Holocene.

All samples examined from Unit I contain *Globorotalia* (*Globoconella*) *inflata*, *Globorotalia* (*Truncorotalia*) *crassaformis*, *Globorotalia* (*Truncorotalia*) *truncatulinoides*, and *Orbulina universa*. Additionally, *Globigerina bulloides*, *Globigerinoides ruber*, *Globorotalia* (*Globorotalia*) *tumida*, and *Globorotalia* (*Hirsutella*) *scitula* are present in some samples (Table T4). On the basis of the occurrence of *Gr. (T.) truncatulinoides*, Sample 330-U1374A-1R-5, 60–62 cm, is correlated to planktonic foraminiferal Zones PL6–PT1b (Pleistocene–Holocene) (Fig. F10).

Unit II

Consolidated volcanic sandstone (Sample 330-U1374A-1R-CC) from Subunit IIA was also analyzed. Although some benthic foraminifers and sea urchin spines were observed, no planktonic foraminiferal tests were found in the washed residue. In addition to these standard analyses, thin sections prepared from consolidated sediment were examined for planktonic foraminiferal content. Of 31 thin sections examined, only 1 thin section from Subunit IIB, 1 from Subunit IID, 2 from Subunit XIB, 2 from Unit XIV, and 1 from Unit XVI contained planktonic foraminifers (Table T6).

Subunit IIB

Sample 330-U1374A-2R-4, 27–32 cm (13.70 mbsf; Subunit IIB), contained *Globotruncanita* cf. *conica*, *Globotruncanita* cf. *stuarti*, and other planktonic foraminifers with globular and keeled morphologies. Although planktonic foraminifers are not common in thin sections, the preservation of those observed is relatively good (Fig. F11). Planktonic foraminifers are embedded in both the micritic part and the calcite cement. In addition, some gastropods and radiolarians were observed in the same sample. Planktonic foraminifers were also found in the infilling sediment within gastropod fossils, which exhibit a horizontal geopetal structure (see “Sedimentology”). Although zonal marker species were not found, the occurrence of *Gl. cf. conica*, which has a stratigraphic range from the *Gansserina gansseri* Zone to the *Abathomphalus mayaroensis* Zone, indicates that Subunit IIB, including this sample, can be correlated to the late Campanian–Maastrichtian (Caron, 1985). The overlying Subunit IIA contains no planktonic foraminifers or macrofossils, so the age of this subunit cannot be identified.

Subunit IID

Sample 330-U1374A-3R-1, 70–72 cm (15.10 mbsf), in Subunit IID contains *Globotruncanella* sp., *Radotruncana* cf. *calcarata*, and other planktonic foraminifers with globular and keeled morphologies. This sample is composed of limestone (see detailed description below) and contains many macrofossil bioclasts and common planktonic foraminifers in its micritic matrix. Although the foraminiferal specimen shown in Figure F12A is not sectioned in the equatorial plane, the spines at the posterior end of each chamber identify it as *R. cf. calcarata*. On the basis of this species' occurrence, the preliminary age of Subunit IID was assigned as late Campanian (75.2–75.7 Ma) (Fig. F10).

Units V, VII, and X

Although some macrofossil bioclasts were found in Units V, VII, and X, no planktonic foraminifers were observed in Units III–X. Samples 330-U1374A-21R-4, 76–80 cm (111.34 mbsf), and 22R-1, 2–6 cm (111.22 mbsf), from Unit XI contain rare planktonic foraminifers with a globular morphology, but no zonal marker species were found (Table T6). Foraminifers with globular and biserial morphologies were also found from Unit XIV. However, most of these foraminifers are dissolved, making taxonomic identification difficult. Nonetheless, a few individuals are relatively well preserved, so these samples will be reanalyzed for further taxonomic and age identification postexpedition.

Macrofossils

In addition to planktonic foraminifers, three ammonoid fossils were discovered in Subunits IIC and IID (Figs. F13, F14, F15). Thin Section 112, taken from Sample 330-U1374A-2R-4, 88–91 cm (14.31 mbsf), in Subunit IIC contains one juvenile ammonoid fossil (Fig. F13). Although its outer shell wall is dissolved, at least two septa were observed. The shell diameter of this individual is 1.1 mm. Because of its size and the divergent septa observed, implying prosepium, this specimen appears to be a hatchling. The second ammonoid fossil from Subunit IIC was found in Sample 3R-1, 23 cm (14.63 mbsf) (Fig. F14), and is preserved underneath a convex-upward bivalve fragment. Three septa and the shell wall of this specimen were visible on the section-half surface. Because this sample was found in the archive half only, further nondestructive analysis will be conducted postexpedition. The third ammonoid fossil was found within the limestone of Subunit IID in Sample 3R-1, 69 cm (15.09 mbsf) (Fig. F15). The diameter of this specimen is estimated to be ~1 cm. Two suture lines were clearly observed on the surface of the working half of the core. The taxonomy of this fossil will be examined postexpedition. The occurrence of ammonoid fossils indicates that Subunits IIC and IID were deposited prior to the end of the Cretaceous, which is consistent with the occurrence of the late Campanian–Maastrichtian foraminifers from Subunit IIB.

Lithostratigraphy and biostratigraphy of Subunits IIC and IID

A complex contact relation was observed between the limestone of Subunit IID (15.05–15.31 mbsf) and the sandstone of Subunit IIC (13.78–15.05 mbsf), which both overlies Subunit IIB and also appears in two burrow infills in the limestone (Fig. F16). Within these two subunits both late Maastrichtian nanno-

fossils (Subunit IIC in burrow infill at 15.10 mbsf) and late Campanian planktonic foraminifers (Subunit IID at 15.10 mbsf) were identified. Although these two samples were collected from the same depth, the stratigraphic ranges of these microfossils (Zone CC26 for nannofossils and *R. calcarata* Zone for planktonic foraminifers) do not overlap (Fig. F17). Subunits IIC and IID are underlain by a basaltic boulder/cobble interval (Subunit IIE) that in some places is coated with relatively thick ferromanganese crusts. On the basis of its texture, color, and chemical composition, the limestone (Ls) in this 11 cm interval can be divided into five sublithologies next to the sandstone (Ss) of Subunit IIC and the basalt cobbles (Ba) of Subunit IIE and manganese crusts (Mn) (Fig. F16). Ls1a consists of fossiliferous micritic limestone from which Thin Section 113 (Sample 330-U1374A-3R-1W, 70–72 cm) was made. Brownish-colored Ls1b, composed of phosphatized limestone, overlies Ls1a. Ls1b is overlain by ferromanganese encrustations with a possible erosional surface, which is overlain by Ls2, including a fragment of the ferromanganese crust and two basalt pebbles. Although not clearly seen, the boundary between Ls2 and overlying Ls3 might again be defined by the ferromanganese encrustations. This limestone sequence from Ls1a–Ls1b to Ls3 is overlain by volcanoclastic sandstone of Subunit IIC at a potential erosional surface. The most interesting feature in this limestone sequence is the quasi-trapezoidal window developed at interval 3R-1, 68–70 cm (Fig. F16). This window is filled with volcanoclastic sandstone of Subunit IIC and Ls4 limestone, and the upper boundary is again encrusted by a thin ferromanganese layer. On the basis of thin section analyses, the lower boundary between Ls1a and Ls4 shows dissolution and a reprecipitation texture, which indicates subaerial dissolution and intertidal cementation (see “Sedimentology”).

The occurrence of *R. cf. calcarata* from Sample 330-U1374A-3R-1, 70 cm, indicates that the Ls1a limestone was deposited during the late Campanian (75.2–75.7 Ma) (Fig. F17). Although the expected paleolatitude of this seamount is relatively high (likely between 45°–51°S; Koppers et al., 2010), the occurrence of keeled globotruncanid foraminifers indicates that the generalized tropical-temperate biostratigraphic zonal scheme is applicable to this site (Caron, 1985). Smear slides made from Sample 3R-1-NANNO 1, 70 cm (α in Fig. F16A), in Ls1a (Subunit IID) are barren of nannofossils, but Sample 3R-1-NANNO 2, 70 cm (β in Fig. F16A), in Ss (Subunit IIC) contains *N. frequens*, indicating nannofossil Zone CC26, which suggests that the volcanoclastic sandstone infills found in the quasi-trapezoidal window

were deposited in the latest Maastrichtian (65.0–65.8 Ma) (Figs. F16, F17). Because the first occurrence datum of *N. frequens* is regarded as globally diachronous, it is correlated to Zones CC25–CC26 in the southern high latitudes (Watkins et al., 1996; Bown, 1998) (Fig. F17). Therefore, the maximum age of the volcanoclastic sandstone infills, together with overlying Subunit IIC, are assigned to the late Maastrichtian (65.0–69.2 Ma). The biostratigraphic age of the Subunit IID limestone and the overlying Subunit IIC volcanoclastic sandstone indicates that the completion of this highly condensed limestone-volcanoclastic cap sequence took 6–9 m.y. (Fig. F17).

At least three eustatic sea level falls were identified in the late Campanian–Maastrichtian at ~72.0, ~68.5, and ~66 Ma (Fig. F17). The potential multiple dissolution cavities or erosional surfaces developed in the Subunit IID limestone may be correlated to these eustatic sea level fluctuations. Considering the significant lithologic change between the Subunit IID limestone sequence and the Subunit IIC volcanoclastic sandstone, the erosional contact between the two may be correlated to the largest sea level fall at ~66 Ma. Precise age estimation and evolution of the depositional environment need to be further analyzed with postexpedition research.

Preliminary age estimation for Site U1374

Unit I of Site U1374 includes material from the Pleistocene–Holocene only (Fig. F10), which differs from the late Miocene–Holocene range of Unit I at Site U1372 on Canopus Guyot (see Fig. F14 in the “Site U1372” chapter [Expedition 330 Scientists, 2012b]). Although their ages are slightly different, the sedimentary covers of both seamounts are composed of winnowed foraminiferal ooze with only a small percentage of fine fraction. Preservation of foraminiferal tests and foraminiferal abundance in comparison to the total sediment grains at these two sites are also quite similar, indicating that both sites have diachronously equivalent sequences of pelagic sedimentation.

The age of Subunit IIA at this site is as yet undetermined with microfossil biostratigraphy. However, the lithology and grain assemblage of Subunit IIA are comparable to those of Subunits IIB and IIC, suggesting that Subunits IIC–IIA may represent a successive sequence (see “Sedimentology”). The occurrence of a thick ferromanganese deposit at the top of Subunit IIA (Section 330-U1374A-1R-5, 64 cm) most likely indicates a time gap between unconsolidated Unit I and consolidated Subunit IIA. Because of the large difference in age, a sharp unconformity (possibly <60 m.y.) is likely present between the uncemented

pelagic sediment of Unit I and the multicolored volcanic sandstone of Subunit IIA.

Planktonic foraminiferal biostratigraphy indicates that Subunit IIB is correlated to *Ga. gansseri*–*A. mayaroensis* Zone (upper Campanian–Maastrichtian). Nonetheless, nannofossil *N. frequens*, indicative of Zones CC25–CC26 (upper Maastrichtian), was found in underlying Subunit IIC, which indicates that the age of Subunit IIB is correlated to the late Maastrichtian (Fig. F10).

Because the age of the volcanoclastic sandstone of Subunit IIC and the limestone of Subunit IID can be estimated as late Maastrichtian and late Campanian, respectively, a significant time gap was identified between Subunits IIC and IID. Subunit IID is mainly composed of basalt pebbles, pure limestone, phosphatized limestone, and ferromanganese crusts (Fig. F16). The composition of this limestone is quite similar to that of Subunit IIB at Site U1372. Although Subunit IIB at Site U1372 was recovered as fragmented pieces and the Subunit IIB/IIC boundary was not recovered, it is also composed of basalt pebbles, pure limestone, phosphatized limestone, and ferromanganese crusts (see “Sedimentology” in the “Site U1372” chapter [Expedition 330 Scientists, 2012b]; see also XL3_EVAL.PDF in XRF in “Supplementary material”). Although the preliminary ages of these limestones differ slightly, the Subunit IID limestone at Site U1374 potentially might be correlated to the Subunit IIB limestone at Site U1372. If this correlation is possible, the phosphatization and ferromanganese encrustation in both limestones might be considered synchronous events. Further discussion of this synchronicity and the cause of the phosphatization and encrustation events requires more precise age determinations and correlations. These analyses will be conducted postexpedition.

Igneous petrology and volcanology

In Hole U1374A, 474.9 m of igneous rock (excluding sedimentary interbeds) was penetrated after the igneous basement was reached at 16.7 mbsf. The igneous sequence was divided into 148 lithologic units, which were grouped into 15 stratigraphic units (Units III–VIII, X, and XII–XIX; Fig. F18). Two sedimentary units (Units IX and XI; 21.03 and 6.59 m thick, respectively) and three thinner sedimentary layers with a combined thickness of 2.81 m are included in the basement section. The uppermost igneous basement begins with a 1.3 m thick flow of olivine-augite-plagioclase-phyric basalt, followed downhole by a series of aphyric basalt lava flows and

volcanic breccias that compose Units III–VII. Below this, the hole is dominated by poorly sorted volcanic breccia. The breccia contains numerous basalt cooling units that could be lava flow lobes or larger clasts. Units XVI–XIX are cut by a series of steeply inclined to vertical intrusive sheets of aphyric basalt. To help achieve the paleomagnetic objectives of this expedition, each of the more massive igneous lithologic units was assigned an in situ confidence index (ISCI) following the procedures described in “**Igneous petrology and volcanology**” in the “Methods” chapter (Expedition 330 Scientists, 2012a). The lithologic units and their ISCI values are summarized in Table T7. In this section we briefly describe the types of igneous clasts found in the sedimentary units, followed by a description of each of the igneous units and our interpretation of the entire igneous succession.

Basaltic clasts in sedimentary Units II, IX, and XI

The larger basaltic clasts within the conglomerate and breccia of Units II, IX, and XI were divided into 12 types on the basis of their appearance in hand specimen. Each clast type is described below, together with the sedimentary subunit(s) in which it was found (see “**Sedimentology**”):

- Type 1 (Subunits IID, IIE, IXA, IXC, and XIB): highly olivine-pyroxene-phyric basalt that is medium gray and mottled orange and green, with 10% olivine phenocrysts (completely altered to iddingsite; maximum size = 10 mm, modal size = 4 mm) and 3% pyroxene phenocrysts (unaltered; maximum size = 8 mm, modal size = 3 mm). The groundmass is fine grained, with 1% vesicles (moderate sphericity, subrounded).
- Type 2 (Subunits IIE and IXC): highly olivine-phyric basalt that is medium gray and mottled orange, with 10% olivine phenocrysts (completely altered to iddingsite; maximum size = 7 mm, modal size = 3.5 mm). The groundmass is fine grained, with 0.1% vesicles (high sphericity, rounded).
- Type 3 (Subunits IID, IIE, IXA, and IXC): aphyric basalt that is medium gray, with 1% olivine microphenocrysts (altered; maximum size = 0.5 mm, modal size = 0.2 mm). The groundmass is fine grained, with 2% vesicles (low sphericity, subangular).
- Type 4 (Subunits IXA, IXB, and IXC): sparsely olivine-phyric basalt that is medium gray to medium reddish gray, with 1% olivine phenocrysts (altered). The groundmass is fine grained, with 10%–20% vesicles.
- Type 5 (Subunits IXA and IXC): aphyric basalt that is medium gray, with 0.2% olivine (altered). The groundmass is fine grained, with 15% vesicles.
- Type 6 (Subunits IXA, IXB, and IXC): basaltic froth in small (modal size = 5 mm) angular clasts that are pale yellow, with 1% olivine (altered) and 0.1% hornblende. The clasts have an aphanitic texture and a vesicularity of 60%.
- Type 7 (Subunits IXA and IXC): very highly olivine-phyric basalt that is mottled orange-gray, with 30% olivine phenocrysts (altered; maximum size = 8 mm, modal size = 4 mm) and 1% pyroxene phenocrysts (unaltered; maximum size = 5 mm, modal size = 3 mm). The groundmass is fine grained, with 5%–10% vesicles (high sphericity, rounded).
- Type 8 (Subunits IXA, IXB, and IXC): sparsely olivine-phyric basalt that is medium gray, with 1% olivine phenocrysts (altered; maximum size = 4 mm, modal size = 1.5 mm), small feldspar laths, and 1% vesicles (high sphericity, rounded).
- Type 9 (Subunits IXA, IXC, XIA, and XIB): aphyric basalt that is medium gray and fine grained, with 0.5% vesicles (elongate, rounded).
- Type 10 (Subunits IXB and IXC): moderately olivine-phyric basalt that is medium gray, with 3% olivine phenocrysts (altered; maximum size = 6 mm, modal size = 2 mm) and 0.5% pyroxene phenocrysts (unaltered; maximum size = 5 mm, modal size = 3 mm). The groundmass is fine grained, with 3% vesicles (elongate, rounded).
- Type 11 (Subunit XIB): moderately plagioclase-olivine-phyric basalt that is greenish medium gray, with 3% plagioclase phenocrysts, 2% pyroxene phenocrysts, and 0.8% olivine phenocrysts (altered). The groundmass is fine grained, with 1% vesicles.
- Type 12 (Subunit XIB): moderately pyroxene-olivine-phyric basalt that is greenish medium gray, with 3% pyroxene phenocrysts, 2% olivine phenocrysts (altered), and 0.5% plagioclase phenocrysts. The groundmass is fine grained, with 1% vesicles.

Lithologic and stratigraphic igneous units

Unit III

Interval: Sections 330-U1374A-3R-2, 89 cm, to 3R-3, 76 cm

Depth: 16.72–18.04 mbsf

Lithology: highly olivine-augite-plagioclase-phyric basalt

Lithologic unit: 1

The conglomerate of Subunit IIE sits on the eroded but apparently unweathered surface of a 1.32 m basalt body, interpreted as a lava flow, that forms Unit III. The original flow top is not preserved at the contact, but fine-grained matrix sand from the overlying conglomerate has infiltrated into cracks (Fig. F19). The lava flow is conspicuously porphyritic, with large olivine and titanite phenocrysts and smaller phenocrysts of plagioclase (Fig. F20). One of the titanite phenocrysts examined in thin section contains an inclusion of hornblende (Fig. F20D), one of only two occurrences of amphibole recorded at Site U1374.

Unit IV

Interval: Sections 330-U1374A-4R-1, 0 cm, to 5R-4, 99 cm

Depth: 20.40–29.69 mbsf

Lithology: aphyric basalt

Lithologic unit: 2

A 2 m thick interval without core recovery separates Units III and IV. The latter unit consists of a single 9.29 m thick aphyric basalt lava flow that in thin section is seen to be composed largely of tiny flow-aligned plagioclase laths, titanite crystals, and some altered groundmass olivine (e.g., Sample 330-U1374A-5R-2, 137–139 cm [Thin Section 120]). There are no phenocrysts. Core recovery in this unit was virtually 100%.

Unit V

Interval: Sections 330-U1374A-5R-4, 99 cm, to 6R-4, 34 cm

Depth: 29.69–33.98 mbsf

Lithology: aphyric basalt breccia

Lithologic unit: 3

Unit V is a 4.29 m thick layer of basalt breccia, the upper 62 cm of which consists of aphyric basalt clasts mingled with bioclast-bearing micrite (see “[Sedimentology](#)”). This sediment-lava mingling may be peperitic (Fig. F21A). Some of the aphyric basalt clasts below the peperitic layer have altered glassy margins, radial cracks at their edges, rare pipe vesicles, and occasional vesicular patches in their centers. Because Unit V is composed of aphyric basalt clasts similar to those forming the more massive units above and below, it is difficult to determine whether Unit V is a separate volcanoclastic entity or is derived from the mingling of Unit IV and/or VI lava flows with wet sediment.

Unit VI

Interval: Sections 330-U1374A-7R-1, 0 cm, to 7R-3, 72 cm

Depth: 34.20–37.60 mbsf

Lithology: aphyric basalt and breccia

Lithologic units: 4–5

Unit VI consists of a 3.25 m thick aphyric basalt lava flow and a lower 15 cm of breccia that is probably the base of the lava flow. Its upper contact with the volcanic breccia of Unit V was not recovered. The breccia at its base has a micritic-sandy matrix.

Unit VII

Interval: Sections 330-U1374A-7R-3, 72 cm, to 8R-3, 52 cm

Depth: 37.60–41.84 mbsf

Lithology: aphyric lithic-vitric sandstone and breccia

Lithologic units: 6–7b

The brecciated base of Unit VI sits on, and mixes with, the top of a 4.24 m thick interval of palagonitized volcanoclastic sandstone composed of aphyric basalt fragments and occasional bioclasts. The sandstone in lithologic Unit 6 has well-defined bedding inclined at angles of up to 25° to horizontal (see “[Structural geology](#)”). An interval of coarser (up to 5 cm) clasts occurs in interval 330-U1374A-8R-1, 84–94 cm. The base of Unit VII (lithologic Subunit 7b) consists of a sparsely olivine-rich basalt breccia with a vitric-lithic volcanic sand matrix that includes bioclasts. Although the phenocryst assemblage in the clasts is similar to that in the unit below, this lithologic unit is grouped with Unit VII on the basis of its sedimentologic features. Further details regarding Unit VII are given in “[Sedimentology](#).”

Unit VIII

Interval: Sections 330-U1374A-8R-3, 52 cm, to 12R-4, 100 cm

Depth: 41.84–63.67 mbsf

Lithology: moderately olivine-phyric breccia

Lithologic unit: 8

Unit VIII is a 21.83 m thick interval of breccia composed of moderately olivine-phyric basalt clasts as large as 22 cm that contain occasional large, sieve-textured plagioclase phenocrysts. The breccia is mostly clast supported; most of the clasts are angular, but some have altered glassy margins. Spaces between clasts are either filled with calcite and zeolite cement or are open. Open-work patches of breccia are noticeably more oxidized than the areas that are cemented. Grains <2 mm are largely absent. The upper contact of Unit VIII may be gradational with Unit VII. The lower contact was not recovered.

Unit IX

Interval: Sections 330-U1374A-12R-4, 100 cm, to 16R-1, 10 cm

Depth: 63.67–84.70 mbsf

Lithology: sedimentary interval

Sedimentary basalt breccia and sandstone separate the olivine-phyric basalts of Unit VIII from Unit X, which consists of aphyric basalt. This sedimentary interval does not include bioclasts. For more details, see [“Sedimentology.”](#) Basaltic clast Types 1–10 are found in the breccia and sandstone. In particular, this unit contains abundant small clasts of pale yellow, altered frothy basalt glass (Type 6).

Unit X

Interval: Sections 330-U1374A-16R-1, 10 cm, to 21R-3, 59 cm

Depth: 84.70–109.86 mbsf

Lithology: aphyric basalt and breccia

Lithologic units: 9–14

Unit X is 25.16 m thick and consists of a 2.71 m thick aphyric basalt lava flow overlying aphyric basalt breccia. Within the breccia are two intervals of massive aphyric basalt interpreted as thin flow lobes that are 1.15 and 1.10 m thick. Clasts in the uppermost 3.30 m of breccia are mingled with a basaltic sand sediment matrix, and some clasts resemble pillows (Fig. [F21B](#)). These clasts may have formed through interaction between magma and wet sediment and, if so, the breccia could be a peperitic base to the lava flow above (see [“Sedimentology.”](#)). In the rest of Unit X the breccia is mostly clast supported, and most of the clasts are angular, as in Unit VIII. Spaces between clasts are either filled with calcite and zeolite cement or are open, again showing distinctive alteration differences between the open-work and cemented zones. As with Unit VIII, grains <2 mm are largely absent from the breccia matrix. Some of the basalt clasts in Unit X contain glass and unaltered groundmass olivine (Fig. [F22](#)).

Unit XI

Interval: Sections 330-U1374A-21R-3, 59 cm, to 22R-5, 24 cm

Depth: 109.86–116.45 mbsf

Lithology: sedimentary interval

Unit XI is another sedimentary interval consisting of two subunits: a thin upper subunit of basaltic sandstone and a 6.17 m subunit of basalt conglomerate, which includes bioclasts. Unit XI grades upward into Unit X and is defined by the dominance of sediment matrix. Thin sections show that the conglomerate is made up of glassy aphyric basalt clasts cemented by carbonate (Sample 330-U1374A-21R-3, 19–21 cm [Thin Section 150]). For a full description of this unit, see [“Sedimentology.”](#) Basaltic clast Types 11

and 12 are found only in this unit, where they occur together with clast Types 1, 5, and 9.

Unit XII

Interval: Sections 330-U1374A-22R-5, 24 cm, to 29R-2, 15 cm

Depth: 116.45–146.06 mbsf

Lithology: highly olivine-plagioclase-augite-phyric basalt and breccia

Lithologic units: 15–31

The polyolithic conglomerate of Unit XI grades down-hole into monolithic breccia that defines the top of Unit XII, the upper limit of which is defined by a weathered horizon. Lithologic Units 15–19 (interval 330-U1374A-22R-5, 24 cm, to 24R-4, 20 cm) are peperitic breccia with a central, incompletely recovered 2.08 m thick interval of massive basalt (lithologic Unit 16), which might be an in situ lava flow. The peperitic breccia is composed of basalt mingled with sandy sediment (Fig. [F21C](#)) containing bioclasts (see [“Sedimentology.”](#)). Seven additional intervals of massive basalt, ranging in thickness from 0.17 to 0.36 m, were recovered within Unit XII, but it is uncertain whether or not they cooled in situ. Overall, the breccia of Unit XII is more poorly sorted than that in Units VIII and X, and the clasts commonly have irregular outlines (Fig. [F23A](#)), suggesting that they are primary volcanic clasts rather than broken and transported lava fragments. The breccia and massive basalt intervals that form Unit XII are highly plagioclase-olivine-augite-phyric and contain large (up to 20 mm) plagioclase phenocrysts that frequently show signs of resorption and are filled with interconnecting inclusions of dark glass (Fig. [F24](#)).

Unit XIII

Interval: Sections 330-U1374A-29R-2, 15 cm, to 43R-6, 7.5 cm

Depth: 146.06–256.75 mbsf

Lithology: sparsely to moderately olivine-phyric basalt and breccia ± plagioclase and/or augite

Lithologic units: 32–87

The uppermost lithologic unit of Unit XIII is a 1.12 m thick layer of a sedimentary basalt breccia supported by a sandy matrix that does not contain bioclasts (see [“Sedimentology.”](#)). The rest of Unit XIII consists of basaltic breccia, in places supported by a sandy matrix (lithologic Units 55 and 57). The breccia contains 27 massive basalt bodies that may be lava lobes or larger fragments in the breccia. These basalt bodies range in thickness from 0.13 to 2.16 m. Some of the smaller bodies in the upper part of this unit have altered glassy margins, vesicular cores, and radial fractures (e.g., lithologic Unit 36), and occasionally have irregular protruding margins.

These features are consistent with in situ lobes or pillows. Some of the lava bodies are autobrecciated (lithologic Units 72–74) and capped by breccia with a sandy matrix (lithologic Units 73 and 74). Most of the breccia, however, is composed of large angular basalt fragments and is free of fine material. Some of these clasts have broken edges, broken altered margins, and sharp contacts with the groundmass, suggesting that they were transported. Spaces between clasts are either empty or filled with calcite and zeolite (Fig. F23B). The basalt bodies and clasts in the breccia are largely olivine-phyric, with most units containing 1–5 vol% olivine phenocrysts, although thin sections (Samples 330-U1374A-29R-4, 17–19 cm [Thin Section 169]; 29R-4, 107–110 cm [Thin Section 170]; and 31R-6, 20–22 cm [Thin Section 175]) show that olivine is absent from, or forms only a minor part of, the phenocryst assemblage in a few clasts. There are also intervals where plagioclase and/or augite join the phenocryst assemblage (Fig. F25A, F25B). One sample (32R-4, 2–5 cm) contains a single 2 mm aggregate of pyroxene and magnetite with the characteristic amphibole outline (Fig. F25C, F25D), suggesting it was a hornblende phenocryst that became unstable in its magmatic environment. Lithologic Unit 84, 9.81 m above the base of Unit XIII, is a 40 cm thick basalt interval that is moderately plagioclase-phyric (Fig. F18). This is the first significant interval encountered downhole in which olivine is absent from the phenocryst assemblage since Unit X, 136.68 m higher in Hole U1374A.

Unit XIV

Interval: Sections 330-U1374A-43R-6, 7.5 cm, to 45R-8, 10 cm

Depth: 256.75–278.73 mbsf

Lithology: aphyric to moderately plagioclase-phyric basalt breccia

Lithologic unit: 88

As with Unit XIII, the top of Unit XIV is defined by a thin (74 cm) sedimentary interval, in this case grain-supported, micrite-bearing, greenish-black basalt breccia with occasional bioclasts (see “[Sedimentology](#)”). Unit XIV is basalt breccia in which many of the clasts exhibit reasonably well preserved glassy margins and could therefore be fragments of pillows (Fig. F26). Occasionally, the clasts are supported by a sandy matrix, but most of the spaces between the clasts are voids filled by calcite and zeolite. Many of the clasts in this unit have sharp broken edges, suggesting transportation. The top of this unit marks a significant downhole change in magmatic character from the predominantly olivine-phyric basalt in the overlying units to plagioclase-phyric and aphyric basalts below (Fig. F18).

Unit XV

Interval: Sections 330-U1374A-45R-8, 10 cm, to 47R-3, 5 cm

Depth: 278.73–290.32 mbsf

Lithology: aphyric basalt and breccia

Lithologic units: 89–91

The top of Unit XV is defined by the disappearance of phenocrysts. Otherwise, the breccia resembles that of Unit XIV in being composed of large angular clasts that may be fragments of pillows (Fig. F26B). As with Units VIII, X, XIII, and XIV, the breccia is clast supported, lacks fine material, and is cemented with calcite and zeolite.

Unit XVI

Interval: Sections 330-U1374A-47R-3, 5 cm, to 53R-5, 87 cm

Depth: 290.32–351.66 mbsf

Lithology: moderately plagioclase-augite-olivine-phyric basalt and breccia with aphyric intrusive sheets

Lithologic units: 92–104

In interval 330-U1374A-47R-3, 4–6.5 cm, the fines-free breccia of Unit XV rests on an inclined surface of sandy breccia that marks the upper boundary of Unit XVI (Fig. F27). This interval is the top of a 95 cm thick sedimentary interval of grain-supported, micrite-bearing, greenish-black basalt breccia with occasional bioclasts and is the deepest interval in Hole U1374A in which bioclasts were found (see “[Sedimentology](#)”). Clasts in Unit XVI are generally less angular than in overlying units and frequently have rounded lobate margins. Only three massive basalt intervals thicker than 30 cm were recovered in Unit XVI (Fig. F18). This unit is marked by increasingly green fragments making up the breccia. The first record of a greenish color in the description of igneous rocks in this hole is just below the sedimentary interval at the top of this unit. The green color appears to reflect increasing amounts of fine altered glass particles (hyaloclastite) filling the spaces between the clasts within the breccia, rather than the pore spaces being empty or filled by light-colored secondary minerals. Initially, the two types of breccia are interspersed, but from the top of lithologic Unit 100 until the bottom of the hole, the breccia is mostly supported by an altered green hyaloclastite matrix. At the top of Unit XVI and in several intervals in the rest of Hole U1374A the clasts are more strongly altered, giving the breccia an orange color. The increasing dominance of green altered hyaloclastite matrix down through Unit XVI and the rest of the hole is seen clearly in the color reflectance data (Fig. F28B). The breccia is composed of plagioclase-augite-olivine-phyric basalt. Unit XVI also contains the first

of a series of aphyric basalt intrusive sheets (lithologic Unit 103) that were encountered at Site U1374. These are described separately in [“Intrusive sheets.”](#)

Unit XVII

Interval: Sections 330-U1374A-53R-5, 87 cm, to 56R-1, 118.5 cm

Depth: 351.66–375.19 mbsf

Lithology: aphyric basalt breccia with aphyric intrusive sheets

Lithologic units: 105–107

Clasts of aphyric basalt start to appear at the bottom of Unit XVI in Section 330-U1374A-53R-3 and become more abundant throughout Sections 53R-4 and 53R-5. The disappearance of clasts of porphyritic basalt at Section 53R-5, 87 cm, defines the upper boundary of Unit XVII. The greenish color noted in the lower part of Unit XVI persists through the upper 2 m of Unit XVII and is then followed downhole by a 7.3 m thick interval in which the smaller clasts are orange in color as a result of alteration of glass to clays and iron oxyhydroxides. This orange zone coincides with an interval in which the breccia is mostly clast supported, the clasts are blockier, and the spaces between clasts are free of fine particles. Increased permeability in this interval probably facilitated circulation of seawater, which caused the observed oxidation. The breccia becomes green again at Section 54R-6, 20 cm (361.90 mbsf), and remains green or greenish gray to the bottom of the hole (Fig. [F28B](#)). A notable feature of Unit XVII is the appearance at Section 54R-6, 140 cm (363.10 mbsf), of highly vesicular and often frothy clasts of altered basaltic glass that are found throughout the lower 12.1 m of the unit. Unit XVII contains another intrusive sheet of aphyric basalt (lithologic Unit 106).

Unit XVIII

Interval: Sections 330-U1374A-56R-1, 119 cm, to 63R-3, 140 cm

Depth: 375.19–445.02 mbsf

Lithology: sparsely to moderately plagioclase-phyric basalt and breccia with aphyric intrusive sheets

Lithologic units: 108–134

The abrupt return of plagioclase phenocrysts at Section 330-U1374A-56R-1, 119 cm, defines the upper boundary of Unit XVIII, which consists mostly of basaltic breccia with eight short (0.32–0.86 m) intervals of massive basalt. Clasts in the breccia are subangular to subrounded and often have lobate margins (Fig. [F23C](#)). Frothy clasts, first seen in the lower 12.1 m of Unit XVII, are also present in the upper 3.8 m of Unit XVIII, down to Section 56R-4, 80 cm

(379.03 mbsf). An angular aphyric basalt clast was noted at Section 60R-7, 95 cm (421.4 mbsf), and aphyric basalt clasts increase steadily in abundance downhole from this point. Unit XVII contains several aphyric basalt intrusive sheets: lithologic Units 116, 120, 122, 124, 125 (interpreted as the peperitic margin of lithologic Unit 124), 126, and 128.

Unit XIX

Interval: Sections 330-U1374A-63R-4, 0 cm, to 73R-1, 81 cm

Depth: 445.02–521.81 mbsf

Lithology: aphyric to moderately plagioclase-phyric basalt and breccia

Lithologic units: 135–148

The base of a 0.86 m thick massive plagioclase-phyric basalt fragment or lava lobe at the bottom of Section 330-U1374A-63R-3 is taken as the upper boundary of Unit XIX because this is the last occurrence downhole of a significant interval of plagioclase-phyric basalt and because angular aphyric basalt clasts become more abundant than lobate plagioclase-phyric clasts around this depth. The last plagioclase-phyric basalt clast was found at Section 63R-7, 90 cm (449.8 mbsf), and thereafter the breccia is composed entirely of aphyric basalt clasts. The transition from the lobate plagioclase-phyric clasts of Unit XVIII to the angular aphyric clasts of Unit XIX occurs over an interval of 13.5 m.

The upper part of Unit XIX is composed of angular aphyric basalt clasts in a matrix of altered hyaloclastite. From Sections 330-U1374A-65R-4, 103 cm (465.23 mbsf), to 66R-1, 22 cm (470.12 mbsf), the hyaloclastite matrix is progressively replaced by calcite cement and the breccia grades into an interval with large jigsaw-fit clasts of aphyric basalt. This interval may represent the remains of an autobrecciated lava flow. Hyaloclastite matrix returns below this interval; the breccia in the lower part of Unit XIX ranges from clast- to matrix-supported, and in two intervals (69R-1, 0 cm, to 69R-4, 28 cm; and 71R-2, 71 cm, to 72R-1, 55 cm) it becomes sufficiently fine grained to be described as vitric-lithic sandstone and gravel-size breccia. The frothy clasts of altered basaltic glass noted in the lower part of Unit XVII and the upper part of Unit XVIII are found again in the lower part of Unit XIX (Sections 66R-1, 22 cm [470.12 mbsf], to 72R-1, 55 cm [518.45 mbsf]). An example of hyaloclastite breccia from the lower part of Unit XIX is shown in Figure [F23D](#). Within Unit XIX five intrusive sheets of aphyric basalt were recovered (lithologic Units 136, 139, 140, 146, and 148). Drilling at Site U1374 terminated in the last of these intrusive sheets at 522 mbsf.

Intrusive sheets

A maximum of 13 intrusive sheets were intersected in interval 330-U1374A-52R-1, 0 cm, to 73R-1, 81 cm (lower part of Unit XVI and Units XVII, XVIII, and XIX). These sheets are composed almost entirely of fine-grained aphyric basalt, although discrete patches of phenocrysts were observed in a few of them. The uppermost sheet drilled (lithologic Unit 103) contains scattered plagioclase phenocrysts in the 1.89 m of interval 52R-1, 0 cm, to 52R-2, 52 cm. Lithologic Unit 126 contains a 13 cm interval (60R-2, 105–128 cm) of sparsely plagioclase-phyric basalt, and in lithologic Unit 146 there is a 12.5 cm interval (71R-2, 23.5–36 cm) of altered olivine phenocrysts (<1%). Some observed contacts dip at 50°–60°, but others are subvertical to vertical. The sheets have bands of small vesicles aligned parallel to their margins, and this allows the orientation of sheets to be assessed in cases where the margin was not recovered. The number of observed and inferred vertical contacts suggests that the sheets are dikes. In two cases the margins are peperitic, and in one of these the peperite is separated from a second intrusion by a thin sliver of green breccia. Examples of these contact relations are shown in Figure F29. The sheets are composed of fine-grained aphyric basalt with rather altered plagioclase laths and titanite prisms. Some samples contain partly resorbed microphenocrysts of plagioclase. The mineralogy of the sheets suggests that the parent magma was moderately to strongly alkaline.

The two lowest intrusive sheets in Hole U1374A (lithologic Units 146 and 148) have several physical characteristics that distinguish them from the other sheet units:

1. They do not contain vesicles, whereas the other sheets have bands of small vesicles parallel to their margins.
2. They are more massive and less altered than the other sheets.
3. The lower contact of lithologic Unit 146 and the upper contact of lithologic Unit 148, which were both recovered, are more irregular than the contacts of the other sheets.

Downhole logging, however, shows that the upper contact of lithologic Unit 146 dips at 60° in the direction of 141°, whereas the lower contact dips at 43° toward 166° (see “[Downhole logging](#)”). The dips are similar to those observed in the intrusions higher in Hole U1374A and suggest that lithologic Unit 146 is also an intrusive feature. Lithologic Unit 148 occurred at the bottom of the hole, so logging was not possible; however, because this unit shares many physical features with lithologic Unit 146, it is also likely to be an intrusive sheet. More detailed postex-

pedition investigations will determine whether these two lithologic units are compositionally similar to the unequivocally intrusive sheets and whether any of the sheets can be matched to stratigraphic units higher in the eruptive sequence.

Interpretation of the igneous succession at Site U1374

The igneous rocks encountered during drilling of Hole U1374A on the western flank of Rigil Guyot will be interpreted in chronological order (oldest first, from the bottom of the hole). These rocks reflect basaltic eruptions that cover the interval from the late submarine constructional phase of the seamount to its emergence as an island. The drilled succession probably accumulated in a volcanoclastic apron around the seamount, similar to but larger than the extensive submarine volcanoclastic fans observed in a recent (2007) multibeam bathymetric survey around the emergent island of Surtsey, off the south coast of Iceland (Fig. F30) (Jakobsson et al., 2009).

The deepest part of the cored succession comprises a >76.8 m interval of volcanic breccia (Unit XIX), dominated in its lower part by hyaloclastite containing angular clasts of aphyric basalt and smaller fragments of frothy basaltic glass, now altered to green clay. Frothy basalt fragments imply that the melt was degassing and fragmenting on eruption and therefore that the magma was emplaced into water shallow enough for magmatic volatiles to be exsolved. The exact depth depends on the original volatile content of the magma, and the occurrence of volatile-induced fragmentation does not provide a useful limit on depth of emplacement because submarine volcanoclastic rocks are now known to form even in deep water (e.g., Head and Wilson, 2002; Clague et al., 2009). The first conglomerates formed in a sub-aerial environment are found ~400 m above the volcanoclastic rocks at the bottom of Hole U1374A, providing an estimate of the minimum water depth at which the lowest volcanoclastic rocks were emplaced. This can only be a minimum estimate because of the possibility of unrecognized erosion surfaces in the volcanoclastic succession. Postexpedition research will enable us to investigate the processes of degassing and fragmentation of the lava in Hole U1374A in more detail.

A gradational change in clast type from aphyric and blocky to plagioclase-phyric and lobate marks the transition to Unit XVIII. This change in clast morphology could reflect a change in the style of eruption and/or magma composition. Unit XVIII contains several intervals of massive basalt that could represent thin flow lobes. The frothy basaltic clasts

noted in the lower part of Unit XIX return in the upper 3.8 m of Unit XVIII and the lower 12.1 m of the overlying Unit XVII, which is defined by a return to blocky, angular aphyric basalt clasts.

A second return to plagioclase-phyric basalt, now with the addition of augite and minor olivine phenocrysts, marks the beginning of Unit XVI, which, like Unit XVIII, is also composed of lobate clasts. Breccia in the lower part of the unit has a green hyaloclastite matrix, but this becomes less prominent uphole through the unit and is a minor component by 328 mbsf. This reduction in the abundance of green hyaloclastite is followed, 37 m farther upsection, by the first appearance of bioclasts in the thin (95 cm) sandy layer at the top of Unit XVI. The presence of bioclasts implies shallow-water conditions nearby and is taken to indicate shoaling of parts of the seamount at a distance from Site U1374 (see [“Sedimentology”](#)).

The lower 186 m of the succession drilled in Hole U1374A is intruded by intrusive sheets of aphyric basalt that we interpret as dikes. We have no way of knowing at this stage how much higher in the succession these dikes extend because they were not encountered at higher levels and we cannot match their composition to any of the lava flows or breccia units that were drilled (see [“Geochemistry”](#)). They could have extended to levels higher than the present guyot surface, or they could have been truncated at a yet-unrecognized erosion surface higher in the succession than 336 mbsf.

The thin sandy layer at the top of Unit XVI is the first of five sedimentary intervals encountered in Hole U1374A, each of which marks the end of a distinctive magmatic episode (Units XVI, XV/XIV, XIII, XII, and X). Units XV and XIV are composed of basaltic breccia and represent the third cycle of aphyric to plagioclase-phyric basalt magmatism. Clasts vary from angular to lobate, and at least some are probably pillow fragments (Fig. [F26](#)). The green hyaloclastite matrix that was so prominent in the lower units is now completely absent. Instead, the breccia is clast supported and the voids between clasts are either open or filled with calcite and/or zeolite. The complete absence of massive basalt intervals that might represent in situ lava lobes suggests that these units could be a talus deposit composed of pillow debris derived from shallow-submarine eruptions higher up on the flanks of the emergent island.

Unit XIV ends with a thin (74 cm) sandy interval that marks a change in the character of the basalt from relatively evolved (plagioclase-phyric or aphyric) below to more magnesium-rich (olivine-phyric) above. Olivine dominates the phenocryst as-

semblage from this interval to the top of Hole U1374A. The basalt of Unit XIII is sparsely to moderately olivine-phyric, occasionally with plagioclase and augite phenocrysts (Fig. [F25A](#), [F25B](#)) and rare euhedral pyroxene-magnetite intergrowths (Fig. [F25C](#), [F25D](#)). The latter are most probably hornblende phenocrysts that have broken down through dehydration reactions. Hornblende is unlikely to have crystallized from the host magma, so these intergrowths provide evidence for mixing with a more evolved magma type not represented by any of the igneous rocks encountered in the two holes drilled on Rigil Guyot.

Unit XIII is mostly basaltic breccia, but, unlike the two preceding units, it has a large number of more massive intervals that have preserved a consistent magnetic inclination (see [“Paleomagnetism”](#)). The fragmentation of lava flows in a subaqueous environment through a process of contact-surface steam explosivity (Kokelaar, 1986) provides a plausible mechanism for the formation of this assemblage of breccia and more massive intervals. In this process, magma becomes coated with a thin film of superheated steam, which expands and collapses on a very short timescale. Kokelaar (1986) argues that the resulting stress waves “can result in magma fragmentation and produce blocky, pyramidal or splinter-like fragments.” A photograph of a typical example of Unit XIII breccia is given in Figure [F23B](#). This breccia may have formed through the fragmentation of lava erupted into water, followed by transport of the fragments downslope to form a talus deposit. This could explain the lack of fine particles but not the presence of what we have described tentatively as lava lobes within Unit XIII, the largest of which preserves consistent magnetic orientations (see [“Paleomagnetism”](#)). A solution to this problem might be that the lava “lobes” are actually large blocks that were still hot enough at their final resting places to preserve a record of the ambient magnetic field.

Unit XIII ends with another thin (1.12 m) sandy horizon, which probably represents a hiatus in magmatic activity at this site. The next episode of volcanism produced Unit XII, a breccia deposit with two thin (~1 m) lava lobes and capped by a 2.7 m thick lava flow, all composed of olivine-augite-plagioclase-phyric basalt. Plagioclase phenocrysts in Unit XII are conspicuous in their large size (up to 2 cm) and disequilibrium textures. Many have rounded outlines, corroded margins, and sieve textures caused by incorporation of glassy groundmass into an interconnected network of aligned and angular inclusions (Fig. [F24](#)). Magma mixing provides a plausible explanation for these disequilibrium features. Shore-based studies will investigate this further.

The volcanoclastic deposits change significantly from the blocky breccia of Unit XIII to more scoriaceous material in Unit XII (Fig. F23A). A likely explanation is that Unit XII was the product of hydrovolcanic eruptions resulting from the interaction of lava flows with either wet sediment or shallow water. In either case the deposits could have fallen from a subaerial tephra plume on the emergent island. The peperitic base and top of the capping lava flow (Fig. F21C) indicate interaction of magma with wet sediment.

The end of Unit XII magmatism is marked by a 6.6 m thick conglomerate unit (Unit XI) that is the first deposit with an unequivocally terrestrial provenance encountered upsection at Site U1374. This provides further evidence that Site U1374 was finally at or close to sea level (see “[Sedimentology](#)”). Unit X repeats the style of Unit XII volcanism, with its scoriaceous breccia and thin flow lobes capped by a lava flow with a peperitic base (Fig. F21B), all composed of aphyric basalt. The end of volcanism in Unit X is marked by another thicker (21 m) sedimentary deposit (Unit IX).

Large sieve-textured plagioclase phenocrysts return in Unit VIII, a hydrovolcanic deposit of moderately olivine-phyric basalt clasts. Plagioclase phenocrysts, though conspicuous, account for <1% of the total phenocrysts. Units VII, VI, V, and IV are, respectively, finely bedded volcanic sandstone, a 3.25 m thick lava flow, volcanic breccia, and a 9.3 m thick lava flow, all composed of aphyric basalt. The Unit V breccia contains jigsaw-fit intervals and is clearly peperitic at the top (Fig. F21A). It is probably the base of the thick Unit IV lava flow. The whole assemblage suggests eruption of basaltic magma into a wet but probably not submarine environment. The final volcanic event recorded at Site U1374 is represented by a thin (1.3 m) lava flow of olivine-augite-plagioclase-phyric basalt. One of the augite phenocrysts in this flow contains an inclusion of hornblende, although hornblende was not seen as a primary phenocryst phase in any of the rocks studied at Sites U1374 or U1373. This provides further evidence for the availability of hornblende-bearing magmas at the time of formation of the Site U1374 succession.

Four patterns emerge from our study of the volcanic basement rocks at Site U1374:

1. Magmatism on the western flank of Rigil Guyot started in a clearly submarine environment and, in the time interval considered here, progressed to a shallow-marine and then subaerial environment. This progression is clearly seen in the various breccia types recovered at Site U1374 (Fig. F23), which range from green hyaloclastite breccia with frothy basaltic clasts (marine), to blocky breccia (shallower marine), to scoriaceous (near

sea level or subaerial) basalt. The proportion of lava flows increases upsection, and peperite is only found in the upper units (Units III–XII). Note that the short succession drilled at Site U1373, nearer to the center of Rigil Guyot, was erupted entirely in a subaerial (but occasionally wet) environment.

2. Distinct eruptive packages are separated by intervals of background sedimentation, five of which were identified at Site U1374. The thicknesses of these intervals increase dramatically when the seamount is inferred to have grown above sea level and erosion could proceed more rapidly (see “[Sedimentology](#)”).
3. The phenocryst assemblage changes from plagioclase-dominated in the lower part of the succession (Units XIV–XIX) to olivine-dominated in the upper part (Units III–XIV), suggesting that the magmas became more basic with time.
4. The magma erupted at Site U1374 was alkalic throughout the drilled interval, but there is some evidence that the later basalt flows were more alkalic than the earlier ones. Basalt from Units III and XII contains titanite, whereas the augite in Units XV and XVI is bottle green in hand specimen and greenish brown in thin section, suggesting Ti-poor ferroaugite. Shore-based studies will determine the exact composition of the pyroxenes.

Alteration petrology

Nineteen stratigraphic units were identified at Site U1374 on Rigil Guyot. The sequence includes 3 sedimentary units and 16 units of volcanic breccia, lava flows, and dikes (see “[Igneous petrology and volcanology](#)”). The entire section of basaltic rock has undergone alteration by low-temperature water-rock interactions or weathering. The overall alteration of the volcanic rocks ranges from slight to complete (5%–95%; Fig. F31), as estimated from core descriptions and thin section observations. Alteration at Site U1374 resulted primarily in replacement of olivine and volcanic glass. In contrast, plagioclase and augite are generally well preserved, both as phenocrysts and groundmass, throughout the entire igneous portion of the core. Plagioclase shows minor alteration to sericite/illite in some rocks but characteristically is fresh. Olivine is typically completely altered to iddingsite, hematite, Fe oxyhydroxides, and carbonates in the uppermost 350 m of core, and at greater depths it is primarily replaced by green clay (Fig. F32). Nevertheless, unaltered olivine was found in Unit XIII, and moderately fresh olivine occurs in Units XII–XIII (Fig. F32). In some cases fresh

olivine and glass were also observed in thin sections (Table T8).

Alteration phases

We distinguished four main groups of alteration minerals in Hole U1374A:

1. Phyllosilicate minerals such as smectite (saponite, nontronite, and montmorillonite), illite, celadonite, and vermiculite are abundant secondary phases (Fig. F33A–F33D). These were identified using optical microscopy and X-ray diffraction (XRD).
2. Carbonates are also abundant secondary minerals as infillings in vesicles, voids, and veins (Fig. F34A–F34C). They sometimes present a botryoidal habit (Fig. F33E). XRD analyses of whole rocks, veins, and vesicles suggest a predominance of Mg calcite (e.g., Samples 330-U1374A-9R-4, 19–21 cm; 9R-4, 108–110 cm; 10R-3, 35–37 cm; 22R-2, 140–143 cm; 25R-2, 8–10 cm; 25R-4, 17–20 cm; 28R-2, 0–4 cm; 29R-1, 47–50 cm; 30R-3, 56–58 cm; and 37R-2, 68–70 cm).
3. Other secondary phases are mostly zeolites (Figs. F33F, F34D–F34F), mainly phillipsite (identified using XRD analyses of Samples 330-U1374A-10R-4, 80–82 cm; 22R-2, 140–143 cm; 25R-2, 8–10 cm; 28R-2, 0–4 cm; and 30R-3, 56–58 cm), analcite (Sample 67R-4, 58–60 cm), natrolite (Sample 68R-5, 73–74 cm), and gmelinite (Sample 68R-5, 73–74 cm). Thaumasite ($\text{Ca}_3\text{Si}[\text{OH}]_6[\text{CO}_3][\text{SO}_4] \cdot 12\text{H}_2\text{O}$), which is a hydrated silicate mineral occurring often with zeolites, was detected by XRD in Samples 59R-6, 74–76 cm; 67R-4, 58–60 cm; 68R-5, 73–74 cm; and 68R-5, 90–91 cm (Figs. F35, F36).
4. Fe oxyhydroxides (Fig. F37A–F37C), hematite, maghemite (Fig. F35), and goethite (Fig. F33F) are also present at various locations in the core, with pyrite being more common in the lowermost 200 m, mostly found within the groundmass and the fractures of the sheet intrusions (Units XVI–XIX).

Overall alteration characteristics

The overall alteration of groundmass ranges from 5% to 95%, as estimated by core description (Fig. F31). The entire hole is very heterogeneous, with slightly to highly altered intervals occurring intercalated from top to bottom. A gradual increase in the degree of groundmass alteration was observed down to 60 mbsf (Units III–VIII), followed by a sequence of highly variable alteration from 60 to ~240 mbsf, below which an overall poorly defined downhole trend to slightly less alteration was observed. Throughout this lower interval, the majority of alteration is slight to moderate, but several intervals of high alteration

are present even at these depths (Fig. F31). Relatively fresh basalt (<20% alteration) is present throughout the core but becomes more abundant below 400 mbsf in the intrusive sheets of Units XVIII and XIX.

On the basis of core descriptions and thin section observations, we defined three general alteration groups: slightly altered gray basalts and two types of pervasive alteration. The main characteristic used to define these pervasive alteration groups is either grayish-brown/reddish-brown or greenish alteration colors (discussed below). Representative logs displaying the distribution of alteration colors with depth are given in Figures F38 and F39.

Gray basalt

Slightly altered gray basalt occurs throughout Hole U1374A. This basalt tends to be in thin units in the uppermost 300 m and becomes relatively abundant only lower in the hole in Units XVIII and XIX. The groundmass of this gray basalt is slightly altered to fine-grained brown and green minerals that are difficult to identify in thin section and will be referred to simply as clay minerals. Pyroxene and plagioclase are relatively fresh. Olivine is often partially replaced by green clay, iddingsite, and Fe oxides (Figs. F32, F40, F41), but some has moderate to high degrees of preservation (Table T8). Some fresh glass is present in several sections (discussed below). In particular, the intrusive sheets in Units XVII and XIX are only slightly altered, yet they exhibit tiny grains of pyrite in the groundmass, veins, and sometimes in vesicles.

Grayish-brown to reddish-brown alteration

Grayish-brown to reddish-brown alteration was observed mainly in the uppermost 350 mbsf of Hole U1374A in a series of basalt breccias extending downhole to Unit XVI. This alteration is not persistent throughout the entire portion of the core and is interrupted in places by greenish alteration that occurs sporadically throughout this interval. Slightly altered basalt occurs throughout this interval. This alteration group is characterized by carbonates, zeolites, and minor brown clay minerals. Olivine is mostly altered to iddingsite, hematite, Fe oxyhydroxides, and brown clay (Fig. F32).

Basalts with greenish alteration

Greenish alteration is present sporadically in the uppermost 340 m of Hole U1374A, with occurrences in only a few thin intervals. However, it becomes dominant below 360 mbsf, where the clay minerals (saponite, nontronite, and montmorillonite) are the dominant alteration minerals of the groundmass. Degree of alteration varies in these rocks, and zeolites are abundant in the more highly altered basalts. Pyrite is

relatively common, especially along vein walls in association with clay minerals.

Brown halos

Throughout Hole U1376A we observed the presence of brown halos, typically 1–5 mm thick, sometimes associated with veins. The halos also appear on chilled margin contacts or surrounding the least altered basalt clasts. Their color ranges from light yellowish brown to dark reddish brown. The brown halos formed by the alteration of basalts by bottom seawater percolating through the oceanic basement (halmyrolysis; Mahoney, Fitton, Wallace, et al., 2001), which takes place at water temperatures of <2°C and under large water/rock ratios and oxidizing conditions. Such alteration is commonly found in permeable basaltic formations such as hyaloclastite and breccia.

Vesicle infillings

Most of the basaltic flows and clasts from Site U1374 contain up to 10% vesicles, with abundance decreasing with depth. The highest percentage of vesicles, reaching 50%, was found in clasts in Cores 330-U1374A-55R and 66R (Units XVI and XVII). Below 384 mbsf, vesicles are rarer. Throughout the entire core most vesicles are partly filled with secondary minerals (Fig. F42), predominantly carbonates and zeolites (Fig. F34). Although carbonates are more common in the uppermost 370 mbsf, zeolites are the most abundant infilling mineral at greater depths (Figs. F34D, F42). Clay minerals (e.g., saponite) often line the vesicle walls, with carbonate and zeolite filling the interiors of the vesicles (Figs. F43, F44). Some intervals have clay formation followed by the crystallization of well-formed acicular or botryoidal crystals of zeolite (Fig. F44B–F44F). The clay becomes progressively darker with depth, with green (smectite) and white clay to ~300 mbsf, followed by black clay to the bottom of the hole. We note an important interval of green to blue-green clay and phyllosilicate minerals (nontronite and celadonite) filling vesicles and voids in Cores 30R through 56R (Units XIII–XVII; Fig. F45). On the basis of microscopic observations, it appears that the green clay formed later than carbonates, zeolites, and brown clay.

Iron oxyhydroxides are sporadically present in vesicles in the uppermost 120 mbsf (down to sedimentary conglomerate Unit XI; Fig. F33F). They are most abundant in Unit VIII (olivine-phyric basalt). After a gap without abundant Fe oxyhydroxides, they appear again in vesicles in Units XVIII and XIX. Another phase present in some vesicles is tiny grains of native copper (interval 330-U1374A-30R-2, 53–54 cm). Native copper is thought to form either from

precipitation from vapors in the initial volcanic rock (Hunter, 2007; Baxter, 2008) or from the release of Cu from Fe-Ti oxides during subaerial weathering, followed by remobilization and precipitation from seawater (LeHuray, 1989).

Vein infillings

A total of 1229 filled or partly filled veins (and 3225 veinlets in vein networks; for details see “[Structural geology](#)”) were counted, yielding an average of 2.4 (8.5 when including veinlets) veins per meter. These veins are mostly small fractures (~1 mm) filled with clay minerals and carbonates in the uppermost 300 m of core (Figs. F46, F47A–F47B). Below 370 mbsf zeolite is the more common vein-filling material (Fig. F47C), but carbonates persist throughout the core and we occasionally observed coexistence of both species in the same vein (Fig. F47E, F47F). Clay is present in veins, with brown clay (Fig. F47D) being limited to the uppermost 360 m of the hole. The presence of brown clay in veins coincides with the reddish and brown alteration colors of the rock (Fig. F46). Both green and black clay minerals are present throughout the hole, but they become the only clay minerals present below ~360 mbsf. In the intrusive sheets of Units XVIII and XIX we observed the common occurrence of pyrite associated with zeolites in some veins (Fig. F48A, F48B). We also noted the occasional presence of colored halos (brown-red) associated with some veins throughout the hole (distinguishable in the wet, cut surfaces of the core; Fig. F37D).

Voids

Hole U1374A consists mainly of numerous units of volcanic breccia, portions of which contain a large number of voids, now (partially) filled in with minerals. For example, void space in the sedimentary conglomerate cover (Unit II) is predominantly strongly cemented by carbonates (see “[Sedimentology](#)”). The same cement is present in voids down to the basaltic breccia of Unit XIII, below which the voids become less abundant and smaller in size. Above 160 mbsf and between 280 and 360 mbsf, carbonates and zeolites are void-filling minerals (Figs. F49, F50). Between 150 and 280 mbsf, carbonate dominates, whereas below Core 58R (Unit XVIII), the voids are almost exclusively filled with zeolites (Figs. F49, F50).

On the basis of a limited number of XRD analyses (Figs. F35, F36), it appears that there may be a progressive change from phillipsite to analcite in the voids with depth. At shallower depths, phillipsite is the main zeolite mineral; at deeper intervals analcite, natrolite, gmelinite, and possibly stilbite and thau-

masite are also present. We identified phillipsite in Samples 330-U1374A-10R-4, 80–82 cm (52.5 mbsf); 22R-2, 140–143 cm (113.9 mbsf); 25R-2, 8–10 cm (126.8 mbsf); 28R-2, 0–4 cm (141.4 mbsf); and 30R-3, 56–58 cm (157 mbsf), whereas analcite was found in Sample 67R-4, 58–60 cm (483.6 mbsf), and natrolite and gmelinite were found in Sample 68R-5, 73–74 cm (483.6 mbsf). A zeolite tentatively identified as stilbite was observed optically in Cores 43R and 44R. Moreover, we identified thaumasite by XRD analysis (Samples 59R-6, 74–76 cm; 67R-4, 58–60 cm; and 68R-5, 90–91 cm). Thaumasite is a hydrothermal alteration mineral occurring after geothermal alteration of basalt and is commonly associated with zeolites, carbonates, and pyrite. Giret et al. (2003) indicated that in the volcanic rocks of Kerguelen archipelago, phillipsite formed at a temperature range of 40°–80°C, whereas analcite crystallized between 70° and 110°C. Stilbite requires temperatures between 100° and 140°C. A similar alteration thermal gradient therefore might also apply to the rocks at Site U1374.

Goethite was found in association with zeolites in some sections (Sample 330-U1374A-9R-2, 109–110 cm; Fig. F33F) and was also observed in Samples: 47R-1, 133–135 cm (Thin Section 200); 48R-8, 20–23 cm (Thin Section 205); 49R-1, 92–94 cm (Thin Section 206); and 54R-4, 38–40 cm (Thin Section 210) (Fig. F41E, F41F).

Olivine alteration

Most of the olivine observed in split-core sections or thin sections is altered to varying degrees, as discussed above. Several intervals have olivine with <50% alteration. A summary of olivine (and glass) preservation as observed in thin section is given in Table T8.

In the uppermost 80 m of the hole, iddingsite is the dominant alteration mineral after olivine. From 110 to 350 mbsf, there is no systematic pattern of olivine alteration. Throughout this interval, olivine is typically partly to completely altered to iddingsite, Fe oxides and oxyhydroxides, green and brown clay minerals, and carbonates. The rims are often altered to iddingsite, and the interiors subsequently altered to clay and iron oxides. The variation from iddingsite to green clay and Fe oxide alteration suggests some degree of variable oxidation conditions throughout this interval (Fig. F32). Below 350 mbsf, green clay minerals are the dominant alteration minerals after olivine, which coincides with the overall greenish alteration observed in the rock, indicating more persistent reducing conditions in the deepest portion of the hole.

Glass alteration

Groundmass glass in most of the thin sections is completely altered to clay minerals or palagonite. Nevertheless, slightly altered groundmass glass is present in thin sections from Sections 330-U1374A-3R-1, 7R-4, 21R-2, 29R-4, 34R-2, and 39R-2 (Table T8). Fresh to moderately altered glass is most abundant in Units XII and XIII. Fresh glass occurs only sporadically in these units because the rocks are highly variable in freshness themselves. Glass was visually observed in Sections 45R-2, 47R-1, 47R-2, 50R-1, 50R-2, 50R-3, 50R-4, 50R-6, and 66R-1.

Interpretation of alteration

Igneous units throughout Hole U1374A at Rigel Guyot are characterized by multistage alteration, mainly dominated by low-temperature fluid-rock interactions. One of the first indicators of alteration conditions is the distinctive colors observed in the core (Figs. F38, F39). Three main alteration colors characterize Hole U1374A, similar to Hole U1372A at Canopus Guyot. Gray reflects less altered basaltic units, whereas reddish brown and green could be directly related to the oxidation state of alteration processes, with the upper reddish-brown units indicating oxidizing conditions and the lower greenish units indicating reducing conditions. Oxidizing zones are characterized mostly by iddingsite, Fe oxyhydroxides, and carbonates replacing groundmass olivine and olivine phenocrysts, whereas reducing zones are characterized by green clay (nontronite and saponite) replacing olivine. Moreover, the presence of sulfides (pyrite) in the groundmass of intrusive sheets is also a good indicator of reducing conditions.

Although the upper part of the hole seems to be dominated by oxidizing conditions, the oxidation state fluctuates in the uppermost 300 mbsf, reflecting environmental changes from submarine to sub-aerial. We observed that both environments were sometimes coeval in the uppermost 300 mbsf, which could reflect episodic changes in the eustatic variations of sea level or different phases of construction of the seamount in different environments. The contact between the oxidizing and reducing zones is gradational between 290 and 360 mbsf (see “[Color reflectance spectrometry](#)” in “Physical properties”; Fig. F28). Deeper than 360 mbsf, reducing conditions prevailed, yet even within this interval a portion of Core 330-U1374A-64R shows minor brownish alteration. Our observations are consistent with those of shipboard igneous petrologists (see “[Igneous petrology and volcanology](#)”), who propose that magmatism started in a submarine environment

(Units XIX–XVII), which corresponds to the greenish reducing zone. Later, the magmatic activity progressed in a shallow-submarine environment (Units XVI–XII), which can explain the coeval existence of green and reddish-brown alteration. From Units XII to III, volcanic activity took place mainly in subaerial or wet, and therefore oxidizing, environments.

The abundance of smectite (saponite and nontronite), illite, Fe oxyhydroxides, celadonite, and zeolites throughout Hole U1374A indicates low temperatures (30°–150°C) typical of the lowest stages of ocean crust alteration (Alt, 1995), as also observed in Holes U1372A and U1373A. Moreover, the presence of significant numbers of veins, vesicles, and voids filled with carbonates in the uppermost 300 mbsf indicates interaction with CO₂-rich seawater-derived hydrothermal fluids at a relatively low temperature (<100°C; Honnorez, 2003). Nevertheless, with depth we also observed increased occurrences of zeolites and especially the transition between zeolite species from phillipsite to analcite and possibly to stilbite. This transition suggests an alteration temperature gradient, perhaps ranging from 40°–80°C to as high as 140°C (Walker, 1951; Neuhoﬀ et al., 1997).

Structural geology

Structures observed, measured, and described at Site U1374 on the western side of Rigil Guyot are sedimentary bedding, geopetals, veins, vein networks, fractures, magmatic flow textures, vesicle bands, and igneous contacts (Fig. F51). The characteristics, orientations, and distribution of these structures at Site U1374 are described below.

Sedimentary rocks are common in the upper parts of Hole U1374A, with thick intervals from 0–16.70 mbsf (Units I and II), 37.60–41.84 mbsf (Unit VII), 63.67–84.70 mbsf (Unit IX), and 109.87–116.45 mbsf (Unit XI) (Fig. F4). Thin sedimentary layers are also interbedded between volcanic units deeper in the hole. Many of these sedimentary units contain prominent bedding (see “Sedimentology”), and the orientations of these layers were recorded in collaboration with the onboard sedimentologists. Dip angles vary mostly from 0° to 33°, with a single ~10 cm wide sedimentary zone at 162.3 mbsf (Unit XIII) having an extremely steep dip of 55° (Fig. F52A, F52D). Excluding Unit II, most sedimentary beds have dips of 20°–25° (Fig. F52B), which is likely close to the maximum angle of repose for water-saturated sand-size sediments. In contrast, bedding in Unit II is much shallower, dominantly between 0° and 5° (Fig. F52C), which reflects the onset of deposition of the seamount’s sedimentary cover in a subtidal to inter-

tidal environment following the initial drowning of the former volcanic island at Site U1374 (see “Sedimentology”). Dip angles within Unit II also change systematically with depth (Fig. F52E). From the bottom upward, Unit II starts with a single relatively steep dip at 15.06 mbsf (arrowed) before abruptly dropping to near-horizontal dips (12.82–11.36 mbsf), followed by a gradual increase of dip angles upsequence (Fig. F52E). These changes in dip angles correspond with other sedimentologic variations in the stratigraphic subunits of Unit II (see “Sedimentology”). If the core can be corrected for drilling-induced core rotation, structural measurements on bedding will yield the paleodeposition direction(s) for these sediments, which will be useful for the sedimentologic reconstruction of this site.

Lower in the sequence, from 16.8 to 139.3 mbsf, 35 geopetal structures were observed within sediments, volcanic breccia, lavas, and peperitic horizons (Table T9; Fig. F53). Except for a single geopetal at 29.6 mbsf where the underlying 6 cm of sediment has clearly slumped, all geopetal infills are horizontal, indicating that this part of the seamount experienced little or no tilting after the geopetals were filled.

The lowermost third of Hole U1374A is cut by at least 10 sheet intrusions of variably vesicular aphyric basalt (Fig. F18). Because of excellent recovery in these cores, in many cases the chilled margins and baked contacts were preserved on both the upper and lower contacts (Figs. F54, F55). The widths of the baked contacts vary from <1 to >7 cm, indicating considerable variability in the amount of heat supplied by the different intrusions. This variability is likely controlled, at least in part, by the length of time during which magma flowed through the intrusion. Other variables include the magma temperature, the type of country rock, and the degree of water saturation in the country rock.

The chilled contacts and baked margins have dips ranging from ~25° to 90° (Fig. F56C), indicating they are moderate to steep intrusions. Within these intrusions there are numerous vesicle bands with high- and low-density vesicle concentrations (Figs. F54, F55). These features likely formed by volatile segregation during magma flow. Near the edge of the intrusions, the vesicle bands run parallel to the chilled margins (Figs. F54, F55). Toward the center of the intrusions, however, the vesicle bands become much steeper. This is the case even for intrusions with moderately dipping contacts, indicating that most of the magma flow within the intrusions was subvertical to vertical (Fig. F56D). The sheet intrusions also contain zones of magmatic foliation within the crys-

talline groundmass (Table T10). Where magmatic foliations and vesicle bands occur adjacent to each other, both features yield (sub)parallel directions.

Lithologic Units 146 and 148 in stratigraphic Unit XIX at the base of Hole U1374A yielded both subhorizontal and subvertical magmatic foliations within 1–2 m of core. As such, these units may not be sheet intrusions, where unidirectional flow is typical. These units could instead represent inflated lava flows, formed in a similar manner to Unit VII of Hole U1373A on the other side of Rigil Guyot. Both lithologic Units 146 and 148 are highly fractured (Fig. F57), in stark contrast to the clearly intrusive sheets that occur from 318 to 496 mbsf but again similar to Unit VII in Hole U1373A. Inspection of the upper margin is the best way to distinguish if these units represent flows or intrusions. Unfortunately, the upper margin for Unit 146 was not recovered and the upper contact for 148 is inconclusive. Because there is no conclusive evidence for these units to be flows, and given the steep margins for Unit 146 observed during downhole logging (see “[Downhole logging](#)”), it was decided that these units are more likely intrusions. Nonetheless, if these units do instead represent flows, they will provide the stratigraphically lowest samples for paleomagnetic, geochronological, geochemical, and petrologic analyses for this seamount.

Magmatic foliations were also observed in numerous lava flows in the upper parts of Hole U1374A (Table T10). These lavas generally yielded gently dipping flow orientations (Fig. F56E). Thin section inspection revealed that the magmatic foliations are defined by aligned plagioclase laths within the groundmass (Fig. F58). Many samples with flow textures also contain aligned titanomagnetite crystals within the groundmass (Fig. F58C, F58D). Such samples have moderate to strong anisotropy of magnetic susceptibility (see “[Paleomagnetism](#)”). After correction for drilling-induced core rotation, these flow orientation structures, including vesicle bands and magmatic foliations, will be useful for the volcanological reconstruction of Rigil Guyot.

Throughout Hole U1374A, veins ($N = 916$ intervals, with 1229 individual veins) and vein networks ($N = 515$, with 3225 individual veinlets) are clearly the dominant structural features (Fig. F51). Veins and vein networks are distinctly more frequent in the lava flow units and intrusive sheets (Fig. F59). The highest density of veins is found in the lava flows of Units IV and VI, with as many as 14 and 18 veins per meter, respectively (Fig. F59). This vein density is midway between the most vein-rich units in Holes U1372A and U1373A. In contrast to these previously drilled sites, an appreciable number of veins and

vein networks is also present within volcanic breccia units, with typically 2–4 veins per meter (Fig. F59). Most of the veins in breccia units are still restricted to the rheologically harder and larger clasts, although very rarely veins also occur within the breccia matrix (Fig. F60). The maximum vein width at Site U1374 is 25 mm, which is wider than at previous Louisville sites. Nonetheless, veins wider than 10 mm are very uncommon, and the overall average vein size (0.8 mm) is still relatively small compared to other seamount settings (e.g., Emperor Seamounts; Tarduno, Duncan, Scholl, et al., 2002), implying relatively low levels of fluid flow at Site U1374. Vein dips are generally steep, with a maximum of 60°–65°, although numerous veins have both steeper and shallower angles (Fig. F56A).

Fractures ($N = 356$) are sparse to nonexistent in most of the breccia in Hole U1374A (Fig. F57). The number of fractures is higher in lava flow units, but the number of fractures per meter in lavas of Hole U1374A is low compared to Sites U1372 and U1373. The only exceptions are lithologic Units 146 and 148 in Unit XIX, which have >130 fractures in 14 m (~9 fractures per meter) and are thus comparable to the highly fractured lowermost Unit VII of Site U1373 (11 fractures per meter). Fractures have a broad range of dip angles ranging from subhorizontal to vertical, with maxima at 85°–90°, 60°–65°, and 15°–20° (Fig. F56B).

Summary

Structural features at Site U1374 are dominated by veins ($N = 1229$), vein networks ($N = 3225$ individual veinlets), and fractures ($N = 356$). Veins are found mostly within lava flows, although veins also occur in larger fragments in the volcanic breccia units and rarely within the breccia matrix. The maximum vein width is 25 mm, but most are considerably smaller, with an average width of 0.8 mm. Fractures are most common in massive units, especially in the lowermost 14 m of the hole, with >14 fractures per meter recorded. Structural measurements were also undertaken for 46 examples of sedimentary bedding, 35 geopetals, 18 igneous contacts, 35 vesicle bands, and 80 cases of flow textures. The dip angles of bedding change downhole and correspond to important lithofacies variations described in “[Sedimentology](#).” Geopetal structures are horizontal, indicating that this part of the seamount has not been tilted since deposition of the geopetal infilling material. Several lava flow units have flow textures with subhorizontal or shallowly dipping orientations. Excellent examples of baked contacts and chilled margins were recorded from ~335 to 500 mbsf in a series of steeply dipping sheet intrusions. These intrusions also con-

tain steeply inclined vesicle bands or flow textures, which indicate that magma flow in these intrusions was subvertical to vertical.

Geochemistry

Igneous rocks

We analyzed 33 samples of igneous rocks from Hole U1374A for concentrations of major elements and several trace elements (Table T11) by inductively coupled plasma–atomic emission spectroscopy (see “Geochemistry” in the “Methods” chapter [Expedition 330 Scientists, 2012a] for information on analytical procedures, instrumentation, and data quality). Most of the samples were collected from lava lobes and clasts in the breccias that dominate this site. Three samples were from stratigraphic units identified unambiguously as flows (Units III, IV, and VI; see “Igneous petrology and volcanology”). Four were from intrusive sheets within Units XVI–XIX (Samples 330-U1374A-52R-2 [Piece 3, 35–37 cm]; 55R-2 [Piece 1, 6–8 cm]; 58R-4 [Piece 1, 64–66 cm]; and 64R-2 [Piece 2B, 37–39 cm], respectively). One sample (72R-2 [Piece 1, 28–31 cm]) was from a lithologic unit at the base of Unit XIX that could be either a lava flow or an intrusive sheet (see “Igneous petrology and volcanology”).

As at Sites U1372 and U1373, total weight percentages for the major element oxides vary significantly, from 92.29 to 102.20 wt%. Possible reasons for this variation are discussed in “Geochemistry” in the “Methods” chapter (Expedition 330 Scientists, 2012a). To better compare results with one another and with data from the literature, we normalized the raw major element values to 100 wt% totals. The normalized values are presented below the raw data in Table T11 and are used in the figures and in the discussion below.

Weight loss on ignition (LOI) varies from 0.6 wt% to 5.0 wt%. Only one Site U1374 sample (the lowermost sample from Unit XIX) has a LOI value of <1 wt%, which is typical for unaltered basalt (e.g., Rhodes, 1996). The majority have LOI values of <2.5 wt% and indicate moderate overall levels of alteration. However, LOI values for 10 samples are >3 wt%, which indicate comparatively high levels of alteration. These results are generally consistent with the petrography of the rocks (see “Alteration petrology” and “Igneous petrology and volcanology”). Of the group of elements measured, K₂O is typically the most affected by alteration (e.g., see “Geochemistry” in the “Site U1372” chapter [Expedition 330 Scientists, 2012b]). No correlation is present between LOI and K₂O, but the sample with the highest LOI, a lava clast from the sedimentary breccia of Unit IX

(Sample 330-U1374A-13R-1 [Piece 1, 5–6 cm]) has markedly higher K₂O (1.87 wt%) than the other samples (0.35–1.20 wt%). This sample also has the highest Na₂O (4.33 wt% vs. 2.39–3.82 wt% for the other samples), and it is possible that its Na₂O concentration also has been elevated by alteration. Besides this sample, K₂O has probably been affected to variable extents by alteration in a number of the other samples because K₂O does not correlate with TiO₂, P₂O₅, Zr, or Y (this is true whether or not the highest-K₂O sample is excluded).

In a total alkalis (Na₂O + K₂O) vs. SiO₂ diagram (Fig. F61), data for Site U1374 samples overlap considerably with data from Sites U1372 and U1373. However, on average the Site U1374 rocks tend to be slightly lower in SiO₂ at similar total alkali concentrations. This combination of characteristics makes the Site U1374 samples slightly more alkalic as a group. For example, alkalinity, a measure of the distance of a data point above or below the alkalic-tholeiitic dividing line in Figure F61, averages 1.8 for Site U1374 compared to 0.9 for both Site U1373 (located on the same seamount as Site U1374) and Site U1372 (on Canopus Guyot). Likewise, no transitional basalts were found, in contrast to the several analyzed for Sites U1372 and U1373. Data for 21 of the Site U1374 samples fall in the field of alkalic basalt, just as the great majority of samples from Sites U1372 and U1373 do. However, data for 12 Site U1374 samples lie in the field of basanite and tephrite. One of these samples is the high-LOI Unit IX sample mentioned above, whose high alkali content appears to be at least partly a result of alteration. This sample has 45.77 wt% SiO₂, and its original composition (i.e., prior to alteration) is likely to have been more basaltic. The other Site U1374 samples possessing basanitic-tephritic compositions in Figure F61 all have <45 wt% SiO₂. Seven have total alkali contents between 4.24 and 4.96 wt%. Six of these samples are from Unit X, and the seventh is from a clast in the sedimentary breccia of Unit XI. The remaining four samples with data points in the basanite-tephrite field have lower total alkali contents (3.25–3.69 wt%) and are from Units XIII, XIV, XVIII, and XIX. The Unit XVIII sample is from an intrusive sheet.

Values of Mg number (Mg# = $100 \times \text{Mg}^{2+}/[\text{Mg}^{2+} + \text{Fe}^{2+}]$, assuming Fe₂O₃/FeO = 0.15) vary from 65.8 to 35.1, whereas Ni contents range from 215 to 39 ppm. Averages for both quantities are relatively low (49.5 for Mg number and 76 ppm for Ni), illustrating the rather evolved nature of the Site U1374 rocks as a group. Except for one sample, MgO concentrations range from 2.78 to 8.54 wt%, with an average of 5.88 wt%. The exception is Unit III Sample 330-U1374A-

3R-2 (Piece 4D, 108–110 cm), which has 10.15 wt% MgO. Like its even higher MgO counterparts from Sites U1372 and U1373 (where MgO ranges to 13.21 and 11.78 wt%, respectively; see “[Geochemistry](#)” in the “Site U1372” chapter [Expedition 330 Scientists, 2012b] and “[Geochemistry](#)” in the “Site U1373” chapter [Expedition 330 Scientists, 2012c]), this sample is highly olivine-augite phyric and likely to contain excess olivine. However, its $\text{CaO}/\text{Al}_2\text{O}_3$ ratio (0.58) is rather low for its MgO content, suggesting that it does not contain excess augite.

In an Al_2O_3 vs. MgO diagram (Fig. [F62A](#)), the Site U1374 data again largely overlap the field defined by samples from Sites U1372 and U1373 and indicate a relatively minor overall role for fractionation of plagioclase. Many of the Site U1374 samples also have similar CaO and $\text{CaO}/\text{Al}_2\text{O}_3$ values to those of the two previous sites. However, most of the samples from the uppermost 240 m of Site U1374 (i.e., most samples from Units III–XIII) have lower CaO and $\text{CaO}/\text{Al}_2\text{O}_3$ for their MgO values (e.g., Fig. [F62B](#)). The very low $\text{CaO}/\text{Al}_2\text{O}_3$ of one sample from Site U1372 is probably a result of alteration (see “[Geochemistry](#)” in the “Site U1372” chapter [Expedition 330 Scientists, 2012b]). Scandium contents are low for these and other Site U1374 samples, averaging 15 ppm. In contrast, the average value of Sc for Site U1373 is 28 ppm (Sc data were not obtained for Site U1372). These characteristics suggest that clinopyroxene was a significant factor in the evolution of the Site U1374 magmas, particularly those supplying units in the upper half of the hole. The rocks from Unit X, which are all aphyric, and several other aphyric samples have relatively high $\text{Fe}_2\text{O}_3^{\text{T}}$ (total iron as Fe_2O_3), with values between 14.17 and 16.15 wt% (Fig. [F62C](#)). Because fractionation of clinopyroxene does not lead to significant iron enrichment, a high relative iron content may be a feature inherited from the parental magmas of these samples. Sample 330-U1374A-12R-4 (Piece 12, 113–115 cm), an aphyric clast from the Unit IX sedimentary breccia, has unusually high CaO (15.63 wt%) and $\text{CaO}/\text{Al}_2\text{O}_3$ (0.98). It also has rather high LOI (4.0 wt%), and we suspect that its CaO content may have been increased by alteration, much like a similarly high $\text{CaO}/\text{Al}_2\text{O}_3$ sample from Site U1372 (Fig. [F62B](#); see “[Geochemistry](#)” in the “Site U1372” chapter [Expedition 330 Scientists, 2012b]).

As with major elements, Site U1374 trace element data overlap data for Sites U1372 and U1373 (e.g., Fig. [F63](#)). However, Site U1374 samples exhibit greater overall variability in Ba, P_2O_5 , Sr, Zr, and Y relative to TiO_2 , ranging to higher Ba, Sr, and Y and to both higher and lower P_2O_5 and Zr for a given

TiO_2 content. These characteristics are consistent with some combination of variability in the amount of partial melting and in source composition at Site U1374 and between Site U1374 and the two previous drill sites. The slightly more alkalic nature of the Site U1374 rocks is also consistent with differences in partial melting or source composition between this site and Sites U1372 and U1373. Sample 330-U1374A-64R-2 (Piece 2B, 37–39 cm), from an intrusive sheet in the upper part of Unit XIX, has an anomalously high Sr concentration (914 ppm vs. 402–739 ppm for the other Site U1374 rocks). The sample is aphyric, so its high Sr content is not a product of accumulation of plagioclase or another common mineral. Strontium can be affected by some types of submarine alteration, and this sample's LOI value (4.1 wt%) is one of the higher values measured for Site U1374. However, concentrations of elements more sensitive to alteration are not unusually high or low (e.g., K_2O = 1.02 wt%, CaO = 11.15 wt%, and P_2O_5 = 0.37 wt%), rendering alteration an unlikely explanation for the sample's anomalous Sr content. Two Site U1373 samples have high Sr for their TiO_2 concentrations, but they also have high Ba (see “[Geochemistry](#)” in the “Site U1373” chapter [Expedition 330 Scientists, 2012c]), whereas this sample has a Ba concentration (199 ppm) close to the Site U1374 average (192 ppm). We have no reason to suspect an analytical artifact. Presently, we have no explanation for the high Sr concentration of this sample.

Although Sites U1373 and U1374 are located on the same seamount within 10.4 km (5.6 nmi) of each other and the samples from each site overlap in major and trace element composition, we cannot correlate any of the Site U1374 samples with those from Site U1373. Presumably, the igneous rocks sampled at the two sites represent distinct eruptive events.

Downhole variations reveal little systematic behavior in the upper part of Hole U1374A. The full range of Mg numbers (35.1–65.8) is observed in the uppermost 100 m in Units III–X (Fig. [F64A](#)). Below this level the olivine-phyric samples from Units XI and XII and the topmost part of Unit XIII exhibit relatively high Mg numbers (56.0–60.2), whereas samples from greater depths all have lower values. A rough trend of decreasing Mg number is evident from Units XII–XV, where a local low of 43.9 is seen, below which values fluctuate between 44.9 and 53.4. Variations in Ni correspond broadly with those in Mg number, consistent with variable control by mafic phases, principally olivine. The incompatible elements Ba, Sr, Zr, TiO_2 , and Y show no simple overall downhole trend (e.g., Fig. [F64C](#)), nor do incompatible-element ratios that serve as indicators of vari-

ation in partial melting or source heterogeneity, such as Ba/Y and Zr/Ti (Fig. F64D, F64E). Barium can be affected by some types of alteration, but neither Ba nor Ba/Y correlates with, for example, LOI or K₂O. Titanium content varies irregularly in Units III–X, reaching high values (3.56–3.78 wt%) in Unit X (Fig. F64C). In Unit XI, the concentration drops significantly (to 2.84 wt%) and then gradually increases in Units XI–XV, mirroring the downhole decrease in Mg number and Ni in this interval. The highest TiO₂ concentration (3.91 wt%) is near the bottom of the hole in Unit XIX.

The Zr/Ti ratios of most of the Site U1374 samples vary within a rather restricted range between 0.010 and 0.014 (Fig. F64E), but six of the seven samples from Unit XIII have distinctly higher values between 0.015 and 0.017. Similarly high Zr/Ti values are found in the upper part of the hole in the Unit III lava flow and in a clast from the sedimentary breccia of Unit IX. However, unlike the Unit III and IX samples, the high Zr/Ti in Unit XIII is not accompanied by a comparable or greater elevation in the Ba/Y ratio. This difference implies that the high Zr/Ti ratios of the Unit XIII samples are probably not solely a result of smaller extents of partial melting than those that produced the lower Zr/Ti rocks. Because Ba is more incompatible than Zr and Y is less incompatible than Ti, smaller amounts of partial melting normally produce greater relative increases in magmatic Ba/Y than in Zr/Ti. As a consequence, the comparatively high Zr/Ti values in Unit XIII may at least partly be a source feature. In contrast to the upper six samples of Unit XIII, the lowermost sample has a Zr/Ti value of only 0.011. We infer that the lava lobe from which this sample was taken belongs to a different magma type than that represented by the other samples of this unit. In addition to the multiple samples collected from Unit XIII, we also collected multiple (six) samples from Unit X. Unit X offers an interesting contrast to Unit XIII in its relative homogeneity (Fig. F64B, F64C, F64E).

The four aphyric samples collected from intrusive sheets are compositionally not very different from one another, except that the Unit XVI sheet sample has lower Ba/Y and slightly lower Zr/Ti and Zr/Y than those in Units XVII–XIX (e.g., Fig. F64D, F64E); the Unit XIX sample has anomalously high Sr, as discussed above. Excluding Sr in this sample, the major and trace element compositions of the sheet samples are within the overall range exhibited by the lava samples. However, we are unable to correlate any of

the sheets with specific lava flows, lobes, or clasts, including the aphyric units higher in Hole U1374A.

Carbon, organic carbon, nitrogen, and carbonate

Six samples of sediment were taken from Core 330-U1374A-1R (1–6 mbsf) for determination of total carbon, total nitrogen, carbonate (as CaCO₃), and total organic carbon. All of the samples were disturbed by the rotary bit used to drill the hole. Carbonate content ranges from 61.1 to 85.1 wt%, slightly less than values measured for samples from Site U1372. Total organic carbon content in the Site U1374 samples is low, ranging from 0.05 to 0.81 wt% (values of >2 wt% are generally considered high, whereas values of <0.5 wt% are considered low). Total nitrogen content is extremely low (from 0.016 wt% to below detection). Total carbon ranges from 7.4 to 10.6 wt%.

Physical properties

Characterization of physical properties was conducted for rocks recovered from Hole U1374A through measurements on whole-round and split-core sections and discrete samples. Measurements of gamma ray attenuation (GRA) bulk density, whole-round and point magnetic susceptibility, laser height, and color reflectance were conducted on all 397 core sections recovered from this hole. Whole-round core sections longer than ~50 cm (385 of 397 available sections) were also run through the Natural Gamma Radiation Logger (NGRL). Discrete measurements included compressional wave (*P*-wave) velocity and moisture and density measurements on 212 discrete oriented rock cubes. Most of these discrete samples were also used for paleomagnetic measurements of alternating-field demagnetization (see “Paleomagnetism”). Thermal conductivity measurements were made at 10 locations along the hard rock split-core face from the upper portion of the hole before being discontinued because of equipment failure. In accordance with core depth below seafloor Method A (CSF-A) conventions for referencing cores to depth (see “Procedures” in the “Methods” chapter [Expedition 330 Scientists, 2012a]), data for cores with >100% recovery (e.g., Cores 330-U1374A-44R through 46R) are shown as overlapping in figures. Generally, all physical property data sets are mutually consistent and show distinctions and trends that often correlate with lithologic changes (see “Igneous petrology and volcanology”) and

with petrologically determined alteration trends (see “[Alteration petrology](#)”).

Whole-Round Multisensor Logger measurements

Throughout the lithified sediments and igneous basement of Site U1374, individual sections generally contain multiple discrete pieces, as is typical of hard rock coring. In order to remove spurious Whole-Round Multisensor Logger (WRMSL) and Section Half Multisensor Logger (SHMSL) data that were affected by the gaps and edge effects from these discontinuities, we applied a data filtering and processing algorithm (see “[Physical properties](#)” in the “Methods” chapter [Expedition 330 Scientists, 2012a]). In this report we show only the filtered data; for raw data we refer the reader to the visual core descriptions (see “[Core descriptions](#)”) and the Laboratory Information Management System (LIMS) database (iodp.tamu.edu/tasapps/).

Magnetic susceptibility

Magnetic susceptibility is sensitive to the mineralogical composition of the rock. The results of whole-round magnetic susceptibility measurements are shown in Figure F65. Significant deviations from a median value of 3.93×10^{-3} SI occur as distinct short wavelength peaks in magnetic susceptibility, with values that exceed 1.00×10^{-2} SI, as well as broad regions of distinctly lower values.

Stratigraphic Unit I, which consists of foraminiferal ooze, has the lowest magnetic susceptibility of all Hole U1374A units, with an average value of 1.76×10^{-3} SI. However, not all units identified as being sedimentary necessarily exhibit low values. The sharp peaks found in the sedimentary conglomerate (Unit XI) exhibit some of the highest values of magnetic susceptibility in the entire hole. These peaks are attributed to large boulders of massive basalt present at the base of the unit. Elsewhere, peaks in magnetic susceptibility tend to correlate with lava flows and dikes. Stratigraphic Units IV–VII, along with the uppermost 6 m of Unit VIII, mark the largest depth interval of relatively high values and are associated with the thick lava flows and brecciated basalts in these units. The remaining portion of Unit VIII is dominated by low magnetic susceptibility, similar to the uppermost 22 m of Unit XIII. Other large peaks in magnetic susceptibility coincide with intrusive sheets or dikes, which are present in Units XVI–XIX. These dikes are limited in depth extent in the core but yield high magnetic susceptibility values, with an average of 8.89×10^{-3} SI. In Unit XVI, however,

this signal is less obvious; in contrast with Units XVII–XIX, magnetic susceptibility values of the dike and lava flows within this unit are not considerably larger than those of the surrounding volcanoclastics. A notable region of low values occurs from ~480 mbsf to the end of the hole, with a further decrease in the area immediately surrounding the dikes that make up lithologic Units 139 and 140. These values are associated with volcanic sand in the interval identified as having a frothy, glassy nature (see “[Igneous petrology and volcanology](#)”). This interval, excluding the dikes, has an average magnetic susceptibility of 3.43×10^{-3} SI.

Gamma ray attenuation bulk density

The results of GRA-derived bulk density are shown in Figure F66. A correction factor of 1.138 was applied to the hard rock cores (Sections 330-U1374A-1R-6 through 73R-1) to account for the smaller diameter (58 mm) of hard rock cores compared to the full core liner diameter of 66 mm (see “[Physical properties](#)” in the “Methods” chapter [Expedition 330 Scientists, 2012a]). Values of <1.00 g/cm³ were attributed to empty portions of core liner and removed. Bulk densities range from 1.02 to 3.01 g/cm³, with an average of 2.38 g/cm³. Although some scatter was observed, as is typical of breccia and conglomerate, the GRA-derived bulk density is consistent throughout most of Hole U1374A, averaging 2.35–2.45 g/cm³. The unconsolidated sediments of stratigraphic Unit I have a much lower bulk density, with an average of 1.55 g/cm³. Moderately lower densities were also observed in stratigraphic Units VII–VIII and in the intervals containing frothy, glassy clasts from 363 to 379 mbsf and 470 to 522 mbsf, excluding the dikes of lithologic Units 139, 140, 146, and 148 (see “[Igneous petrology and volcanology](#)”). These lighter intervals average 2.14, 1.97, and 2.08 g/cm³, respectively. The dikes in Units XVI–XIX and the larger lava flows of Units IV and VI have consistently higher densities, with averages of 2.57 and 2.76 g/cm³, respectively.

Natural Gamma Radiation Logger

Natural gamma radiation (NGR) measurements reflect the combined total amount of uranium, thorium, and potassium present in the rock. Because of the exceptionally high recovery at this site, count times were reduced to 60 min for sections containing potential lava flows or lobes and 30 min for all other sections beginning with Section 330-U1374A-42R-3 to keep up with core flow. Results from the NGRL are shown in Figure F67. NGR ranges from 0.90 to 40.94 counts per second (cps), with an average of 15.20

cps. The unconsolidated sediments of Unit I have consistently low levels of NGR, with an average of 6.90 cps. Units II–XIII are characterized by an essentially featureless band of NGR between 13 and 21 cps, with an average of 16.20 cps. This overall pattern ends abruptly at the base of Unit XIII, below which Units XIV–XIX have a lower overall average of 14.31 cps. These lower units exhibit distinctly less short-wavelength scatter but greater overall variability, with several well-defined peaks and troughs. Many of the peaks correlate with the intrusive dikes observed in Units XVI–XIX, which average 19.47 cps. Other peaks and lows also appear primarily connected to the basaltic components of the units; the very low levels of NGR observed below 490 mbsf correspond to an almost complete absence of basaltic clasts in the volcanic sands between lava flows. In contrast, the interval of high NGR from 450 to 470 mbsf contains a high percentage of basalt and increased magnetic susceptibility, which may indicate a distinct volcanic or alteration history affecting the material in this interval. Finally, the peak at 278–288 mbsf correlates with a zone of increased alteration.

Section Half Multisensor Logger measurements

Color reflectance spectrometry

Color reflectance spectrometry results are summarized in Figure F28. L^* (lightness) of the recovered core averages 33.1. L^* is fairly uniform throughout the hole but shows a gradual reduction in scatter downhole beginning at ~240 mbsf, decreasing more rapidly between 280 and 370 mbsf, and continuing to slowly decrease to the bottom of the hole.

Figure F28 also shows values of a^* and b^* , which correspond to redness versus greenness and yellowness versus blueness, respectively. Overall, a^* gradually changes from a predominantly red spectrum in Units I–XV, to a transitional zone in Units XVI and XVII, followed by a predominantly green spectrum in Units XVIII and XIX. This is very well correlated with the transition from red and brown alteration to green alteration (Figs. F38, F39) and likely represents the transition through time from a submarine reducing environment to a subaerial or shallow-marine oxidizing environment. The distinct red interval from 353 to 362 mbsf at the base of the transition zone is characterized by red alteration in the smaller basaltic clasts, possibly indicating subaerial eruption or shoaling in the surrounding region. Another strongly red interval occurs from 278 to 295 mbsf, which may indicate local shoaling (see “Sedimentology” and “Igneous petrology and volcanology”).

Other distinct features include a strong shift toward more green and yellow spectra in the frothy hyaloclastite interval from 470 to 522 mbsf. A moderately green spectrum was also observed in the conglomerate of Unit XI and the olivine-plagioclase-augite-phyric rocks of Unit XII. The lava flow of Unit IV has a distinctly blue spectrum and very uniform, neutral a^* values.

Point magnetic susceptibility

Point magnetic susceptibility results are shown in Figure F65 together with whole-round magnetic susceptibility data. This data set agrees well with the whole-round data and shows clear contrasts between the background signal of the breccia and the lava flows and dikes.

Moisture and density

Results of bulk density, dry density, grain density, void ratio, water content, and porosity measurements on discrete samples are listed in Table T12. Bulk density ranges from 1.89 to 2.93 g/cm³, with an average of 2.47 g/cm³. Porosity ranges from 0.9% to 47.1%, with an average of 18.3%. As illustrated in Figure F68, a strongly linear negative correlation between bulk density and porosity was observed. Bulk density measurements from discrete samples also agree well with GRA-derived bulk density measurements, as shown by Figure F69. The near one-to-one linear relationship between the two supports our 1.138 volume correction factor for GRA-derived bulk density. GRA-derived bulk density values may be affected by the presence of fractures and cracks in the whole-round cores, slight variations in core radius (approximately ± 1 –2 mm), and distortions of the core's cylindrical shape near the ends of pieces or from large voids. For Hole U1374A, a slight decrease (2–3 mm) in average core diameter resulting from bit wear was observed near the base of the hole. However, variability in diameter also increased, so these changes could not be incorporated into the volumetric correction. These factors can cause overestimates of the total volume used in the GRA-derived bulk density calculations even after the correction factor is applied, thus explaining why some GRA-derived bulk densities remain slightly lower than the corresponding results from discrete samples. The two outliers with anomalously low GRA-derived bulk densities appear to be affected by underestimates resulting from measurements taken in partial cores with a highly noncylindrical shape.

Figure F66 shows the variation of bulk density with depth based on both discrete samples and GRA-

derived bulk density and further illustrates the strong correlation between the two. Regions of consistently high density mark stratigraphic Units IV and VI and the lowermost dikes of Unit XIX, whereas the majority of the basalt breccia units have a significant amount of scatter in the data. Distinct intervals of lower density values exist in Unit VIII, near the boundary between Units XVII and XVIII, and surrounding the dikes of the lower portion of Unit XIX. These low-density volcanoclastics in Unit XIX (starting at 470 mbsf) contain clasts and fragments of frothy, glassy basalt and have an average density of 2.08 g/cm³. The nearby dikes have a significantly higher average density of 2.57 g/cm³.

The percent porosity measured in the discrete samples also shows distinct changes with depth (Fig. F70), which agrees well with the density observations discussed above. Although porosity values vary widely throughout most the basalt breccia units, Units IV, VI, and the upper portion of Unit X are marked by consistently low values. Many of the lowest values can be attributed to lava flow lobes within the breccia. Additionally, the dikes that appear intermittently in Units XVI–XIX are also typically low in porosity (average = 9.7%) but have values that are generally higher than those obtained from lava flow lobes. A region of high porosity was observed in the lower two-thirds of Unit XIX in material identified as containing frothy basalt glass. This interval begins at 470 mbsf and has an average porosity of 37.4%.

Compressional wave (*P*-wave) velocity

The measured *P*-wave velocity of discrete samples shows a strong linear relationship with bulk density (Fig. F71). Downhole variations in *P*-wave velocity are shown in Figure F66 and Table T13. The *P*-wave velocities are widely scattered in general because the majority of the material is breccia with intermittent lava flows and large boulders, leading to large variability over even short depth intervals. For the entire hole, *P*-wave velocities range from 2.10 to 6.81 km/s, with an average of 4.70 km/s. Many of the highest values can be attributed to lava flow lobes interspersed throughout the basalt breccia, particularly the aphyric basalt flows found in stratigraphic Units IV, VI, and X. The dikes that appear in Units XVI–XIX also demonstrate distinctly high *P*-wave values, with an average of 5.59 km/s. The most notable grouping of low *P*-wave velocities begins at 470 mbsf, where clasts of frothy basalt glass were identified. This lowermost interval (470–522 mbsf) of Unit XIX has an average compressional velocity of 3.26 km/s. Most samples show no statistically significant anisotropy; of those that do, the anisotropy has no consistent relationship with depth or lithology.

Thermal conductivity

Thermal conductivity is largely a function of the porosity and mineralogical composition of the rock. The limited thermal conductivity values for Site U1374 range from 0.77 to 1.65 W/(m·K), with an average of 1.38 W/(m·K). Note, however, that values were only available for roughly the uppermost 50 m of Hole U1374A because of equipment failure and thus are not representative of the entire hole. Available thermal conductivity measurements are listed in Table T14 and plotted against GRA bulk density in Figure F72.

Large-scale trends in physical properties

In addition to the patterns noted above, most of the physical properties measured show large-scale variations in average and distribution. These variations typically correlate with broad petrologic differences, either between the olivine-dominated package of stratigraphic Units II–XIII and the plagioclase-dominated package of Units XIV–XIX or above and below the first appearance of hyaloclastites at 327 mbsf. The unconsolidated sediment of Unit I and the intrusive dikes in Units XVI–XIX were also treated separately because they are petrologically and potentially temporally distinct.

The distinction between the plagioclase- and olivine-dominated packages is reflected in the magnetic susceptibility and NGR data, properties likely to be sensitive to subtle mineralogical variations. NGR values average 16.47 cps in the olivine-dominated Units II–XIII, compared with 13.63 cps in the plagioclase-dominated Units XIV–XIX. For magnetic susceptibility data, variation in background magnetic susceptibility better reflects large-scale changes than do the localized peaks caused by individual pieces of basalt or alteration zones. This background level is best reflected in the median magnetic susceptibility, with the olivine-dominated package having a median whole-round magnetic susceptibility of 5.74×10^{-3} SI, which is almost twice the median value of the plagioclase-dominated package of 2.91×10^{-3} SI. Point magnetic susceptibility shows a similar distinction, with median values of 3.74×10^{-3} SI and 2.05×10^{-3} SI for the olivine- and plagioclase-dominated packages, respectively.

The differences between units containing a high proportion of hyaloclastites, those deeper than 327 mbsf, and those above 327 mbsf are reflected in *L** (which measures the lightness versus darkness of the core), *P*-wave velocity, and porosity. A further difference is also seen at 470 mbsf in the hyaloclastite package, marking the beginning of the interval containing frothy, glassy clasts. *L** in the hyaloclastite

units (327–522 mbsf) is characterized by a lower average of 29.5 and a smaller standard deviation of 6.8 compared to units above the hyaloclastites, which have an average of 35.1 and a standard deviation of 8.9. Despite the presence of both high and low outliers, median *P*-wave velocities decrease downhole from a median of 4.99 km/s above the hyaloclastites, to 4.35 km/s in the first hyaloclastite package (327–470 mbsf), to 3.42 km/s in the interval containing clasts of frothy basalt glass (470–522 mbsf). Porosity exhibits the opposite trend, increasing downhole from 13.4% to 24.4% to 36.2%, respectively. This marked increase in porosity is clearly reflected in the density of the interval containing frothy, glassy clasts and fragments (median density = 2.07 g/cm³) but is less clear between the upper hyaloclastite package and those units without hyaloclastites, whose median densities are higher and more similar (2.36 and 2.46 g/cm³, respectively).

The intrusive dikes, which were excluded from the above analysis, are characterized by high median density (2.58 g/cm³), high median magnetic susceptibility (9.16×10^{-3} SI for whole-round magnetic susceptibility), high median NGR (19.3 cps), high median *P*-wave velocity (5.38 km/s), and low median porosity (10.7%). The unconsolidated sediment is characterized by low median density (1.59 g/cm³), low median magnetic susceptibility (1.51×10^{-3} SI for whole-round magnetic susceptibility), high *L** (42.7), and low NGR (6.97 cps).

Paleomagnetism

The deep penetration and high core recovery from Hole U1374A provided a detailed record of magnetization variations in Rigil Guyot. The highest remanent magnetization intensities are associated with lava flows, lava lobes, and intrusive sheets, but the volumetrically dominant volcanic breccia has only slightly lower intensities. The uppermost ~45 m of Hole U1374A is characterized by reversed polarity, whereas predominantly steep negative inclinations (normal polarity) occur in the interval between ~45 and 522 mbsf. Remarkably consistent normal polarity magnetizations were observed for intervals containing a wide range of lithologies, including lava flows, dikes, and volcanic breccia. Both archive-half and discrete sample data reveal steep inclinations, similar to or greater than that expected from a geocentric axial dipolar field at the current location of the Louisville hotspot at 51°S.

Archive-half core remanent magnetization data

The remanent magnetization of archive halves from Sections 330-U1374A-1R-6 through 73R-1 was mea-

sured at 2 cm intervals using the cryogenic magnetometer. All data acquired within 4.5 cm of either piece end were filtered out prior to further processing, and thus only pieces longer than 9 cm were considered.

The natural remanent magnetization (NRM) intensity varies by more than four orders of magnitude (Fig. F73B) from a maximum of ~19 A/m (associated with intrusive sheets in Unit XVIII) to a minimum of ~10⁻³ A/m (in Unit II sediments). Several lithologic units and some stratigraphic units are broadly associated with changes in NRM intensity or magnetic susceptibility (Fig. F73B, F73C). For example, many of the isolated intrusive sheets and lava flows in the dominantly volcanoclastic sequence are accompanied by an increase in both NRM intensity and magnetic susceptibility (e.g., the lava of lithologic Unit 2 at ~20–30 mbsf and the dikes of lithologic Unit 103 at ~328 mbsf). The enhanced NRM intensity of stratigraphic Unit XV relative to that of surrounding units and the increase in magnetization toward its base are apparently responsible for a distinctive magnetic anomaly signature in the borehole at this depth (see “[Downhole logging](#)”).

The deep penetration and exceptionally high recovery at Hole U1374A resulted in a substantial number of archive-half measurements that, in turn, allow some general assessment of the NRM intensity for many of the recovered lithologies (Fig. F73B). Units identified as intrusive sheets have the highest NRM intensities (geometric mean = 5.5 A/m ± 0.3 log units). Lava flows and lava lobes have geometric mean intensities of 2.1 A/m ± 0.5 log units and 3.3 A/m ± 0.3 log units, respectively. Slightly lower geometric mean magnetization values characterize volcanic/volcanoclastic breccia (0.7 A/m ± 0.5 log units) and sedimentary breccia/conglomerates (0.8 A/m ± 0.5 log units).

Best-fit principal component directions were calculated for each 2 cm interval of the archive halves using an automated routine that maximizes the percentage of remanence incorporated and minimizes the scatter about the best-fit direction and the deviation of this vector from the origin (see “[Paleomagnetism](#)” in the “Methods” chapter [Expedition 330 Scientists, 2012a]). On the basis of the misfit value distribution, only directions with misfit values of <3.42 were considered; this represents ~40% of the total number of 2 cm interval principal component directions. Representative demagnetization results from archive-half core intervals with misfit values below and near the cutoff value of 3.42 are shown in Figure F74. The resulting inclinations, intensities, and stability (median destructive field of the vector difference sum [MDF]) are shown in Figure F73D (dark red circles), F73B (black circles), and F73E.

Inclinations from Hole U1374A are dominantly negative and steep, indicative of Southern Hemisphere normal polarity. This consistent normal polarity signal extends from ~45 mbsf to the base of the hole and is interrupted by intervals with increased scatter. In some cases, this increased scatter is associated with sedimentary breccia and conglomerates (e.g., stratigraphic Units IX and XI). Scattered inclinations, however, are not diagnostic of breccia units because most volcanic breccia also has consistent normal polarity (Fig. F73D). Such consistent inclinations are present in volcanic breccia composed of pillow fragments, clasts with lobate margins, and in some cases clasts with sharp margins (e.g., Sections 330-U1374A-46R-3, 57R-3, and 67R-3, respectively; see “[Igneous petrology and volcanology](#)”). A large fraction of directions that were excluded from further consideration on the basis of their calculated misfit values nonetheless have inclinations that are consistent with more reliable (lower misfit) data (cf. Fig. F74D, F74E, F74F, F74H). More moderate negative inclinations were observed in the lowermost 20 m of the hole, corresponding to lithologic Units 143–148. The uppermost ~45 m of the hole, which includes intercalated sediments, lavas, and breccia (Fig. F74A–F74C), is characterized by positive inclinations, indicating reversed polarity.

Discrete sample remanent magnetization data

NRM and magnetic susceptibility were measured for all discrete samples ($N = 236$; Table T15). NRM intensities for lavas, intrusive sheets, and basalt clasts in volcanic breccia/conglomerate range widely from 0.19 to 23.5 A/m (arithmetic mean = 6.29 A/m), whereas volcanic breccia samples have generally lower values (mean = 1.56 A/m; Fig. F75). Volcanic sandstones from stratigraphic Units II and VII have distinctly lower magnetizations, averaging 0.52 A/m. Discrete sample NRM intensities are generally consistent with the ranges measured for the same lithologies on the archive halves (Fig. F73). The Königsberger ratio (Q_n ; calculated for a field intensity of 36.6 A/m) for most lavas and intrusive sheets is >10 , indicating that the overall magnetization is dominated by remanent rather than induced magnetization. Other lithologies have relatively lower Q_n values, and the lowest values are associated with sediments (volcanic sandstone) from the upper portion of the hole (Fig. F75C). Although induced magnetization might complicate interpretation of demagnetization data at sea, more reliable remanent magnetization data can be acquired in the low-field environment of shore-based laboratories.

Results from alternating-field (AF; $N = 140$) and thermal ($N = 96$) demagnetization of discrete samples generally reveal relatively simple characteristic remanent magnetization (ChRM) directions (Fig. F76). Both normal and reversed polarity ChRM directions were observed, with reversed polarity generally confined to the uppermost ~45 m of the hole, as noted in the archive-half core data. Most samples show nearly univectorial behavior during demagnetization, with a small to negligible lower stability component (Fig. F76A–F76D, F76F). There is little evidence of any drilling-related remanence, which is consistent with the high MDF values for the discrete samples, as shown above for the archive-half core data (Fig. F73E). AF and thermal demagnetization generally recover the same magnetization component. This correspondence also extends to some samples where a small, nearly antipodal lower stability component is present (Fig. F76E).

For a small number of sample pairs (particularly those from the upper portion of the hole), the lower temperature magnetization component agrees well with the ChRM direction determined by AF demagnetization (Fig. F76B), but at higher temperature steps ($>400^\circ\text{C}$) an additional positive inclination component is present. The emergence of this higher temperature component coincides with an order-of-magnitude increase in magnetic susceptibility (monitored after each heating step), and its origin is uncertain. This component is typically poorly defined (maximum angular deviation $>5^\circ$) and does not pass our reliability criteria. Shore-based studies will further examine this discrepancy.

Anisotropy of magnetic susceptibility

Anisotropy of magnetic susceptibility was measured for all discrete samples (Table T16). Discrete samples were collected from 10 intervals identified as intrusive sheets, with two adjacent samples taken in most of these intervals. The eigenvectors associated with the minimum eigenvalues for these intrusive sheets are dominantly subhorizontal (Fig. F77A), compatible with flow in steeply inclined dikes (Knight and Walker, 1988). Eigenvectors from adjacent sample pairs in these intrusive sheets typically agree within 5° – 10° . For lava flows highly likely to be in situ (i.e., in situ confidence index [ISCI] = 3; see “[Igneous petrology and volcanology](#)” in the “Methods” chapter [Expedition 330 Scientists, 2012a]), the eigenvectors associated with the minimum eigenvalues are subvertical, whereas those associated with the maxima are subhorizontal, as might be expected for lava flows (Fig. F77B). Many samples with lower ISCI values also exhibit the same pattern, although with more dispersion.

Discussion

The uppermost portion of Hole U1374A is characterized by reversed polarity, whereas remanent magnetizations with consistent normal polarity were observed for a fairly long stratigraphic interval between ~45 mbsf and the base of the hole at 522 mbsf (Fig. F78). This consistency is especially pronounced in the lower portion of the hole (Cores 330-U1374A-56R through 68R), where numerous volcanoclastic units as well as intercalated lava flows and lobes display less scattered inclinations. In this interval, most individual 2 cm principal component analysis directions as well as piece-average inclinations and discrete sample inclinations are between -60° and -90° (Fig. F78B, F78D, F78F). Most of the intrusive sheets intruding these volcanoclastic materials also have similar steep negative remanence vectors. The lowermost ~20 m (Cores 330-U1374A-68R through 73R) have somewhat shallower negative inclinations, with most values ranging between -45° and -70° .

A small number of positive inclination (reversed polarity) zones are also present in the dominantly normal polarity interval from ~45 mbsf to the base of the hole. Some positive inclinations, particularly where inclinations are scattered, undoubtedly represent clasts with random orientations. The origin of more narrow intervals of positive inclinations (e.g., ~95, ~109, and ~160 mbsf) is uncertain. Some may be related to isolated core pieces that were inverted during curation or measurement (several such inverted core pieces were noted and corrected, but it is possible others were not detected). Others may reflect unstable remanent magnetization that was reset by drilling. Drilling-related overprints are typically removed by low to moderate AF demagnetization (5–20 mT), and therefore the moderate to very high coercivity evident in both the archive halves and many discrete samples suggests that the observed steep inclinations are likely not related to drilling. The use of nonmagnetic core barrels appears to have significantly reduced the drilling-related remanent magnetization in the Expedition 330 cores. However, some positive inclination (reversed polarity) intervals may be geologically significant. For example, a 50 cm interval in the archive-half data for Section 330-U1374A-63R-3 (~445 mbsf) has essentially vertical, positive inclination. A single thermally demagnetized sample in this interval has a comparable final magnetization component (inclination = $+89^\circ$) with a less stable normal polarity overprint. This and other apparent short polarity intervals will be the subject of postexpedition research.

The archive-half core and discrete sample data from Hole U1374A provide a consistent inclination record,

whether the data are treated individually or grouped by lithologic unit. The most reliable (misfit ≤ 3.42 ; $n = 5496$) archive-half core data from Hole U1374A (Fig. F78B) are strongly focused toward steep negative inclinations (Fig. F79A). The average inclination remains steep when inclination-only averages are considered (Fig. F78C; Table T17) as calculated for the most likely in situ lithologic units (ISCI = 2 or 3). The resulting inclination-only mean is $-73.5^\circ \pm 4.3^\circ$ (α_{95} ; $n = 19$; with the single positive inclination result that corresponds to lithologic Unit 4 inverted) (Fig. F79B). If we consider the Fisher piece-average inclinations for each piece occurring in lithologic units assigned an ISCI value of 2 or 3 (Fig. F78D), then a bimodal distribution is observed (Fig. F79C). Inclination-only statistics (Arason and Levi, 2010) for lithologic units using these piece averages show the same bimodal distribution but with smaller n (Figs. F78E, F79D), resulting in an inclination-only mean of $-79.5^\circ \pm 7.5^\circ$ (α_{95} ; $n = 23$). Using the same data set, lithologic Units 1, 2, and 4, which record reversed magnetic polarity, have an inclination-only mean of $57.9^\circ \pm 11.4^\circ$ (α_{95}) that is distinct from that of the overall data set ($-79.9^\circ \pm 7.5^\circ$ [α_{95} ; $n = 23$]).

Discrete sample demagnetization data and the manual principal component analysis directions picked for this data subset provide the most reliable inclination estimates (Fig. F79E). Two distinct polarity groups are also seen in these data, and the arithmetic mean inclination ($-68.7^\circ \pm 13^\circ$; $n = 50$) is equal to that expected for the present-day location of the Louisville hotspot. However, the inclination-only maximum likelihood estimate is $-80.2^\circ \pm 7.2^\circ$ (α_{95}), which corresponds to a paleolatitude of 71° . For either conclusion to be validated, further shore-based analyses are required to refine the inclination for each lithologic unit and to test whether secular variation has been adequately averaged. Shore-based research will also include an assessment of whether the data from this site can be combined with paleomagnetic data from Hole U1373A, also drilled on Rigil Guyot.

Downhole logging

Downhole logging measurements obtained from Hole U1374A include natural total and spectral gamma ray, density, neutron porosity, electrical resistivity, electrical images, *P*-wave velocity, acoustic images, and three-component magnetic field. Following some initial issues with rock bridges in the borehole and an extensive period of borehole preparation, an open hole section of 393.9 m was logged with four tool strings.

Operations

Downhole logging of Hole U1374A started once rotary coring to a total depth of 522 mbsf ended on 18 January 2011 at 0545 h (all times are New Zealand Daylight Time, Universal Time Coordinated [UTC] + 13 h). The drill pipe was initially set at 101 mbsf for logging. For details on hole preparation for logging, please see “[Operations](#).”

In a first attempt, the triple combination (triple combo) tool string was lowered into Hole U1374A at 1101 h on 19 January. The wireline heave compensator was optimized while the tool string was in the pipe because of a possible drill pipe sticking issue. At 1622 h, following some effort, the run was aborted because of the occurrence of a rock bridge in the hole immediately below the drill pipe. The tool was returned to the surface and was rigged down by 1855 h. To remove the bridging issue in the hole, mud was circulated in the hole and the pipe was run down to 143.6 mbsf. The pipe was set slightly deeper for a second logging attempt at 110.8 mbsf to avoid the rock bridge. The triple combo was run into the hole at 0037 h (20 January), but again numerous tight spots were encountered and only a wireline log depth below seafloor (WSF) of 139 m was reached, only 28.52 m below the end of pipe. Logging was aborted at 0249 h, and the tools were rigged down at 0400 h. A short string comprising only the Hostile Environment Natural Gamma Ray Sonde (HNGS) and the Hostile Environment Litho-Density Sonde (HLDS) caliper was made up, but again logging was unsuccessful and the tools were rigged down by 0745 h.

Because Hole U1374A was the deepest hole drilled during Expedition 330 at the old end of the Louisville Seamount Trail, it was decided that one final attempt should be made at a successful logging program. All drill pipe was tripped to the surface and then run back down with a standard bit and mechanical bit release (0815–1730 h). The hole was washed and reamed from top to bottom and swept with 35 bbl of sepiolite mud. The hole was displaced with 165 bbl of 1.26 g/cm³ heavy mud (barite), the pipe was set at 128.1 mbsf, and the bit was released at the bottom of the hole. This significantly improved hole conditions, allowing four tool strings to be deployed in Hole U1374A: (1) the triple combo, (2) the Göttingen Borehole Magnetometer (GBM), (3) the Formation MicroScanner (FMS)-sonic, and (4) the Ultrasonic Borehole Imager (UBI). For tool and measurement acronyms, see “[Downhole logging](#)” in the “Methods” chapter (Expedition 330 Scientists, 2012a).

The triple combo tool string, which includes the HNGS, Accelerator Porosity Sonde, HLDS, General

Purpose Inclinometry Tool (GPIT), and Dual Induction Tool (DIT), was lowered into the hole at 0545 h on 21 January. The tool string reached the bottom of the hole at 520.6 m WSF, and a first uphole pass started at 0804 h (Fig. [F80](#)). The tool string was lowered back down to 170 m WSF, and a repeat pass started at 0952 h. This repeat control pass ended when the tool string crossed the seafloor, marked by a peak in natural radioactivity clearly visible in the HNGS gamma ray measurement. The seafloor was detected at 1570 m wireline log depth below rig floor (WRF), which concurs with the drillers seafloor depth estimate. The triple combo reached the rig floor and was rigged down at 1250 h on 21 January.

The second tool string deployed in Hole U1374A was the GBM (Fig. [F81](#)). The GBM was rigged up, and the tool was oriented by simultaneously sighting the tool along the ship’s long axis while recording the position of two GPS receivers of known location and also the ship’s heading using the ship’s main gyro. The GBM began measuring at 1325 h on 21 January while still on the rig floor and was lowered into the hole at 1550 h, taking continuous measurements from the rig floor to the bottom of the hole and back up to the rig floor. The GBM reached the bottom of the hole (2096.4 m WRF) at 2015 h, but unfortunately we lost communication with the GBM at 2250 h (1035 m WRF) on the uplog journey to the rig floor. This will not, however, affect further data processing. The GBM reached the rig floor and was rigged down by 0015 h on 22 January.

The third tool string deployed in Hole U1374A was the FMS-sonic tool string, comprising the HNGS, Dipole Shear Sonic Imager (DSI), GPIT, and FMS (Fig. [F82](#)). The FMS-sonic tool string was lowered in the hole at 0015 h on 22 January and reached the bottom of the hole (2090.1 m WRF) at 0310 h. The first uphole logging pass started at 0311 h and ended at 0348 h. After the tool string was returned to the bottom of the hole, the second pass started at 0411 h and ended after reaching the seafloor at 1570.1 m WRF. Rig down was completed at 0723 h.

The fourth tool string deployed was the UBI, comprising the HNGS, GPIT, and UBI (Fig. [F83](#)). Because of the quality of the borehole and the tool requirement that the borehole be <30 cm in diameter, only specific optimal sections (five in total) of the hole were targeted. The tool string was lowered in the hole at 0823 h. Section 1 was logged at 1001 h (2086–2076 m WRF). However, in order to check the UBI’s rotating sub, we returned to bottom for a repeat of this section and extended the log accordingly (2087–2046 m WRF). Section 2 (2035–1994.4 m WRF) was logged at 1042 h, Section 3 (1885–1866.6 m WRF) was logged at 1112 h, Section 4 (1827–1790

m WRF) was logged at 1126 h, and finally Section 5 (1775–1730 m WRF) was logged at 1147 h. The last imaged section was completed by 1208 h, and the tool string was rigged down by 1420 h on 22 January.

The final tool string deployed was the GBM for its second full pass. The GBM was rigged up, and the tool was again oriented by simultaneously sighting the tool along the ship's long axis and recording the position of two GPS receivers of known location and the ship's heading using the ship's main gyro. The tool began its measurement on the rig floor at 1439 h and was lowered into the hole at 1500 h. The tool reached a total depth of 2090 m WRF at 1759 h and began its journey back up to the surface with no major communication problems. The tool was back on the rig floor at 2100 h and rigged down by 2144 h on 22 January following a final tool sighting and orientation check, at which time logging operations in Hole U1374A were completed.

Data processing and quality assessment

The standard logging data were recorded on board the R/V *JOIDES Resolution* by Schlumberger and archived in DLIS format. Data were sent via satellite transfer to the Borehole Research Group of the Lamont-Doherty Earth Observatory, processed, and transferred back to the ship for archival in the shipboard database. Processing and data quality notes are given below. The GBM data were acquired from the tool using GBMlog software and processed with GB-Mdatenverarbeitung software (see “[Downhole logging](#)” in the “Methods” chapter [Expedition 330 Scientists, 2012a]).

Depth shifts applied to the logging data were performed by selecting a reference (base) log (usually the total gamma ray log from the run with the greatest vertical extent and no sudden changes in cable speed) and aligning features in equivalent logs from other tool string passes by eye. In the case of Hole U1374A, the base log was the gamma ray profile from Pass 1 (main) of the triple combo (HNGS-HLDS-GPIT-DIT) tool string. The original logs were first shifted to the seafloor (1570 m WRF), which was determined by the step in the gamma ray value, consistent with the seafloor depth given by the drillers.

Proper depth shifting of wireline logging depths relative to core depths was essential to correlate downhole logging data with all other measurements and observations made on core recovered from Hole U1374A. The seafloor was the only target that offered potential wireline logging depth references. However, it should be noted that data acquired through the seafloor resulted from logging through the bottom-hole assembly (BHA), so data from this

interval are of poor quality and highly attenuated and should only be used qualitatively. However, they are adequate to pick out the seafloor. The quality of wireline logging data was assessed by evaluating whether logged values were reasonable for the lithologies encountered and by checking consistency between different passes of the same tool. Specific details of the depth adjustments required to match logging runs/data are available in the logging processing notes on the log database for Hole U1374A (iodp.ldeo.columbia.edu/DATA/).

A wide (>30 cm) or irregular borehole affects most recordings, such as the HLDS (bulk density), which requires decentralization and good contact with the borehole wall, and the UBI, which requires a borehole diameter of <30 cm. Density logs typically correlate well with resistivity logs, but this correlation is strongly affected by borehole conditions. Borehole diameter was recorded by the hydraulic caliper on the HLDS tool and by the FMS calipers. The FMS calipers only show one area in the hole where the borehole is >40 cm in diameter (~363–374 m wireline log matched depth below seafloor [WMSF]), and thus there are large areas where the borehole is “in gauge.” These areas were targeted for UBI logging (2087–2046 m WRF; 2035–1994.4 m WRF; 1885–1866.6 m WRF; 1827–1790 m WRF; and 1775–1730 m WRF; Fig. F83). Good repeatability was observed between the main and repeat passes of the triple combo and FMS-sonic tool strings, particularly for measurements of electrical resistivity, gamma ray, density, and compressional wave velocity (V_p) (Fig. F84).

Bulk density (HLDS) data were recorded with a sampling rate of 197 measurements per minute (2.54 cm at 300 m/h), in addition to the standard sampling rate of 32 measurements per minute (15.24 cm at 300 m/h). The enhanced bulk density curve is the result of the Schlumberger enhanced processing technique performed on the MAXIS system on board the *JOIDES Resolution*. In normal processing, short-spaced data are smoothed to match long-spaced data (depth matched and resolution matched); in the enhanced processing, the raw detail obtained from the short-spaced data is added to the standard compensated density (Flaum et al., 1987). Where there is good contact between the HLDS pad and the borehole wall (low-density correction) the results are improved because the short spacing has better vertical resolution (i.e., it has the capability to resolve thinner beds/units).

The DSI was operated in the following modes: P&S monopole and upper dipole for both the downlog and Pass 1 (all with standard frequency). For Pass 2 the DSI was operated in the two above-mentioned

modes in addition to Stoneley. The slowness data from DTCO and DT2 (see Table T12 in the “Methods” chapter [Expedition 330 Scientists, 2012a]) are of good quality for these passes and were thus converted to acoustic velocities (VCO and VS2, respectively). Reprocessing of the original sonic waveforms is highly recommended to obtain more reliable velocity results.

The FMS images are of excellent quality over the entire hole, with the exception of a very short interval between 363 and 374 m WMSF, where the borehole diameter is larger than the 40 cm limit of the FMS calipers. This prevents some FMS pads from being in direct contact with the formation, resulting in poor image resolution or, in this case, dark images. Hence, FMS images (and the high-resolution resistivity logs) should be used with caution in this short depth interval.

Preliminary results

Downhole logging measurements obtained from Hole U1374A include natural total and spectral gamma ray, density, neutron porosity and electrical resistivity, electrical images, *P*-wave velocity, acoustic images, and three-component magnetic field. The results are summarized below.

Electrical resistivity measurements

Two main electrical resistivity curves were obtained with the DIT: deep induction phasor-processed resistivity (IDPH) and medium induction phasor-processed resistivity (IMPH). The IMPH and IDPH resistivity profiles represent different depths of investigation into the formation (76 and 152 cm, respectively) and different vertical resolutions (152 and 213 cm, respectively). The DIT reached the bottom of the logged interval in Hole U1374A because it was the bottommost tool in the logging tool string (Fig. F80). The IDPH measurement is the most reliable for lithologic interpretation because it has a deeper investigation depth and hence is less influenced by drilling-induced fractures and the presence of mud cake in the borehole.

Both resistivity curves show considerable variability throughout the hole (Fig. F84). Below 128.1 m WMSF Hole U1374A is composed mostly of breccia units interlayered with more massive basaltic lava flows/intrusions as thick as 3.12 m. Values of IMPH range from 2.16 to 965.24 Ωm , and IDPH values range from 9.48 to 1866.36 Ωm . Higher resistivities seem to relate to more solid layers in the breccia and well-cemented breccia units. Some of the highest resistivities correlate to intrusive units observed in the recovered core (e.g., lithologic Units 139 and 140; ~492 m WMSF). Two notable areas of low resistivity are consistent across both resistivity curves. These

are located at 370 and 480 m WMSF (log Units VI and VIII; see “Log units”). The former relates to a washed out zone in the borehole, which indicates a more friable, poorly cemented breccia (stratigraphic Unit XVII), and the latter relates to a frothy, glassy lithology (stratigraphic Unit XIX), observed in the recovered core from Hole U1374A.

Gamma ray measurements

Standard, computed, and individual spectral contributions from ^{40}K , ^{238}U , and ^{232}Th were part of the gamma ray measurements obtained in Hole U1374A with the HNGS (see Table T12 in the “Methods” chapter [Expedition 330 Scientists, 2012a]). The total gamma ray measurements through the BHA show one main anomaly from the seafloor to ~20 m WMSF (log Unit I), and the open hole gamma ray measurements covered a total of 361.9 m downhole (log Units III–IX). The shorter overall coverage of this tool compared with the DIT is the result of the topmost position of the HNGS in the tool string (Fig. F80).

Gamma ray measurements in basaltic oceanic crust are typically low (e.g., Bartetzko et al., 2001; Barr et al., 2002), and the lithologic units penetrated and logged in Hole U1374A follow this trend. Total spectral gamma ray values obtained with the HNGS in Hole U1374A range from 11.93 to 37.98 gAPI, with a mean of 25.29 gAPI. Potassium values are relatively high, with values ranging between 0.27 and 1.55 wt% and a mean of 0.73 wt% (Fig. F85), which correlates well with values obtained on the core (0.53–1.20 wt%; see “Geochemistry”). Uranium values range between 0.002 and 2.46 ppm and have a mean of 0.52 ppm. In contrast, thorium values are relatively high, ranging from 0.7 to 4.49 ppm, with a mean of 2.63 ppm. Areas of elevated potassium, such as at ~270–300 m WMSF, relate to a zone of higher neutron porosity and illustrate a higher degree of fracturing and moderate alteration (see “Alteration petrology”). An area of elevated thorium seems related to a frothy and glassy altered unit (in stratigraphic Unit XIX) at ~470–490 m WMSF, where there are also high porosity values. The peak in uranium at ~410 m WMSF is closely associated with the occurrence of a number of intrusive units (Fig. F85) and also coincides with an increase in potassium. Comparison of measurements of natural gamma radiation in counts per second taken on whole-round cores with downhole gamma ray data shows good agreement (Fig. F85).

Density

Density ranges from 1.35 to 2.94 g/cm³ in Hole U1374A (Fig. F84). Comparison between discrete physical property samples and the downhole density

log shows good agreement (Fig. F84). Low density values correspond to both intervals with enlarged borehole dimensions and sections that exhibit high porosities (Fig. F84). Pronounced high density values relate mostly to intrusive units, lava lobes(?), and well-cemented breccia zones (e.g., lithologic Units 139 and 140 at 492 m WMSF in stratigraphic Unit XIX).

Neutron porosity

Neutron porosity ranges from 4.92% to 78.34%, with a mean of 29.09%. Neutron porosity correlates very well (inversely) with density, resistivity, and velocity measurements. Additionally, there is good agreement between moisture and density porosity measurements (see “Physical properties”) and downhole logging porosity data (Fig. F84). Overall, moisture and density porosity values are slightly lower, but this is because the measurement is biased in the respect that it does not take into account fractures in the formation. In contrast, downhole measurements give an overall in situ porosity measurement for the entire formation. There is a trend of lower neutron porosity with higher density, resistivity, and V_p (Fig. F84). Two main high-porosity zones are clear in Hole U1374A, and these correlate to the oversized borehole at 360–380 m WMSF and the frothy hyaloclastite material in stratigraphic Unit XIX at 470–490 m WMSF. Low resistivity, density, and velocity were also observed in these two depth intervals.

Elastic wave velocity

V_p ranges from 2.67 to 7.11 km/s, with trends in the data correlating very well with discrete physical property measurements (Fig. F84). There is a clear relationship between V_p and density, porosity, and resistivity, whereby high V_p correlates with high resistivity and density and low porosity. Some peaks in V_p can be related to lava lobes or intrusive units found in the breccia sequences. The lowest V_p values can be related to two main zones at 360–380 m WMSF (oversized borehole region) and 470–490 m WMSF (stratigraphic Unit XIX; frothy unit). Compressional wave velocity measured on discrete samples taken on the core correlates well with downhole logging data (Fig. F84). However, velocity values obtained with logging give an overall value for the formation measured (including fractures and clast and matrix mixtures), unlike measurements on core, which are taken on specific discrete cube samples.

Magnetic field measurements

Two different tools were used to obtain magnetic data in Hole U1374A. The GPIT was run as part of

both the FMS-sonic and UBI tool strings, whereas the GBM was run on its own dedicated tool string. Magnetic field data in the drill pipe were only collected by the GBM and were heavily affected by the magnetized pipe, which saturated the magnetometers.

Borehole deviations

Both the GPIT and the GBM measure the deviation of the borehole from vertical, and the results of these measurements are shown in Figure F86 (note that the logs shown are depth shifted to match the depth of GBM Run 1). The deviation differs slightly between the tool strings, primarily because of their different lengths and geometries. Because the GBM tool string is shorter, it shows more pronounced kinks in the deviation caused by washouts in the formation (e.g., at 370 mbsf), and its mean deviation is shallower than that of the longer tool strings. The mean deviation measured by the GBM is $2.64^\circ \pm 0.32^\circ$, whereas the mean deviation measured by the GPIT is $3.16^\circ \pm 0.32^\circ$. The borehole azimuth for Hole U1374A ranges from 235° – 250° . This range is determined by the GPIT using the magnetic field measurements. However, these values are influenced by the magnetic/magnetized neighboring components on the sonde's associated tool string, and thus this range is approximate.

Magnetic measurements

The magnetic logs of the GPIT and GBM show the same trend within the formation and correlate well with the lithology observed in the core recovered from Hole U1374A. The raw magnetic field data of the different tools are shown in Figures F87 and F88. These data were corrected for all sensor errors (sensor offsets, scale factors, and errors in orthogonality) but not for borehole deviation. This means that the horizontal and vertical fields presented here are not yet aligned to the Earth's reference frame. The horizontal magnetic components in the GPIT and GBM agree well, but the vertical components have differing offsets. This is mainly caused by the influence of magnetized components above the GPIT magnetometers in both the FMS and UBI tool string (Figs. F82, F83).

To reduce the magnetic influence of the tool string on the magnetometers of the GBM, a nonmagnetic aluminum sinker bar was custom-made for this expedition and run directly above the tool (Fig. F81). Thus, the magnetic field data measured with the GBM are more reliable and cleaner than those obtained with the GPIT. The influence of the Schlumberger sinker bar and the centralizer was found to be on the order of 350 nT (total field) during extensive testing in Houston, Texas (USA), in August 2010. The

aluminum sinker bar reduces this influence to <50 nT by almost doubling the distance between the magnetometers and the magnetized/magnetizable parts of the tool string. This positive effect can be clearly seen in the difference in the vertical component of the magnetic field measured by the GPIT and the GBM shown in Figure F88. In the case of the GPIT, the surrounding magnetized parts of the associated tool string have an influence on the inclination of the magnetic field measured by this tool (Fig. F89). The actual magnetic field inclination in the borehole is steeper than the average magnetic field inclination given by the GPIT. The UBI tool string, which measures a lower vertical component than the FMS tool string (Fig. F88), also shows a shallower inclination. We expect that a more accurate inclination will be derived from the GBM data (postexpedition).

Determination of rotation history: fiber-optic gyros

In addition to the fluxgate sensors, three angular rate sensors measured the rotations of the GBM. These data will be used to reorient the recorded magnetic field to the Earth's reference frame. Figure F90 shows the accumulated rotation angle for all gyros during both GBM runs. The data are not yet corrected for the rotation of the Earth. Nevertheless, the Rz gyro already provides an approximate rotation history about the vertical axis of the tool. During the first run, the GBM turned ~27 times counterclockwise in the downlog and started turning clockwise during the uplog. During the second run the GBM turned ~19 times counterclockwise during the downlog and ~11 times counterclockwise (negative) during the uplog. In the pipe, rotations were generally more frequent during the downlog and less pronounced during the uplog. In open hole, the tool hardly rotated at all (a total of ~1 turn). The speed during the first run was ~900 m/h in the drill pipe, compared to >1150 m/h during the second run; increasing the speed seemed to slow the rotation of the tool. The lower rates of rotation in the open hole are likely caused by the influence of the heavy drilling mud and the rougher surface of the open hole.

Figure F91 shows the raw magnetic data for the first GBM run together with the lithology from the core recovered from Hole U1374A. The GBM does not record data against depth, but both magnetic field and depth were recorded against time, and later these data sets were combined. The log was depth shifted to the approximate core depth but has not been matched to the other downhole logs (this will be done postexpedition).

Because of the influence of the drill pipe, the uppermost ~130 m of the hole could not be measured with

the GBM. The magnetic influence of the pipe at the start of the open hole section is strongest on the vertical axis, but this influence significantly decays by ~10 m below the end of the pipe. The horizontal component is less disturbed. Because of the way the hole was prepared for logging, a drill bit was present at the bottom of the hole, and as a result both the horizontal and vertical components are disturbed at the lower end of the logs to ~5 m above the bottom of the hole.

Several igneous units observed in core recovered from Hole U1374A were identified in the magnetic data. Examples of these are the basalt intrusive sheets or dikes at 175 and 231 mbsf. Stratigraphic Unit XV can also be clearly separated from the surrounding intervals in the magnetic data (see “**Igneous petrology and volcanology**” for more details of this interval). At ~460 mbsf the vertical field strength drops considerably downhole, coinciding with a change from a hyaloclastite matrix to an interval of large jigsaw-fit clasts of aphyric basalt. Further detailed investigation of the data collected with the GBM will focus on separating and identifying the magnetic signals of the different flow units and determining the inclination and declination of the natural remanent magnetization, with the intention of determining the virtual geomagnetic pole position and the paleolatitude of the Louisville hotspot.

Log units

Preliminary interpretation of the downhole log data divided Hole U1374A into a number of logging units (Fig. F84). Logging units in the section covered or partially influenced by the BHA were interpreted on the basis of downhole gamma ray. Logging units in the open hole section were characterized using the resistivity, density, porosity, and velocity logs.

Two logging units were identified in the section covered by the BHA (Fig. F84):

- Log Unit I (seafloor to 20 m WMSF) shows a significant increase in total gamma ray measurements.
- Log Unit II (20–128.1 m WMSF) shows generally low gamma ray values, with small increases where a sedimentary sequence is present (~65–85 mbsf; stratigraphic Unit IX).

The sequence in open hole was divided into seven additional logging units (Fig. F84):

- Log Unit III (128.1–240 m WMSF) has fluctuating values for density, resistivity, porosity, and velocity, which are related to the interbedded massive lava/intrusions and breccia units in the sequence recovered at this depth interval in stratigraphic Unit XIII. Additionally, the GBM data show strong

fluctuations in both horizontal and vertical magnetic field throughout this logging unit.

- Log Unit IV (240–278 m WMSF) has more consistent values for density, velocity, porosity, and resistivity. Resistivity values are slightly higher (~100 Ω m) in this unit than in other logging units and are related to the lower ~16 m of stratigraphic Unit XIII and stratigraphic Unit XIV.
- Log Unit V (278–358 m WMSF) is characterized at its top by a dramatic decrease in resistivity and a general change from the previous log unit, with greater variability observed in all characterizing log data. A significant increase in the vertical and horizontal magnetic field components of the GBM can also be seen at the top of this log unit. This elevation in magnetic field values relates to stratigraphic Unit XV, and the overall log unit relates to stratigraphic Units XV and XVI.
- Log Unit VI (358–380 m WMSF) shows a marked decrease in density, resistivity, and velocity values and an increase in porosity, which correlates to a band of breccia with green alteration and an enlarged section of the borehole (stratigraphic Unit XVII).
- Log Unit VII (380–469 m WMSF) exhibits characteristics similar to log Unit V, with relatively consistent density of ~2.0 g/cm³ in conjunction with higher stable resistivity, lower porosity, and higher velocity values. Peaks in density and velocity correlate to the presence of intrusive sheets or dikes in the surrounding brecciated formation (stratigraphic Unit XVIII).
- Log Unit VIII (469–490 m WMSF) is characterized by a significant decrease in resistivity, density, and velocity and an increase in porosity. The top of this log unit is also marked by a significant positive kick in the GBM data, which is seen in both the horizontal and vertical magnetic field components. This correlates with frothy altered hyaloclastite material in stratigraphic Unit XIX.
- Log Unit IX (490–507 m WMSF) represents the lower limit of the logging data acquired. However, the top of this unit shows a marked increase in density, velocity, and resistivity and a decrease in porosity. Additionally, the top of this log unit is marked by both a large negative kick in the horizontal magnetic field component and a large positive kick in the vertical magnetic field component measured by the GBM. These significant changes correlate well to intrusive units recovered in the core at this depth interval (stratigraphic Unit XIX). Immediately beneath log Unit IX there is a marked increase in resistivity (manifested as a

double peak) that correlates well with lithologic Unit 146 (aphyric basalt).

Electrical and acoustic images

In Hole U1374A we also acquired FMS electrical resistivity images (Figs. F92, F93) and UBI acoustic images (Fig. F94). The quality of electrical resistivity image measurements depends on close contact between the measuring pads on the tool and the borehole wall. The FMS borehole images are of high quality throughout the borehole (except between 363 and 374 m WMSF, where the borehole was enlarged), and they accurately reproduce breccia and massive igneous unit layering. UBI images require a borehole with a maximum diameter of 30 cm, and therefore only portions of the borehole were imaged with this tool. However, where images were taken, a good virtual hardness of the entire borehole wall was obtained to complement and enhance the information collected with the FMS (Fig. F94).

Figure F92 gives examples of the quality of the FMS images obtained at different depths in Hole U1374A. The images highlight clast-rich breccia areas compared with more matrix-dominated zones. Moreover, they show texture in more massive layers and help refine lithologic boundaries where contacts are not recovered in the core. Another strength of FMS imagery is that the images are oriented to geographic north (using the GPIT), and by picking sinusoidal traces on the images one can obtain important oriented structural information on key boundaries, fractures, and other features of interest (Fig. F93). Extensive structural picking is a key part of postexpedition research. Figure F93 shows some provisional sinusoid picks that highlight some of the high-angle relationships observed in adjacent units and lithologies. Such structural picks can aid overall interpretation of the lithologic sequence observed in the core.

Microbiology

The goals of microbiology sampling at Site U1374 were to collect samples for shore-based cell counts, molecular biological analyses, and $\delta^{34}\text{S}$ and $\delta^{13}\text{C}$ stable isotope analyses; to inoculate media for cultivation of subseafloor microbes; and to set up stable isotope addition bioassays whereby the rate of incorporation of compounds labeled with ^{14}C , ^{15}N , and ^{34}S can be measured. These bioassays will allow for calculation of metabolic rates of subseafloor microbes at Rigel Guyot. Twenty-nine whole-round samples (5–13 cm long) were collected for microbiological analysis (Figs. F95, F96). The samples were

unconsolidated sediment (1), volcanic sandstone (2), volcanic or sedimentary basalt breccia (23), and aphyric basaltic lava flows (3). All samples were preserved for shore-based DNA analysis, cell counting, and $\delta^{34}\text{S}$ and $\delta^{13}\text{C}$ analyses. Eleven samples were used to inoculate culturing experiments with as many as seven different types of cultivation media (Table T18). Five samples were used to set up stable isotope addition bioassays to determine rates of carbon and nitrogen utilization by subsurface microbes at Rigil Guyot (Table T19). Two cores were seeded with fluorescent microspheres, and samples from these cores were collected for shipboard analysis of contamination via fluorescent microsphere counts (Table T20).

Cell counts

Performing shipboard cell counts on rock samples is difficult to nearly impossible because of the combination of autofluorescence from rock particles and the difficulty of focusing using a 100 \times objective paired with a 10 \times eyepiece (1000 \times total magnification) on a moving ship. Therefore, cell counts were not attempted on samples from Site U1374.

Culturing experiments

Eleven samples were used to inoculate culturing experiments with as many as seven different types of cultivation media targeting autotrophic sulfur oxidizers, heterotrophic sulfur oxidizers, autotrophic iron oxidizers, autotrophic iron reducers, heterotrophic iron reducers, and nonspecific heterotrophs (Table T18; for details on media recipes, see Table T14 in the “Methods” chapter [Expedition 330 Scientists, 2012a]). On the basis of visual observation of turbidity, several vials had obvious growth in them. Media targeting sulfur-oxidizing bacteria and general heterotrophic bacteria appear to have yielded growth in multiple samples; however, media targeting methanogens and sulfate-reducing bacteria were not successful, probably because of the continued difficulty in maintaining anoxic conditions, which are required for the growth of both groups of bacteria. The deepest depth from which positive results were obtained is 400 mbsf (Sample 330-U1374A-58R-6, 50–62 cm). All preliminary results will be verified during shore-based research.

Stable isotope addition bioassays

Five samples were used to initiate stable isotope addition bioassays to study rates of carbon, nitrogen, and sulfur cycling by subsurface microbes at Rigil Guyot (Table T19). A more effective method for obtaining large amounts of uncontaminated rock sample for these bioassays (“enhanced extraction”) was

developed during processing of Sample 330-U1374A-15R-2, 79–89 cm (see “Microbiology” in the “Methods” chapter [Expedition 330 Scientists, 2012a]). Enhanced extraction was carried out on all samples from Hole U1374A used to initiate stable isotope analyses.

Depending on the volume of rock obtained, one or two experiments were executed with two sets of conditions. The first experiment was addition of ^{13}C bicarbonate and ^{34}S elemental sulfur. This experiment was conducted with all samples. Beginning with Sample 330-U1374A-21R-2, 111–119 cm, ^{15}N compounds were also added to all samples. To bioassays with ^{13}C carbonate, ^{15}N ammonia was added. When large volumes of sample were available for stable isotope addition bioassays, an additional experiment with ^{13}C glucose, ^{13}C acetate, ^{34}S elemental sulfur, and ^{15}N nitrate was conducted. This combination of stable isotope additions aimed to quantify C, N, and S cycling specifically among heterotrophic microbes. Because quantification of elemental cycling by heterotrophs was a secondary goal of the stable isotope addition bioassays, addition of ^{13}C glucose, ^{13}C acetate, ^{34}S elemental sulfur, and ^{15}N nitrate was not always done (Table T19). Additionally, the amount of ^{13}C glucose available was depleted after adding it to two samples (330-U1374A-21R-2, 111–119 cm, and 24R-3, 90–101 cm) and it was therefore not used further.

Incubations from Samples 330-U1374A-31R-3, 142–150 cm, and 71R-3, 47–55 cm, included two “killed” control vials. These vials were treated in the same way as the other experimental vials, with the exception that after adding the rock chips, the vials were combusted at $>400^\circ\text{C}$ for 3 h to kill all microbes. After the vials were cooled to room temperature, basic seawater media (see “Microbiology” in the “Site U1373” chapter [Expedition 330 Scientists, 2012c]) and stable isotopes were added to the vials, and they were then treated as the other experiments. This treatment acts as a negative control and provides a baseline stable isotope reading for the rocks in the experiment. One vial will be terminated at t_2 (2 months) and the other will be terminated at t_3 (6 months).

As with the stable isotope addition bioassay performed at Site U1373, stable isotopes and rock chips were added to 125 mL serum vials, followed by 100 mL of basic seawater media. The vials were then placed in a 4°C incubator in the dark. At time points of 2 weeks, 2 months, and 6 months, the incubation in one or more vials (depending on number of vials per condition) will be terminated, and the rocks will

be collected to measure incorporation of labeled carbon, nitrogen, and sulfur.

Contamination testing

Fluorescent microspheres were deployed during drilling for Cores 330-U1374A-8R and 45R. As the core arrived on the rig floor, a rig floor worker collected the drill fluid draining out of the core liner with a beaker (Fig. F97). Analysis of this drill fluid should provide the concentration of microspheres delivered to the core. Water samples for microsphere counts were also collected from each of the three separate sterile seawater rinses that every microbiology whole-round sample is subjected to before subsampling. For each wash, 50 mL of sterile seawater was used. After the microbiology (MBIO) whole round was washed, subsamples were taken during standard microbiology sampling and preserved the same way as cell count samples. The subsamples were analyzed via fluorescent microscopy to quantify microspheres in the rocks. Additionally, following MBIO sterile processing, a ~1 cm thick whole-round slab was cut from the remainder of the whole-round sample with the Feckler saw. This slab was divided into five sections with the Feckler saw (Fig. F97) for microsphere counting of specific areas. Subsamples from these sections were taken specifically from the middle of the section (area shown between dashed lines in Fig. F97).

Shipboard counts of fluorescent microspheres revealed that the microspheres were indeed delivered within the core liner, as indicated by their presence in the drill fluid (Table T20). Microsphere counts of the rinse water are lower than those in the drill fluid and are zero by the third wash. This indicates that few, if any, microspheres were left on the surface of the whole round when the microbiologist began processing samples. The absence of any microspheres on or inside the whole-round samples indicates that the potential for microbial contamination was extremely low during drilling of Hole U1374A.

As an additional test for microbial contamination, drill fluid was collected from a tap located on the drill rig floor. One liter of the fluid was filtered on a 0.2 μm polycarbonate filter. One liter was also frozen unfiltered. The filter will be analyzed for microbial community composition during shore-based research. Drill fluid is composed primarily of surface seawater that is circulated down through the borehole. It is unlikely that microbes resident in surface seawater would also be present in the deep subsurface of a seamount. Therefore, if microbes detected in the drill fluids were also detected in one or more samples, we would know that the samples were most

likely contaminated. An example of obvious drill fluid contamination would be the presence of cyanobacteria, which require sunlight for survival.

References

- Alt, J.C., 1995. Subseafloor processes in mid-ocean ridge hydrothermal systems. In Humphris, S.E., Zierenberg, R., Mullineaux, L., and Thomson, R. (Eds.), *Seafloor Hydrothermal Systems: Physical, Chemical, Biological and Geological Interactions within Hydrothermal Systems*. Geophys. Monogr., 91:85–114.
- Arason, P., and Levi, S., 2010. Maximum likelihood solution for inclination-only data in paleomagnetism. *Geophys. J. Int.*, 182(2):753–771. doi:10.1111/j.1365-246X.2010.04671.x
- Bach, W., Hegner, E., Erzinger, J., and Satir, M., 1994. Chemical and isotopic variations along the superfast spreading East Pacific Rise from 6 to 30°S. *Contrib. Mineral. Petrol.*, 116(4):365–380. doi:10.1007/BF00310905
- Barr, S.R., Révillon, S., Brewer, T.S., Harvey, P.K., and Tarnay, J., 2002. Determining the inputs to the Mariana Subduction Factory: using core-log integration to reconstruct basement lithology at ODP Hole 801C. *Geochem., Geophys., Geosyst.*, 3(11):8901–8925. doi:10.1029/2001GC000255
- Bartetzko, A., Pezard, P., Goldberg, D., Sun, Y.-F., and Becker, K., 2001. Volcanic stratigraphy of DSDP/ODP Hole 395A: an interpretation using well-logging data. *Mar. Geophys. Res.*, 22(2):111–127. doi:10.1023/A:1010359128574
- Baxter, N.L., 2008. Magmatic sulphur and chlorine abundances at Stromboli, Italy, and their role in the formation of vesicle-hosted metal alloys [M.S. thesis]. Brigham Young Univ., Provo, Utah.
- Beier, C., Vanderkluisen, L., Regulous, M., Mahoney, J.J., and Garbe-Schönberg, D., 2011. Lithospheric control on geochemical composition along the Louisville Seamount Chain. *Geochem., Geophys., Geosyst.*, 12:Q0AM01. doi:10.1029/2011GC003690
- Bown, P.R. (Ed.), 1998. *Calcareous Nannofossil Biostratigraphy*: Dordrecht, The Netherlands (Kluwer Academic Publ.).
- Caron, M., 1985. Cretaceous planktic foraminifera. In Bolli, H.M., Saunders, J.B., and Perch-Nielsen, K. (Eds.), *Plankton Stratigraphy*: Cambridge (Cambridge Univ. Press), 17–86.
- Cheng, Q., Park, K.-H., Macdougall, J.D., Zindler, A., Lugmair, G.W., Hawkins, J., Lonsdale, P., and Staudigel, H., 1987. Isotopic evidence for a hot spot origin of the Louisville Seamount Chain. In Keating, B.H., Fryer, P., Batiza, R., and Boehlert, G. (Eds.), *Seamounts, Islands and Atolls*. Geophys. Monogr., 43:283–296.
- Clague, D.A., Moore, J.G., Dixon, J.E., and Friesen W.B., 1995. Petrology of submarine lavas from Kilauea's Puna Ridge, Hawaii. *J. Petrol.*, 36(2):299–349.

- Clague, D.A., Paduan, J.B., and Davis, A.S., 2009. Wide-spread strombolian eruptions of mid-ocean ridge basalt. *J. Volcanol. Geotherm. Res.*, 180(2–4):171–188. doi:10.1016/j.jvolgeores.2008.08.007
- Courtillot, V., Davaille, A., Besse, J., and Stock, J., 2003. Three distinct types of hotspots in Earth's mantle. *Earth Planet. Sci. Lett.*, 205(3–4):295–308. doi:10.1016/S0012-821X(02)01048-8
- Duncan, R.A., Tarduno, J.A., and Scholl, D.W., 2006. Leg 197 synthesis: southward motion and geochemical variability of the Hawaiian hotspot. In Duncan, R.A., Tarduno, J.A., Davies, T.A., and Scholl, D.W. (Eds.), *Proc. ODP, Sci. Results*, 197: College Station, TX (Ocean Drilling Program), 1–39. doi:10.2973/odp.proc.sr.197.001.2006
- Expedition 330 Scientists, 2012a. Methods. In Koppers, A.A.P., Yamazaki, T., Geldmacher, J., and the Expedition 330 Scientists, *Proc. IODP*, 330: Tokyo (Integrated Ocean Drilling Program Management International, Inc.). doi:10.2204/iodp.proc.330.102.2012
- Expedition 330 Scientists, 2012b. Site U1372. In Koppers, A.A.P., Yamazaki, T., Geldmacher, J., and the Expedition 330 Scientists, *Proc. IODP*, 330: Tokyo (Integrated Ocean Drilling Program Management International, Inc.). doi:10.2204/iodp.proc.330.103.2012
- Expedition 330 Scientists, 2012c. Site U1373. In Koppers, A.A.P., Yamazaki, T., Geldmacher, J., and the Expedition 330 Scientists, *Proc. IODP*, 330: Tokyo (Integrated Ocean Drilling Program Management International, Inc.). doi:10.2204/iodp.proc.330.104.2012
- Fitton, J.G., and Godard, M., 2004. Origin and evolution of magmas on the Ontong Java Plateau. In Fitton, J.G., Mahoney, J.J., Wallace, P.J., and Saunders, A.D. (Eds.), *Origin and Evolution of the Ontong Java Plateau*. Geol. Soc. Spec. Publ., 229(1):151–178. doi:10.1144/GSL.SP.2004.229.01.10
- Flaum, C., Galford, J.E., and Hastings, A., 1987. Enhanced vertical resolution processing of dual detector gamma-gamma density logs. *Trans. SPWLA Annu. Logging Symp.*, 28.
- Flügel, E., 1982. *Microfacies Analysis of Limestones*: New York (Springer-Verlag).
- Frey, F.A., Garcia, M.O., Wise, W.S., Kennedy, A., Gurriet, P., and Albarede, F., 1991. The evolution of Mauna Kea Volcano, Hawaii: petrogenesis of tholeiitic and alkalic basalts. *J. Geophys. Res.*, [Solid Earth], 96(B9):14347–14375. doi:10.1029/91JB00940
- Frey, F.A., Wise, W.S., Garcia, M.O., West, H., Kwon, S.-T., and Kennedy, A., 1990. Evolution of Mauna Kea Volcano, Hawaii: petrologic and geochemical constraints on postshield volcanism. *J. Geophys. Res.*, [Solid Earth], 95(B2):1271–1300. doi:10.1029/JB095iB02p01271
- Garcia, M.O., Pietruszka, A.J., and Rhodes, J.M., 2003. A petrologic perspective of Kilauea Volcano's summit magma reservoir. *J. Petrol.*, 44(12):2313–2339. doi:10.1093/petrology/egg079
- Giret, A., Weis, D., Grégoire, M., Mattielli, N., Moine, B., Michon, G., Scoates, J., Tourpin, S., Delpech, G., Gerbe, M.C., Doucet, S., Ethien, R., and Cottin, J.-Y., 2003. L'Archipel de Kerguelen: les plus vieilles îles dans le plus jeune océan. *Géologues*, 137:15–23.
- Gradstein, F.M., Agterberg, F.P., Ogg, J.G., Hardenbol, J., van Veen, P., Thierry, J., and Huang, Z., 1994. A Mesozoic time scale. *J. Geophys. Res.*, [Solid Earth], 99(B12):24051–24074. doi:10.1029/94JB01889
- Haq, B.U., Hardenbol, J., and Vail, P.R., 1987. Chronology of fluctuating sea levels since the Triassic. *Science*, 235(4793):1156–1167. doi:10.1126/science.235.4793.1156
- Hardenbol, J., Thierry, J., Farley, M.B., Jacquin, T., de Graciansky, P.-C., and Vail, P.R., 1998. Mesozoic and Cenozoic sequence chronostratigraphic framework of European basins. In de Graciansky, P.-C., Hardenbol, J., Jacquin, T., and Vail, P.R. (Eds.), *Mesozoic and Cenozoic Sequence Stratigraphy of European Basins*. Spec. Publ.—SEPM (Soc. Sediment. Geol.), 60:3–13. doi:10.2110/pec.98.02.0003
- Hawkins, J.W., Lonsdale, P., and Batiza, R., 1987. Petrologic evolution of the Louisville Seamount Chain. In Keating, B.H., Fryer, P., Batiza, R., and Boehlert, G.W. (Eds.), *Seamounts, Islands, and Atolls*. Geophys. Monogr., 43:235–254.
- Head, J.W., III, and Wilson, L., 2002. Deep submarine pyroclastic eruptions: theory and predicted landforms and deposits. *J. Volcanol. Geotherm. Res.*, 121(3–4):155–193. doi:10.1016/S0377-0273(02)00425-0
- Honnorez, J., 2003. Hydrothermal alteration vs. ocean-floor metamorphism. A comparison between two case histories: the TAG hydrothermal mound (Mid-Atlantic Ridge) vs. DSDP/ODP Hole 504B (equatorial East Pacific). *C. R. Geosci.*, 335(10–11):781–824. doi:10.1016/j.crte.2003.08.009
- Hunter, E.A., 2007. The smallest base and precious metal deposits in the world: vapor transport and deposition of Co-Cu-Sn-Ag alloys in vesicles [M.S. thesis]. Brigham Young Univ., Provo, Utah.
- Jakobsson, S.P., Thors, K., Vésteinsson, Á.T., and Ásbjörnsdóttir, L., 2009. Some aspects of the seafloor morphology at Surtsey Volcano: the new multibeam bathymetric survey of 2007. *Surtsey Res.*, 12:9–20. http://www.surtsey.is/SRS_publ/2009-XII/high_res/2009-XII_009-020_Some-aspects--hi.pdf
- Kataoka, K., 2005. Distal fluvio-lacustrine volcanoclastic resedimentation in response to an explosive silicic eruption: the Pliocene Mushono tephra bed, central Japan. *Geol. Soc. Am. Bull.*, 117(1–2):3–17. doi:10.1130/B25379.1
- Knight, M.D., and Walker, G.P.L., 1988. Magma flow directions in dikes of the Koolau complex, Oahu, determined from magnetic fabric studies. *J. Geophys. Res.*, [Solid Earth], 93(B5):4301–4319. doi:10.1029/JB093iB05p04301
- Kokelaar, P., 1986. Magma-water interactions in subaqueous and emergent basaltic volcanism. *Bull. Volcanol.*, 48(5):275–289. doi:10.1007/BF01081756
- Koppers, A.A.P., Duncan, R.A., and Steinberger, B., 2004. Implications of a nonlinear $^{40}\text{Ar}/^{39}\text{Ar}$ age progression along the Louisville Seamount Trail for models of fixed

- and moving hot spots. *Geochem., Geophys., Geosyst.*, 5(6):Q06L02–Q06L23. doi:10.1029/2003GC000671
- Koppers, A.A.P., Yamazaki, T., and Geldmacher, J., 2010. Louisville Seamount Trail: implications for geodynamic mantle flow models and the geochemical evolution of primary hotspots. *IODP Sci. Prosp.*, 330. doi:10.2204/iodp.sp.330.2010
- LeHuray, A.P., 1989. Native copper in ODP Site 642 tholeiites. In Eldholm, O., Thiede, J., Taylor, E., et al., *Proc. ODP, Sci. Results*, 104: College Station, TX (Ocean Drilling Program), 411–417. doi:10.2973/odp.proc.sr.104.137.1989
- Le Maitre, R.W., Bateman, P., Dudek, A., Keller, J., Lameyre, J., Le Bas, M.J., Sabine, P.A., Schmid, R., Sorensen, H., Streckeisen, A., Woolley, A.R., and Zanettin, B., 1989. *A Classification of Igneous Rocks and Glossary of Terms*: Oxford (Blackwell).
- Lipman, P.W., Rhodes, J.M., and Dalrymple, G.B., 1990. The Ninole basalt—implications for the structural evolution of Mauna Loa Volcano, Hawaii. *Bull. Volcanol.*, 53(1):1–19. doi:10.1007/BF00680316
- Macdonald, G.A., 1968. Composition and origin of Hawaiian lavas. In Coats, R.R., Hay, R.L., and Anderson, C.A. (Eds.), *Studies in Volcanology—A Memoir in Honor of Howel Williams*. Mem.—Geol. Soc. Am., 116:477–522.
- Macdonald, G.A., and Katsura, T., 1964. Chemical composition of Hawaiian lavas. *J. Petrol.*, 5(1):82–133. <http://petrology.oxfordjournals.org/content/5/1/82.abstract>
- Mahoney, J.J., Fitton, J.G., Wallace, P.J., et al., 2001. *Proc. ODP, Init. Repts.*, 192: College Station, TX (Ocean Drilling Program). doi:10.2973/odp.proc.ir.192.2001
- Mahoney, J.J., Sinton, J.M., Kurz, M.D., Macdougall, J.D., Spencer, K.J., and Lugmair, G.W., 1994. Isotope and trace element characteristics of a super-fast spreading ridge: East Pacific Rise 13–23°S. *Earth Planet. Sci. Lett.*, 121(1–2):173–193. doi:10.1016/0012-821X(94)90039-6
- Mahoney, J.J., and Spencer, K.J., 1991. Isotopic evidence for the origin of the Manihiki and Ontong Java oceanic plateaus. *Earth Planet. Sci. Lett.*, 104(2–4):196–210. doi:10.1016/0012-821X(91)90204-U
- Moore, J.G., and Clague, D.A., 1992. Volcano growth and evolution of the island of Hawaii. *Geol. Soc. Am. Bull.*, 104(11):1471–1484. doi:10.1130/0016-7606(1992)104<1471:VGAEOT>2.3.CO;2
- Neuhoff, P.S., Watt, W.S., Bird, D.K., and Pedersen, A.K., 1997. Timing and structural relations of regional zeolite zones in basalts of the East Greenland continental margin. *Geology*, 25(9):803–806. doi:10.1130/0091-7613(1997)025<0803:TASROR>2.3.CO;2
- Rhodes, J.M., 1996. Geochemical stratigraphy of lava flows sampled by the Hawaii Scientific Drilling Project. *J. Geophys. Res., [Solid Earth]*, 101(B5):11729–11746. doi:10.1029/95JB03704
- Rhodes, J.M., and Hart, S.R., 1995. Episodic trace element and isotopic variations in historical Mauna Loa lavas: implications for magma and plume dynamics. In Rhodes, J.M., and Lockwood, J.P. (Eds.), *Mauna Loa Revealed: Structure, Composition, History, and Hazards*. Geophys. Monogr., 92:263–288.
- Richards, M.A., and Griffiths, R.W., 1989. Thermal entrainment by deflected mantle plumes. *Nature (London, U. K.)*, 342(6252):900–902. doi:10.1038/342900a0
- Riisager, P., Hall, S., Antretter, M., and Zhao, X., 2003. Paleomagnetic paleolatitude of Early Cretaceous Ontong Java Plateau basalts: implications for Pacific apparent and true polar wander. *Earth Planet. Sci. Lett.*, 208(3–4):235–252. doi:10.1016/S0012-821X(03)00046-3
- Sinton, J.M., Smaglik, S.M., Mahoney, J.J., and Macdonald, K.C., 1991. Magmatic processes at superfast spreading mid-ocean ridges: glass compositional variations along the East Pacific Rise 13°–23°S. *J. Geophys. Res., [Solid Earth]*, 96:6133–6155. doi:10.1029/90JB02454
- Smith, G.A., and Lowe, D.R., 1991. Lahars: volcano-hydrologic events and deposition in the debris flow—hyperconcentrated flow continuum. In Fisher, R.V., and Smith, G.A. (Eds.), *Sedimentation in Volcanic Settings*. Spec. Publ.—SEPM (Soc. Sediment. Geol.), 45:59–70. doi:10.2110/pec.91.45.0059
- Smith, W.H.F., and Sandwell, D.T., 1997. Global sea floor topography from satellite altimetry and ship depth soundings. *Science*, 277(5334):1956–1962. doi:10.1126/science.277.5334.1956
- Steinberger, B., 2002. Motion of the Easter hot spot relative to Hawaii and Louisville hot spots. *Geochem., Geophys., Geosyst.*, 3(11):8503–8529. doi:10.1029/2002GC000334
- Steinberger, B., and Antretter, M., 2006. Conduit diameter and buoyant rising speed of mantle plumes: implications for the motion of hot spots and shape of plume conduits. *Geochem., Geophys., Geosyst.*, 7(11):Q11018–Q11042. doi:10.1029/2006GC001409
- Steinberger, B., and Calderwood, A., 2006. Models of large-scale viscous flow in the Earth's mantle with constraints from mineral physics and surface observations. *Geophys. J. Int.*, 167(3):1461–1481. doi:10.1111/j.1365-246X.2006.03131.x
- Steinberger, B., Sutherland, R., and O'Connell, R.J., 2004. Prediction of Emperor–Hawaii Seamount locations from a revised model of global plate motion and mantle flow. *Nature (London, U. K.)*, 430(6996):167–173. doi:10.1038/nature02660
- Tarduno, J.A., Duncan, R.A., Scholl, D.W., Cottrell, R.D., Steinberger, B., Thordarson, T., Kerr, B.C., Neal, C.R., Frey, F.A., Torii, M., and Carvallo, C., 2003. The Emperor Seamounts: southward motion of the Hawaiian hotspot plume in Earth's mantle. *Science*, 301(5636):1064–1069. doi:10.1126/science.1086442
- Tarduno, J.A., Duncan, R.A., Scholl, D.W., et al., 2002. *Proc. ODP, Init. Repts.*, 197: College Station, TX (Ocean Drilling Program). doi:10.2973/odp.proc.ir.197.2002
- Tejada, M.L.G., Mahoney, J.J., Duncan, R.A., and Hawkins, M.P., 1996. Age and geochemistry of basement and alkalic rocks of Malaita and Santa Isabel, Solomon Islands, southern margin of Ontong Java Plateau. *J. Petrol.*, 37(2):361–394. doi:10.1093/petrology/37.2.361

- Tejada, M.L.G., Mahoney, J.J., Neal, C.R., Duncan, R.A., and Pettersen, M.G., 2002. Basement geochemistry and geochronology of central Malaita, Solomon Islands, with implications for the origin and evolution of the Ontong Java Plateau. *J. Petrol.*, 43(3):449–484. [doi:10.1093/petrology/43.3.449](https://doi.org/10.1093/petrology/43.3.449)
- Vanderkluyzen, L., Mahoney, J.J., Koppers, A.A., and Lonsdale, P.F., 2007. Geochemical evolution of the Louisville Seamount Chain. *Eos, Trans. Am. Geophys. Union*, 88(52)(Suppl.):V42B-06. <http://www.agu.org/meetings/fm07/waisfm07.html>
- Walker, G.P.L., 1951. The amygdale minerals in the Tertiary lavas of Ireland. I. The distribution of chabazite habits and zeolites in the Garron plateau area, County Antrim. *Min. Mag.*, 29:773–791.
- Watkins, D.K., Wise, S.W., Jr., Pospichal, J.J., and Crux, J., 1996. Upper Cretaceous calcareous nannofossil biostratigraphy and paleoceanography of the Southern Ocean. In Mokuilevsky, A., and Whatley, R. (Eds.), *Microfossils and Oceanic Environments*: Univ. Wales (Aberystwyth Press), 355–381.
- Wessel, P., and Kroenke, L.W., 1997. A geometric technique for relocating hotspots and refining absolute plate motions. *Nature (London, U. K.)*, 387(6631):365–369. [doi:10.1038/387365a0](https://doi.org/10.1038/387365a0)
- West, H.B., Garcia, M.O., Frey, F.A., and Kennedy, A., 1988. Nature and cause of compositional variation among the alkalic cap lavas of Mauna Kea Volcano, Hawaii. *Contrib. Mineral. Petrol.*, 100(3):383–397. [doi:10.1007/BF00379747](https://doi.org/10.1007/BF00379747)

Publication: 11 February 2012

MS 330-105

Figure F1. Bathymetric map of the old end of the Louisville Seamount Trail in the southwest Pacific, showing the location of Osborn Guyot, Site U1372 on Canopus Guyot, and Sites U1373 and U1374 on Rigil Guyot. GMT-generated bathymetric map is based on a combination of SIMRAD EM120 multibeam data collected during the AMAT02RR site survey expedition aboard the R/V *Roger Revelle* and the global predicted bathymetry (v8.2) from Smith and Sandwell (1997). The current motion of the Pacific plate is indicated with the black arrow. The map uses a linear projection (i.e., horizontal and vertical scales differ) based on WGS-84.

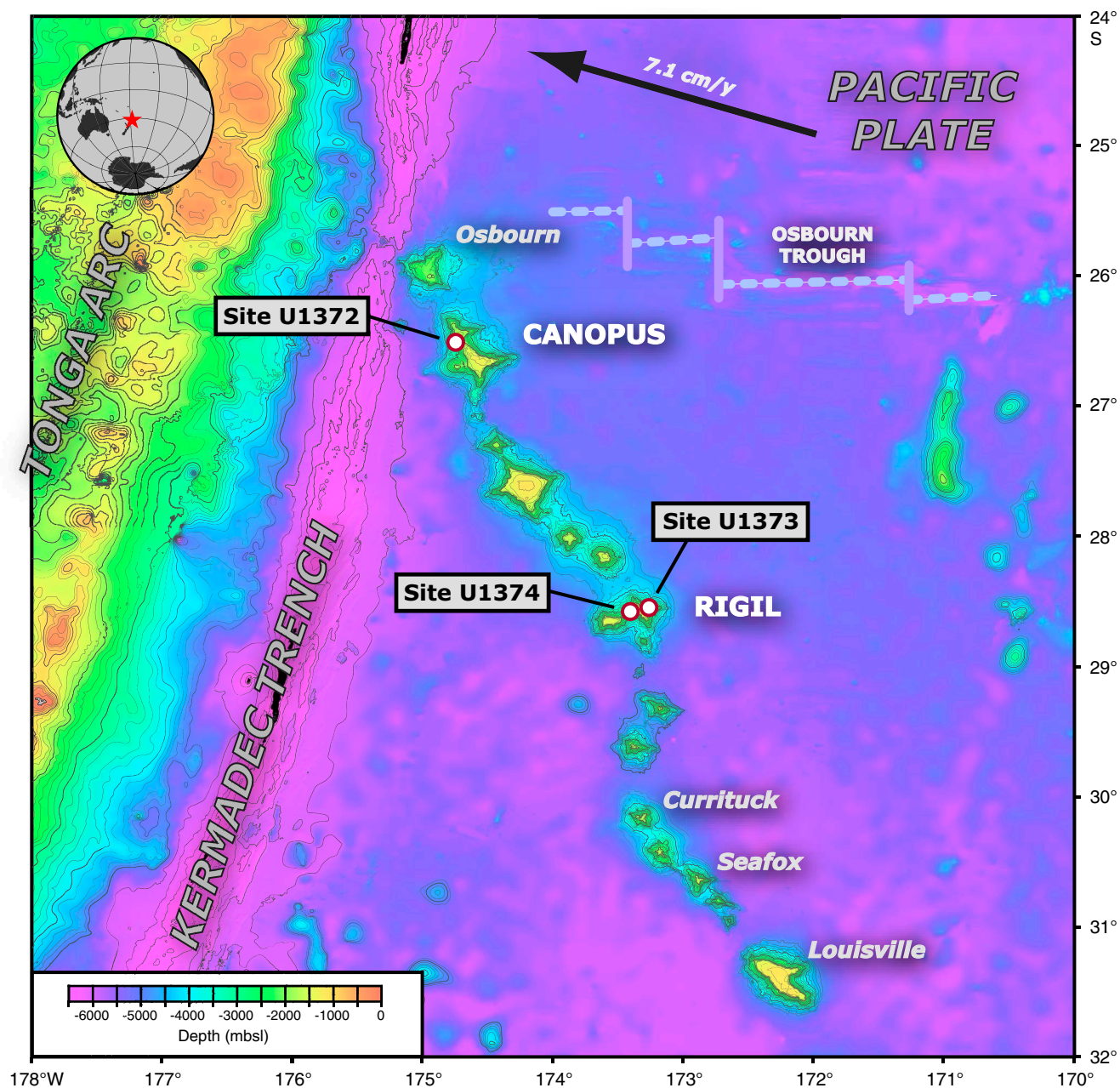


Figure F2. Detailed bathymetric map of Sites U1373 and U1374 on Rigil Guyot and three neighboring guyots or seamounts at 28.2°S, 28.7°S, and 28.8°S. GMT-generated bathymetric map is based on a combination of SIMRAD EM120 multibeam data collected during the AMAT02RR site survey expedition aboard the R/V *Roger Revelle* and global predicted bathymetry (v8.2) from Smith and Sandwell (1997). Dredge locations from previous cruises are indicated by open squares. Crossing multichannel seismic reflection lines collected during the AMAT02RR site survey are shown in blue (for details, see Koppers et al., 2010). Map uses a linear projection (i.e., horizontal and vertical scales differ) based on WGS-84.

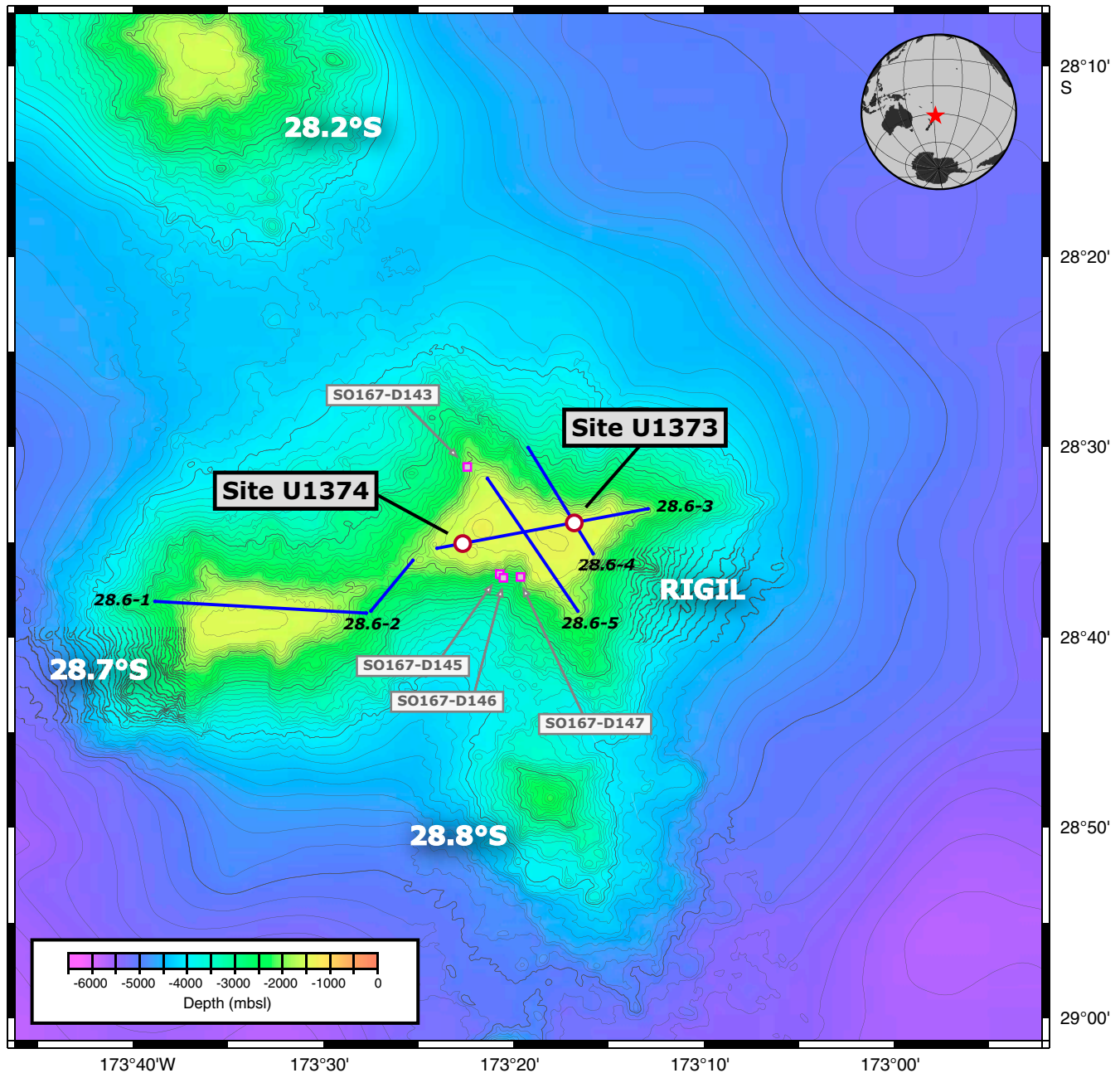


Figure F3. Operation time vs. penetration depth, Hole U1374A. Major operation milestones are labeled. Dashed line = planned penetration, solid red line = actual penetration. Rot. = rotation, ROP = rate of penetration. FFF = free-fall funnel, BHA = bottom-hole assembly, triple combo = triple combination, GBM = Göttingen Borehole Magnetometer, FMS = Formation MicroScanner-sonic, UBI = Ultrasonic Borehole Imager.

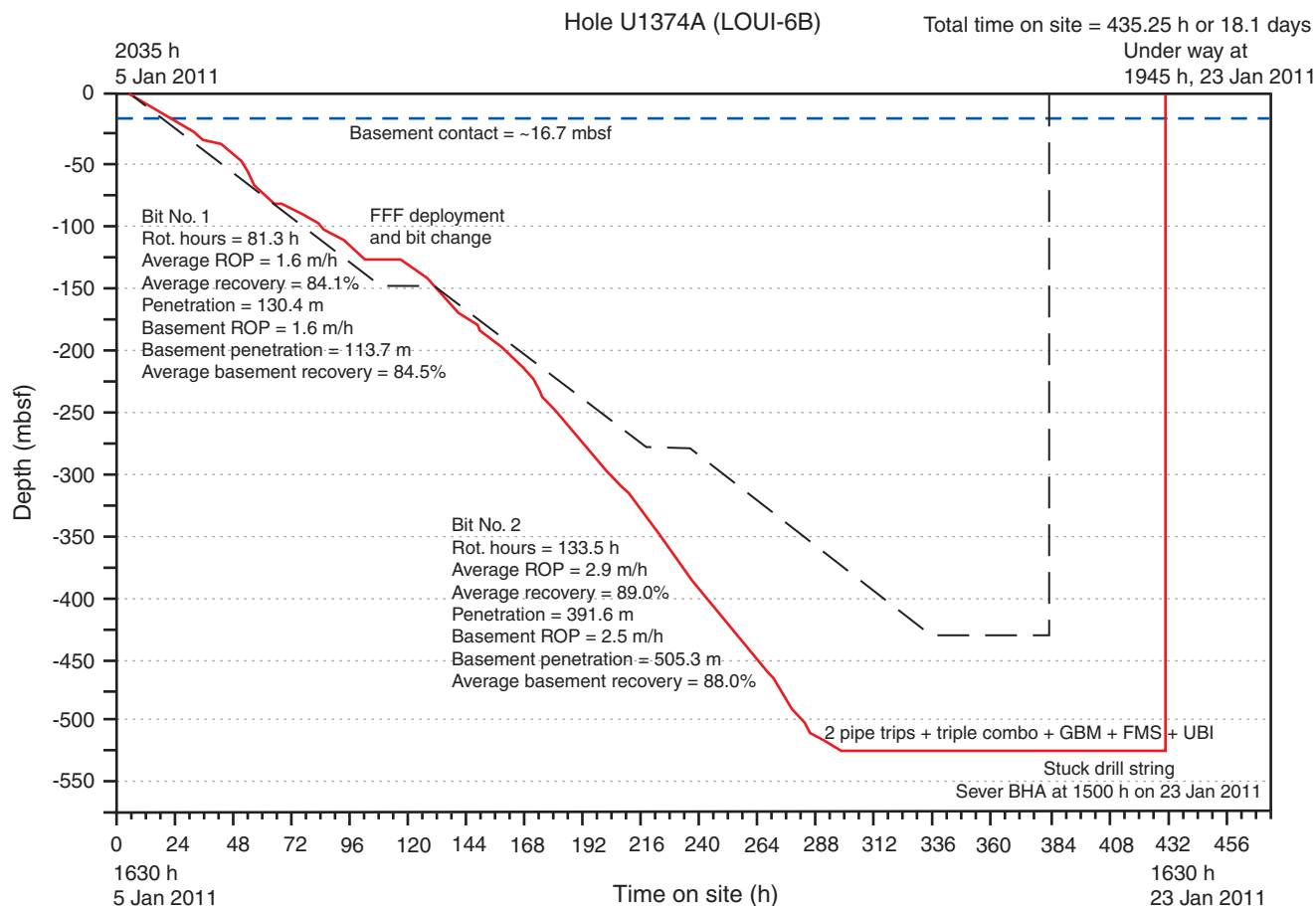


Figure F4. Stratigraphic summary of sedimentary sequences with selected lithologic parameters, Site U1374. See U1374A.XLS in SIZE in SEDIMENT in “**Supplementary material**” for estimates of grain size and roundness with depth (see also “**Sedimentology**” in the “Methods” chapter [Expedition 330 Scientists, 2012a]).

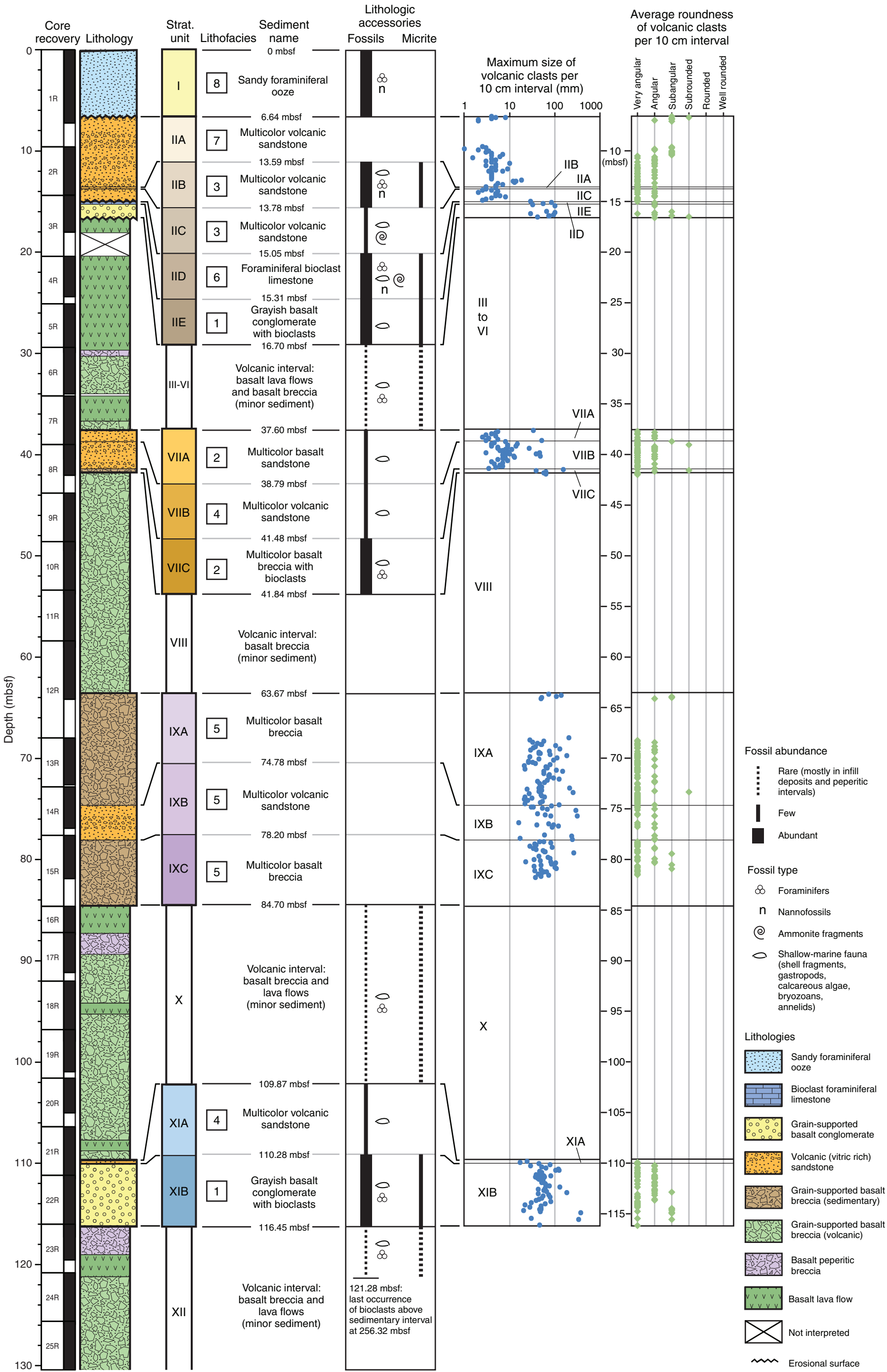


Figure F5. Close-up photographs of representative lithologies and lithofacies, Site U1374. **A.** Sandy foraminiferal ooze in Unit I (interval 330-U1374A-1R-5A, 10–50 cm) deposited in a pelagic environment and corresponding to youngest sedimentary cover sampled on Rigil Guyot. **B.** Multicolor volcanic sandstone in Subunit IIA (interval 330-U1374A-2R-2A, 89.3–129.3 cm), interpreted as air fall volcanic products emplaced in a submarine environment with limited postdepositional reworking. **C.** Multicolor volcanic sandstone in Subunit IIB (interval 330-U1374A-2R-4A, 16.1–34.6 cm) with (1) burrow and (2) gastropods, interpreted as subaerial to shallow-marine volcanic products deposited or reworked in a shallow-marine to hemipelagic environment. **D.** Multicolor volcanic sandstone in Subunit IIC (interval 330-U1374A-3R-1A, 0.3–27.3 cm); inset shows larger molluscan fragments with (1) bivalve, (2) gastropod, and (3) ammonite, interpreted as subaerial to shallow-marine volcanic product deposited or reworked in a shallow-marine to hemipelagic environment. (Continued on next three pages.)

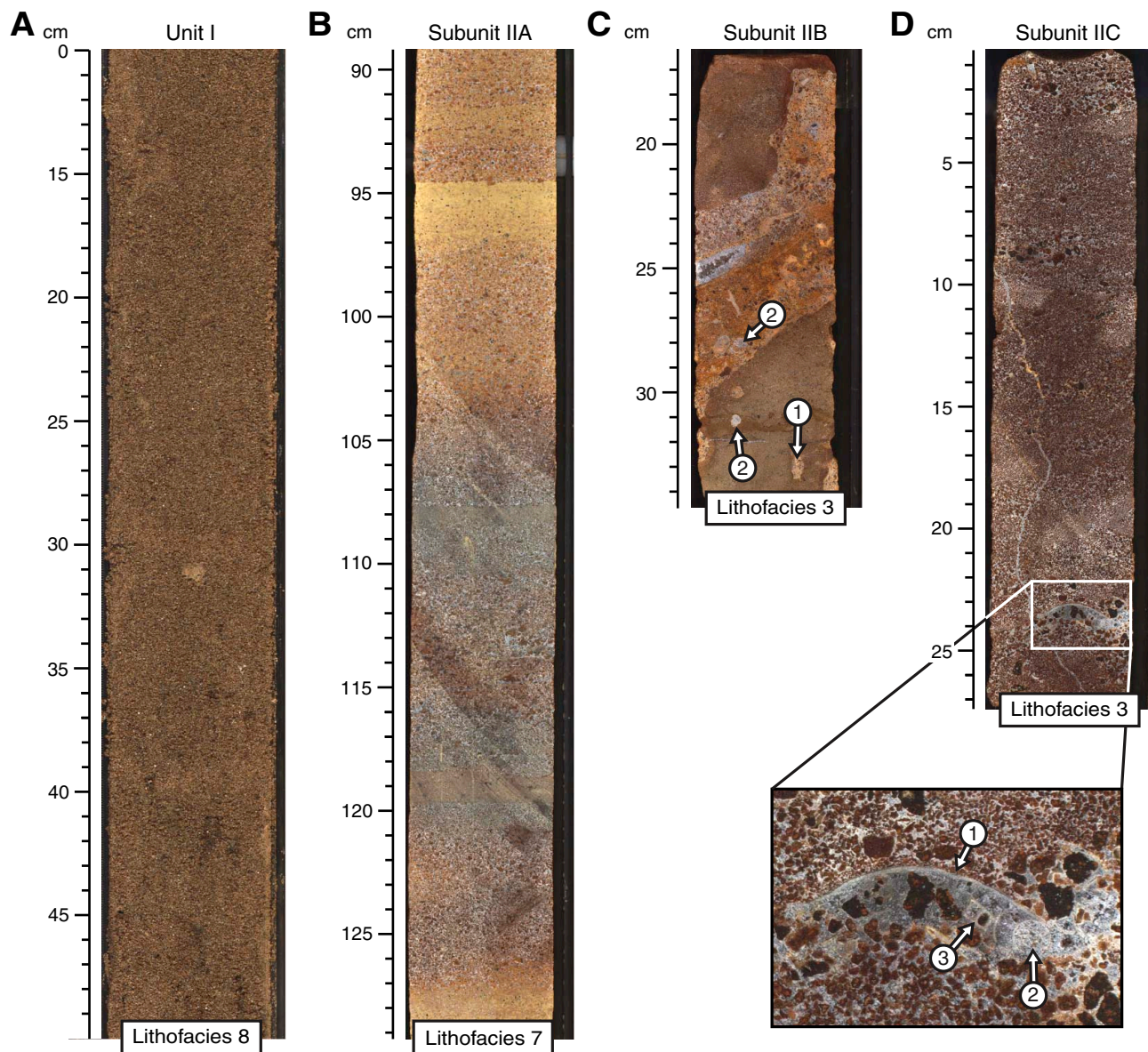


Figure F5 (continued). E. Foraminiferal bioclast limestone in Subunit IID (interval 330-U1374A-3R-1A, 65–79 cm), corresponding to a condensed hemipelagic interval with several hiatuses and hardground surfaces and probably reflecting initial drowning of Rigil Guyot at Site U1374 (see also Fig. F6). Cement textures, erosional contact ages between Subunits IIC and IID (arrow), and paleontological ages also support a late-stage reemergence of the seamount at Site U1374. F. Grayish basalt conglomerate with bioclasts in Subunit IIE (interval 330-U1374A-3R-2A, 25–65 cm), deposited in an intertidal to subtidal environment and believed to represent the first sedimentary record after or during flattening of the top of Rigil Guyot at Site U1374. G. Multicolor basalt sandstone in Subunit VIIA (interval 330-U1374A-7R-3A, 95–135 cm), showing a gastropod and bioclast-rich inclined layer (arrow), interpreted to have emplaced on a shallow-marine slope as a debris flow. (Continued on next page.)

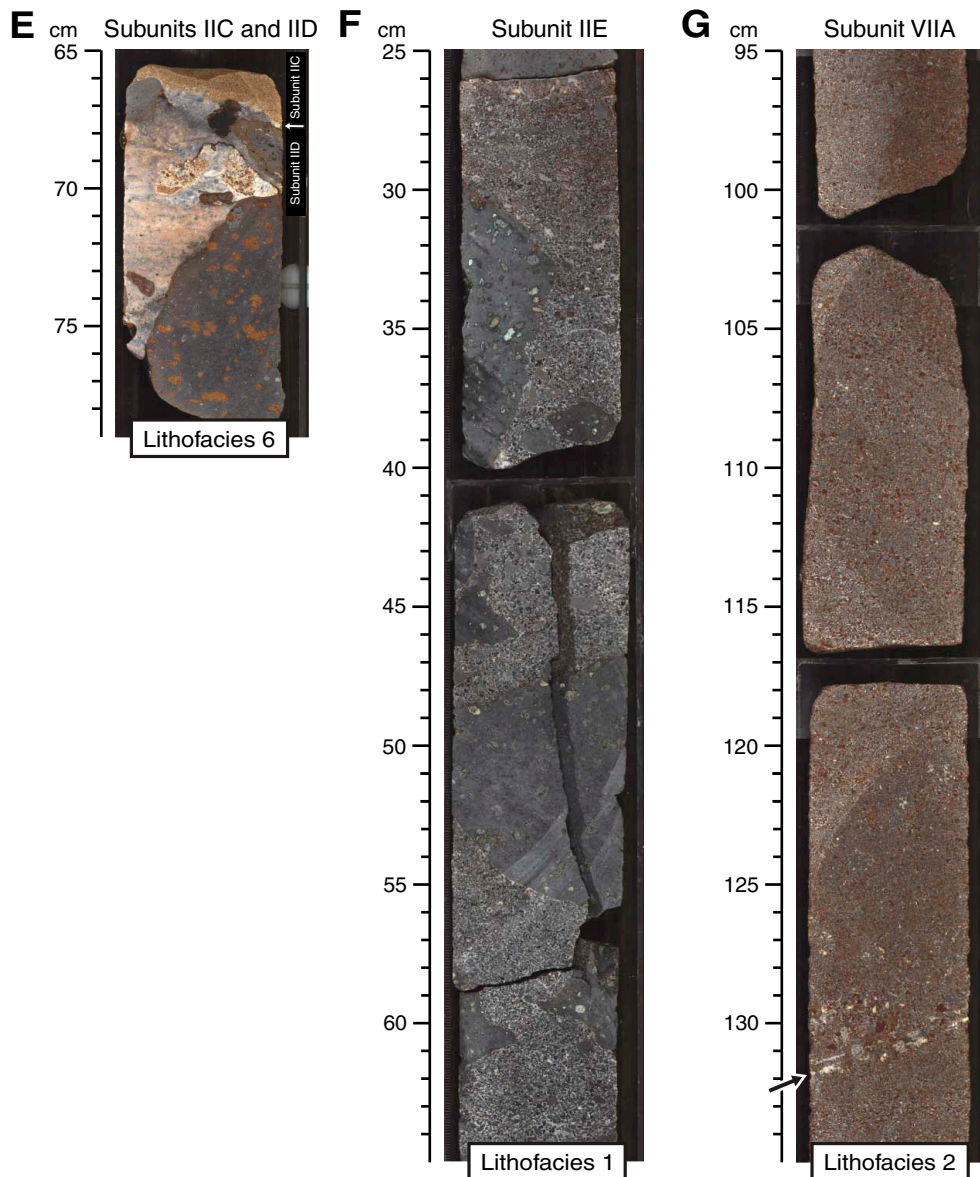


Figure F5 (continued). H. Multicolor volcanic sandstone in Subunit VIIB (interval 330-U1374A-8R-1A, 10–50 cm), interpreted as one or several hyperconcentrated flow deposit(s) emplaced on a shallow-marine slope. I. Multicolor basalt breccia with bioclasts in Subunit VIIC (interval 330-U1374A-8R-3A, 19–59 cm), interpreted to record the emplacement of debris flows in a shallow-marine environment. Arrow indicates a larger bioclast (possible algal fragment). J, K. Sediments interpreted to have emplaced on a shallow-marine or subaerial slope as a debris flow: (J) multicolor basalt breccia in Subunit IXA (interval 330-U1374A-13R-1A, 25.5–65.5 cm), (K) multicolor volcanic sandstone in Subunit IXB (interval 330-U1374A-14R-3A, 32–72 cm). (Continued on next page.)

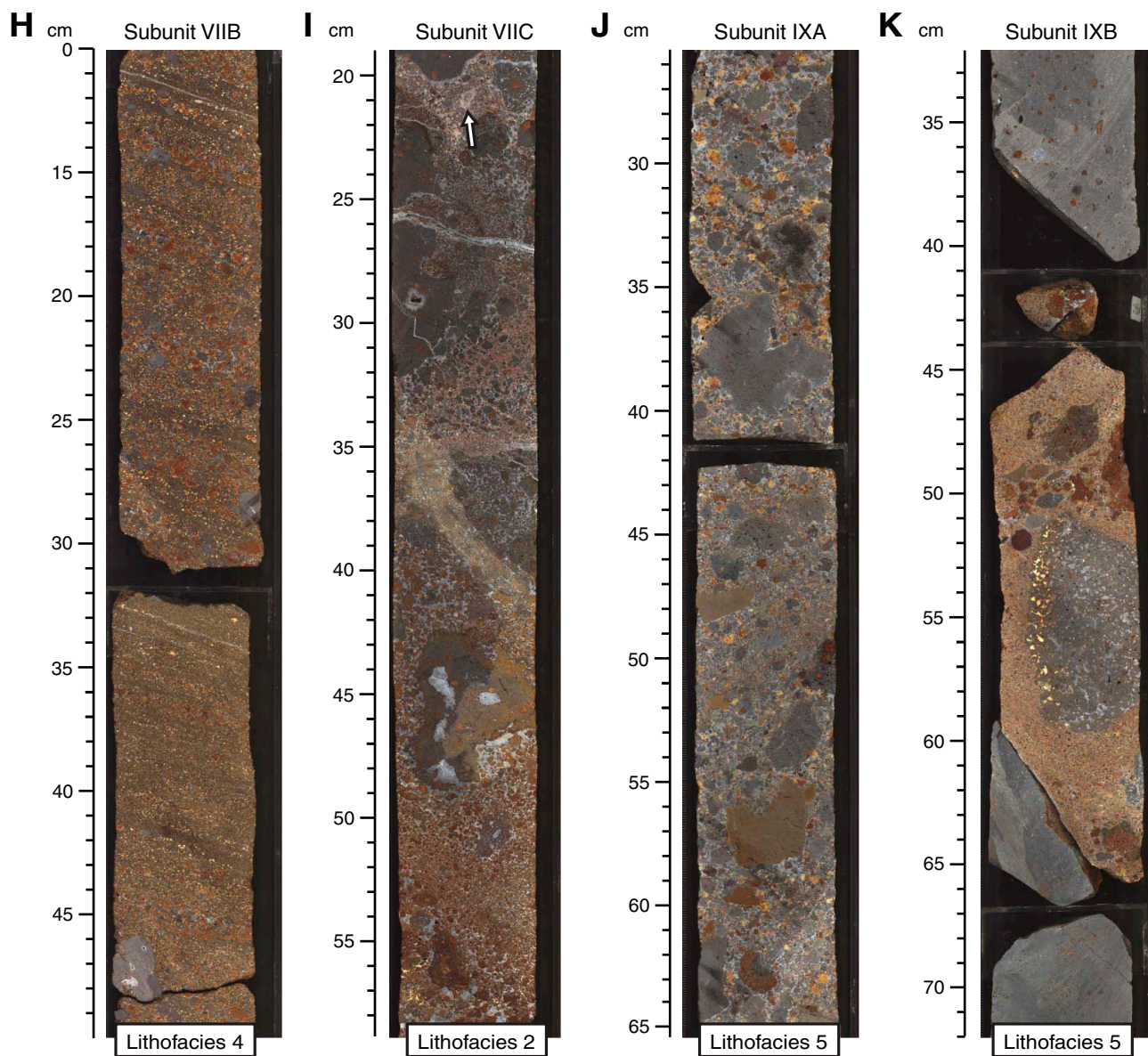


Figure F5 (continued). L. Multicolor basalt breccia in Subunit IXC (interval 330-U1374A-15R-2A, 1–41 cm), interpreted as a debris flow deposit emplaced on a shallow-marine slope. M. Multicolor volcanic sandstone in Subunit XIA (interval 330-U1374A-21R-3A, 74–114 cm), interpreted as a hyperconcentrated flow deposit emplaced on a shallow-marine slope. N. Grayish basalt conglomerate with bioclasts in Subunit XIB (interval 330-U1374A-22R-1A, 55–95 cm), with (1) dissolved bivalve shell and (2) algal and possible bryozoan encrustation on a basalt clast, interpreted to have formed in an intertidal to subtidal environment on the slope of Rigil Guyot.

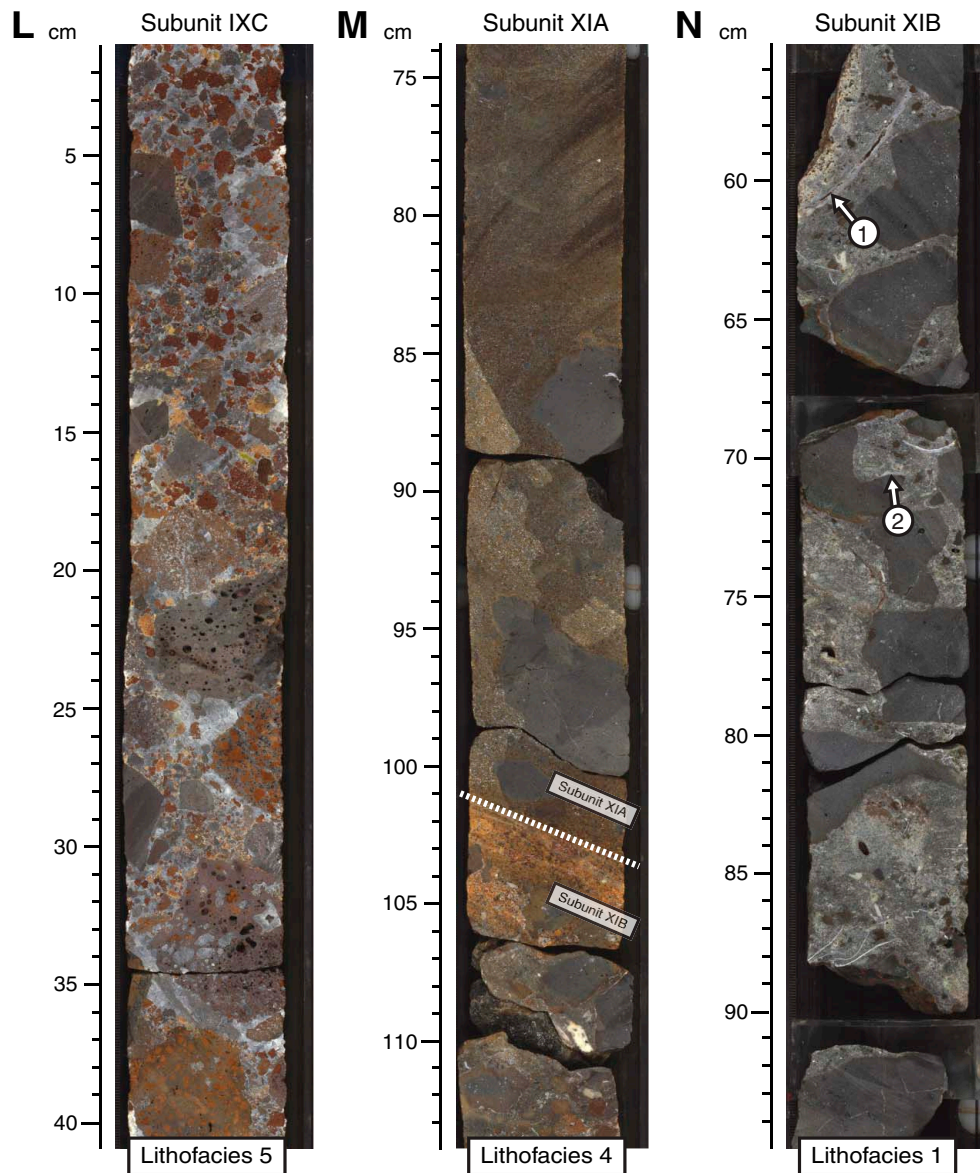


Figure F6. Core photograph and diagram of condensed interval observed at top of Subunit IID (foraminiferal bioclast limestone; interval 330-U1374A-3R-1A, 65–79 cm) showing several limestone types (Lm1–Lm3), ferromanganese-phosphate encrustations (Mn), basalt clasts (B), and ferromanganese phosphate-coated basalt clasts (Mn-B). Note that volcanic sandstone (Snd) of Subunit IIC fills burrows in the limestone of Subunit IID. The limestone (Lm3) and sandstone (left infill) were dated to the late Campanian and late Maastrichtian, respectively, on the basis of foraminiferal and nannofossil assemblages (see [“Paleontology”](#)). 1 = erosional surface between Subunits IIC and IID, 2–4 = possible hiatuses and hardground surfaces in condensed interval at top of Subunit IID.

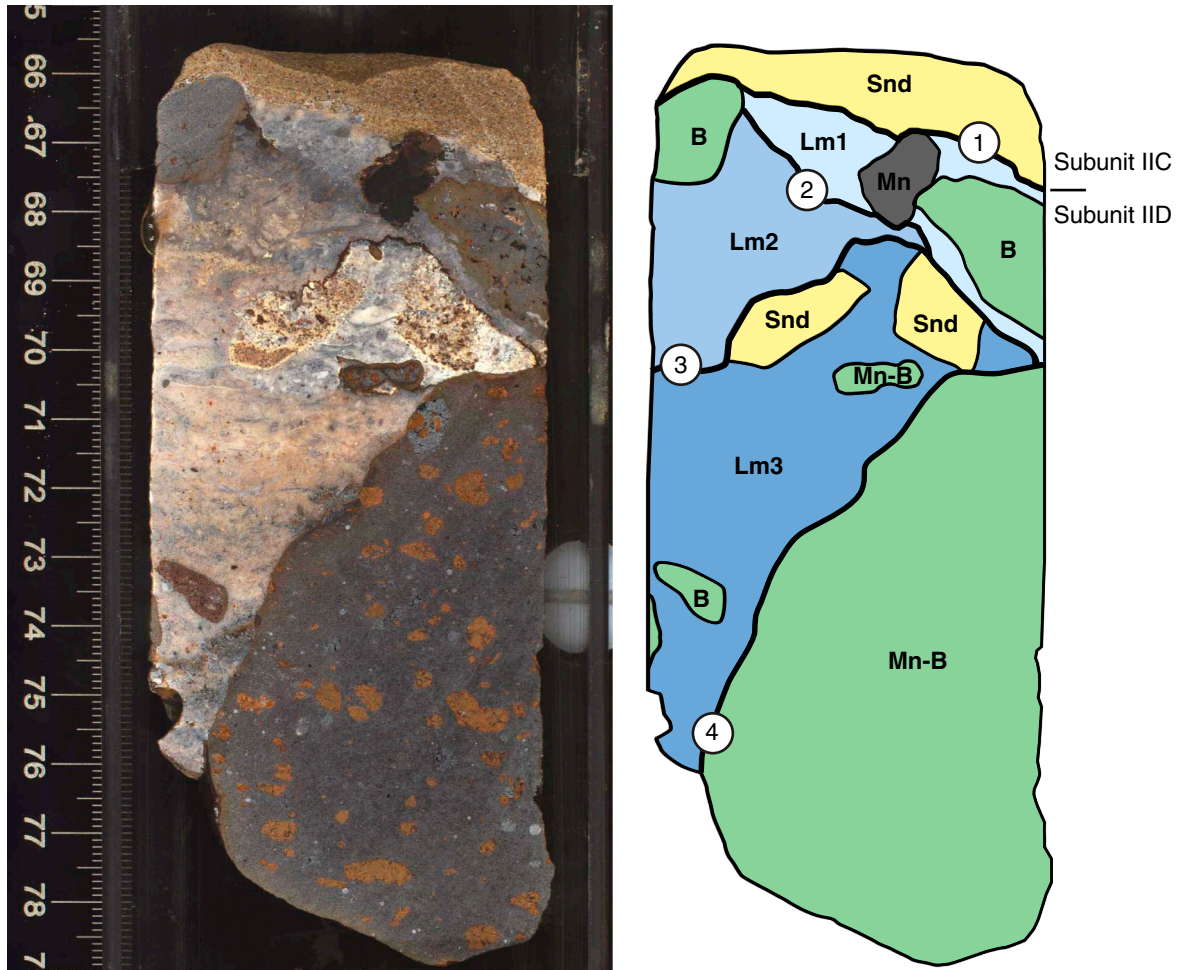


Figure F7. Thin section photomicrographs of cement types and dissolution features typical of a vadose environment (Flügel, 1982) (single polarization). Orange arrows point toward top. **A.** Geopetal structure in foraminiferal bioclast limestone in Subunit IID (Sample 330-U1374A-3R-1, 70–72 cm; Thin Section 113). Mold of dissolved shell fragment shown includes (1) vadose silt and (2) dogtooth and granular cements. Dissolution of shells and vadose cements occurred probably after the lithification of the limestone. **B.** Dripstone cement (white arrows) under pristine bivalve shell fragment in basalt conglomerate with bioclasts in Subunit IIE (Sample 330-U1374A-3R-2, 65–68 cm; Thin Section 117). Cementation pattern indicates cementation in a vadose environment. **C.** Geopetal structures defined by (1) vadose silt and (2) sparry calcite cement in a basalt conglomerate with bioclasts in Subunit IIE (Sample 330-U1374A-3R-2, 65–68 cm; Thin Section 117). Vadose silt indicates cementation in a vadose environment. **D.** Dripstone cement (white arrows) under dissolved bivalve shell fragment in basalt conglomerate with bioclasts in Subunit XIB (Sample 330-U1374A-21R-4, 76–81 cm; Thin Section 152). Shell fragment was replaced by dogtooth and intergranular cements and, possibly, vadose silt.

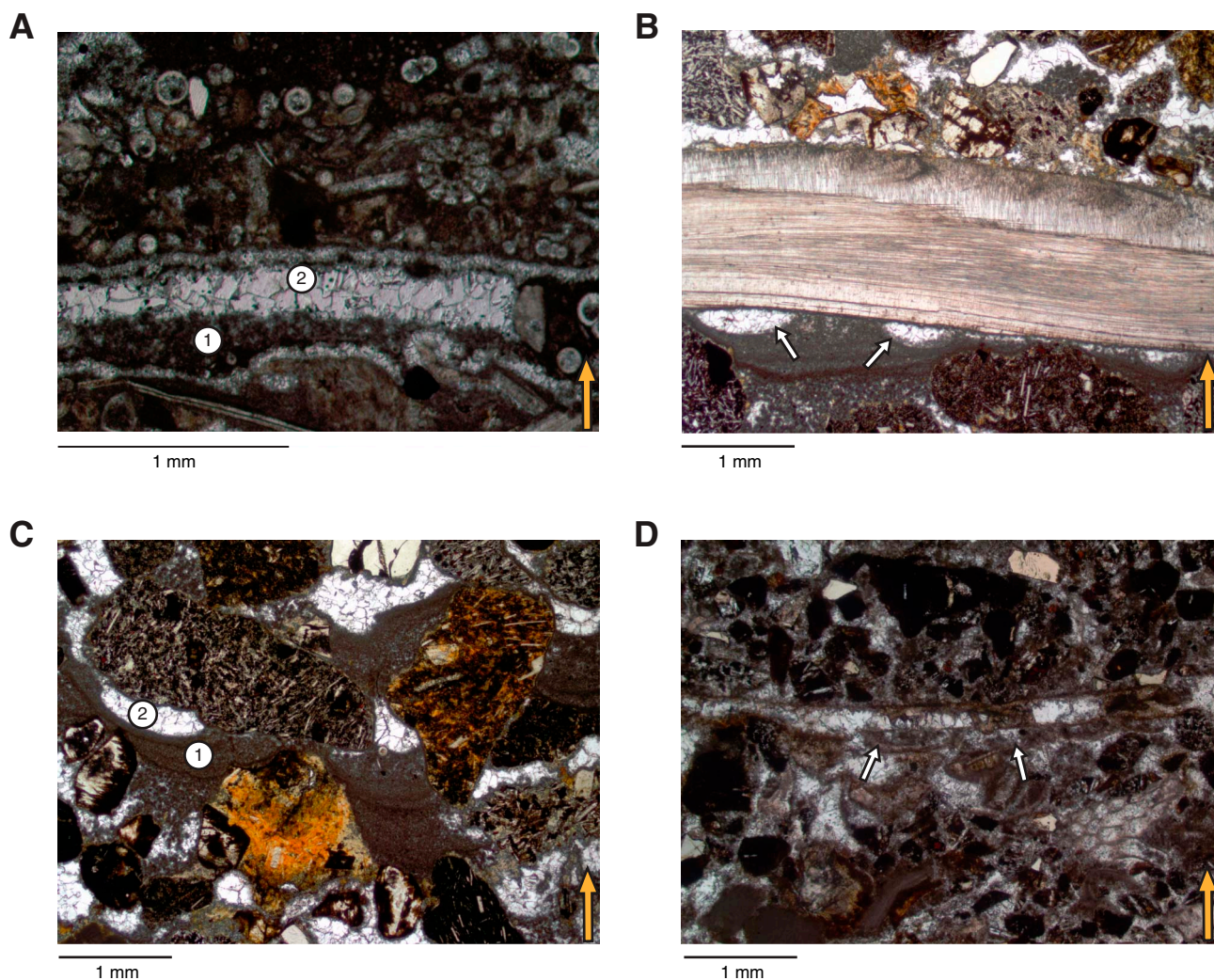


Figure F8. Close-up photographs of representative infill textures and synvolcanic features of volcanic breccia, Site U1374. **A.** Volcanic basement in Subunit XIII with possible (1) sedimentary basalt breccia and (2) volcanic basalt breccia (interval 330-U1374A-32R-3A, 31–61 cm). **B.** Peperitic texture at base of lava flow with deformed micrite-bearing volcanoclastic limestone in Unit V (interval 330-U1374A-5R-4A, 101–119 cm). **C.** (1) Jigsaw puzzle fit indicating in situ brecciation of a volcanic breccia, with (2) later infill deposit in Unit XIII (interval 330-U1374A-33R-3A, 52–62 cm). **D.** Sedimentary basalt breccia showing evidence of infill deposits coeval to calcite cementation, with (1) early calcite cement, (2) infill deposit, and (3) late calcite cement in Subunit IXC (interval 330-U1374A-13R-2A, 59–70 cm). **E.** Volcanic basalt breccia with infill deposit of (1) fossil- and micrite-bearing sandstone in Unit X (interval 330-U1374A-19R-1A, 13–19 cm).

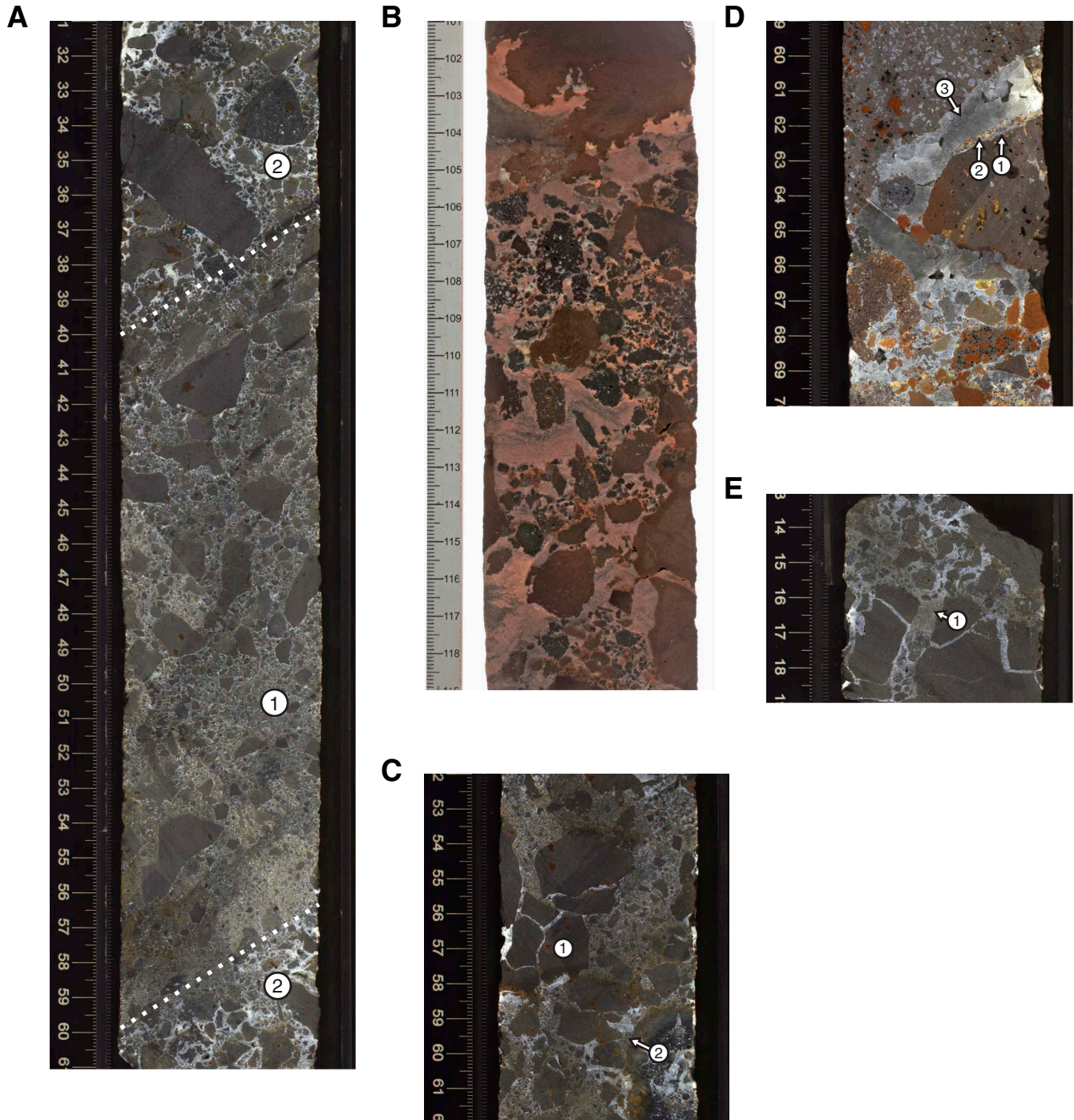


Figure F9. Preliminary interpretation of stratigraphic development of Rigil Guyot, based on sedimentary, paleontological, volcanological, and structural observations at Site U1374.

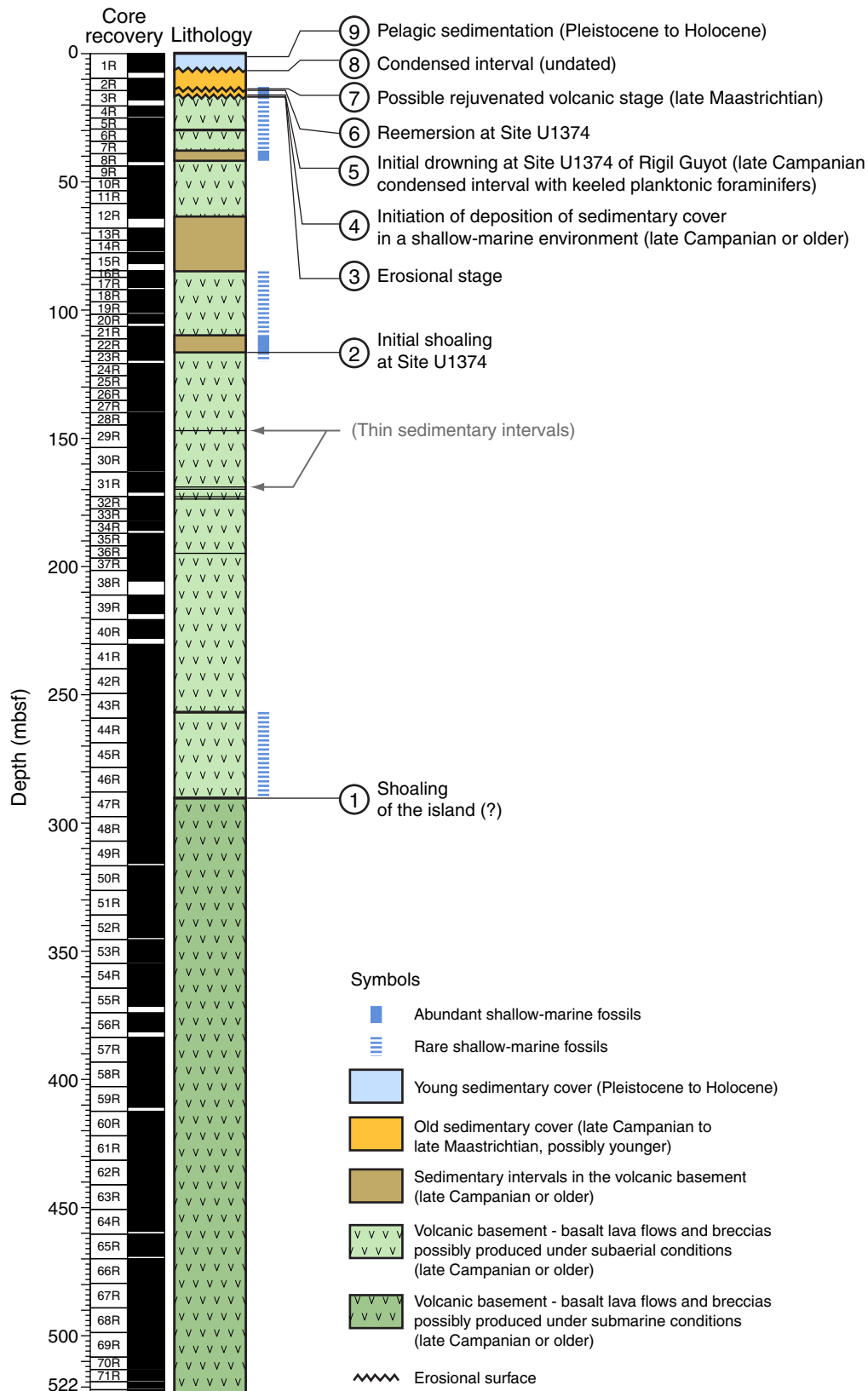


Figure F10. Calcareous nannofossil and planktonic foraminiferal biozonation, Hole U1374A. Gray shaded areas = intervals barren of age-diagnostic calcareous microfossils, wavy lines = unconformities. For legend of lithology patterns, see Figure F4.

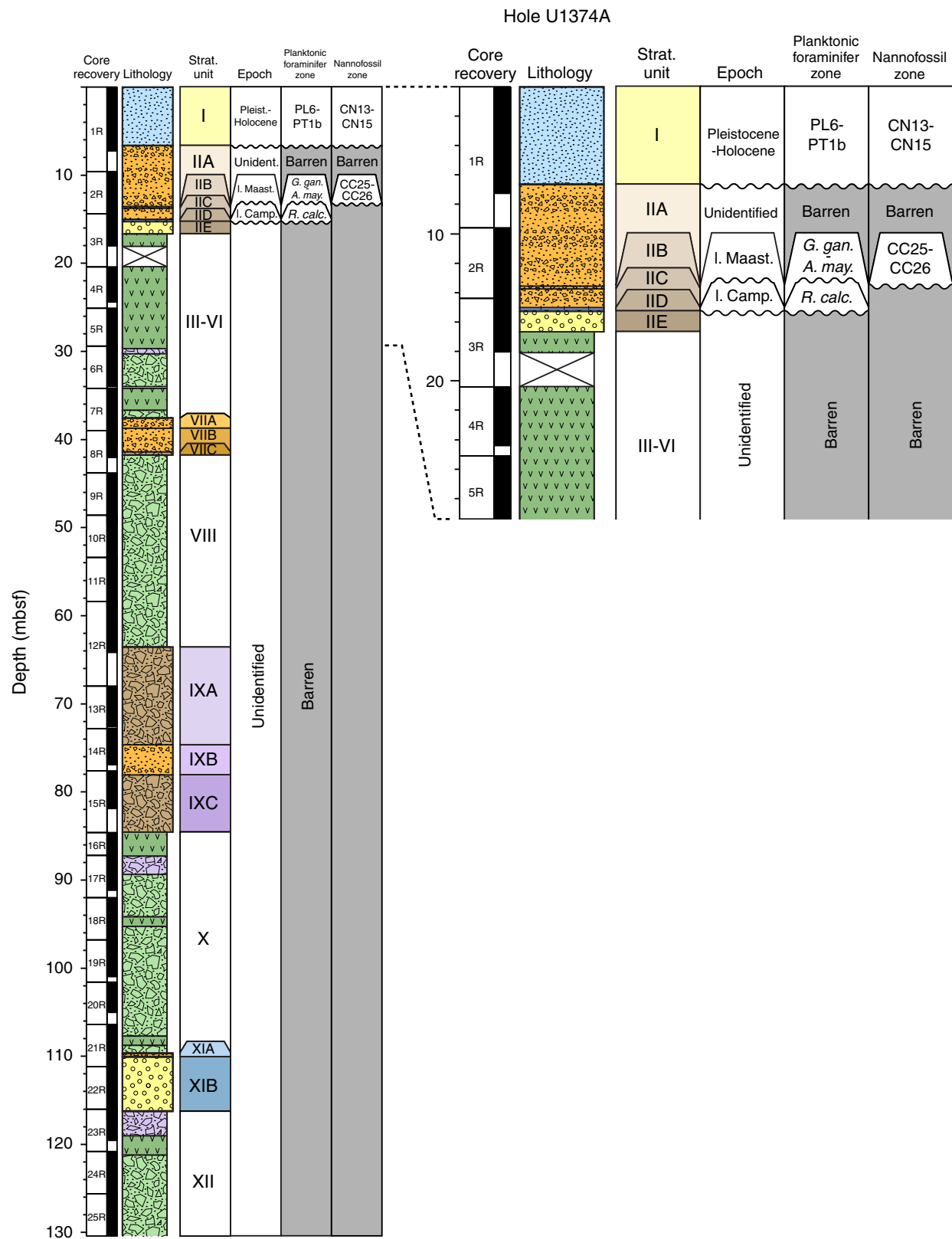


Figure F11. Thin section photomicrographs of planktonic foraminifers (Sample 330-U1374A-2R-4W, 27–32 cm; Thin Section 111). **A.** *Globotruncanita* cf. *conica*. **B.** *Globotruncanita* cf. *stuarti*.

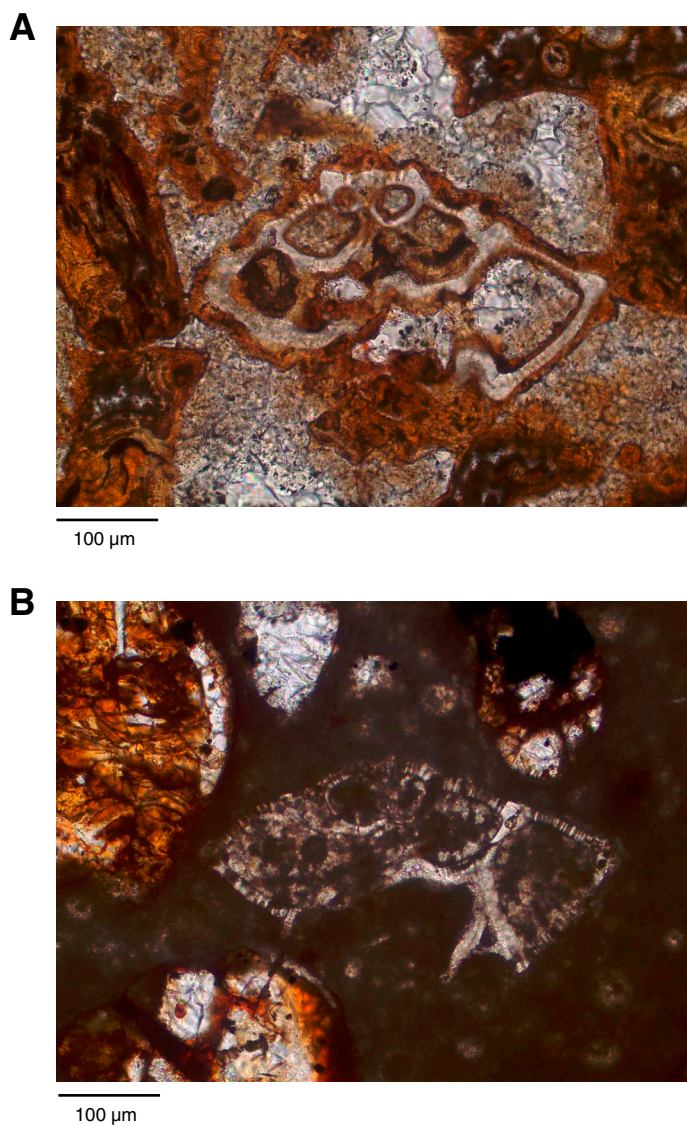


Figure F12. Thin section photomicrographs of planktonic foraminifers (Sample 330-U1374A-3R-1W, 70–72 cm; Thin Section 128). **A.** *Radotruncana* cf. *calcarata*. **B.** *Globotruncanella* sp.

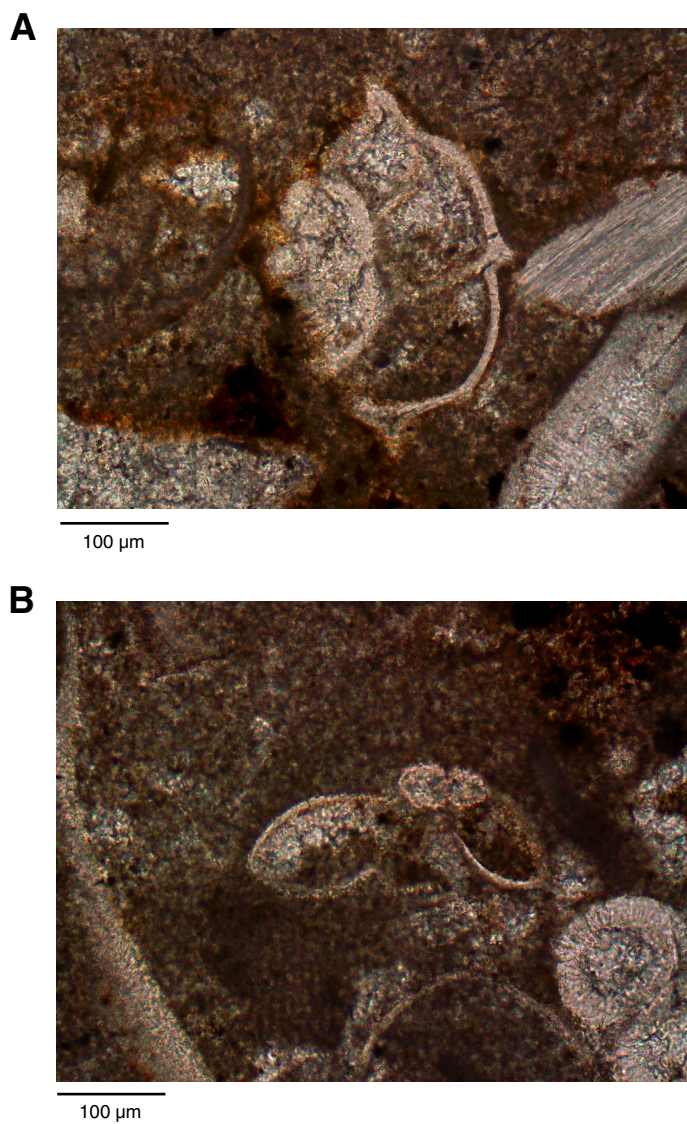


Figure F13. Thin section photomicrograph of juvenile ammonoid fossil (Sample 330-U1374A-2R-4W, 88–91 cm; Thin Section 112).

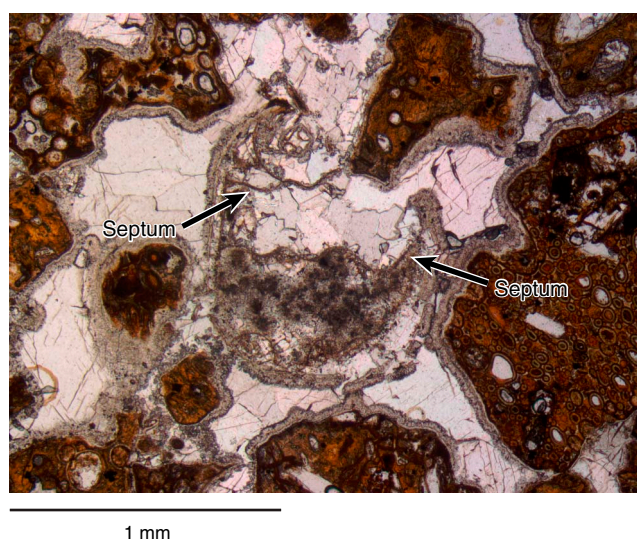


Figure F14. Juvenile ammonoid fossil (Sample 330-U1374A-3R-1A, 23–24 cm). **A.** Close-up photograph of Section 330-U1374A-3R-1A (Piece 1). Green and red rectangles indicate areas of B and C, respectively. **B.** Close-up photograph of convex-up bivalve, gastropod, and ammonoid shell fragments. **C.** Binocular photomicrograph of juvenile ammonoid in Sample 330-U1374A-3R-1, 24 cm. **D.** Binocular photomicrograph and trace lines of outer shell and septa of ammonoid fragment.

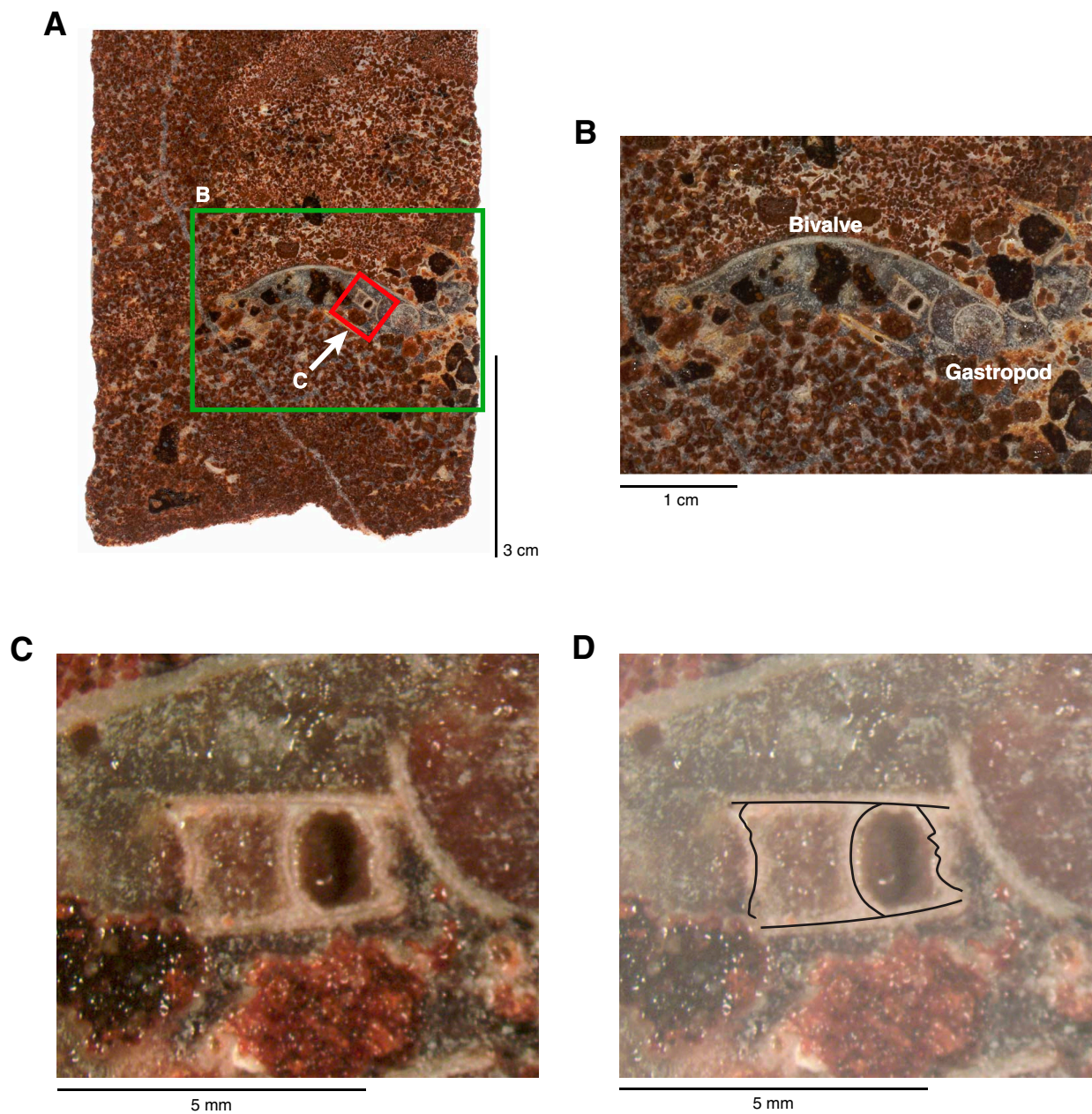


Figure F15. Close-up photographs of ammonoid fossil (Sample 330-U1374A-3R-1 [Piece 10, 69–70 cm]) in Subunit IID (see also Fig. F16). **A.** Front view (archive half). Rectangle shows area of **B.** **B.** Back view (working half). Rectangle indicates ammonoid fossil, and arrows show views for **C** and **D.** **C.** Lateral view. **D.** Diagonal view.

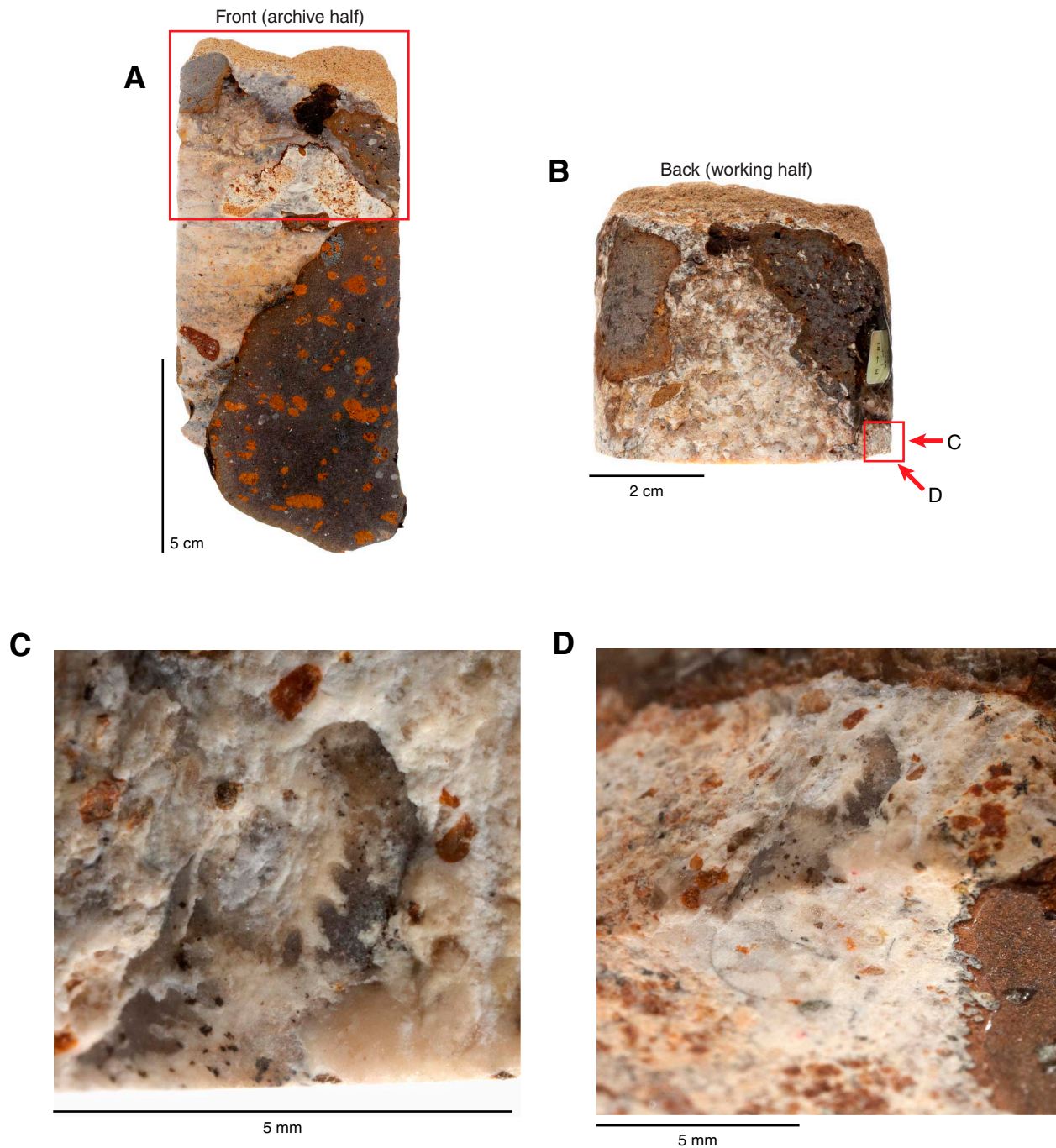


Figure F16. Close-up photograph and sketch of Subunit IID. Rectangles indicate position of thin section billet. A. Interval 330-U1374A-3R-1A (Piece 10, 65–78.5 cm). α and β show positions of nannofossil samples in Subunits IID and IIC, respectively (see “[Paleontology](#)”). B. Subdivisions of Subunit IIC, IID, and IIE in this 11 cm interval based on XRF analyses (see XL3_EVAL.PDF in XRF in “[Supplementary material](#)”), and macro- and microscopic (thin section) observations.

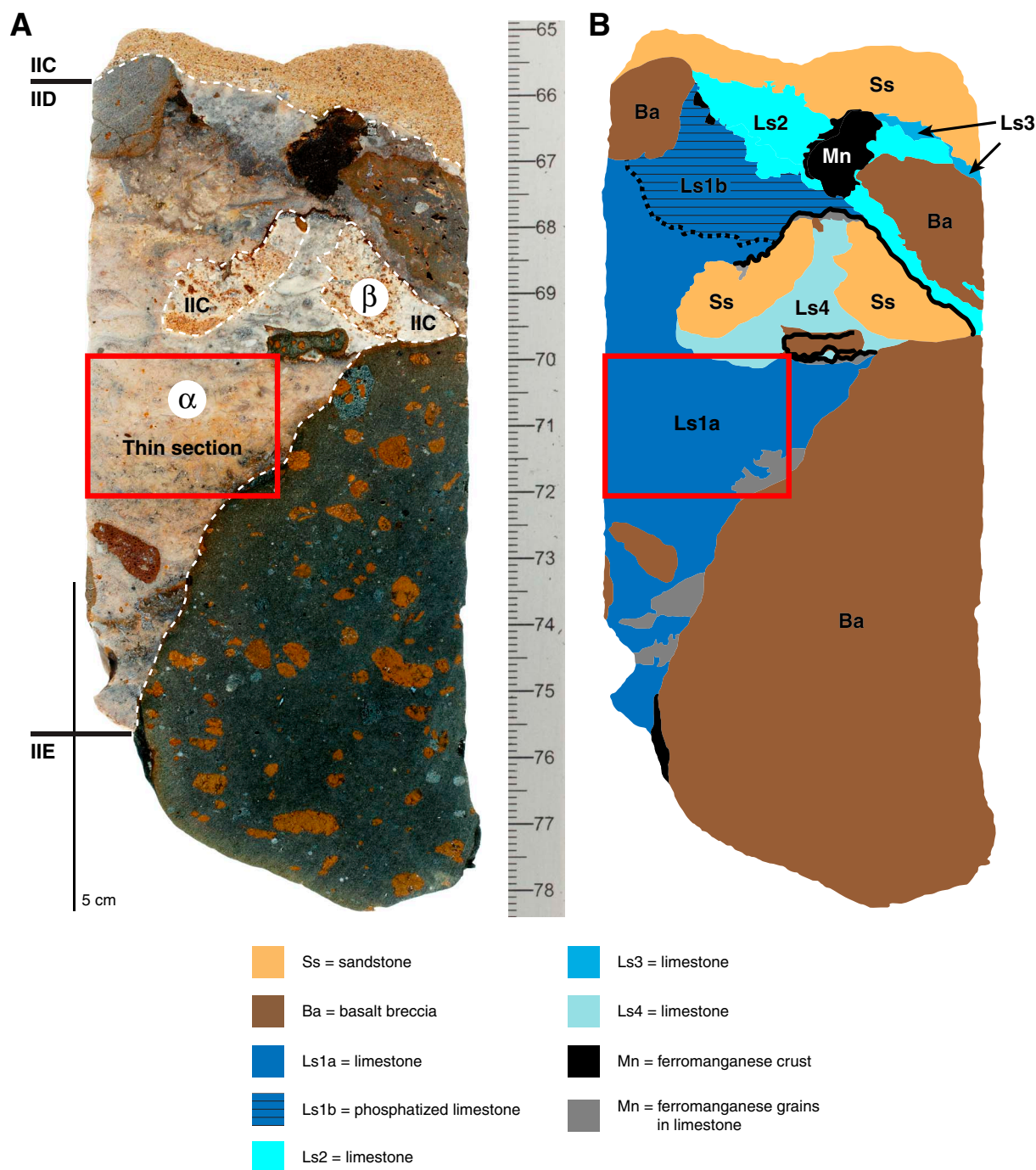


Figure F17. Eustatic sea level fluctuations during the Late Cretaceous–early Paleocene. Sea level curve is adopted from Hardenbol et al. (1998). Blue shaded area = age of Subunit IID limestone. Orange and light orange shaded areas = minimum and maximum ages, respectively, of Subunit IIC volcanoclastic sandstone (see “Paleontology”).

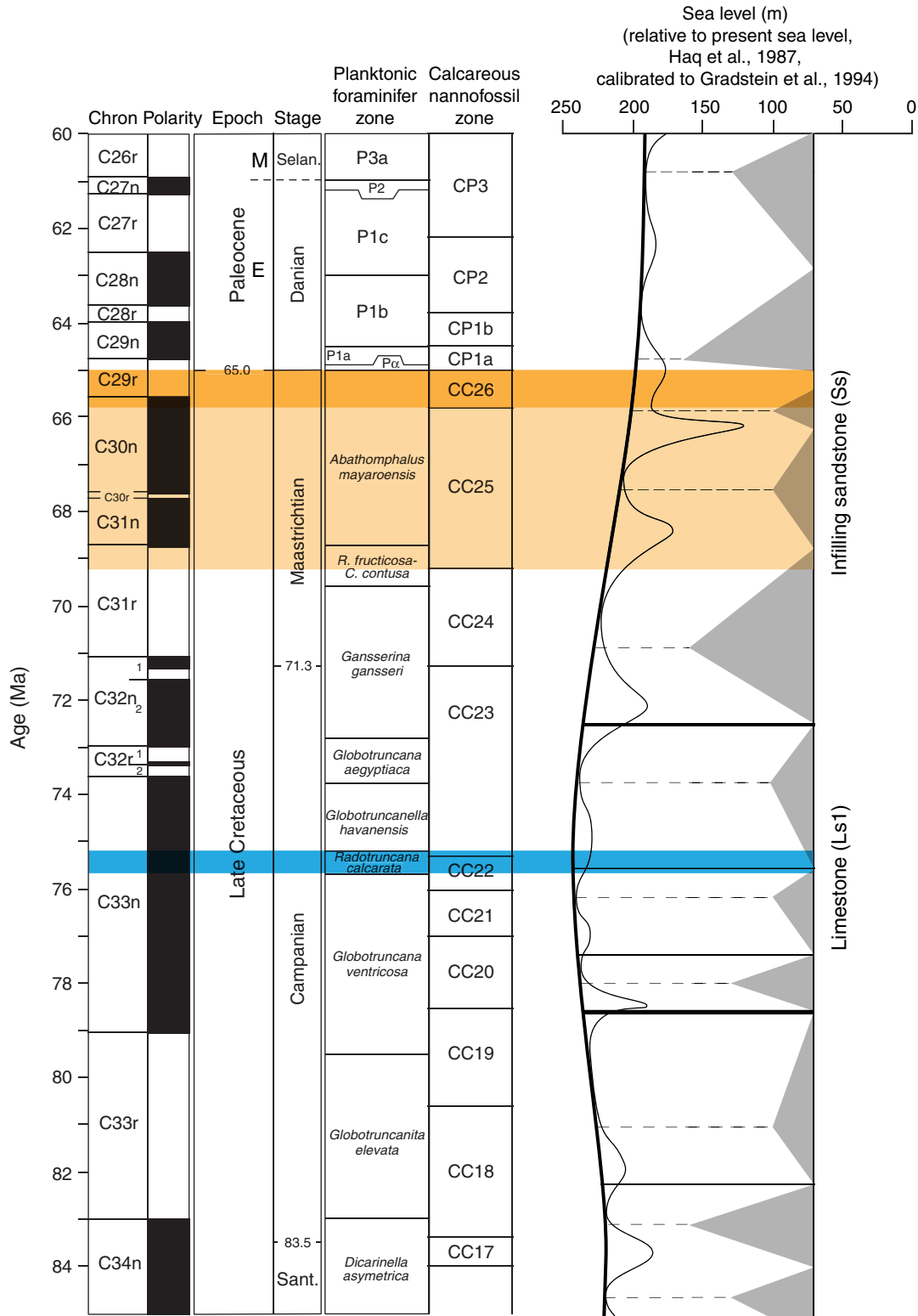


Figure F18. Stratigraphic summary of igneous rocks and lithologic features, Hole U1374A.

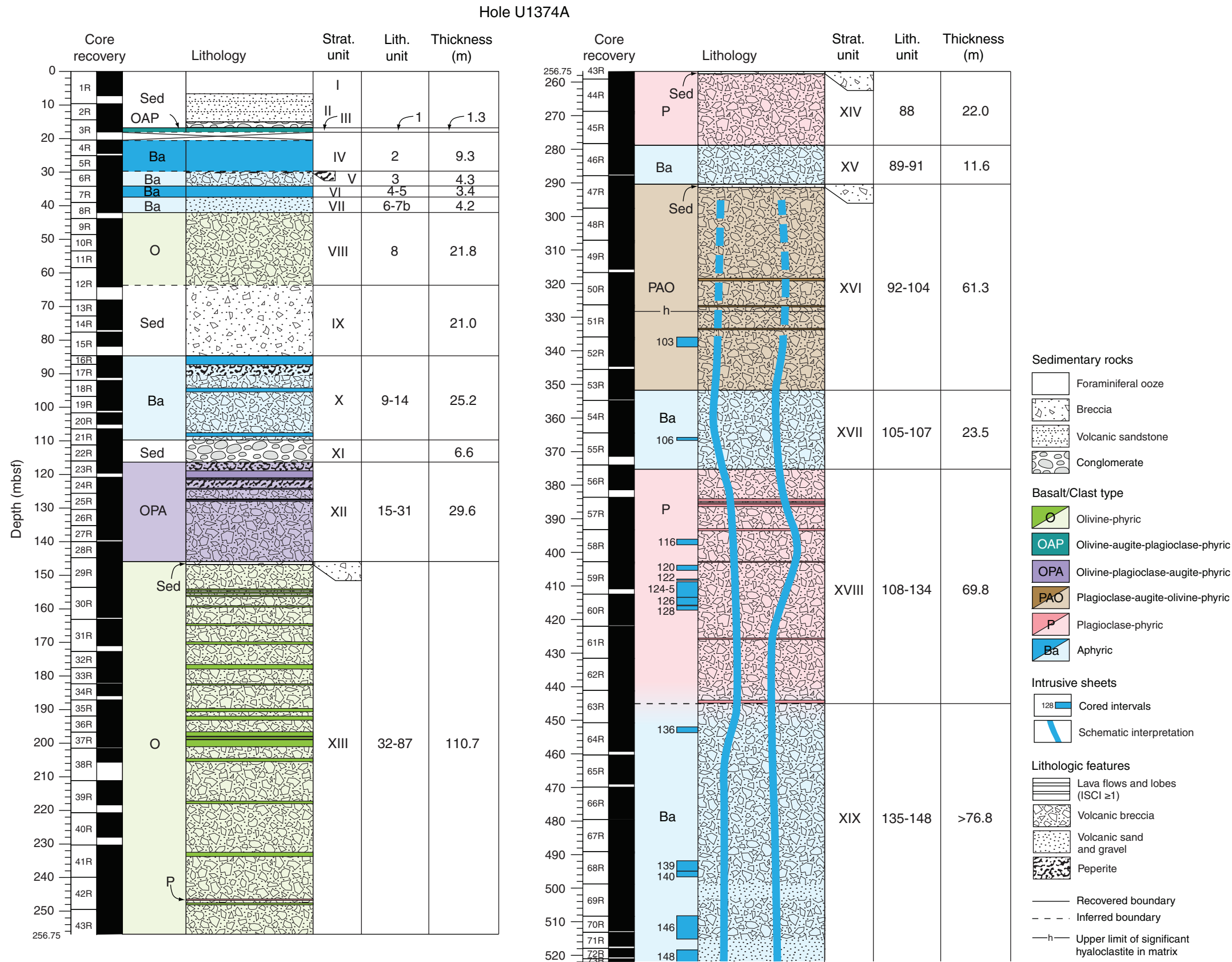


Figure F19. Scanned core photograph of contact (dashed line) of basement basalt with overlying conglomerate (interval 330-U1374A-3R-2A, 74–98 cm). Inclined surface of lava flow shows no sign of weathering, but original flow top is not preserved. Sand from matrix of overlying conglomerate has infiltrated cracks in surface of lava flow.

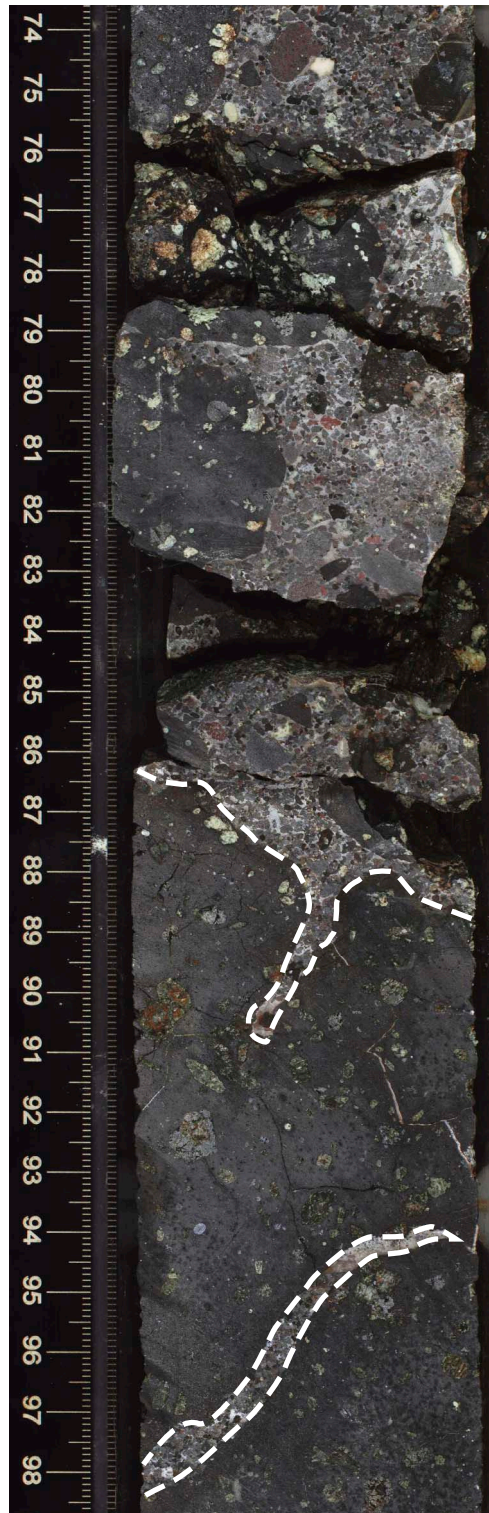


Figure F20. Thin section photomicrographs of highly olivine-augite-plagioclase-phyric basalt showing large olivine, titanaugite, and small plagioclase phenocrysts from Unit III (Sample 330-U1374A-3R-2W, 108–110 cm; Thin Section 118). A. Plane-polarized light. B. Crossed polars. C. Close-up of groundmass. D. Hornblende inclusion in titanaugite phenocryst.

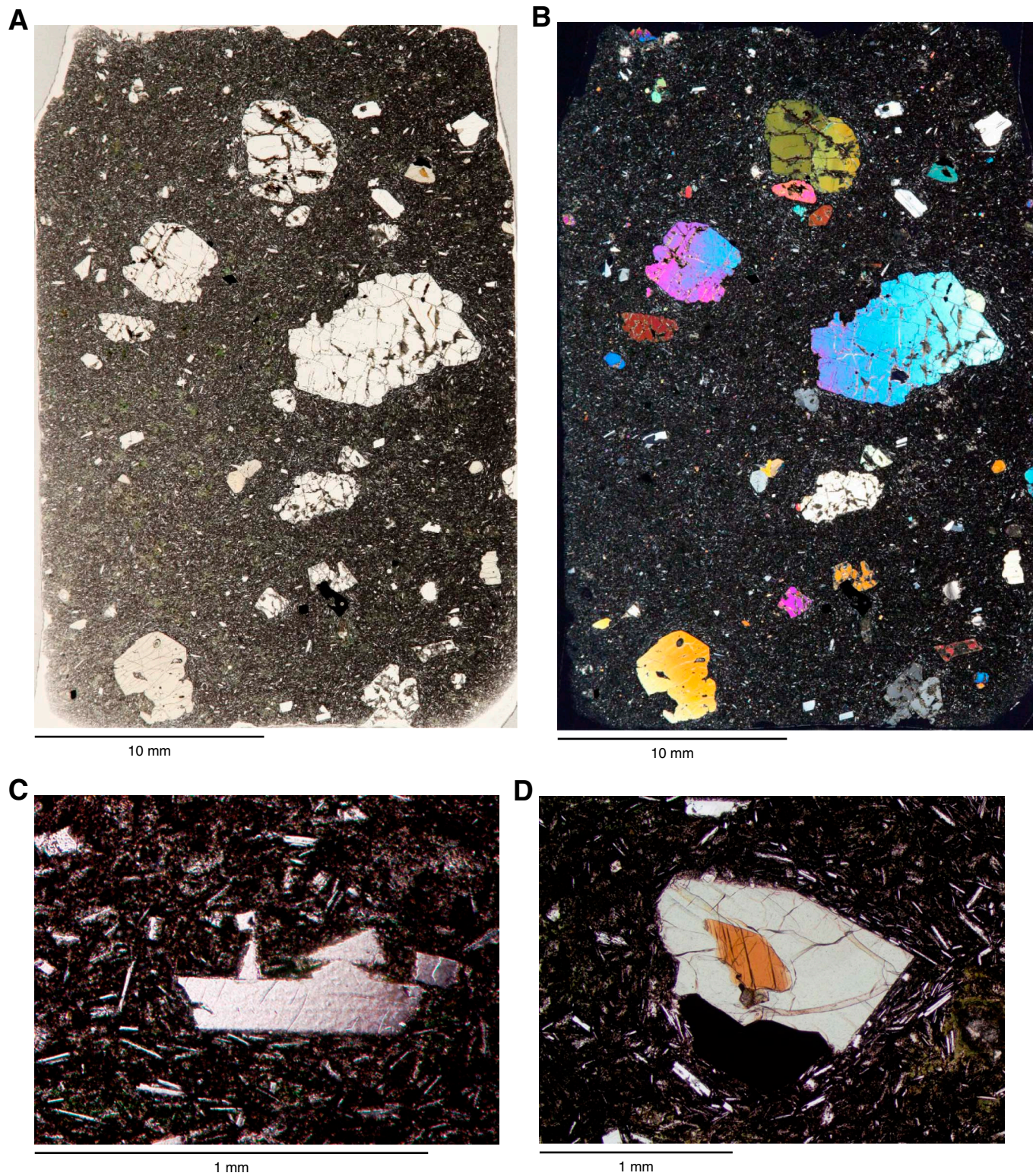


Figure F21. Scanned core photographs showing evidence of magma-sediment (peperitic) interaction observed in Hole U1374A. **A.** Basalt clasts mingled with bioclast-bearing micrite (Unit V; interval 330-U1374A-5R-4A, 100–120 cm). **B.** Basaltic breccia with a basaltic sand matrix. The large clast in the center resembles a small pillow (Unit X; interval 330-U1374A-17R-3A, 20–40 cm). **C.** Peperitic breccia composed of basalt mingled with sandy sediment (Unit XII; interval 330-U1374A-23R-2A, 107–127 cm).

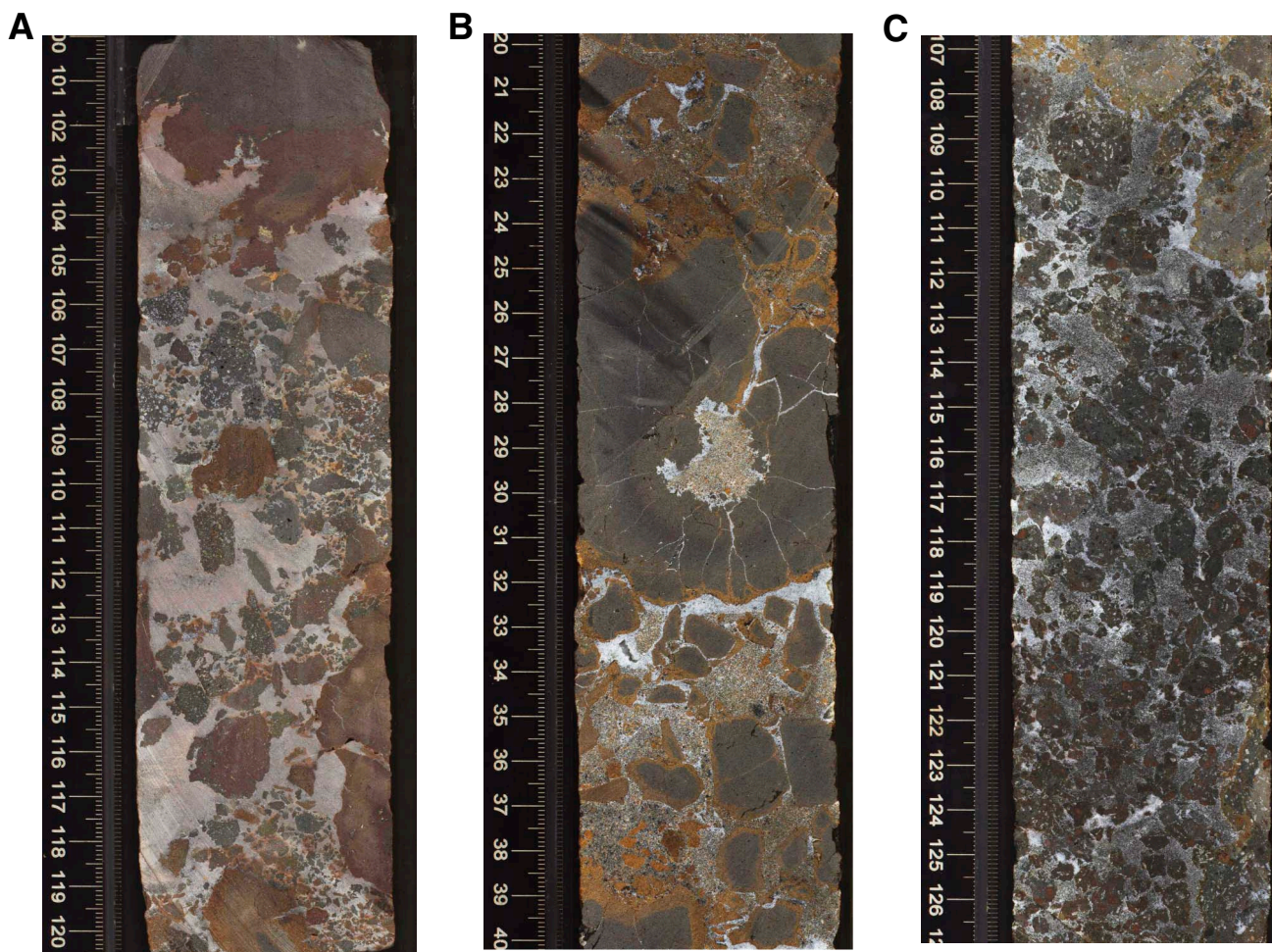


Figure F22. Thin section photomicrographs of aphyric basalt from Unit X showing glassy groundmass, unaltered groundmass olivine, and flow-aligned plagioclase laths (Sample 330-U1374A-19R-1W, 50–53 cm; Thin Section 147). **A.** Plane-polarized light. **B.** Crossed polars.

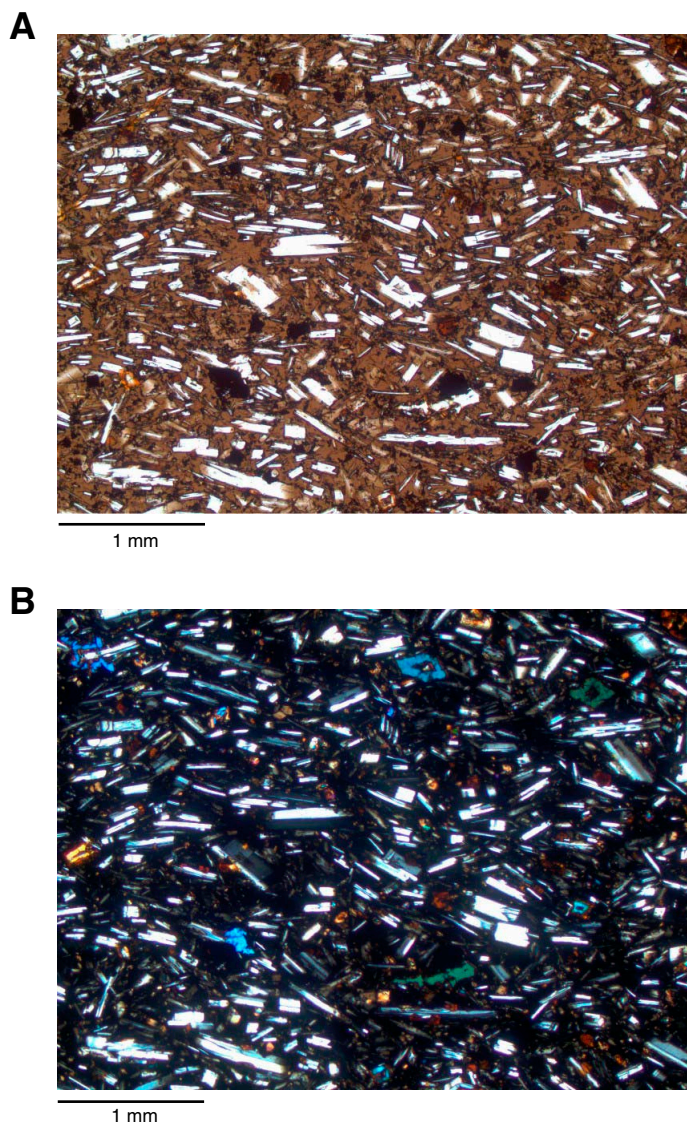


Figure F23. Scanned core photographs of four breccia types in Hole U1374A. **A.** Poorly sorted breccia with irregular scoriaceous clasts that probably formed in a hydrovolcanic eruption (Unit XII; interval 330-U1374A-29R-1A, 76–90 cm). **B.** Fines-free breccia with angular, blocky clasts with broken edges and sharp contacts (Unit XIII; interval 330-U1374A-43R-1A, 77–91 cm). **C.** Lobate, plagioclase-phyric clasts in hyaloclastite matrix (Unit XVIII; interval 330-U1374A-57R-3A, 129–143 cm). **D.** Angular, aphyric basalt clasts in hyaloclastite matrix (Unit XIX; interval 330-U1374A-66R-6A, 55–69 cm).

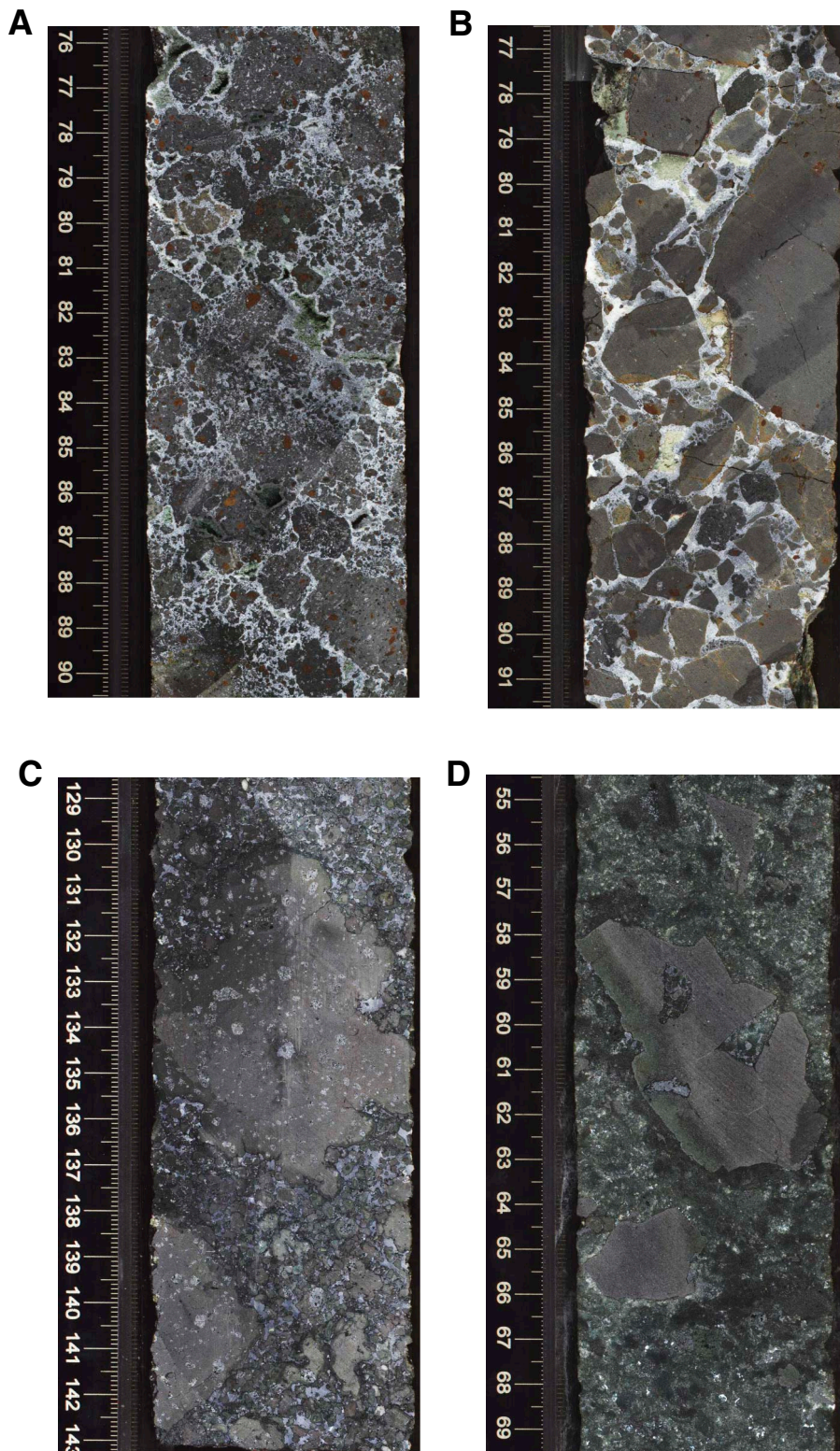


Figure F24. Thin section photomicrographs of highly olivine-plagioclase-augite-phyric basalt from Unit XII. A, B. Sample 330-U1374A-24R-2W, 82–86 cm (Thin Section 167), showing partly resorbed phenocrysts: (A) plane-polarized light, (B) crossed polars. C, D. Sample 330-U1374A-24R-1W, 77–80 cm (Thin Section 158), showing a plagioclase phenocryst filled with interconnecting inclusions of dark glass (plane-polarized light). D is a close-up image of part of the plagioclase phenocryst in C.

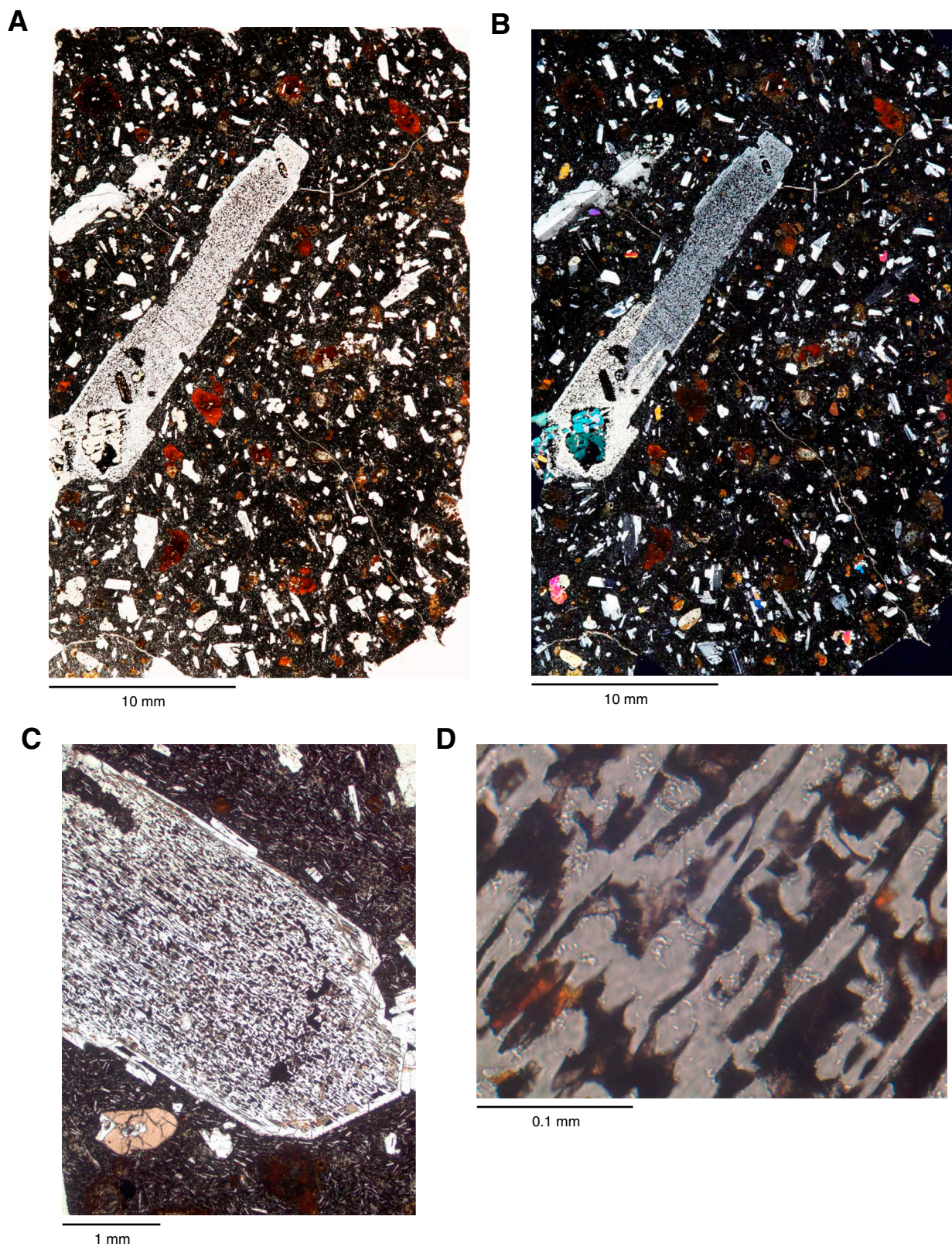


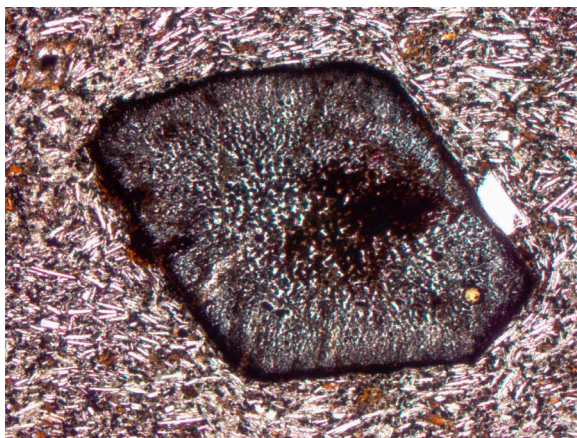
Figure F25. A, B. Thin section photomicrographs of moderately olivine-augite-phyric basalt from Unit XIII (Sample 330-U1374A-30R-5W, 12–15 cm; Thin Section 173): (A) plane-polarized light, (B) crossed polars. C, D. Thin section photomicrographs of euhedral intergrowth of pyroxene and magnetite with characteristic hornblende outline from lithologic Unit 58 (Sample 330-U1374A-32R-4W, 2–5 cm; Thin Section 176): (C) plane-polarized light, (D) crossed polars.

A

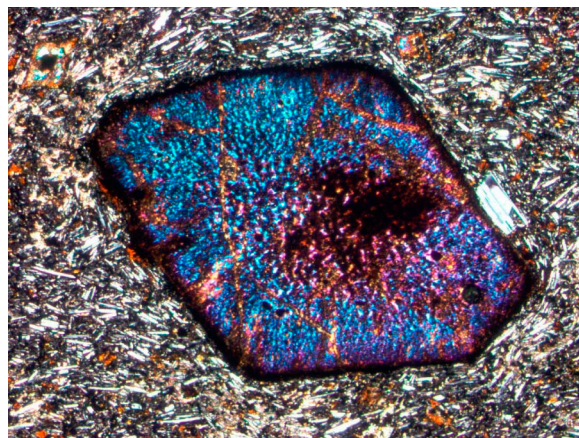
10 mm

B

10 mm

C

1 mm

D

1 mm

Figure F26. Scanned core photographs of pillow fragments showing distinctive glassy margins, radial fractures, and characteristic pillow shape. **A.** Unit XIV (interval 330-U1374A-43R-6A, 28–50 cm). **B.** Unit XV (interval 330-U1374A-46R-3A, 0–14 cm). Note how the smaller clasts in B have altered glass margins on one side only, suggesting that they are fragments of pillows that were fractured and then transported and redeposited.



Figure F27. Scanned core photograph showing contact (dashed line) between angular aphyric basalt breccia at base of Unit XV and sandy breccia at top of Unit XVI (interval 330-U1374A-47R-3A, 0–29 cm). Sandy layer is 95 cm thick and contains bioclasts.

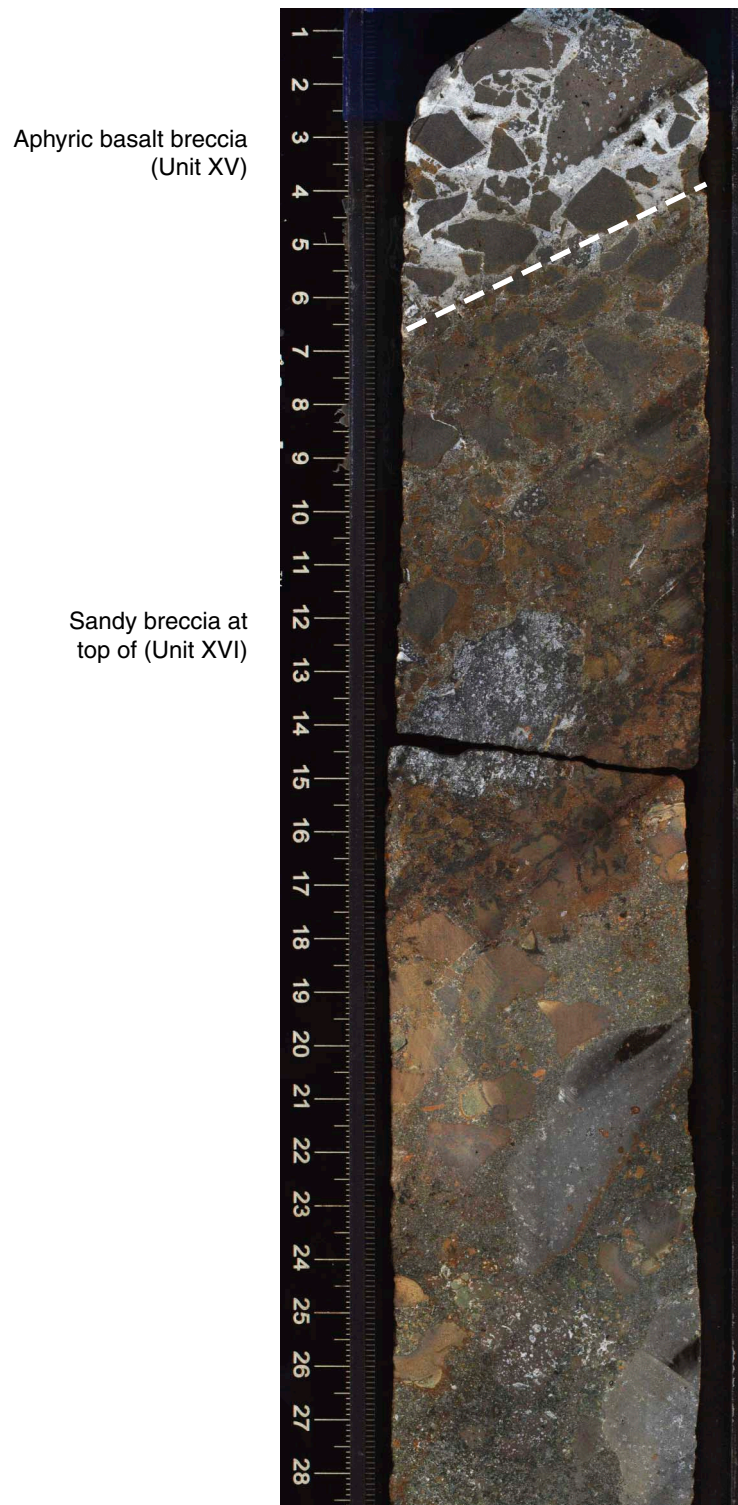


Figure F28. Depth profile of color reflectance parameters L^* , a^* , and b^* , Hole U1374A. Higher L^* values indicate lighter colors. a^* = relative color position between red (positive) and green (negative), b^* = relative color position between yellow (positive) and blue (negative). Stratigraphic column is shown for reference. For explanation of stratigraphy, see Figure F18. A. Stratigraphic Units I–XIII (0–256.75 mbsf). (Continued on next page.)

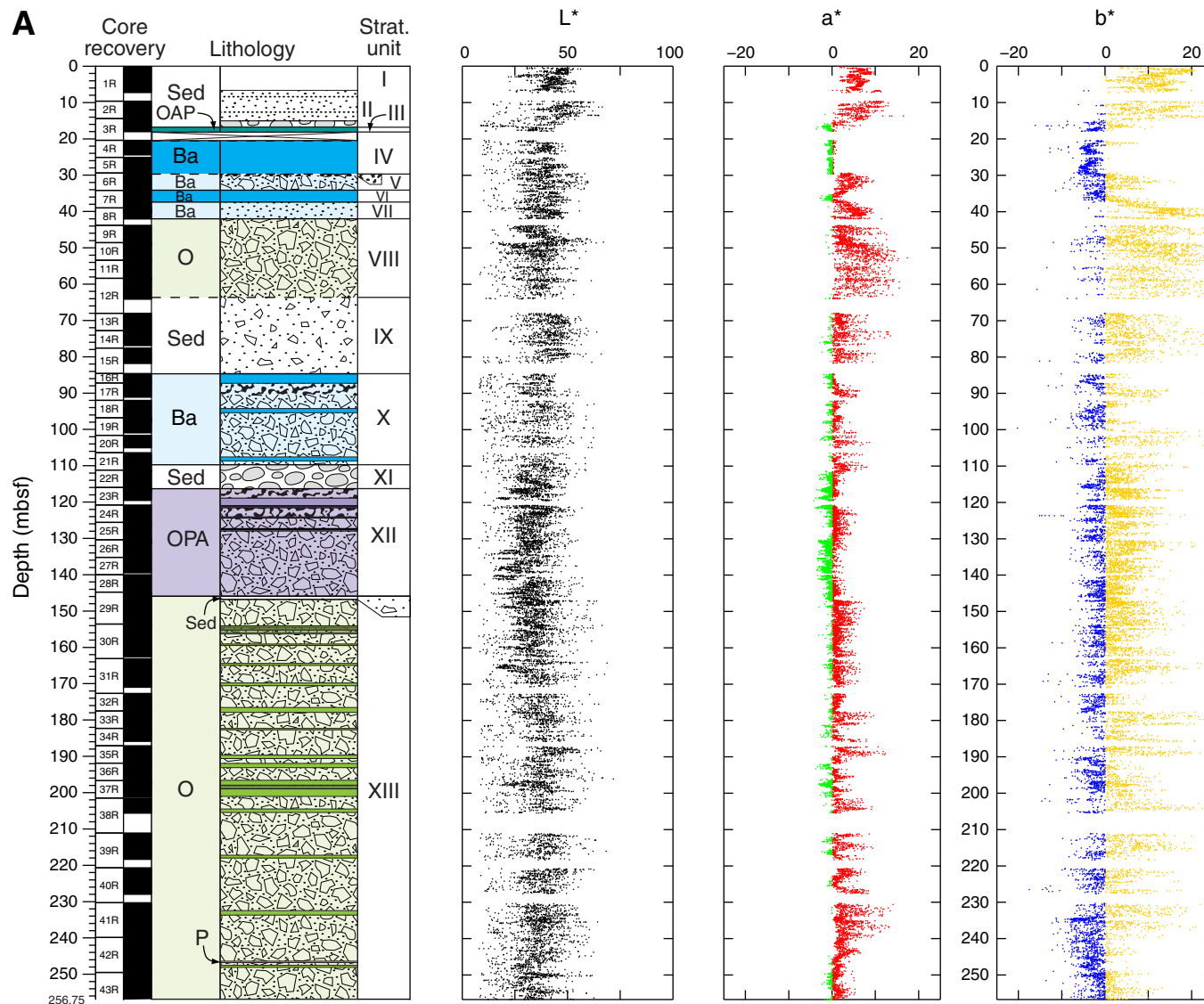


Figure F28 (continued). B. Stratigraphic units XIV–XIX (256.75–522 mbsf).

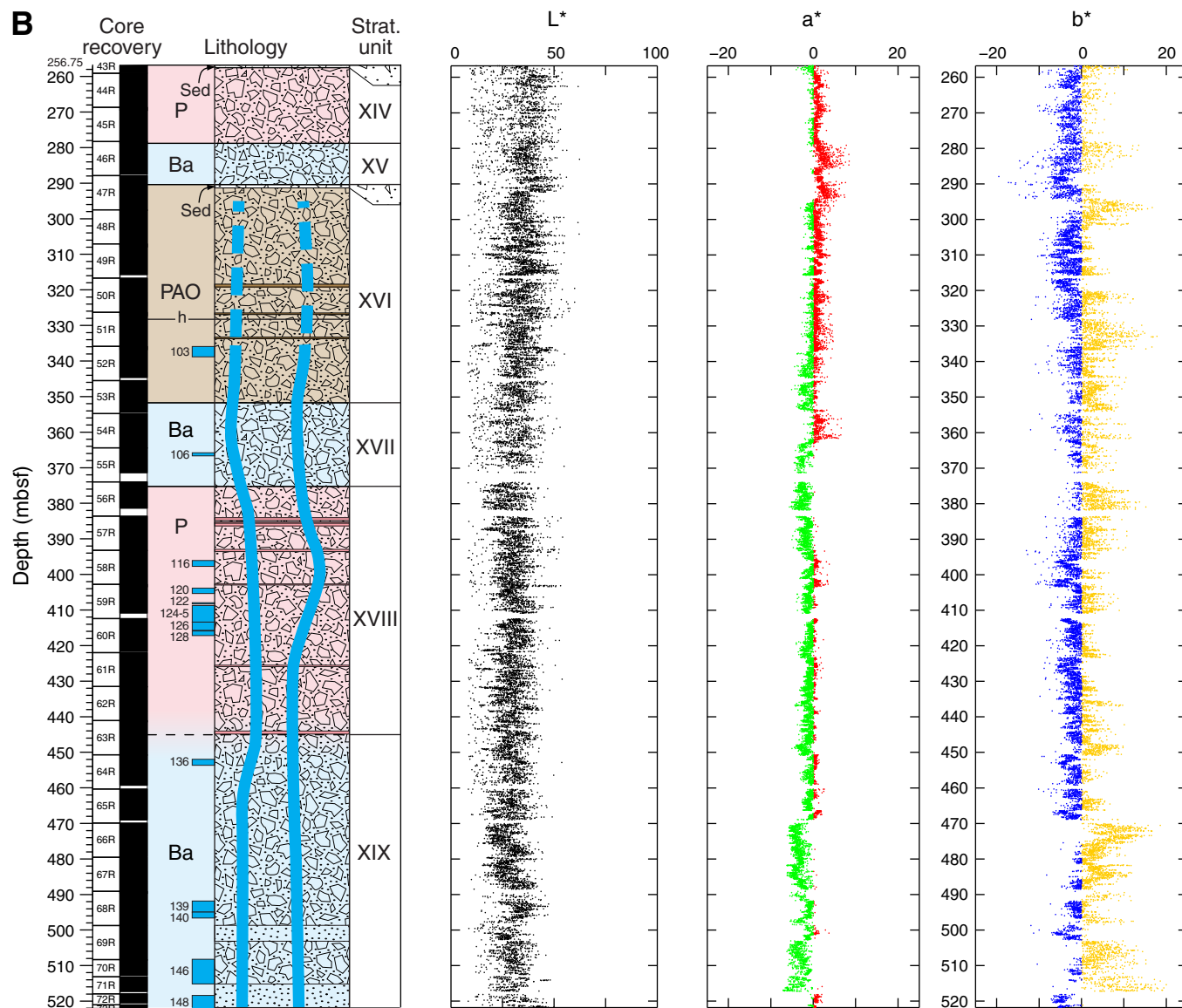


Figure F29. Scanned core photographs of dike margins, Hole U1374A. **A.** A 15 mm wide dike intruding hyaloclastite breccia (interval 330-U1374A-55R-4A, 82–91 cm). **B.** Steeply inclined chilled upper margin (interval 330-U1374A-58R-3A, 30–41 cm). **C.** Near-vertical margin (interval 330-U1374A-59R-1A, 120–134 cm). Note near-vertical bands of vesicles running parallel to sheet margin. **D.** Steeply inclined lower margin (interval 330-U1374A-59R-2A, 121–134 cm). **E.** Peperitic sheet margin in contact with hyaloclastite breccia (interval 330-U1374A-60R-1A, 31–55 cm). **F.** Peperitic sheet margin (top) separated from normal margin of second sheet or second phase of sheet injection by thin sliver of hyaloclastite breccia (interval 330-U1374A-68R-5A, 91–129 cm).

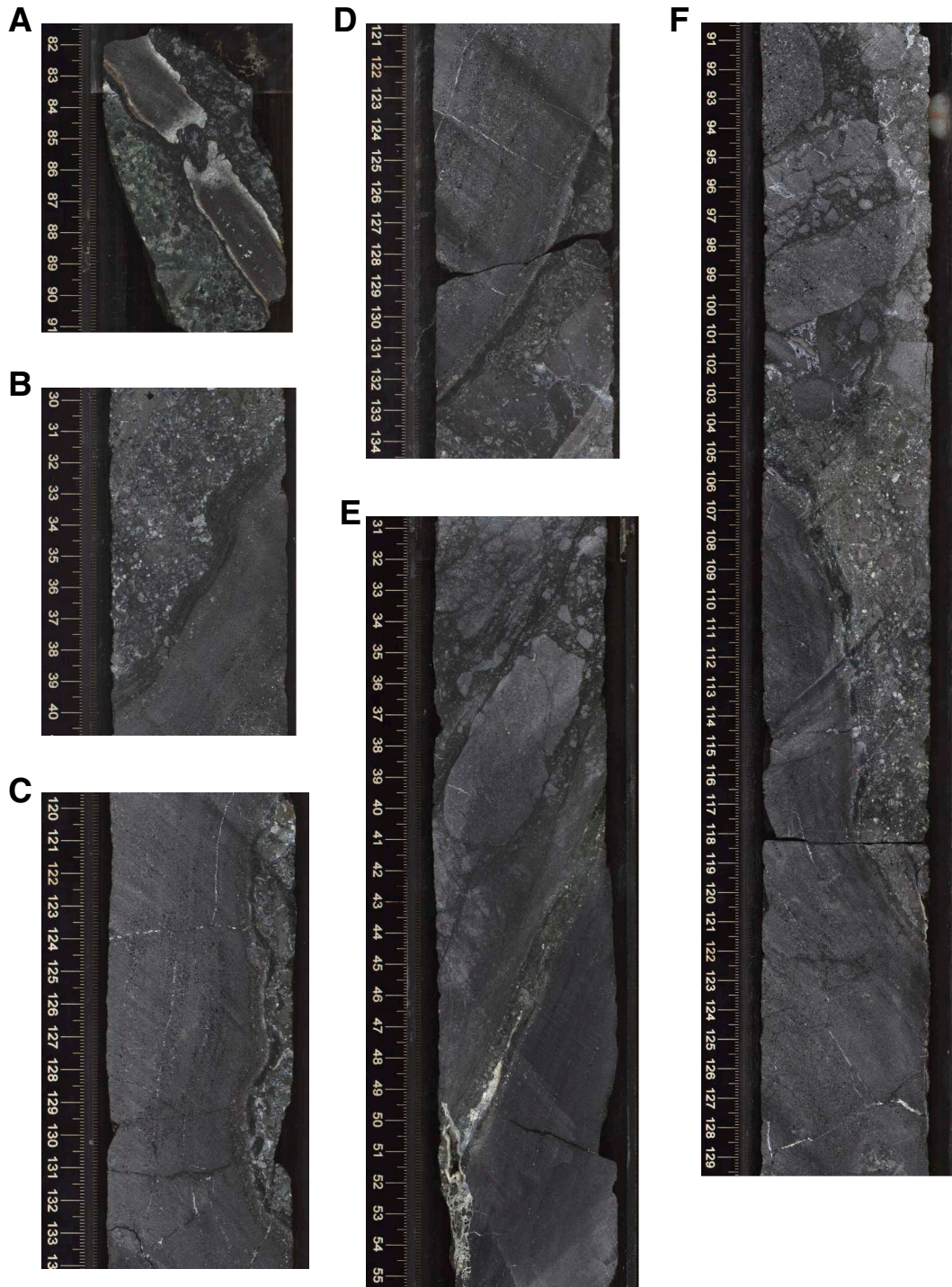


Figure F30. Multibeam bathymetric map of seafloor around Island of Surtsey off the south coast of Iceland, showing large submarine lobes of volcanoclastic debris that built up during the formation of the island. Site U1374 is probably located on a similar but larger lobe of volcanoclastic debris that built up around Rígil Guyot. From Jakobsson et al. (2009).

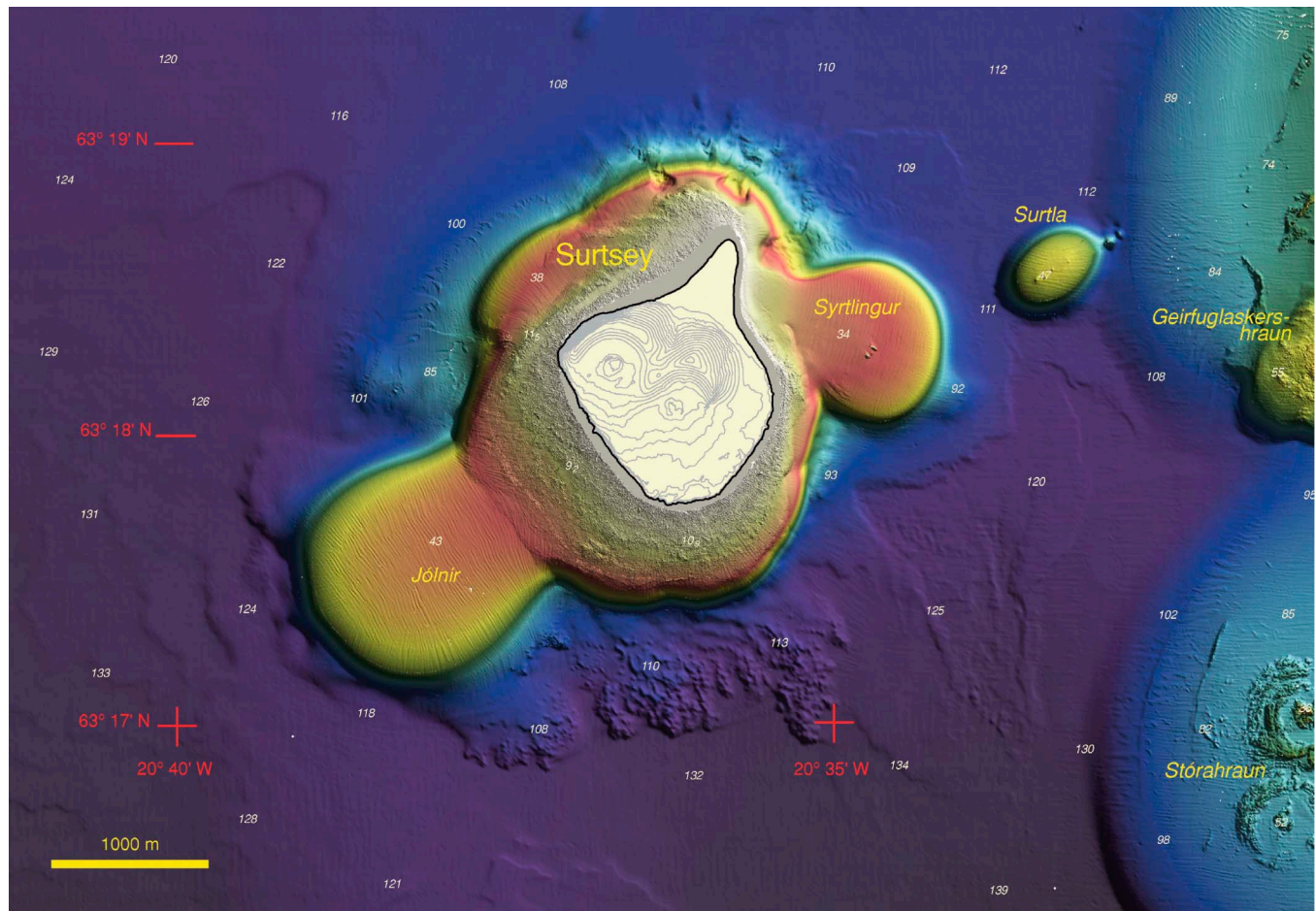


Figure F31. Plot of downhole distribution of percentage of groundmass alteration for each alteration interval defined by the alteration petrology group. Circles are located at center depth for each interval. Gray shading represents sedimentary units.

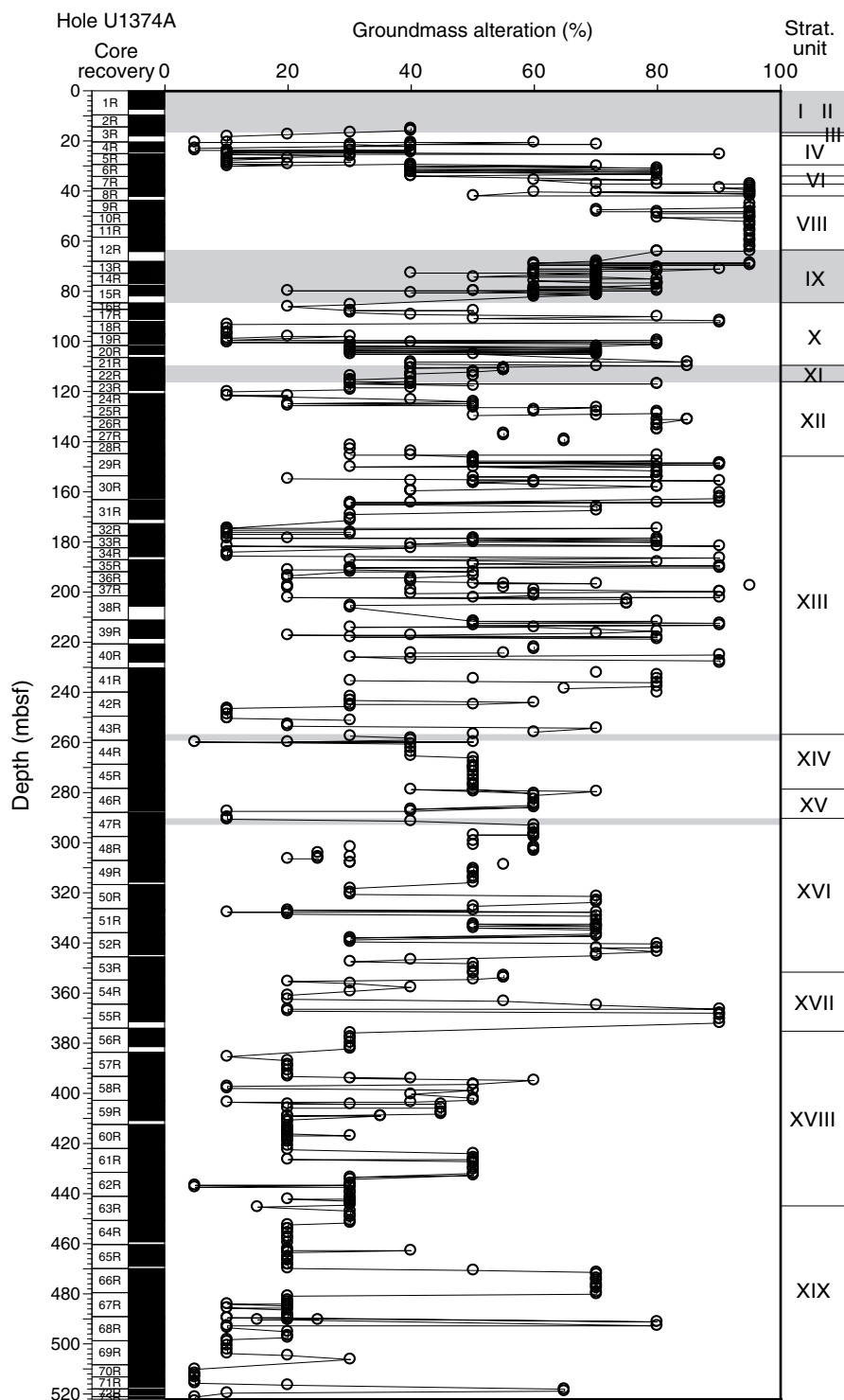


Figure F32. Plot of downhole distribution of secondary minerals replacing olivine for each alteration interval defined by the alteration petrology group. Symbols are located at center depth of each interval. Occurrence of fresh to moderately altered olivine is based on macroscopic observations; for thin section observations, see Table T8. Gray shading represents sedimentary units, pink and green shading represent basalts that were altered under oxidized and reduced conditions, respectively.

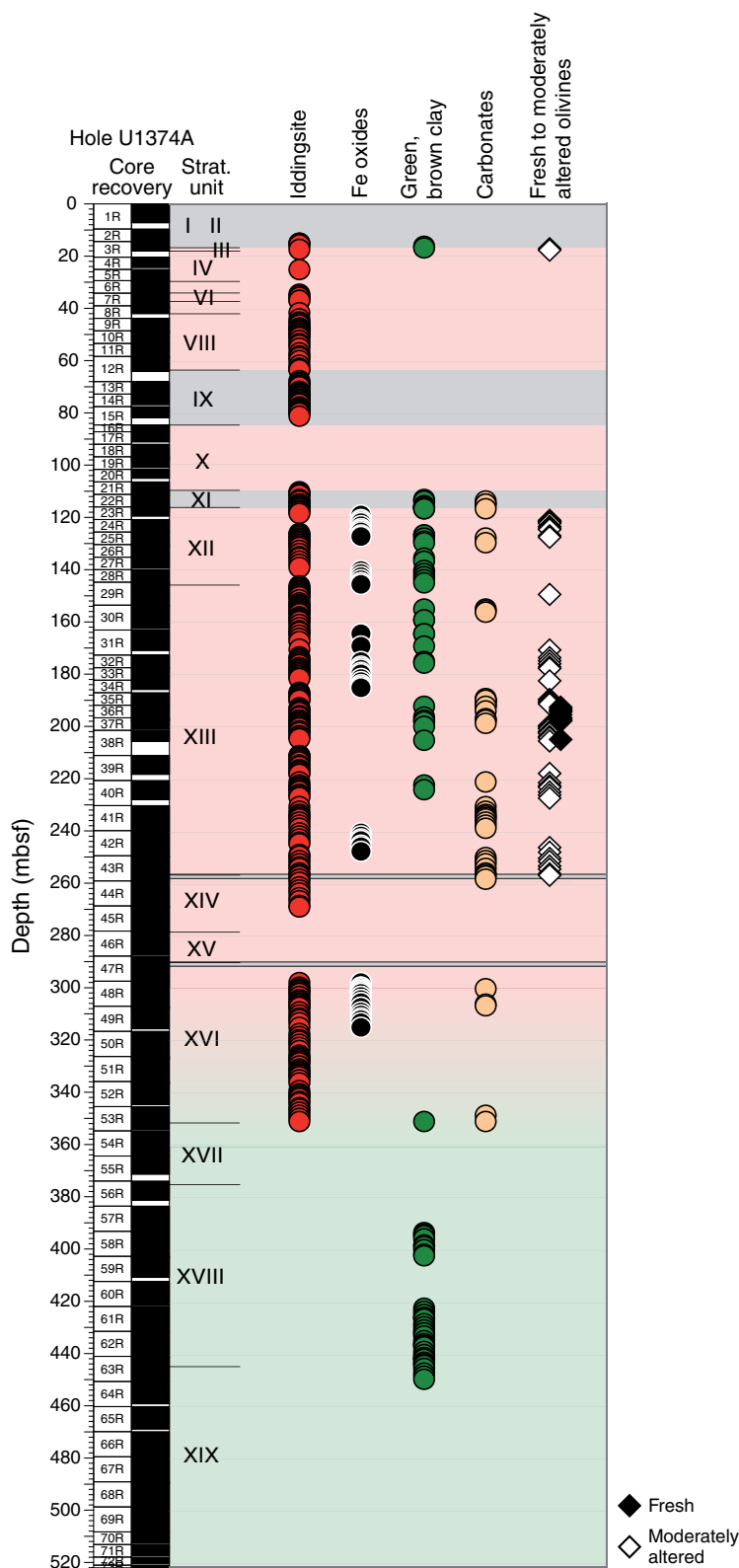


Figure F33. Close-up photographs of different infillings in vesicles, vugs, and voids from hand specimen basaltic samples. Core surfaces were photographed dry. Arrows point toward top of core. **A.** Vesicles (in aphyric basalt breccia) containing small, well-crystallized zeolites and showing a blue coating (interval 330-U1374A-5R-2, 19–29 cm). **B.** Subangular vesicle (in aphyric basalt lava flow) totally filled with blue-green celadonite (interval 330-U1374A-7R-2, 63–69 cm). **C.** Vesicle (in moderately olivine-phyric basalt breccia) filled with carbonates and botryoidal black, brown, and green-blue celadonite (interval 330-U1374A-43R-5, 75–81 cm). **D.** Voids in sedimentary breccia showing coating with carbonates associated with green clay minerals (interval 330-U1374A-22R-1, 118–126 cm). **E.** Vesicles (in highly plagioclase-olivine-augite-phyric basalt breccia) displaying botryoidal, well-crystallized carbonates (interval 330-U1374A-26R-2, 120–135 cm). **F.** Well-formed crystals of zeolite associated with goethite in a vug (interval 330-U1374A-9R-2, 109–110 cm). (Figure shown on next page.)

Figure F33 (continued). (Caption shown on previous page.)

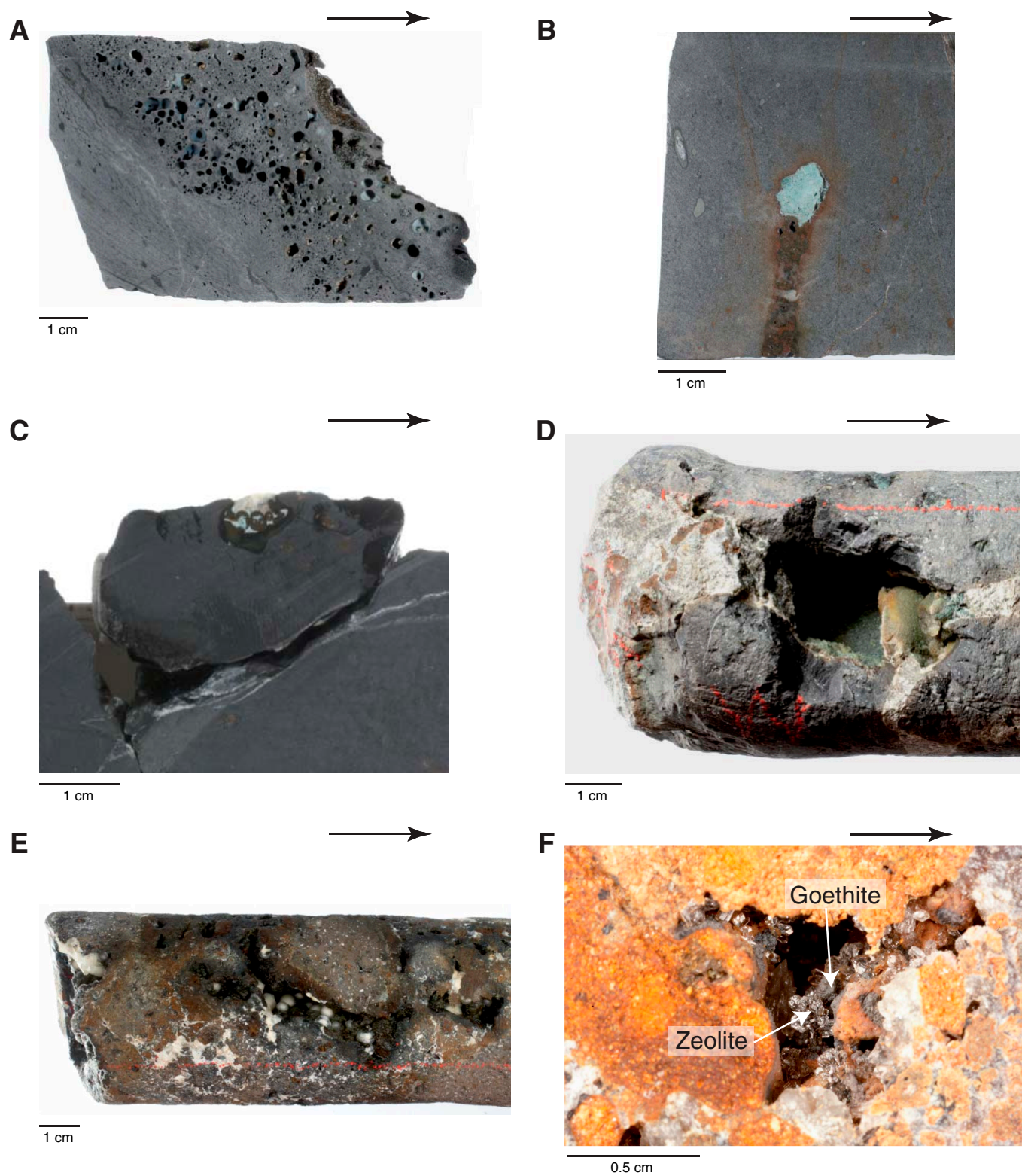


Figure F34. Close-up photographs of centimeter-size crystals observed in vesicles, vugs, and voids in hand specimen basaltic samples. Core surfaces were photographed dry. Arrows point toward top of core. A, B. Voids (in moderately olivine-phyric basalt breccia) showing well-crystallized carbonates and zeolites: (A) intervals 330-U1374A-11R-2, 75–81 cm, and (B) 11R-2, 127–142 cm. C. Voids (in moderately olivine-phyric basalt breccia) showing well-crystallized globular carbonates and associated zeolites (interval 330-U1374A-11R-4, 73–81 cm). D, E. Coating of zeolite crystals in aphyric basalt breccia. Note the presence of well-formed crystals: (D) intervals 330-U1374A-68R-2, 100–106 cm, and (E) 68R-2, 110–113 cm. F. Radial crystal of zeolite filling a void (in aphyric basalt, intrusive sheet) (interval 330-U1374A-68R-5, 62–70 cm).

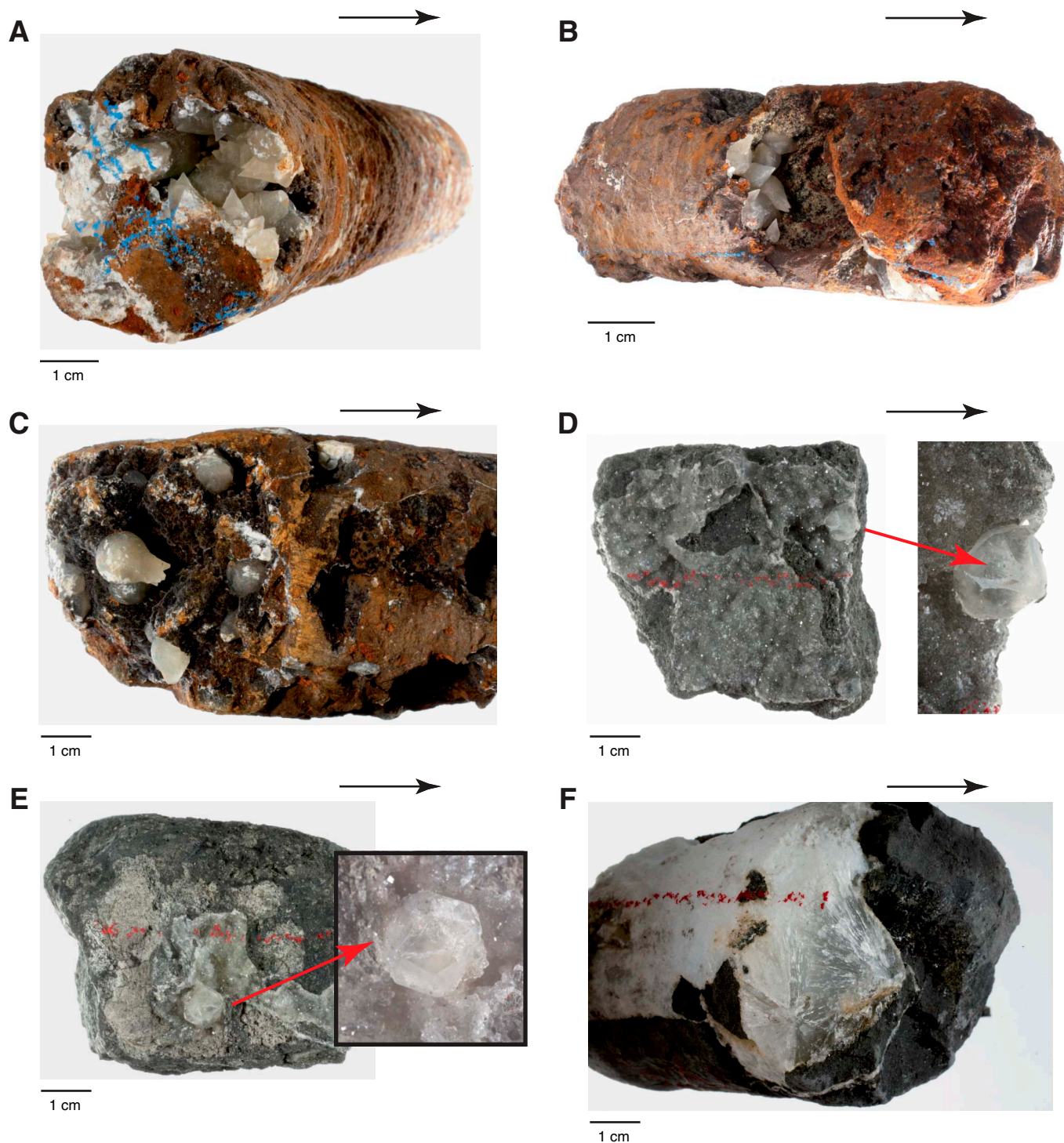


Figure F35. X-ray diffraction spectra and associated core photographs (analyzed zones are highlighted with red circle). **A.** Vug showing filling with zeolite (phillipsite), Mg calcite (not labeled), and maghemite (Sample 330-U1374A-25R-2, 8–10 cm). **B.** Vein showing filling with thaumasite (Sample 330-U1374A-59R-6, 74–76 cm).

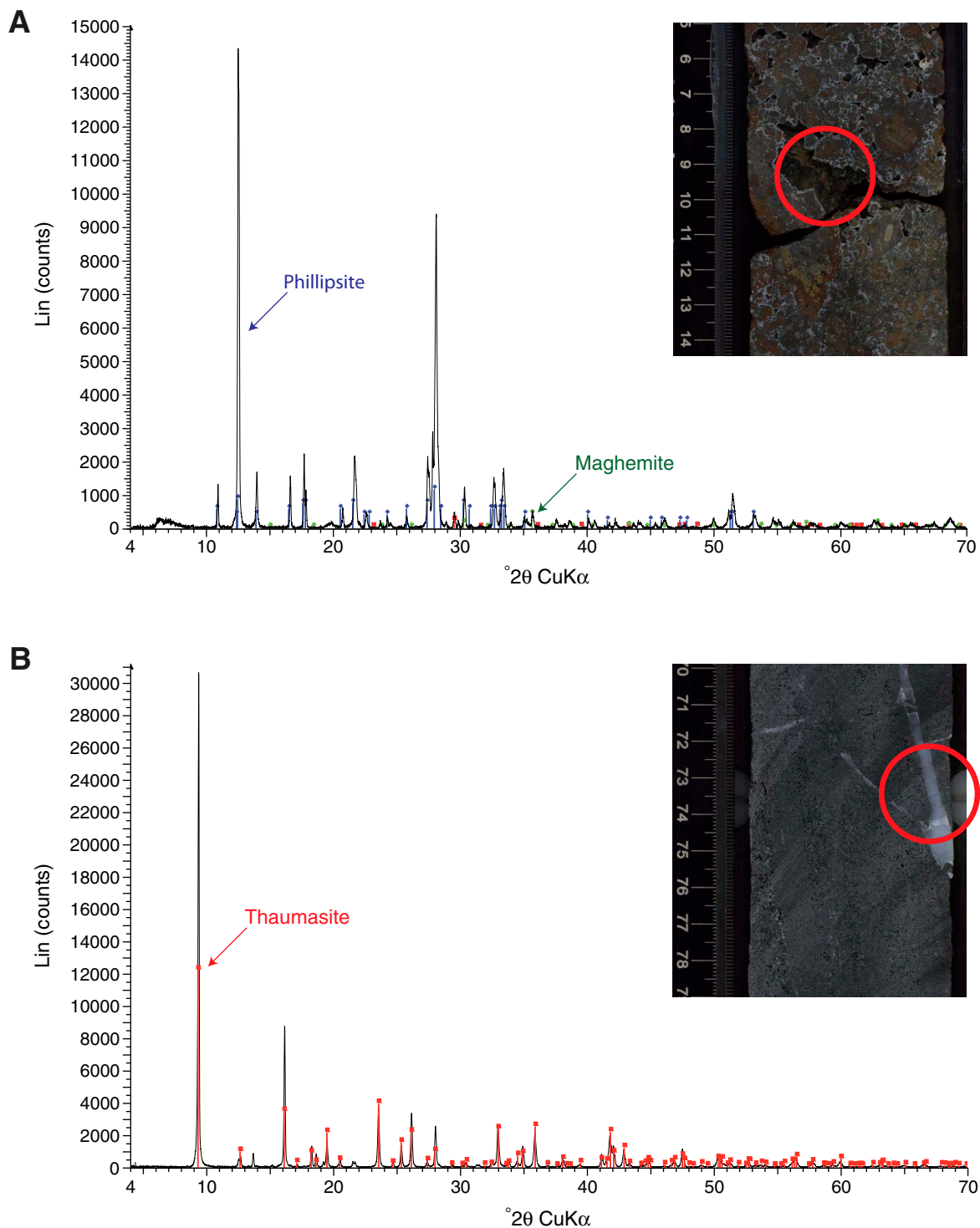


Figure F36. X-ray diffraction spectra and associated core photographs (analyzed zones are highlighted with red circles). **A.** Voids showing filling with thaumasite (Sample 330-U1374A-68R-5, 90–91 cm). **B.** Vein predominantly composed of tetranatrolite, gmelinite, and thaumasite (not labeled) (Sample 330-U1374A-68R-5, 73–74 cm).

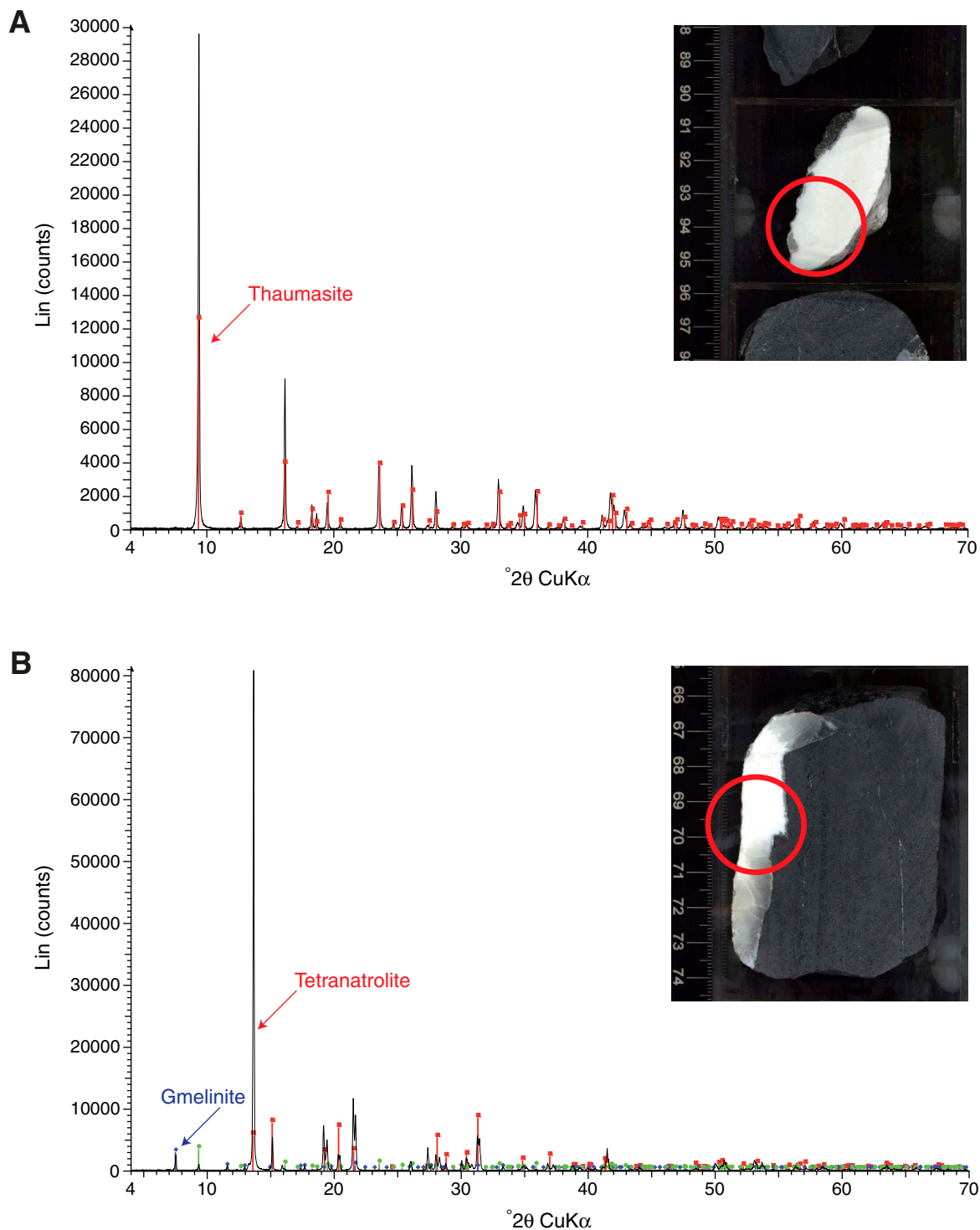
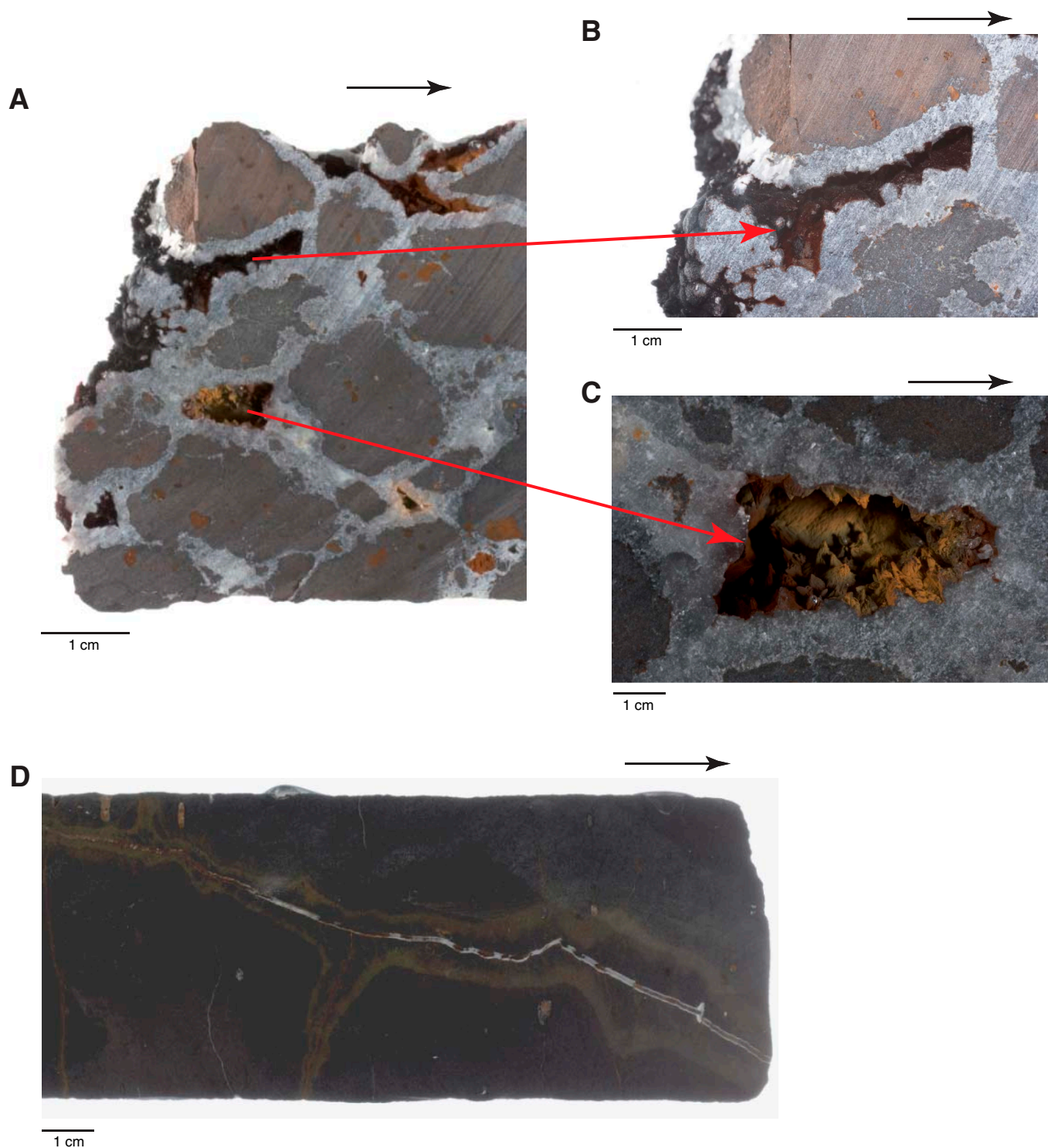


Figure F37. Close-up core photographs (arrows point toward top of core). A–C. Infillings of carbonates with a coating of reddish-brown minerals (goethite, Fe oxyhydroxides) in a sparsely olivine-phyric basalt breccia: (A) intervals 330-U1374A-37R-2, 62–68 cm, and (B, C) 37R-2, 65–68 cm. D. Carbonates and brown and black clay minerals in conjugate veins with centimeter-wide brown halo (interval 330-U1374A-7R-2, 80–94 cm). Core surfaces shown in A–C were photographed dry; core surface shown in D was photographed wet.



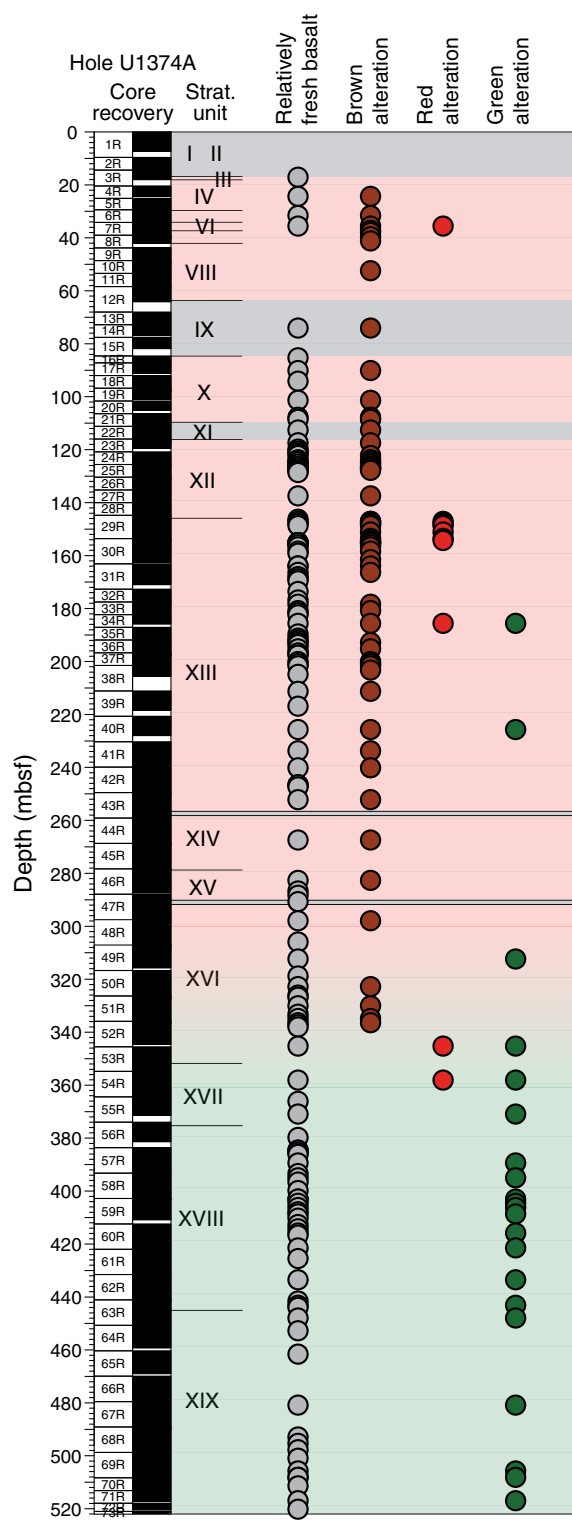


Figure F39. Plot of downhole distribution of alteration colors for each alteration interval defined by the alteration petrology group. Circles are located at center depth for each interval. Gray shading represents sedimentary units, pink and green shading represent basalts that were altered under oxidized and reduced conditions, respectively.

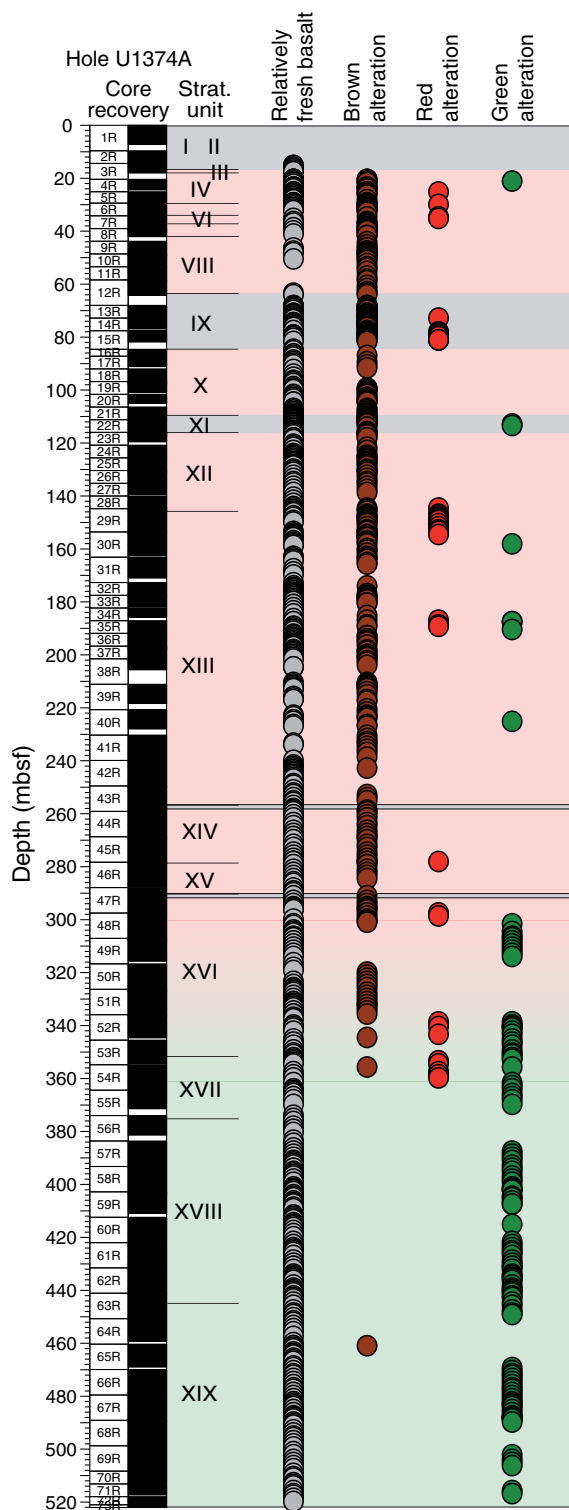


Figure F40. Thin section photomicrographs of altered olivine and plagioclase. **A.** Microphenocrysts of olivine completely altered to iddingsite and iron oxyhydroxides in a moderately olivine-phyric basalt clast (Sample 330-U1374A-9R-1, 24–28 cm; Thin Section 132; plane-polarized light). **B.** Phenocryst of olivine completely altered to iddingsite (moderately olivine-phyric basalt clast) (Sample 330-U1374A-9R-4, 25–29 cm; Thin Section 133; plane-polarized light). **C, D.** Moderately altered olivine partly replaced by green clay and iron oxyhydroxides (highly plagioclase-olivine-augite-phyric basalt) (Sample 330-U1374A-25R-1, 112–115 cm; Thin Section 161): (C) plane-polarized light, (D) crossed polars. **E.** Slightly altered phenocrysts of plagioclase with dusty micrograins of carbonates with sieve texture (clasts in sedimentary conglomerate/breccia) (Sample 330-U1374A-22R-4, 49–51 cm; Thin Section 156; crossed polars).

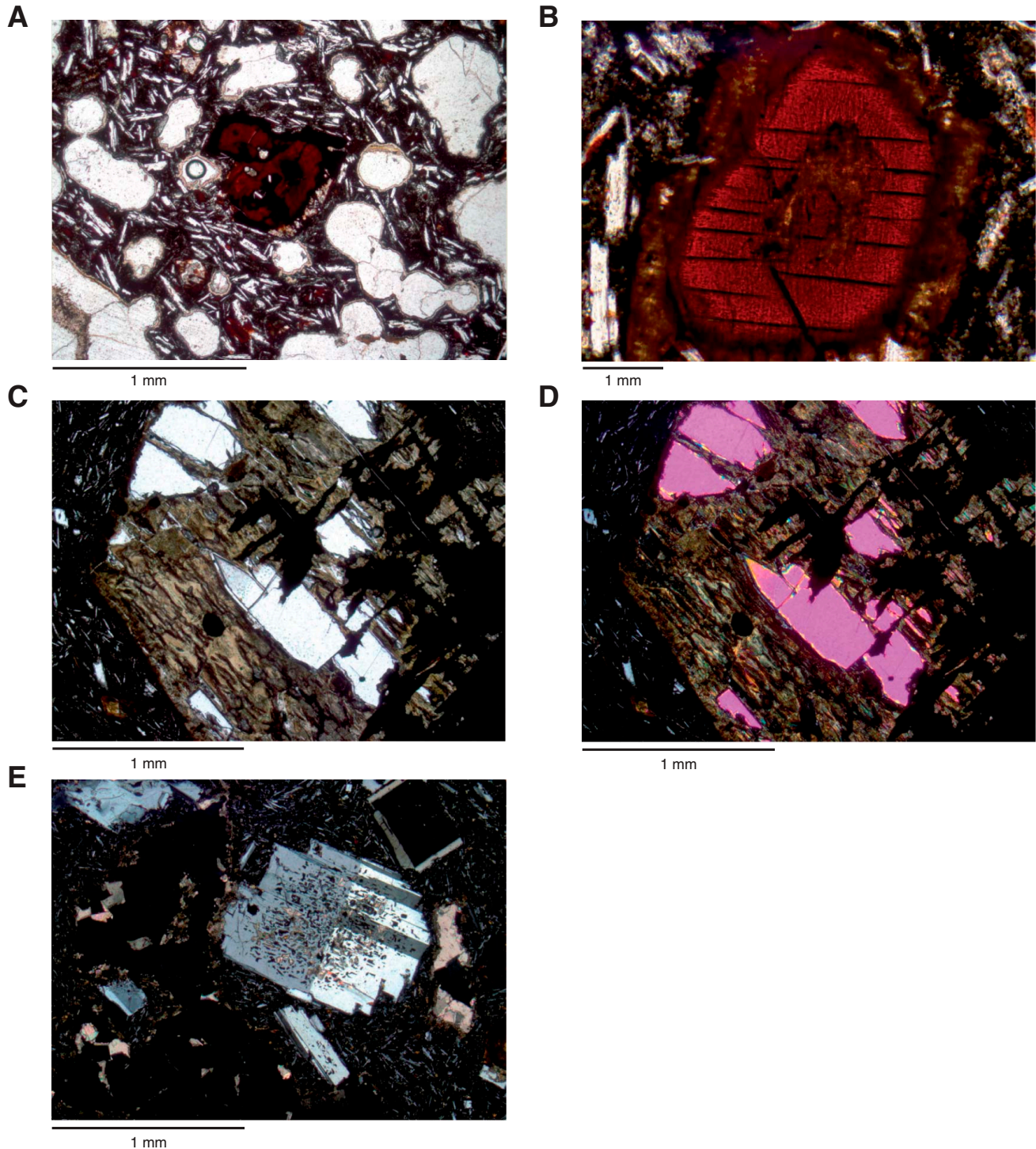


Figure F41. Thin section photomicrographs of completely altered olivine. **A.** Alteration to iddingsite, hematite, and minor carbonate (highly plagioclase-olivine-augite-phyric basalt breccia) (Sample 330-U1374A-24R-4, 100–102 cm; Thin Section 160; plane-polarized light). **B.** Detail of association of carbonate and iddingsite after olivine (highly plagioclase-olivine-augite-phyric basalt breccia) (Sample 330-U1374A-25R-2, 128–131 cm; Thin Section 163; plane-polarized light). **C, D.** Olivine completely altered to iddingsite and carbonate (aphyric to moderately olivine-phyric basalt breccia) (Sample 330-U1374A-24R-4, 100–102 cm; Thin Section 160): (C) plane-polarized light, (D) crossed polars. **E, F.** Olivine completely altered to iddingsite, Fe oxyhydroxides, and large amount of carbonate in the interior portions of the altered phenocrysts (moderately plagioclase-phyric basalt) (Sample 330-U1374A-48R-8, 20–23 cm; Thin Section 205): (E) plane-polarized light, (F) crossed polars.

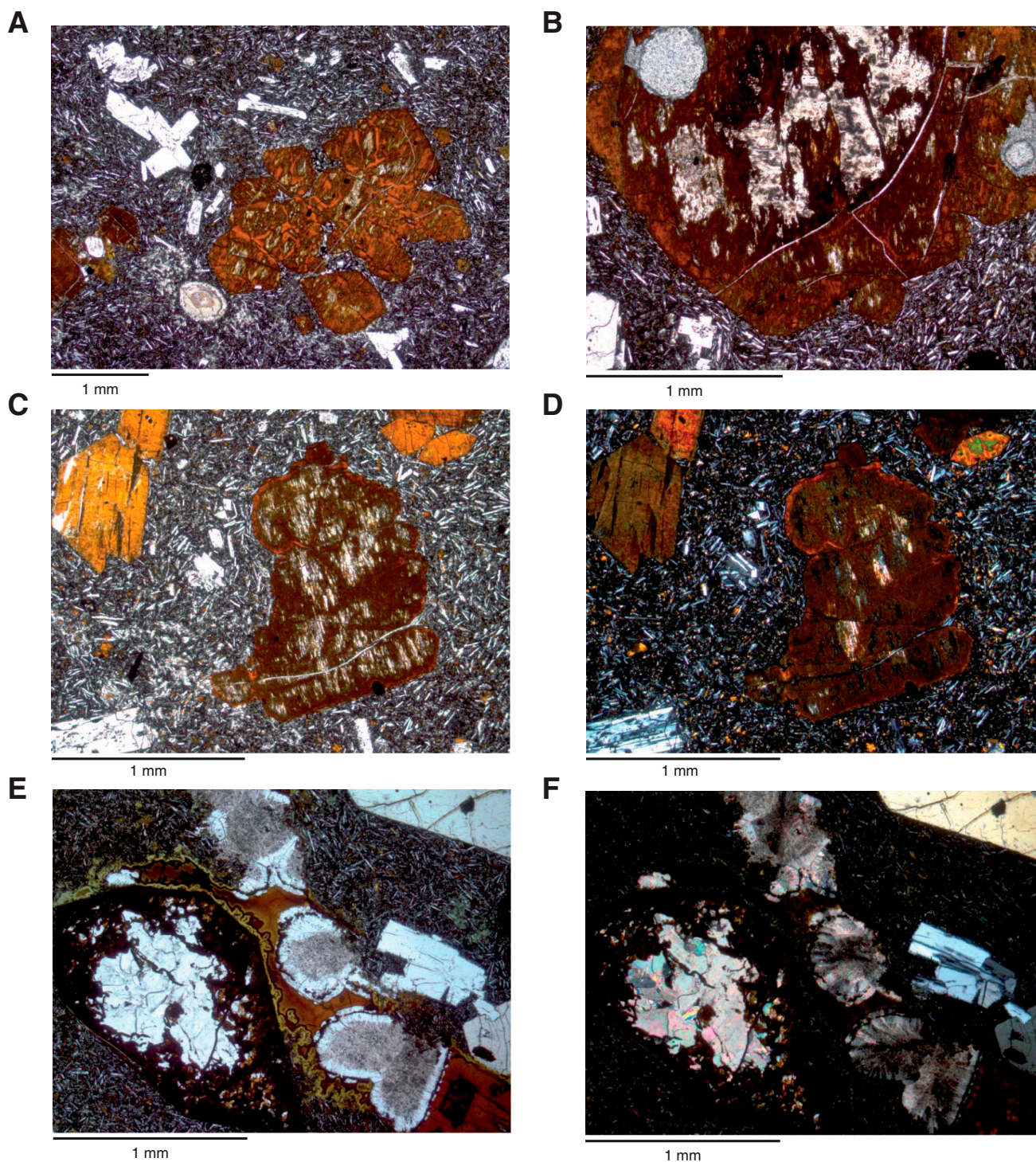


Figure F42. Plot of downhole distribution of secondary minerals filling vesicles for each alteration interval defined by the alteration petrology group. Symbols are located at center depth for each interval. The background color represents the main alteration color of the core (from Fig. F38). Gray shading represents sedimentary units, pink and green shading represent basalts that were altered under oxidized and reduced conditions, respectively.

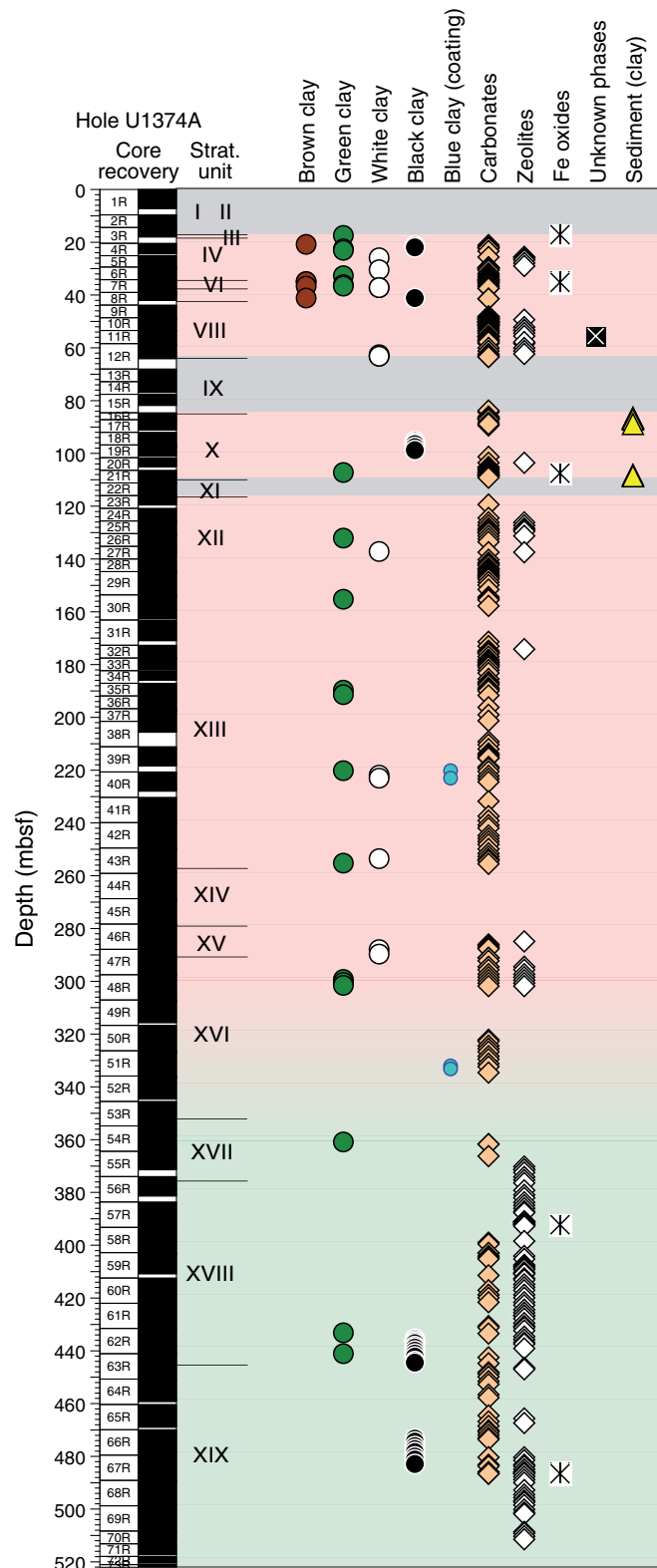


Figure F43. Thin section photomicrographs of vesicles. Each pair is shown with plane-polarized light (left) and with crossed polars (right). A, B. Vesicle (moderately olivine-phyric basalt breccia) filled with two stages of carbonates separated by a layer of brown clay (Sample 330-U1374A-9R-1, 24–28 cm; Thin Section 132). C, D. Vesicles (moderately olivine-plagioclase-phyric basalt breccia) filled with carbonates and botryoidal brown clay minerals (Sample 330-U1374A-29R-7, 80–82 cm; Thin Section 171). E, F. Vesicle (aphyric to moderately plagioclase-phyric basalt breccia) filled with zeolites, green clay minerals, and carbonates (Sample 330-U1374A-44R-2, 121–125 cm; Thin Section 196).

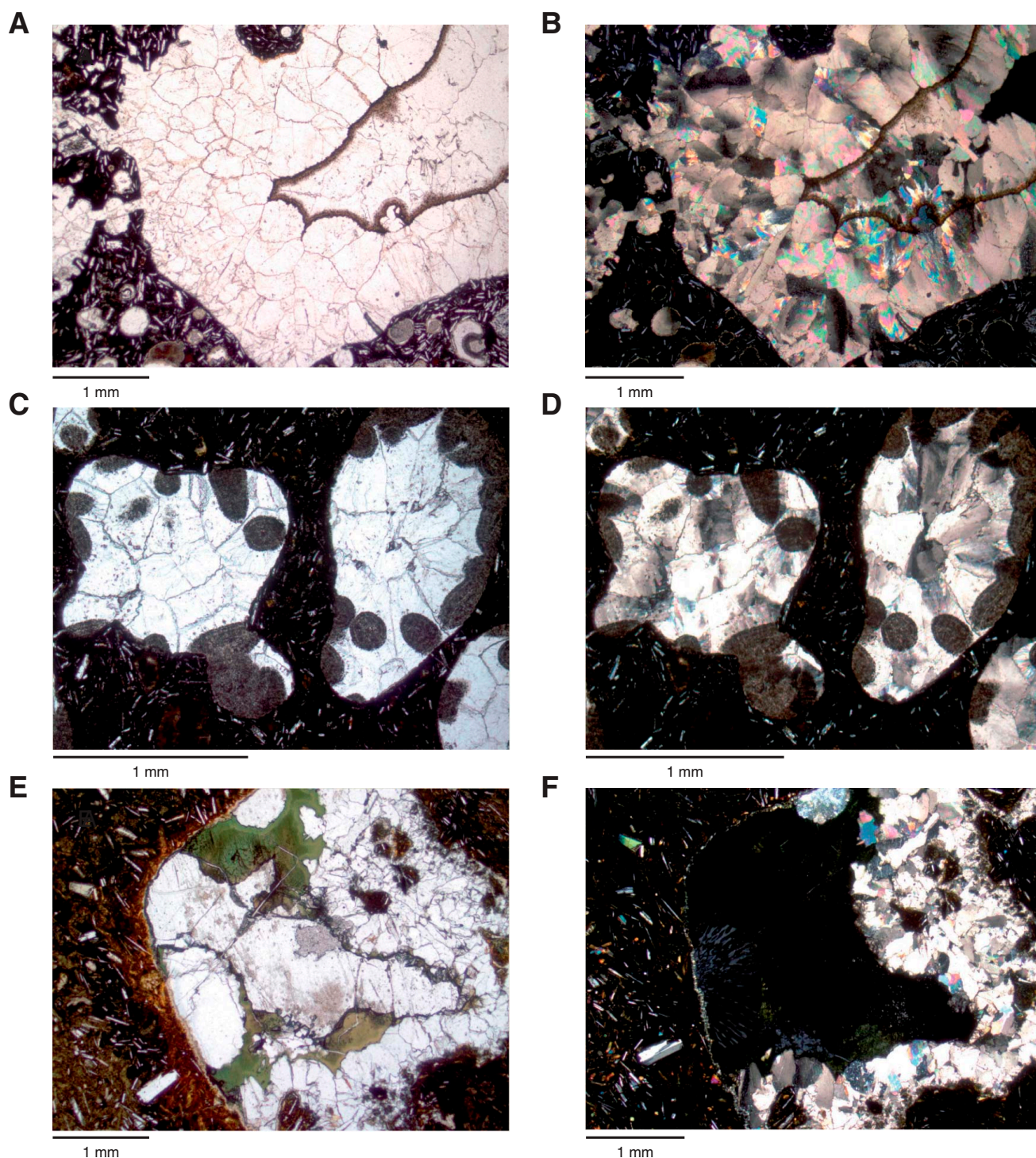


Figure F44. Thin section photomicrographs of vesicles and voids. **A.** Vesicle (aphyric basalt breccia) showing multistage infillings with black clay, iron oxyhydroxides, and carbonates (Sample 330-U1374A-6R-1, 114–116 cm; Thin Section 123; plane-polarized light). **B–E.** Vesicles and vuggy voids (in lithic-vitric volcanic sand, volcanic breccia, and sedimentary breccia) filled with well-crystallized zeolites: (B) Sample 330-U1374A-9R-4, 25–29 cm (Thin Section 133; plane-polarized light); (C, D) Sample 7R-4, 112–114 cm (Thin Section 126; plane-polarized light); (E) Sample 13R-1, 50–53 cm (Thin Section 137; plane-polarized light). **F.** Vesicle (moderately olivine-plagioclase-phyric basalt, lava fragment) filled with botryoidal zeolite (Sample 330-U1374A-29R-4, 107–110 cm; Thin Section 170; crossed polars).

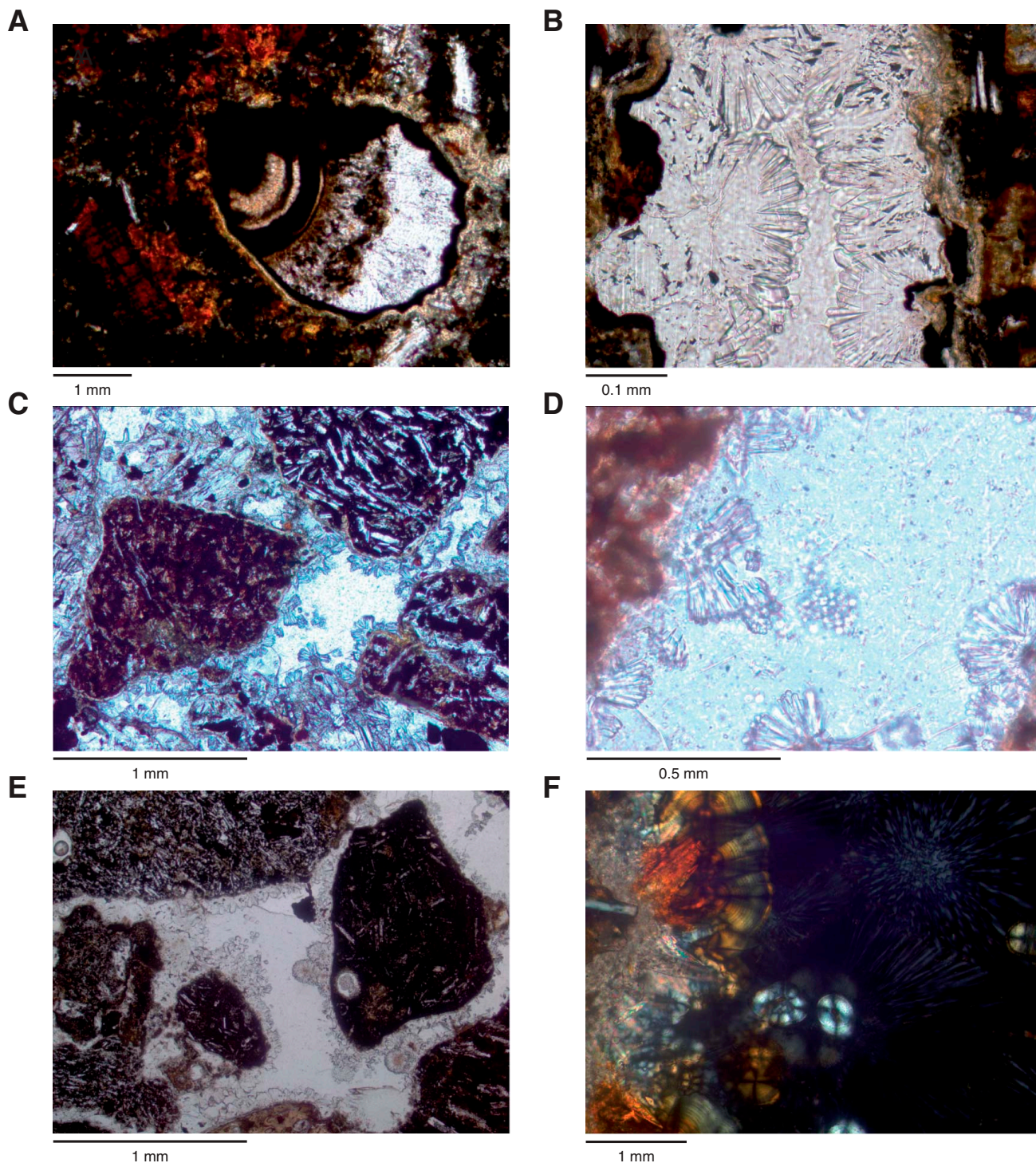


Figure F45. Thin section photomicrographs of vesicles initially filled with carbonate followed by brown (saponite, montmorillonite?) and then green (nontronite, celadonite) minerals. A–C. Sample 330-U1374A-44R-2, 121–125 cm (Thin Section 196): (A, C) plane-polarized light, (B) crossed polars. D. Sample 330-U1374A-45R-7, 22–24 cm (Thin Section 198; plane-polarized light). E, F. Sample 330-U1374A-47R-1, 133–135 cm (Thin Section 200): (E) plane-polarized light, (F) crossed polars.

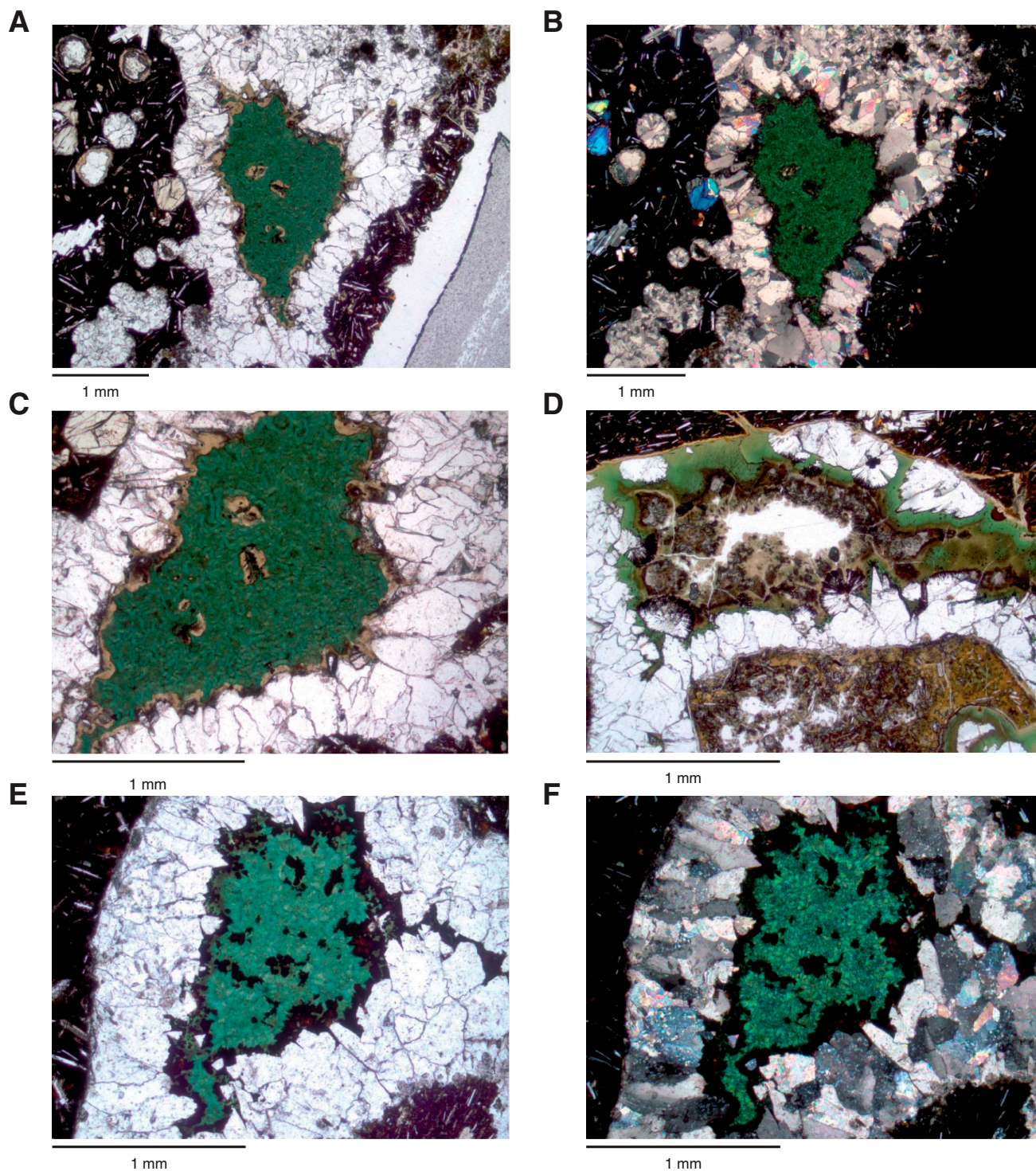


Figure F46. Plot of downhole distribution of vein minerals for each alteration interval defined by the alteration petrology group. Symbols are located at center depth for each interval. Note the predominance of carbonate throughout and the occurrence of zeolite mainly from ~370 mbsf to the bottom of the hole. The background color represents the main alteration color of the core (from Fig. F38). Gray shading represents sedimentary units, pink and green shading represents basalts that were altered under oxidized and reduced conditions, respectively.

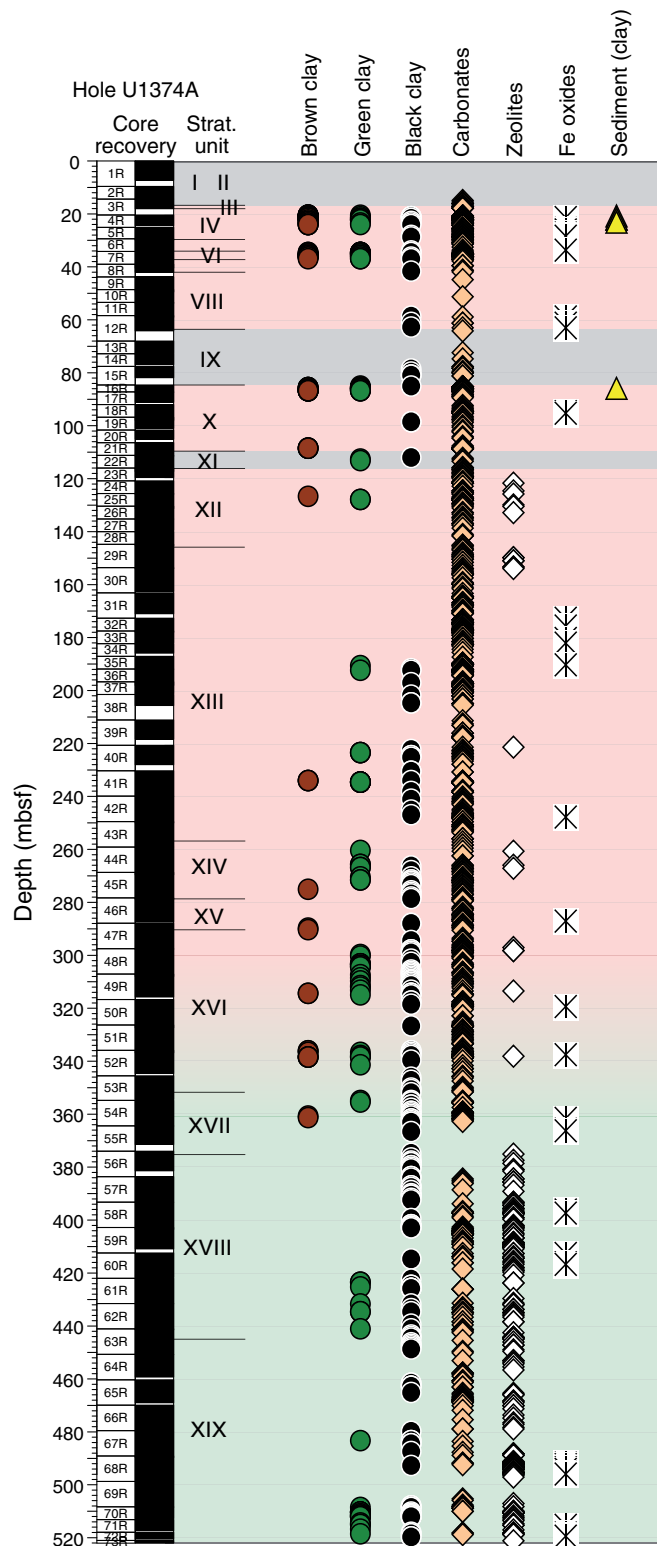


Figure F47. Thin section photomicrographs of veins. A, B. Millimeter-thick conjugate veins (aphyric basalt breccia) filled with calcite and zeolite (Sample 330-U1374A-18R-1, 31–33 cm; Thin Section 145): (A) plane-polarized light, (B) crossed polars. C. Submillimeter-thick vein (aphyric basalt breccia) partially filled with zeolites showing botryoidal habit (Sample 330-U1374A-21R-3, 19–21 cm; Thin Section 150; plane-polarized light). D. Millimeter-thick vein (aphyric basalt breccia) filled with minor brown clay and zeolites on wall, followed by carbonates in vein interior (Sample 330-U1374A-6R-1, 114–116 cm; Thin Section 123; plane-polarized light). E, F. Millimeter-thick vein (highly plagioclase-olivine-augite-phyric basalt, lava flow) filled with botryoidal zeolites on wall, followed by carbonates (Sample 330-U1374A-25R-2, 84–86 cm; Thin Section 162): (E) plane-polarized light, (F) crossed polars.

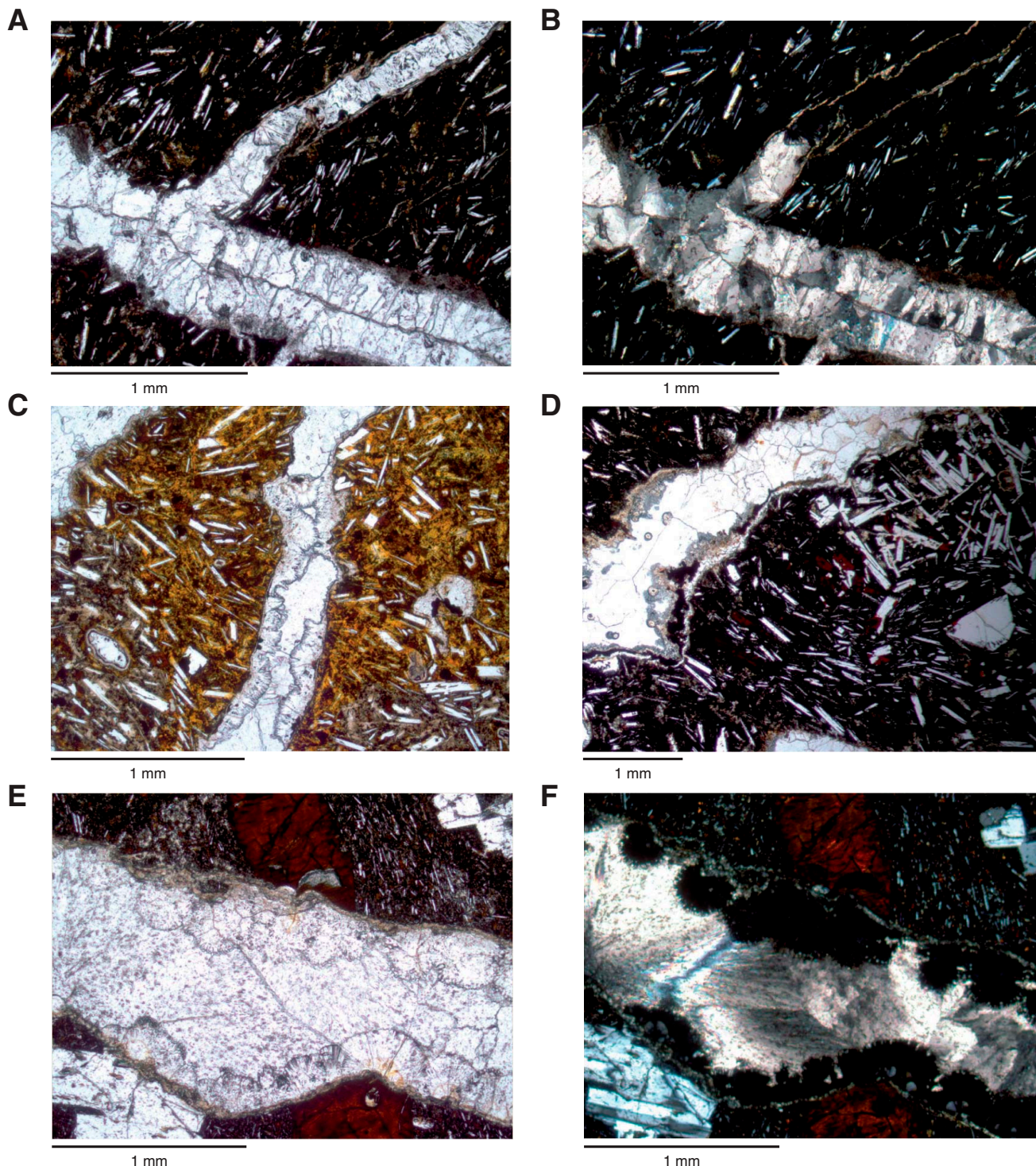


Figure F48. Thin section photomicrographs of veins and voids. A, B. Millimeter-thick vein (aphyric basalt, intrusive sheet) filled with calcite and pyrite (Sample 330-U1374A-58R-4, 28–32 cm; Thin Section 214): (A) transmitted light (plane-polarized), (B) reflected light. C, D. Voids (moderately plagioclase-augite-olivine-phyric basalt breccia) filled with zeolite (Sample 330-U1374A-49R-1, 92–94 cm; Thin Section 206): (C) plane-polarized light, (D) crossed polars.

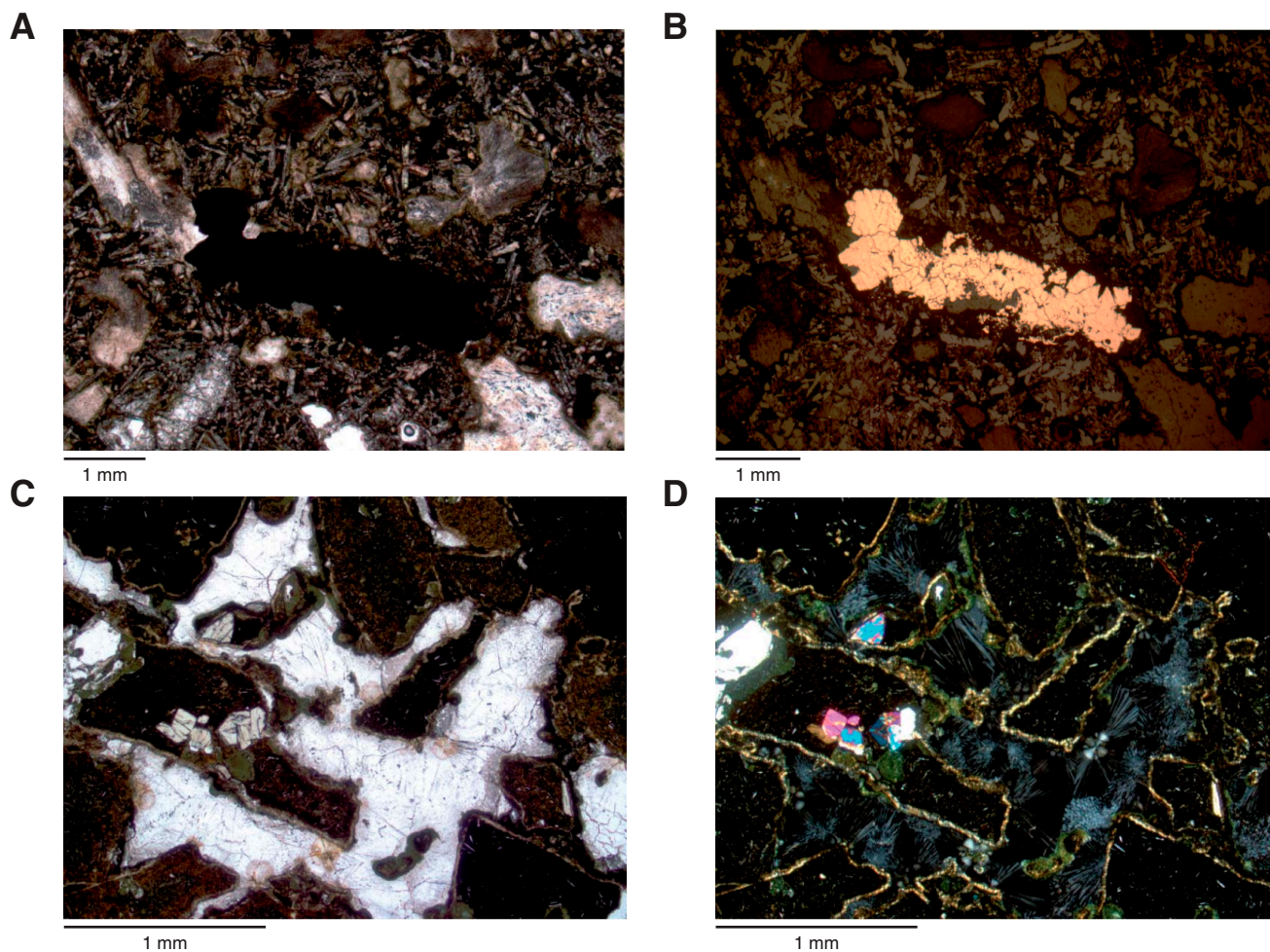


Figure F49. Plot of downhole distribution of void secondary minerals for each alteration interval defined by the alteration petrology group. Symbols are located at center depth for each interval. Note the predominance of carbonate in the uppermost ~300 mbsf, followed by the predominance of zeolite from ~300 mbsf to the bottom of the hole. Gray shading represents sedimentary units, pink and green shading represent basalts that were altered under oxidized and reduced conditions, respectively.

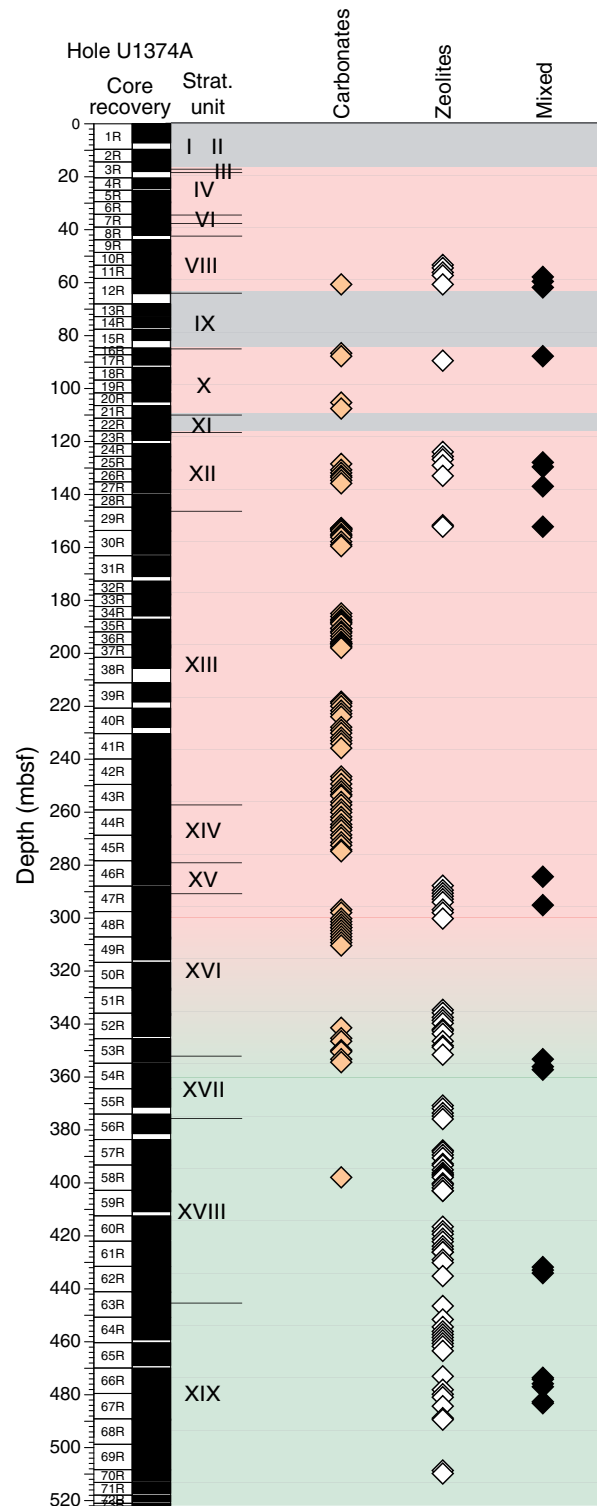


Figure F50. Plot of downhole distribution of void secondary minerals and filling (%) for each alteration interval defined by the alteration petrology group. Circles are located at center depth for each interval. Carbonates (blue circles) are the main phase in the uppermost 300 m, whereas zeolites (purple circles) dominate in the lowermost 200 m. Filling with dark clay (orange plus symbols) becomes more abundant with increasing depth. Pink and green shading represent oxidized and reduced conditions of host rock alteration, respectively.

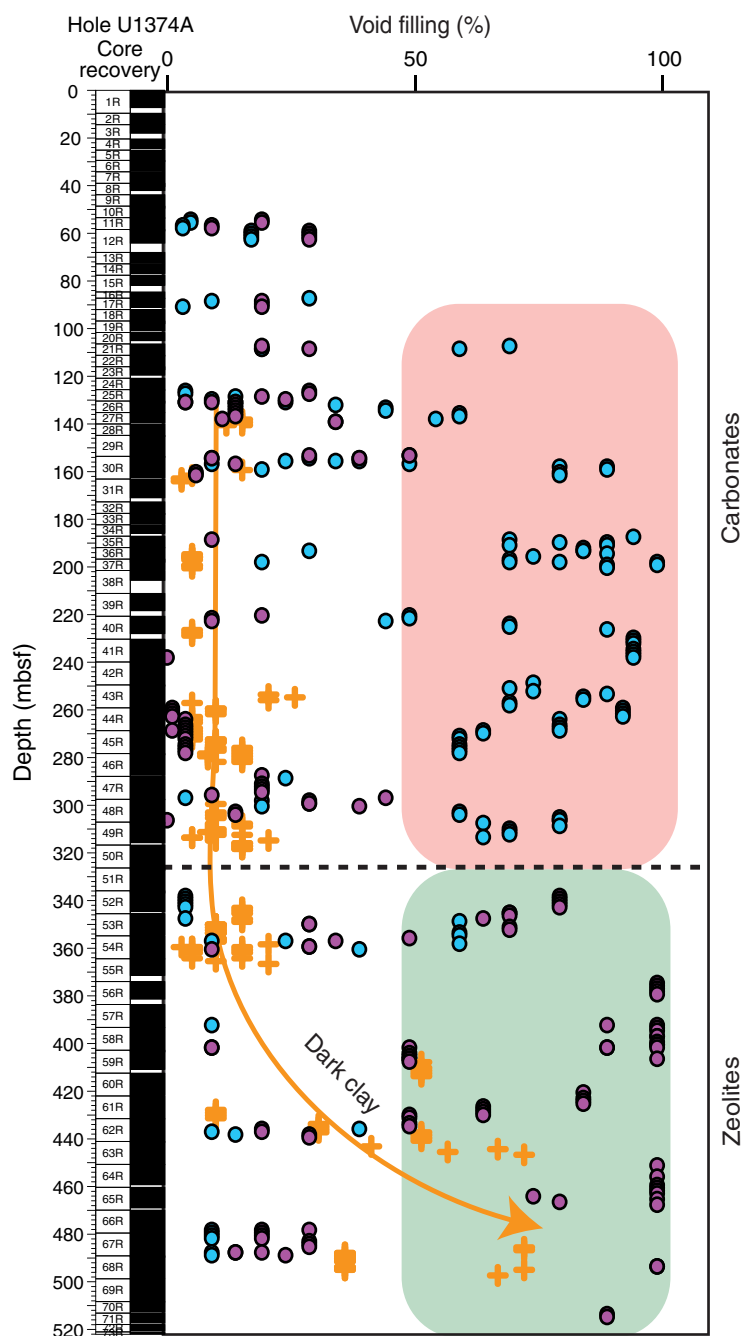


Figure F51. Number of structural features in Hole U1374A, representing total number of features with individual row entries in the DESClogik database entry template. For fractures, veins, and especially vein networks, a single entry may comprise multiple features (e.g., 12 veinlets in a vein network). When multiple fractures and veinlets are considered, 3225 vein networks, 1229 veins, and 356 fractures were recorded in cores from Hole U1374A.

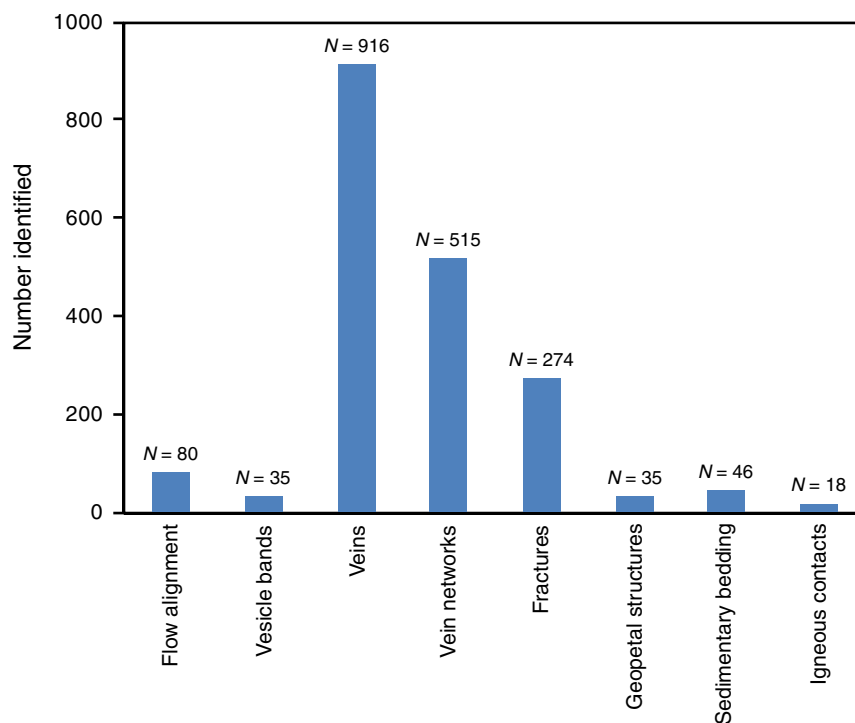


Figure F52. A–C. Rose diagrams showing dip angles of sedimentary bedding in Hole U1374A relative to the core reference frame. Most sedimentary horizons at this site have dips of 20°–25°, likely close to the maximum angle of repose for these wet sand-size sediments. In contrast, bedding in Unit II has shallower dips of mostly 0°–5°, with relatively fewer dips at 5°–20°. **D.** Plot of dip angle vs. depth for all sedimentary units. A single extremely steep dip angle of 55° is located at 162.3 mbsf in Unit XIII. **E.** Plot of dip angle vs. depth for Unit II only. Except for the lowermost part of Unit II (black arrow), dip angles in Unit II gradually increase uphole ($r^2 = 0.53$).

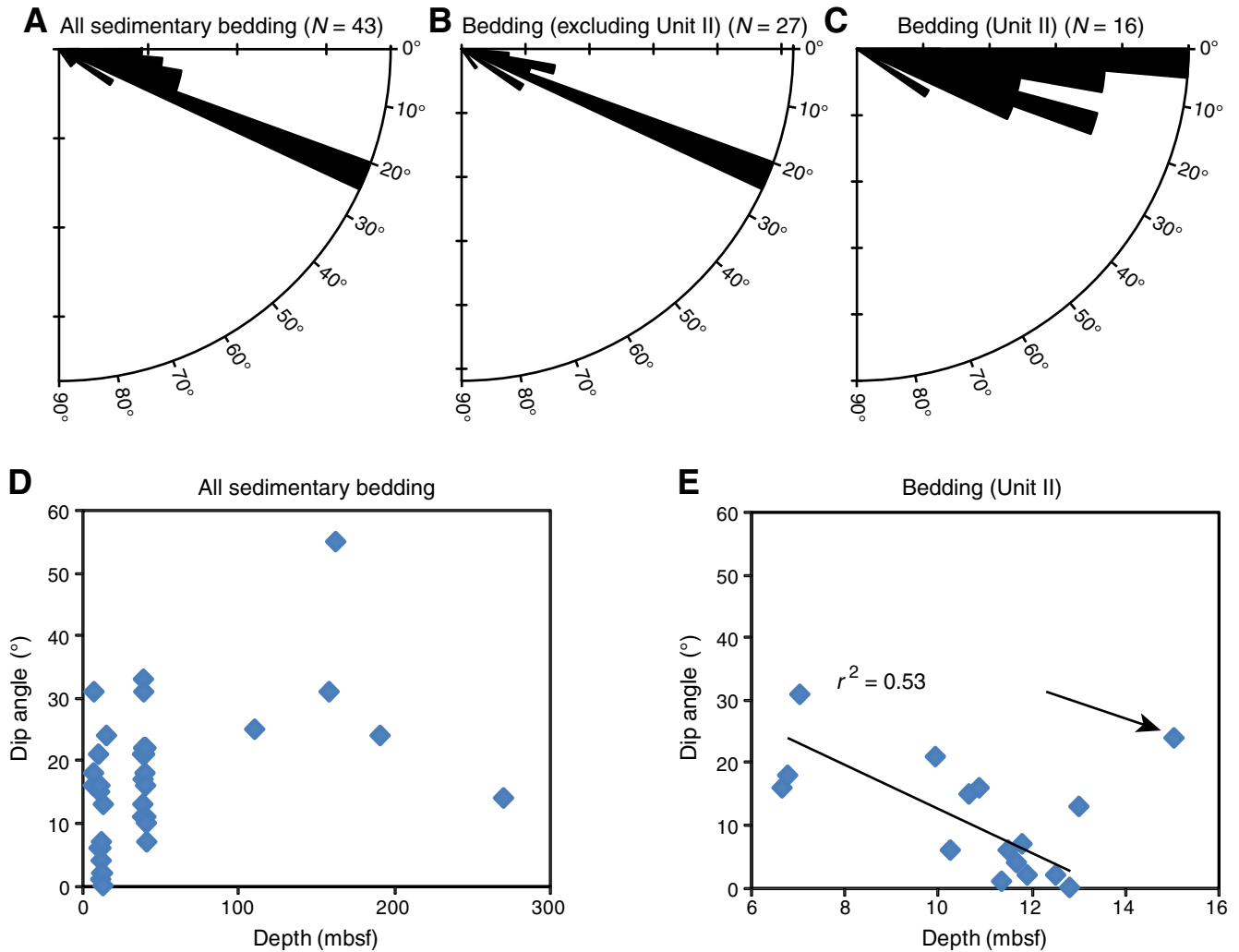


Figure F53. Representative close-up photographs of geopetal structures and their stratigraphic positions in the upper half of Hole U1374A. **A.** Geopetal within a fossil, with the lower portion filled by pink micrite and the upper portion filled by clear calcite (interval 330-U1374A-3R-1A, 99.7–101.8 cm [wet]). **B.** Fracture in the uppermost lava flow, with the base filled by dark sandy sediments and the upper portion filled by lighter sediments (interval 3R-2A, 93.5–96.4 cm [dry]). **C.** Peperitic lava, with the lower portion of the geopetal filled with pink sediments and the upper half with calcite (interval 5R-4A, 101–104.6 cm [dry]). **D.** Fractures in breccia, with the lower portion filled with dark sand-size sediments and the top filled with calcite (interval 18R-1A, 102–107.5 cm [dry]). In all cases the geopetal structures are still in their original horizontal sedimentary position, indicating that no tilting of these rocks occurred since deposition. For explanation of lithology symbols and patterns, see Figure F18.

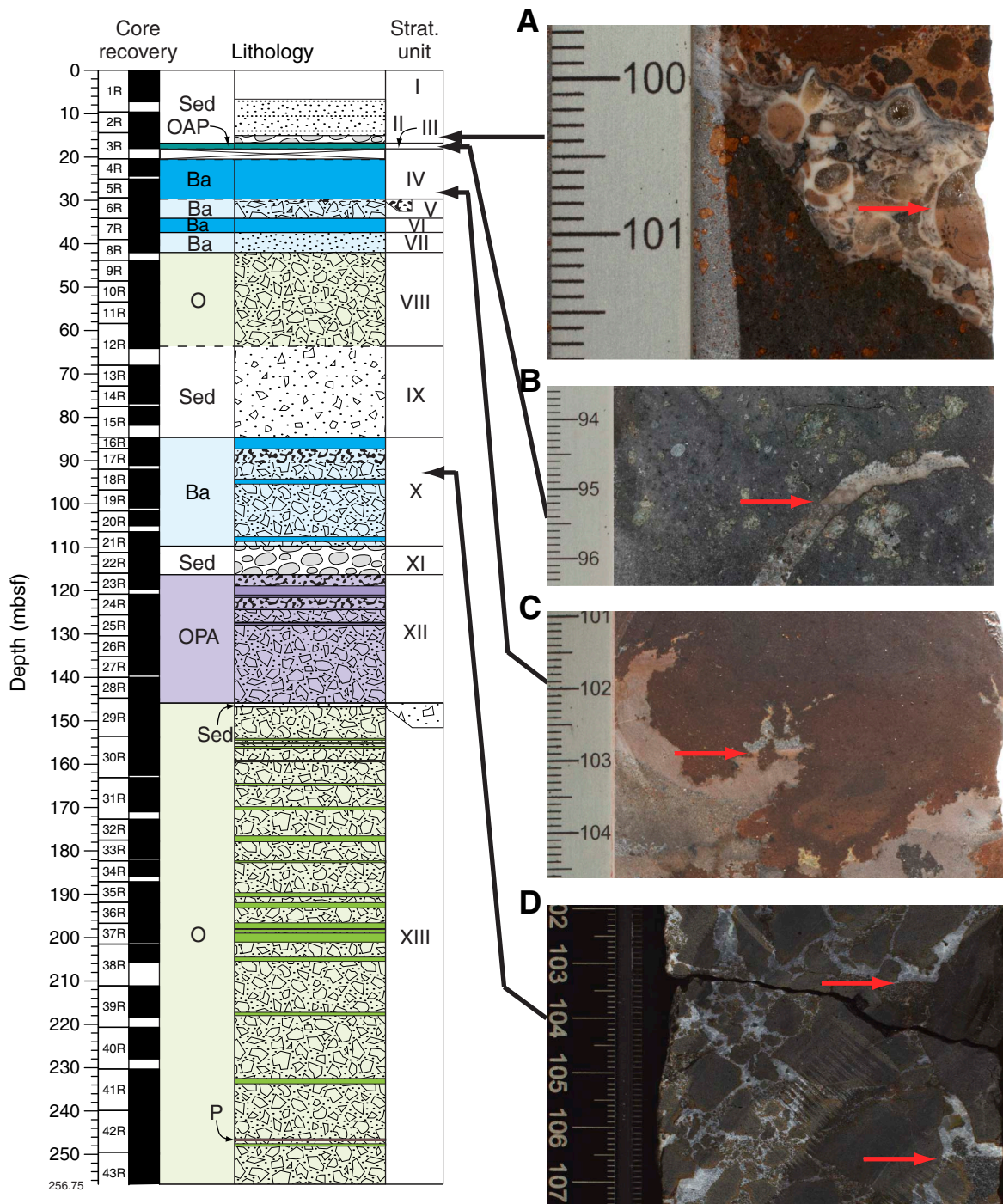


Figure F54. Representative core photographs of contacts between sheet intrusions and country rocks. Interpreted overlays of these images are shown in Figure F55. Note how traces of vesicle bands (dashed black lines in Fig. F55) are parallel to the intrusion margins. **A.** Moderately dipping upper contact with a ~7 cm wide baked margin (interval 330-U1374A-55R-1A, 114.5–137 cm). **B.** Moderately dipping contact with much thinner (<1 cm) baked margin (interval 58R-3A, 30–40.7 cm). **C.** Smallest intrusion recovered (only 2 cm wide) (interval 55R-4A, 81.3–91.2 cm). **D.** Curved intrusive margin into volcanic breccia (interval 60R-1A, 90.4–129.6 cm). **E.** Contact between younger massive intrusion (lower right) with older fragmented intrusion (upper left) (interval 68R-5A, 30.6–55.5 cm). Above 25 cm (off image), the older intrusion is unfragmented, and fragmentation becomes progressively more intense toward the contact with the younger intrusion, suggesting this fragmentation is caused by the younger intrusion. Between the two intrusions is a narrow zone of greenish material, which may be “country rock” breccia or highly altered material from the older intrusion. Fluids were mobilized along this zone, as indicated by the ~10 mm wide zeolite vein that runs from 48 to 55.5 cm in this image. This vein becomes ~25 mm wide between 91 and 95 cm (off image), which is the widest vein recorded at Site U1374. **F.** Near-vertical intrusion margin and vesicle bands (interval 59R-1A, 119.5–134.1 cm). (Figure shown on next page.)

Figure F54 (continued). (Caption shown on previous page.)

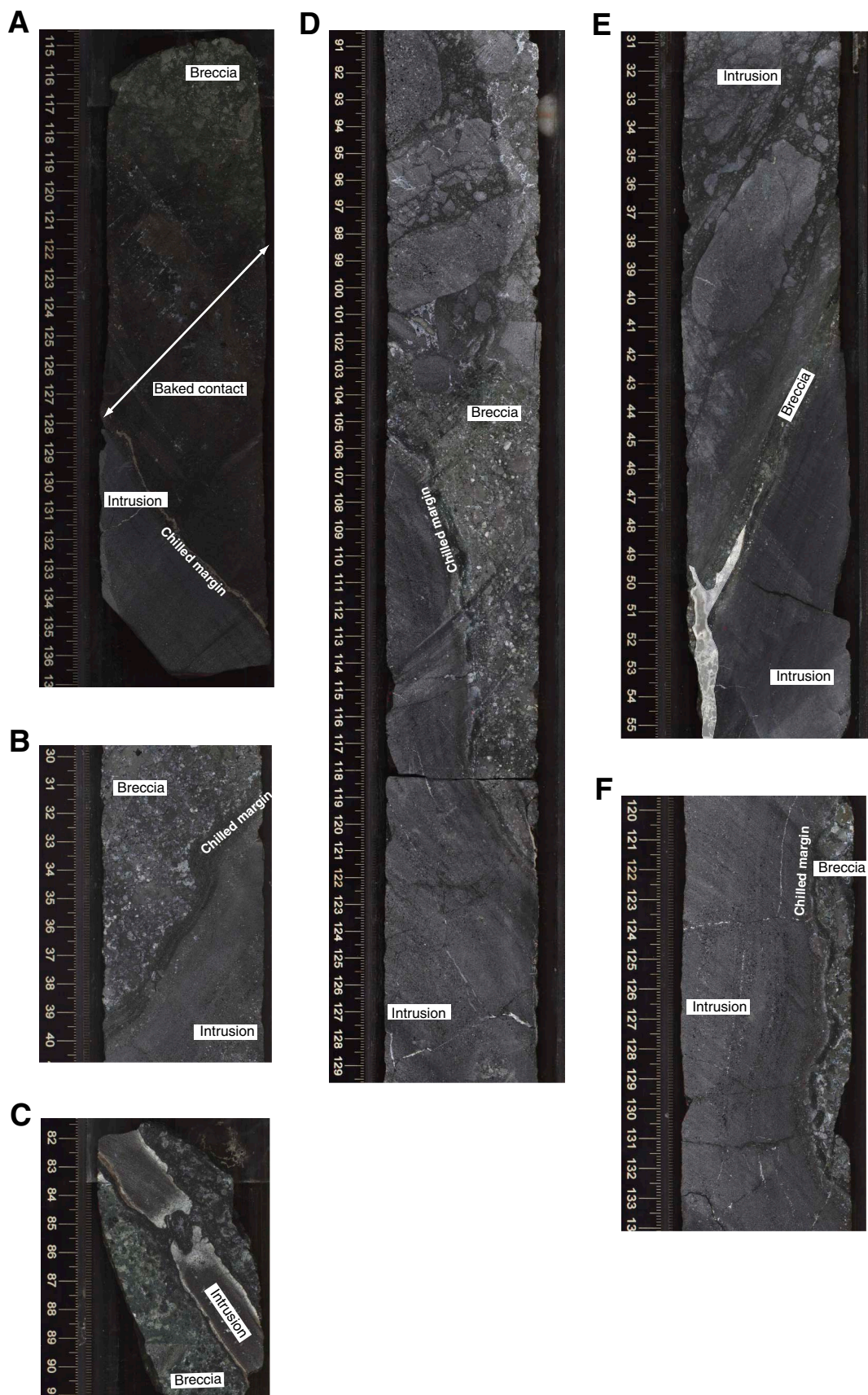


Figure F55. Interpreted overlays of representative core photographs of contacts between sheet intrusions and country rocks. Intrusions = light gray, chilled margins = dark gray, breccia country rock = light green, baked contact = dark green. Dashed lines indicate traces of vesicle bands. Raw images with labels are shown in Figure [F54](#). **A.** Moderately dipping upper contact with baked margin (interval 330-U1374A-55R-1A, 114.5–137 cm). **B.** Moderately dipping contact with much thinner baked margin (interval 58R-3A, 30–40.7 cm). **C.** Smallest intrusion recovered (interval 55R-4A, 81.3–91.2 cm). **D.** Curved intrusive margin into volcanic breccia (interval 60R-1A, 90.4–129.6 cm). **E.** Contact between younger massive intrusion (lower right) with older fragmented intrusion (upper left) (interval 68R-5A, 30.6–55.5 cm). **F.** Near-vertical intrusion margin and vesicle bands (interval 59R-1A, 119.5–134.1 cm). (Figure shown on next page.)

Figure F55 (continued). (Caption shown on previous page.)

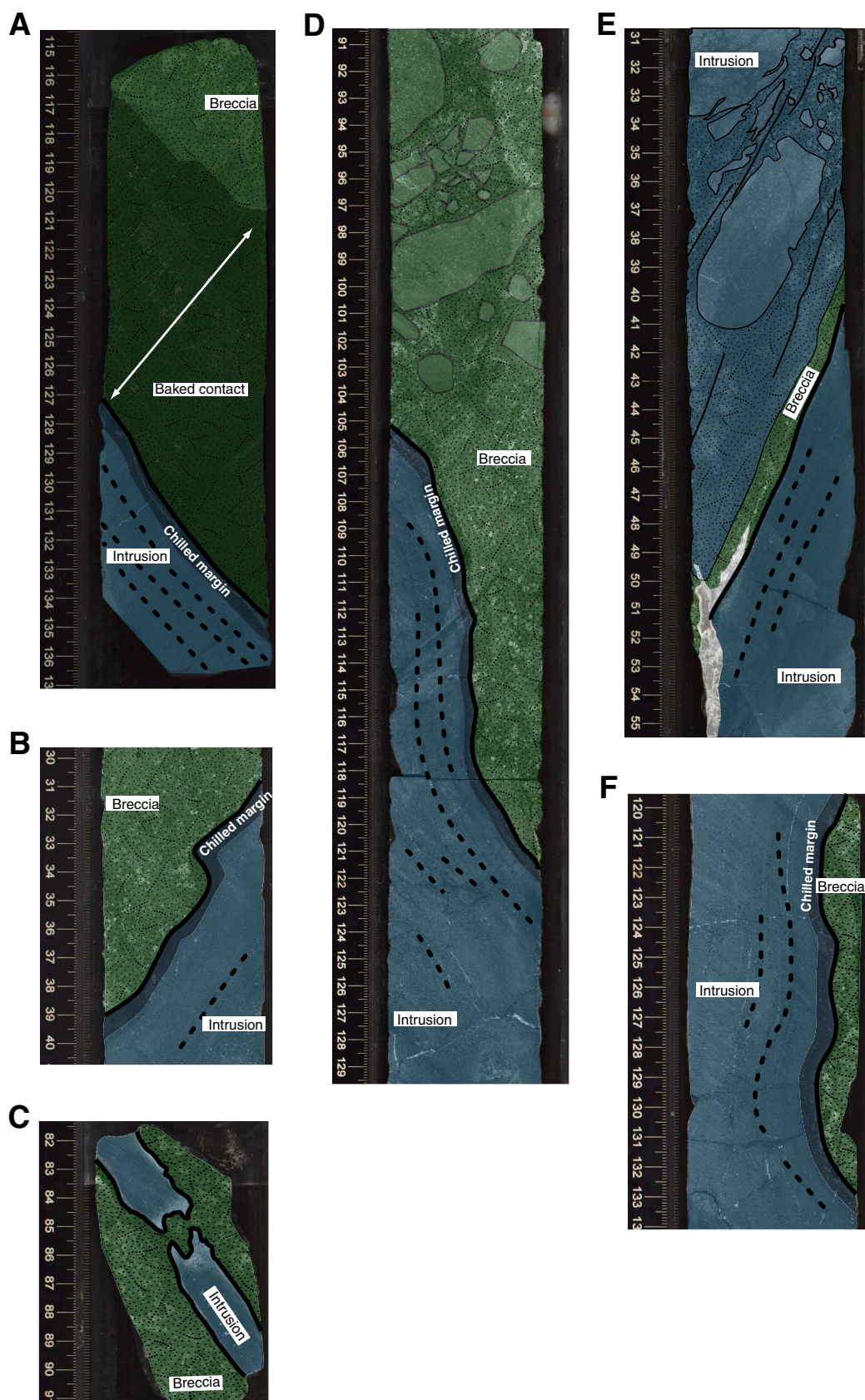


Figure F56. Rose diagrams showing dip angles of structures in Hole U1374A relative to core reference frame. **A.** Veins are dominantly steeply dipping, with a maximum at $\sim 65^\circ$, although numerous veins have shallower dips of 10° – 25° . **B.** Fractures have a broad range of dips, with maxima at $\sim 90^\circ$, 65° , and 10° – 30° . **C.** Fifteen structural measurements of magmatic contacts from the edges of intrusive sheets indicate that most of these intrusions have moderate to steep dips (25° – 70°), with few subvertical dips and no subhorizontal dips. **D.** Vesicle bands within these intrusive sheets are steeply dipping, with maxima at $\sim 75^\circ$ and 90° , indicating that magma flow through these sheets was steep to vertical. **E.** Most magmatic foliations at Site U1374 were measured on lava flows, which have subhorizontal (0° – 15°) dips. Only a limited number of sheet intrusions have magmatic foliation textures in hand samples (most have vesicle bands), resulting in relatively few instances of steep magmatic foliations in the rose diagram.

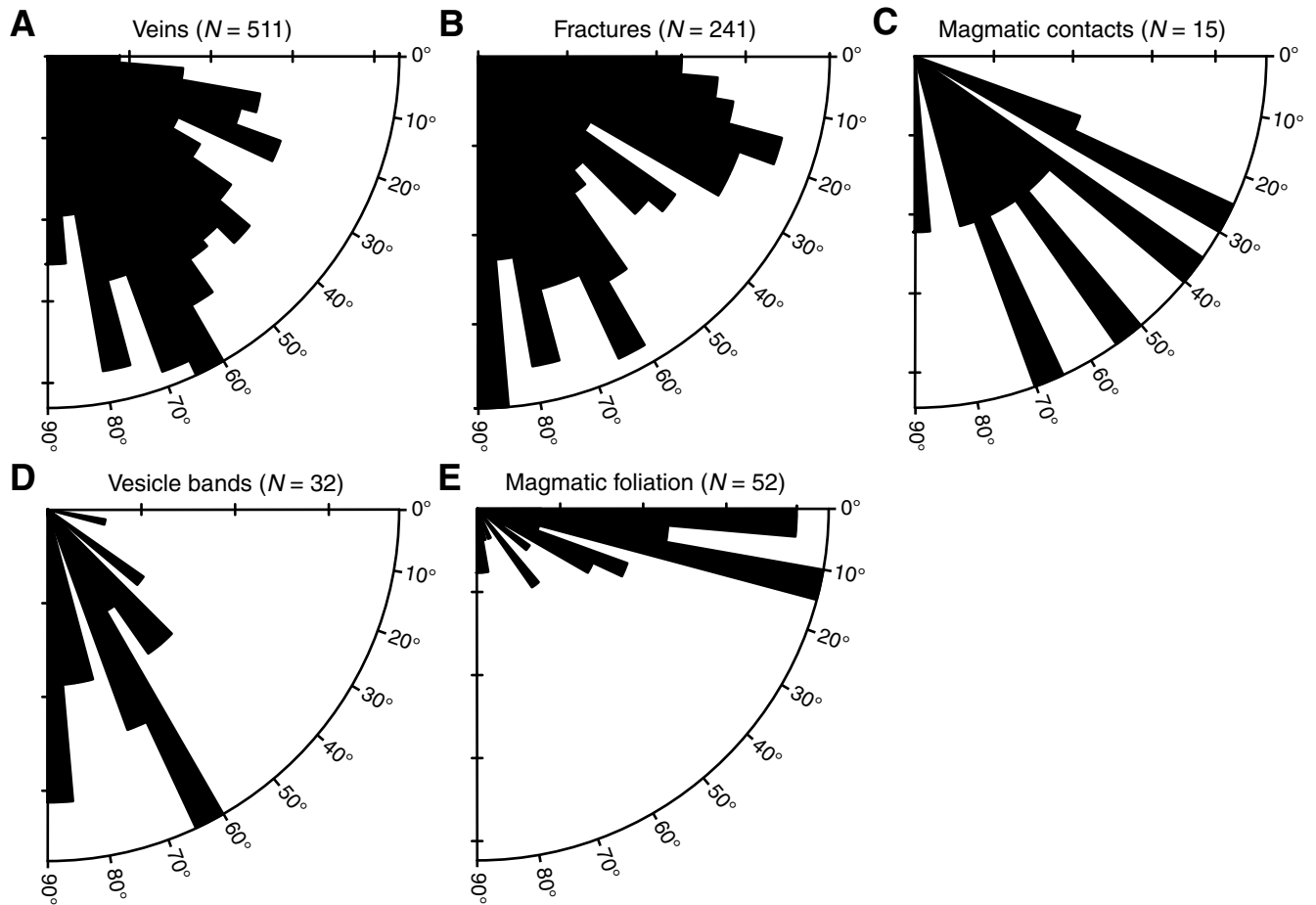




Figure F57. Distribution of fractures, Hole U1374A. Fractures are most common in the rheologically hard lava flows and intrusive sheets but are scarce to nonexistent in the breccia. For explanation of lithology patterns, see Figure F18.

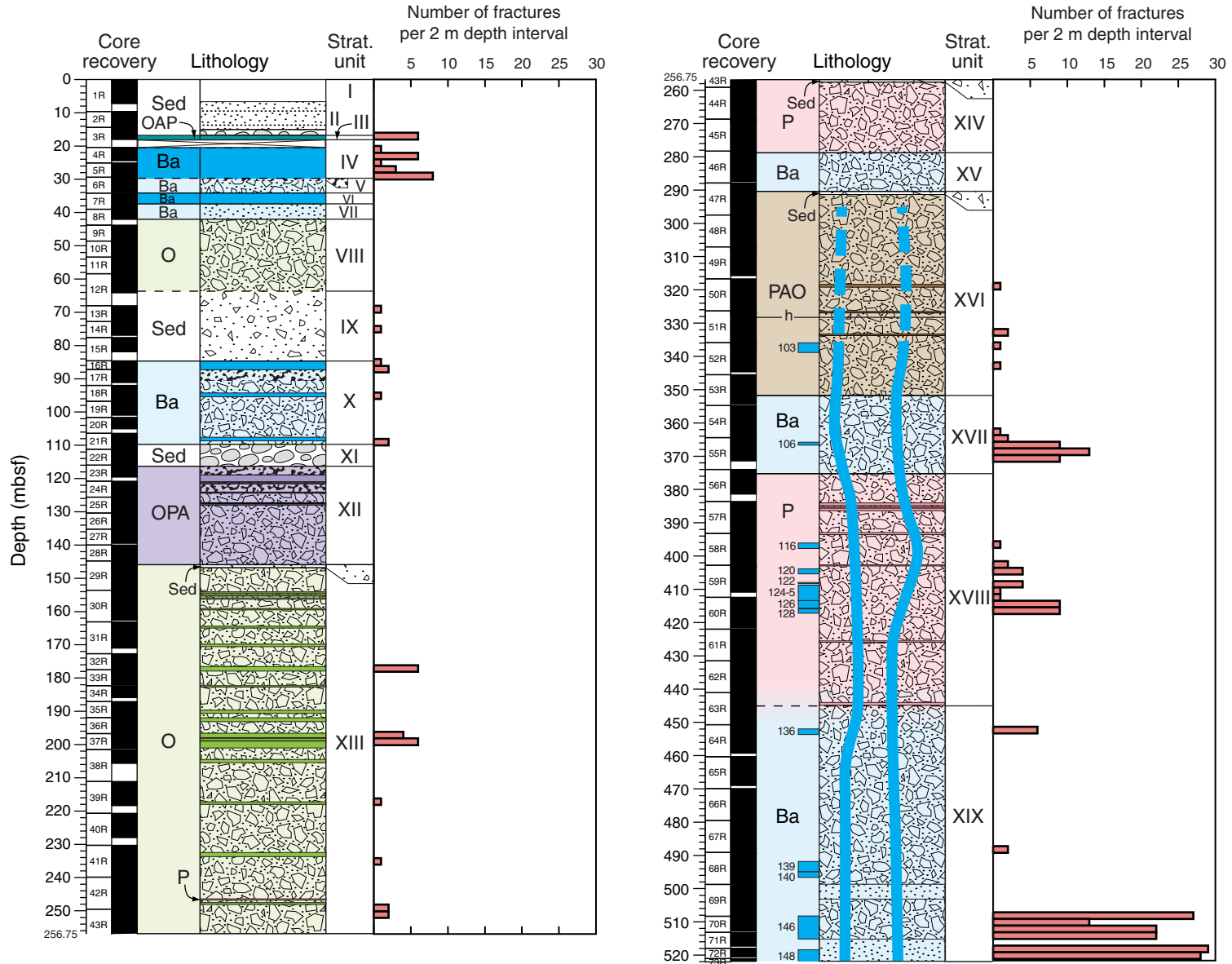


Figure F58. A–D. Thin section photomicrographs of flow alignment textures from an olivine-phyric lava flow from Unit XIII (Sample 330-U1374A-36R-4W, 76–78 cm; Thin Section 182). All photomicrographs are oriented with the black arrow pointing upward toward the top of the core. The flow texture (red arrow) is defined by a strong alignment of plagioclase laths, which are particularly apparent in (A) plane-polarized light and (B) with crossed polars. The reflected light images at (C) moderate and (D) high magnifications reveal two styles of titanomagnetite crystal growth: larger crystals that are euhedral–subhedral but randomly oriented and smaller crystals, often with aligned skeletal textures, particularly between plagioclase laths.

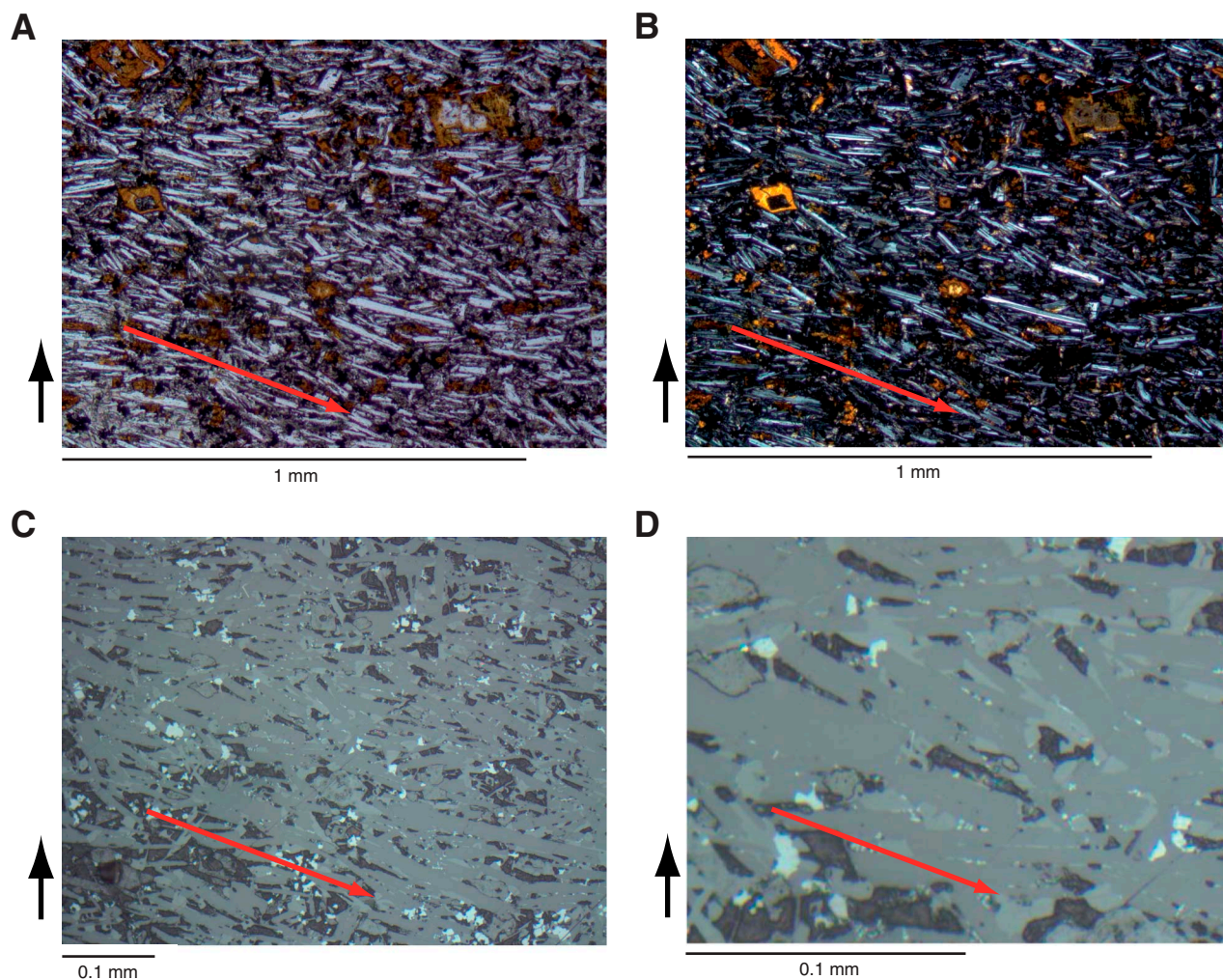




Figure F59. Distribution of veins and vein networks, Hole U1374A. Veins are dominantly hosted in rheologically hard lava flows and intrusive sheets, although several veins are also present within breccia units (especially within clasts). For explanation of lithology symbols, see Figure F18.

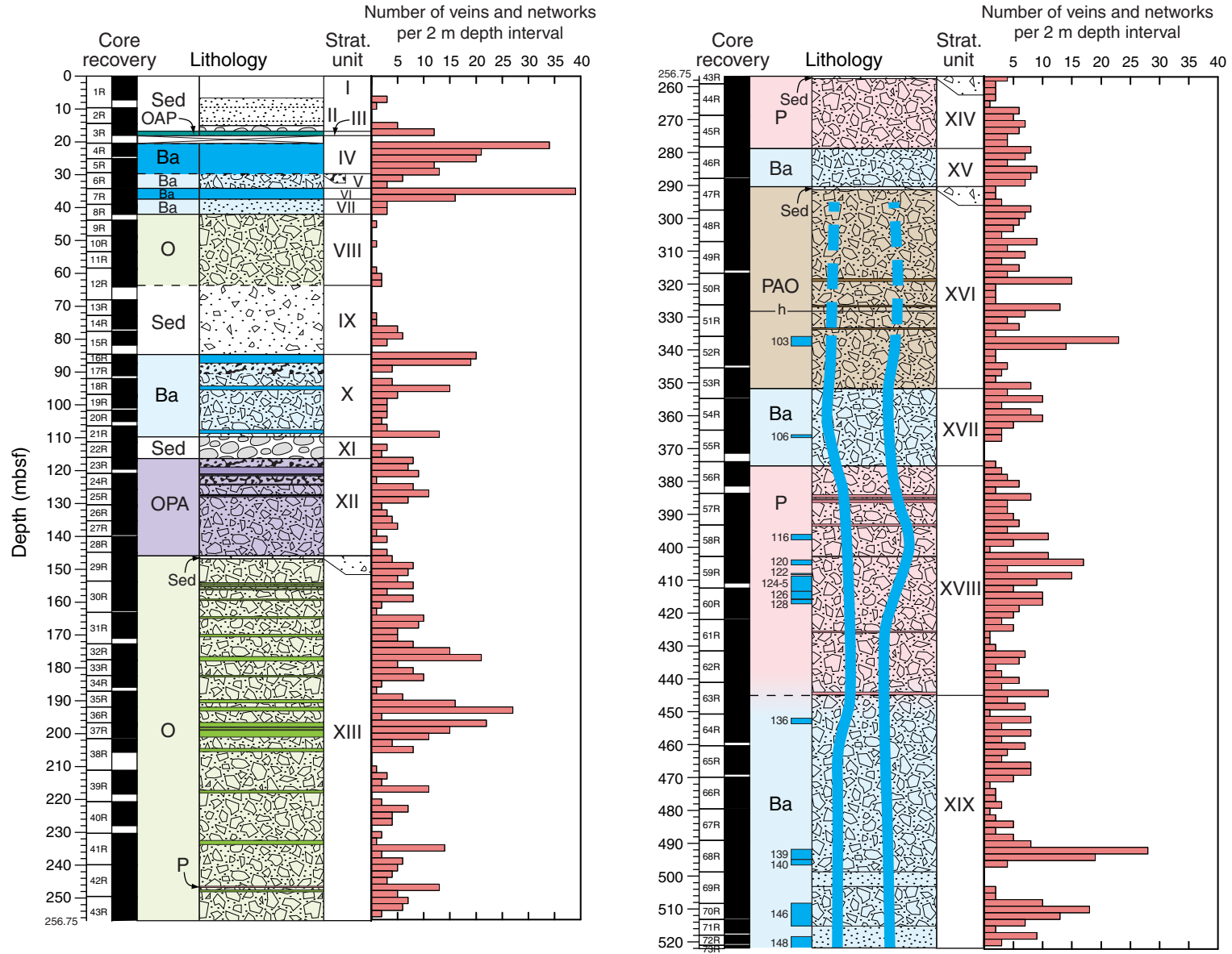


Figure F60. Representative core photographs of veins. **A.** Veins within a rheologically hard lava flow of aphyric basalt in Unit IV (interval 330-U1374A-5R-3A, 86.5–97.5 cm). A thicker vein runs nearly vertical, with several smaller subhorizontal offshoots or conjugate veins. The subhorizontal magmatic foliation of this lava (Table T10) asserts some control on conjugate vein orientation. **B.** Fragment of aphyric lava within Unit X (interval 17R-2A, 21.5–35 cm). This piece has lobate margins, a quenched rim, and a vesicular core, suggesting it may be a small pillow. Several irregular veins radiate away from the vesicular core. Note how the veins are restricted to the rheologically harder lava and do not extend into the surrounding matrix, where fluid flow would have been easier and more diffuse. **C.** One of the rare examples of a vein crosscutting the breccia matrix (interval 62R-2A, 92.5–109.5 cm). This steeply dipping vein is located close to one of the sheet intrusions, which may have enhanced fluid flow in the vicinity. (Figure shown on next page.)

Figure F60 (continued). (Caption shown on previous page.)

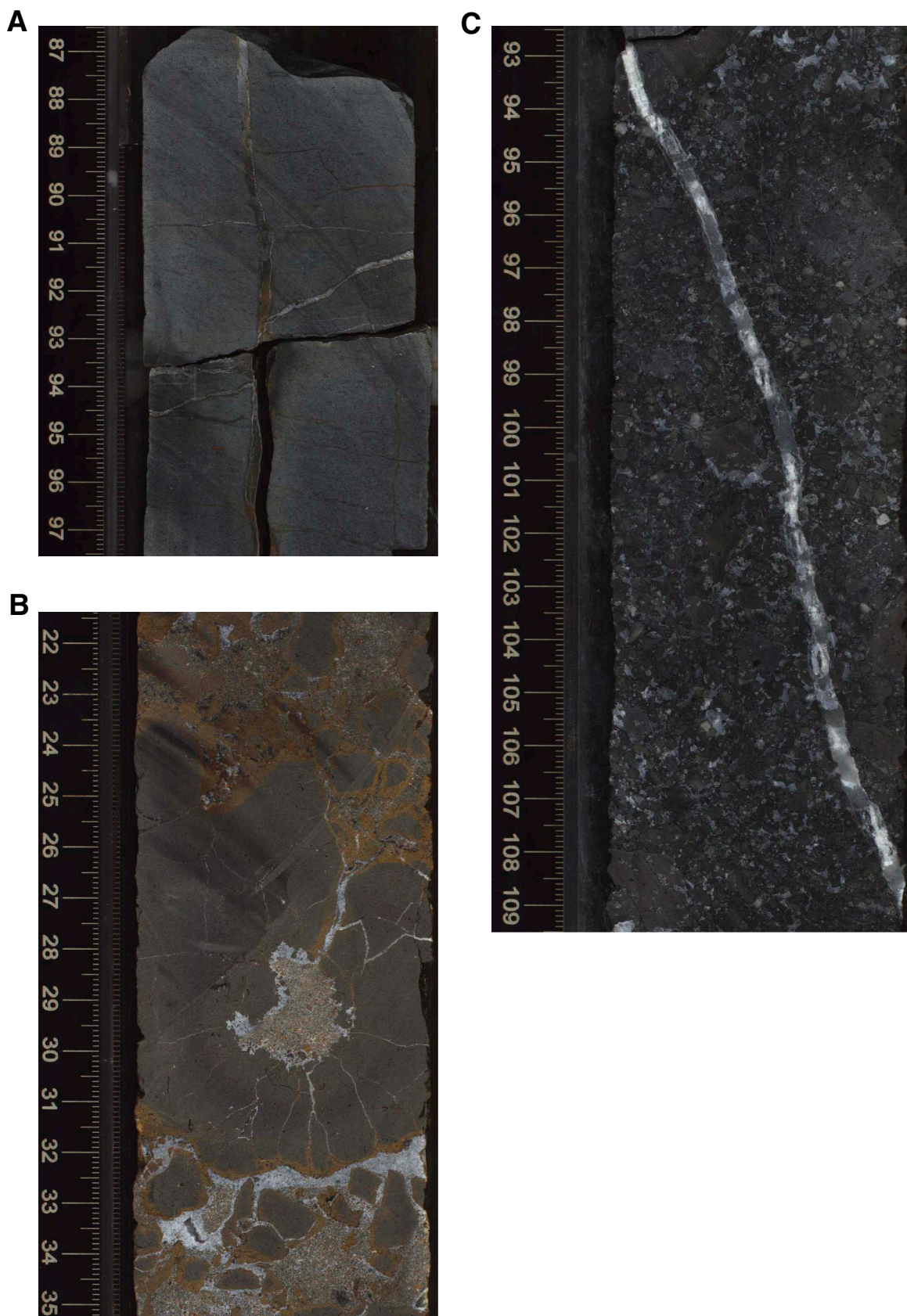


Figure F61. Total alkalis vs. silica for Sites U1372–U1374, with Le Maitre et al.'s (1989) classification of volcanic rock types. The dashed line divides data for tholeiitic and alkalic rocks of Hawaii (Macdonald and Katsura, 1964; Macdonald, 1968). Expedition 330 data are normalized to 100 wt% totals. Shown for comparison are data for dredge samples from the length of the Louisville Seamount Trail (only data for dredge samples with LOI < 6 wt% are included; data of Hawkins et al., 1987; Vanderkluyesen et al., 2007; Beier et al., 2011). Also shown are fields for the southern East Pacific Rise (EPR; data of Sinton et al., 1991; Bach et al., 1994; Mahoney et al., 1994) and Ontong Java Plateau (OJP; data of Tejada et al., 1996, 2002; Fitton and Godard, 2004).

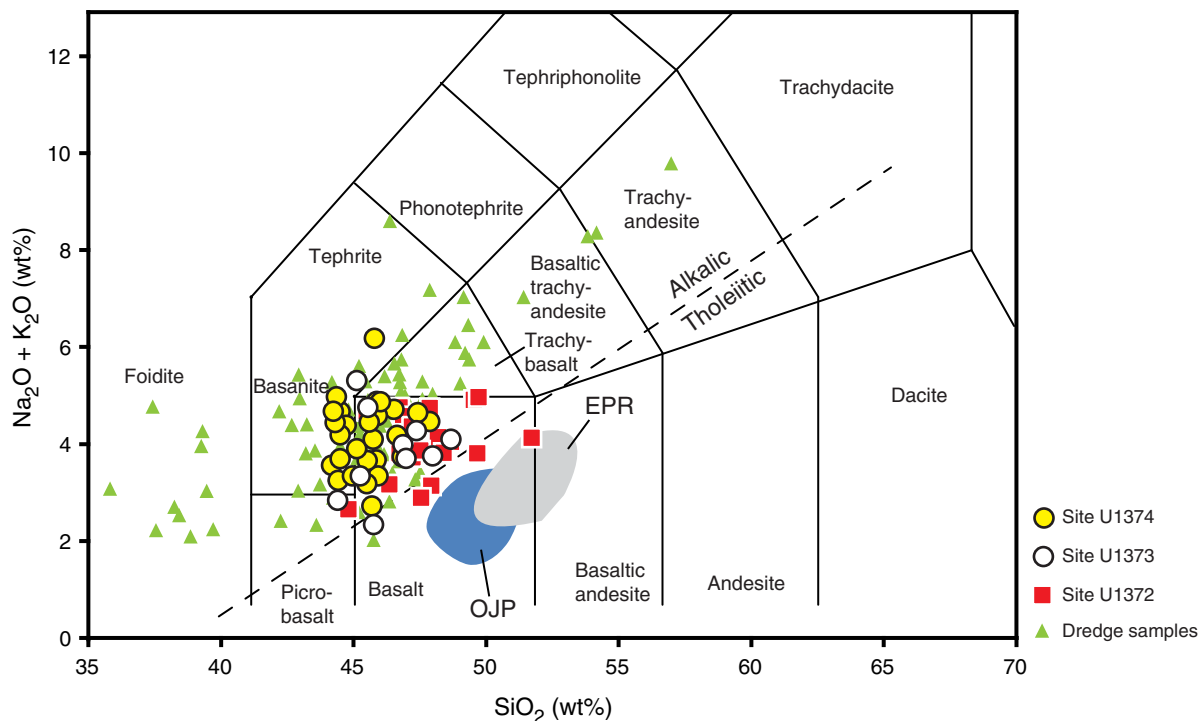


Figure F62. MgO vs. (A) Al_2O_3 , (B) $\text{CaO}/\text{Al}_2\text{O}_3$, and (C) $\text{Fe}_2\text{O}_3^{\text{T}}$ for Sites U1372–U1374. Expedition 330 data are normalized to 100 wt% totals. Data for dredge samples include only samples with LOI < 6 wt% (data of Hawkins et al., 1987; Vanderkluyssen et al., 2007; Beier et al., 2011). Fields for several Hawaiian volcanoes are shown. “Hawaii shield” fields are for Mauna Kea (blue line), Mauna Loa (green line), and Kilauea (red line) (data of Lipman et al., 1990; Frey et al., 1991; Moore and Clague, 1992; Clague et al., 1995; Rhodes and Hart, 1995; Garcia et al., 2003). “Hawaii postshield” fields include Lapahoehoe and Hamakua lavas (data of Frey et al., 1990; West et al., 1988). Also shown are fields for the southern East Pacific Rise (EPR; data of Sinton et al., 1991; Bach et al., 1994; Mahoney et al., 1994) and Ontong Java Plateau (OJP; data of Tejada et al., 1996, 2002; Fitton and Godard, 2004).

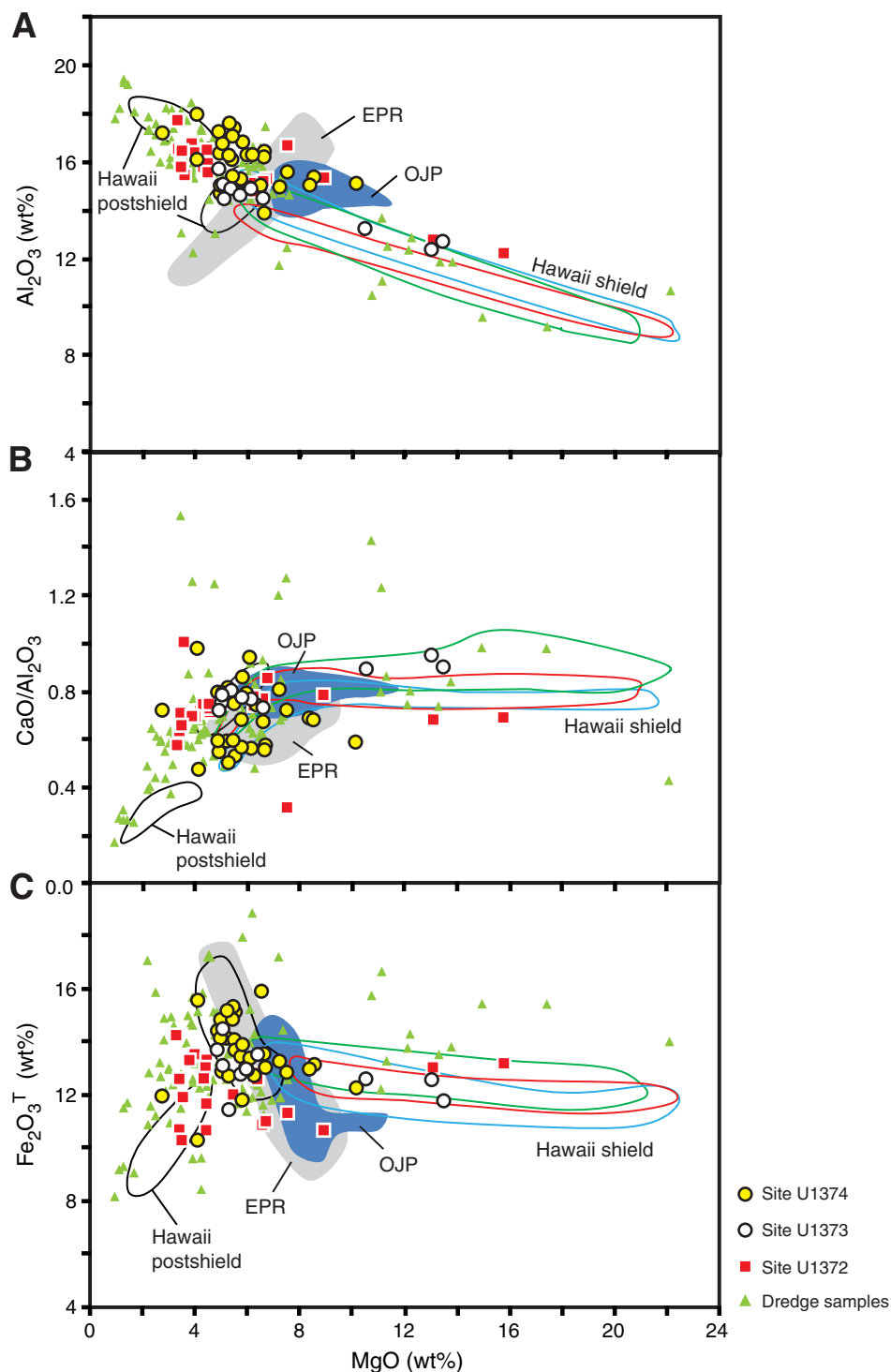




Figure F63. TiO_2 vs. (A) Ba, (B) Sr, (C) P_2O_5 , and (D) Y for Sites U1372–U1374. Note that major element data for Expedition 330 are normalized to 100 wt% totals. Data for dredge samples from the Louisville Seamount Trail include only samples with LOI < 6 wt% (data of Hawkins et al., 1987; Vanderkluyssen et al., 2007; Beier et al., 2011). Fields for several Hawaiian volcanoes are shown (“Hawaii shield” fields are for Mauna Kea [blue outline], Mauna Loa [green outline], and Kilauea [red outline]; data of Lipman et al., 1990; Frey et al., 1991; Moore and Clague, 1992; Clague et al., 1995; Rhodes and Hart, 1995; Garcia et al., 2003; “Hawaii postshield” fields include Lapahoehoe and Hamakua lavas; data of Frey et al., 1990; West et al., 1988), along with fields for the southern East Pacific Rise (EPR; data of Sinton et al., 1991; Bach et al., 1994; Mahoney et al., 1994), and Ontong Java Plateau (OJP; data of Tejada et al., 1996, 2002; Fitton and Godard, 2004).

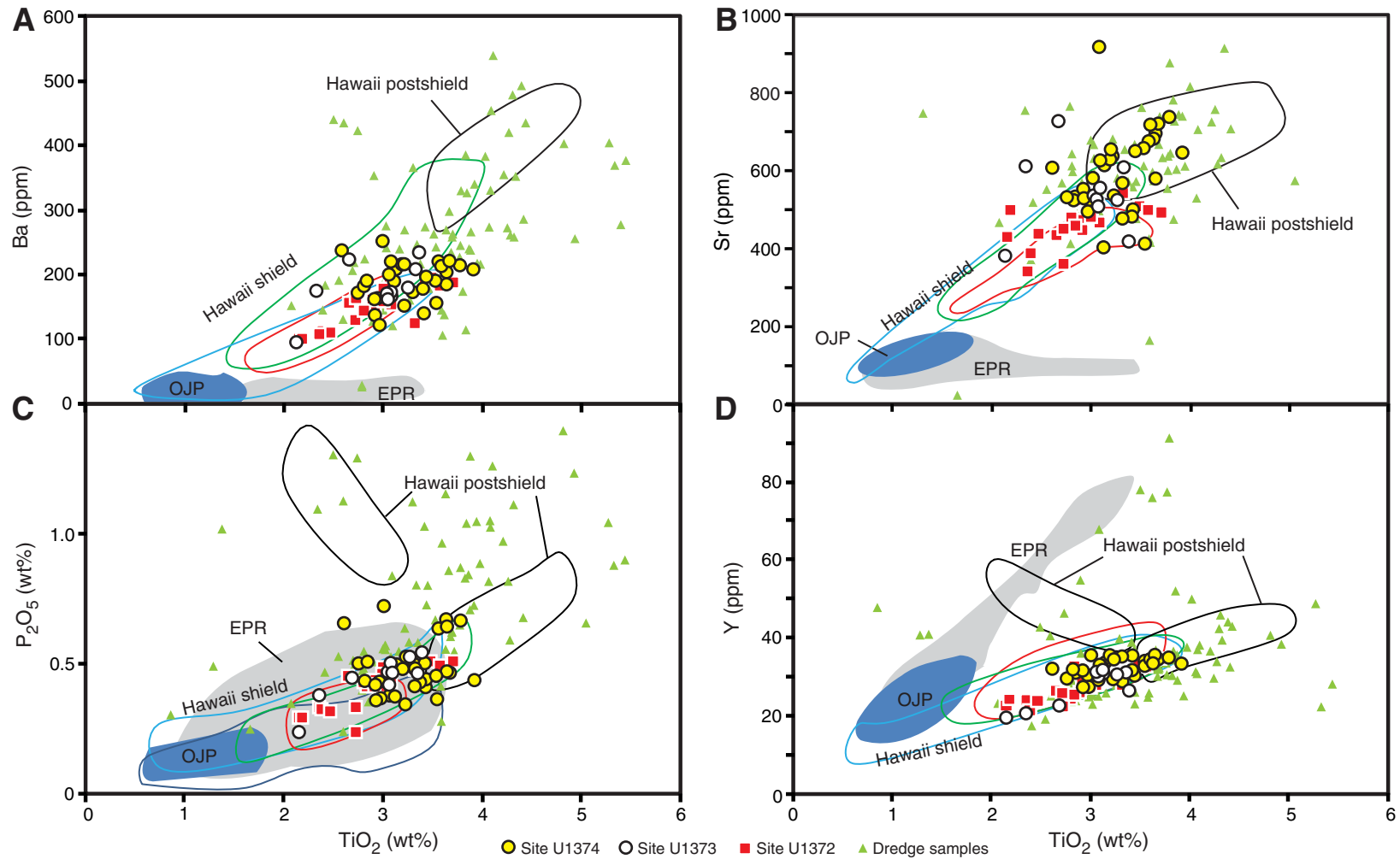


Figure F64. Downhole variation of (A) Mg#, (B) Ni, (C) TiO₂, (D) Ba/Y, and (E) Zr/Ti for Site U1374 igneous rocks. Yellow circles = lava flows, lobes, and clasts; blue circles = intrusive sheets. Note that the lithologic unit represented by the bottommost sample of Unit XIX could be a lava flow or an intrusive sheet (see “[Igneous petrology and volcanology](#)”). Dashed lines mark stratigraphic unit boundaries. See Figure F18 for explanation of stratigraphic units. Major element data are normalized to 100 wt% totals.

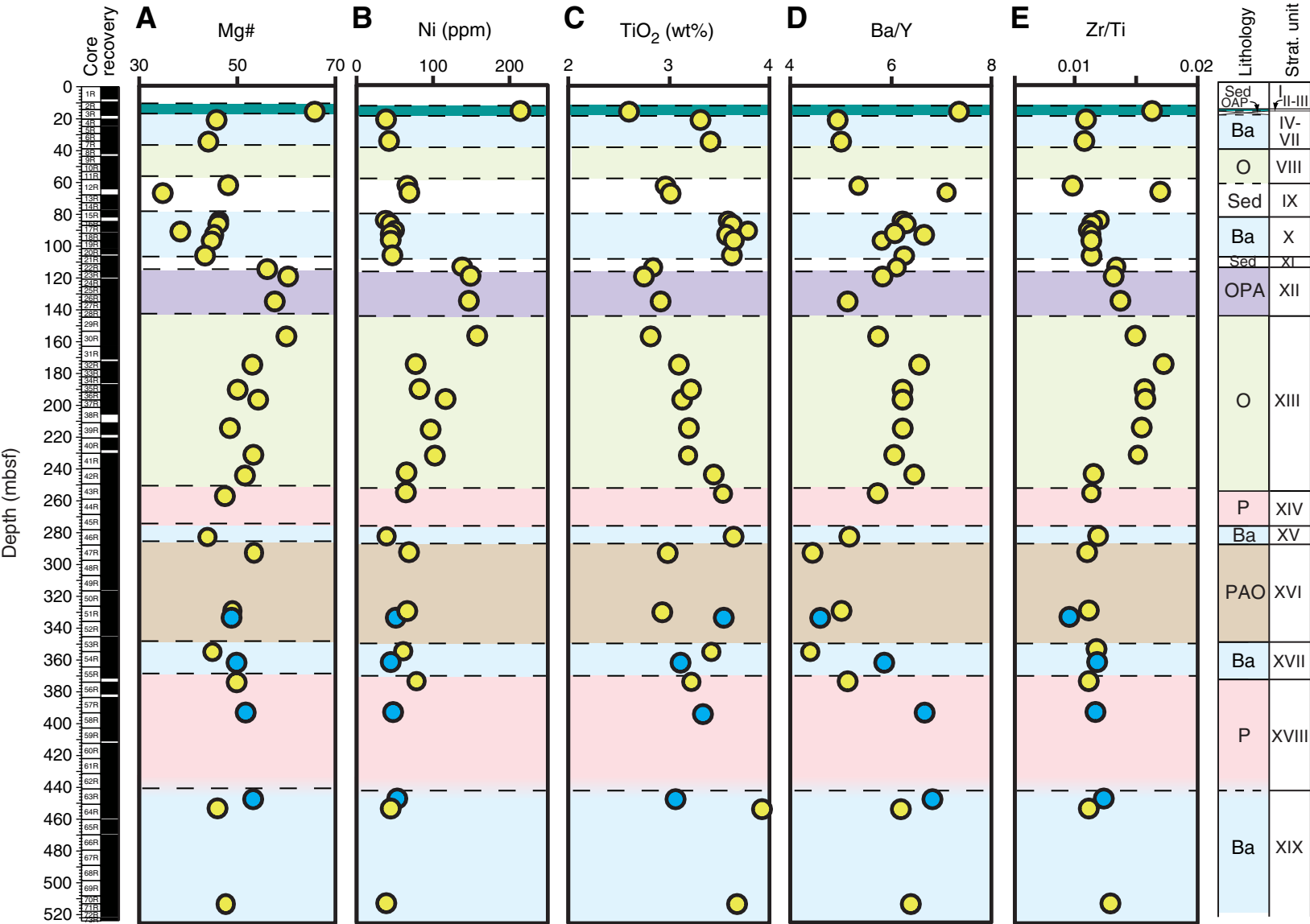


Figure F65. Depth profiles of magnetic susceptibility, Hole U1374A. Core recovery and stratigraphic columns are shown for reference. For explanation of stratigraphy, see Figure F18. A. Stratigraphic Units I–XIII (0–256.75 mbsf). (Continued on next page.)

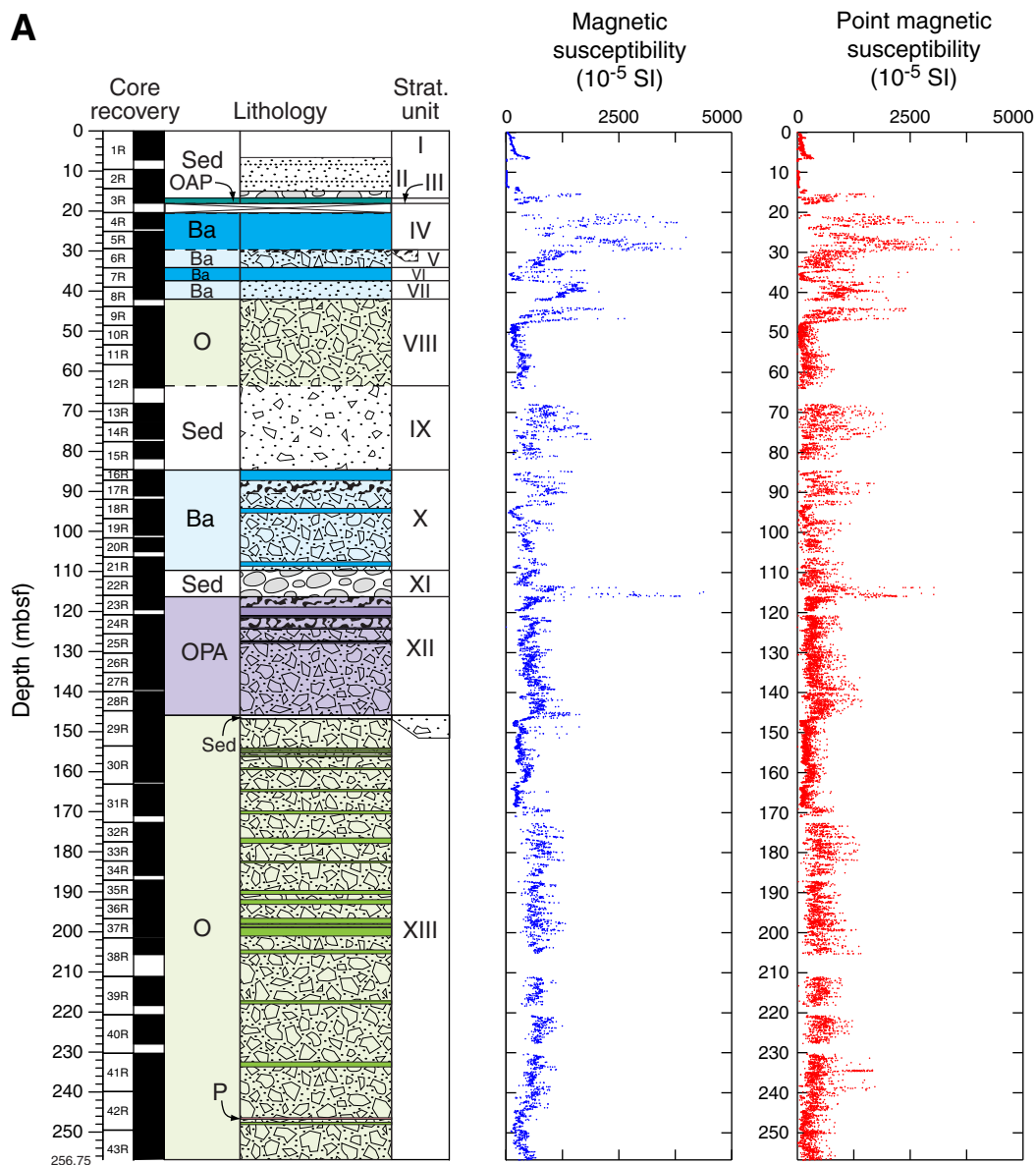


Figure F65 (continued). B. Stratigraphic Units XIV–XIX (256.75–522 mbsf).

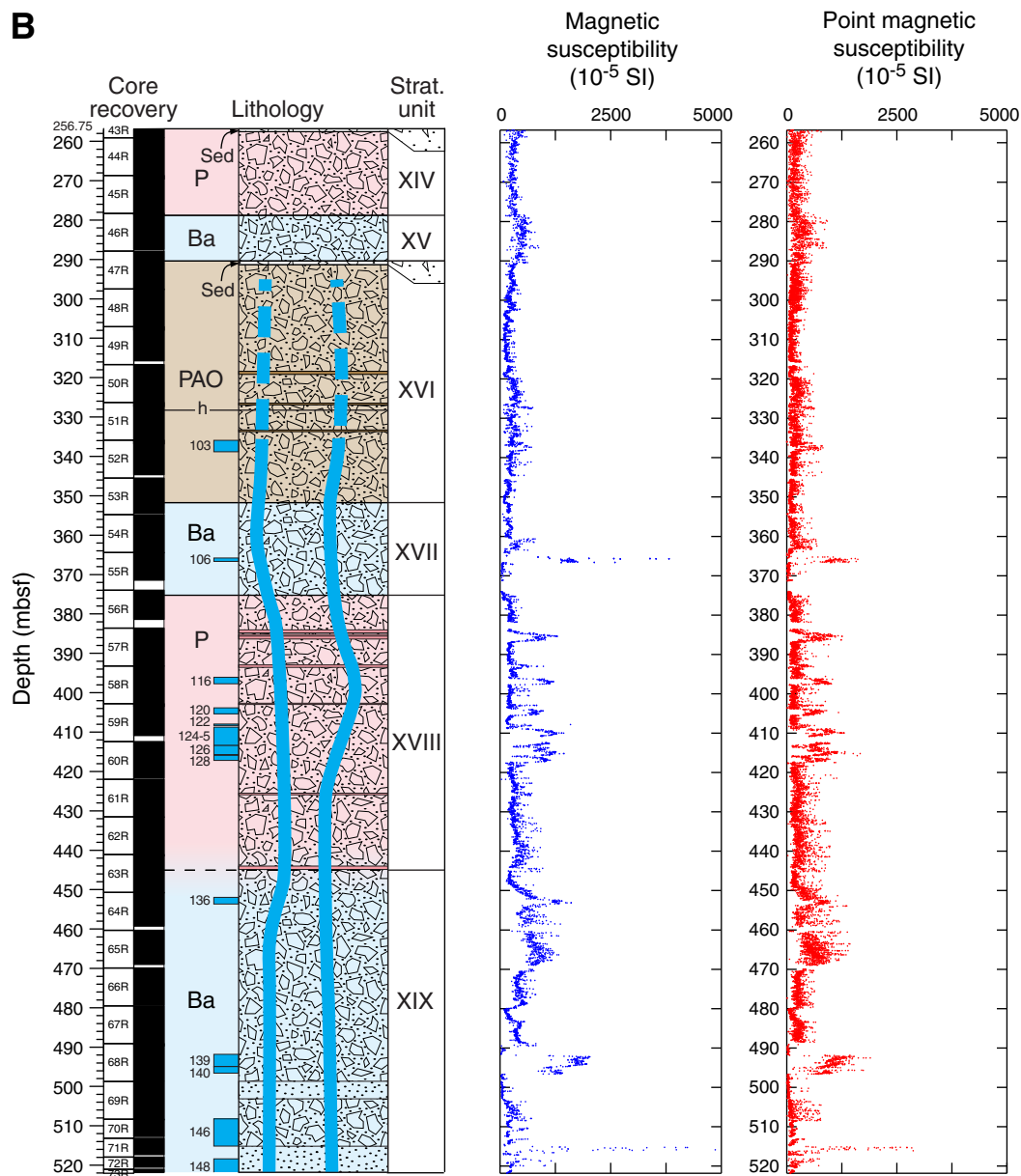


Figure F66. Depth profiles of bulk density and *P*-wave velocity for Hole U1374A, shown with corresponding stratigraphic column. Bulk density: red squares = MAD-C measurements taken on discrete samples, black dots = GRA bulk density. *P*-wave velocity: blue = *x*-axis (normal to the split-core surface), red = *y*-axis (parallel to the split-core surface), green = *z*-axis (downcore). For explanation of stratigraphy, see Figure F18. A. Stratigraphic Units I–XIII (0–256.75 mbsf). (Continued on next page.)

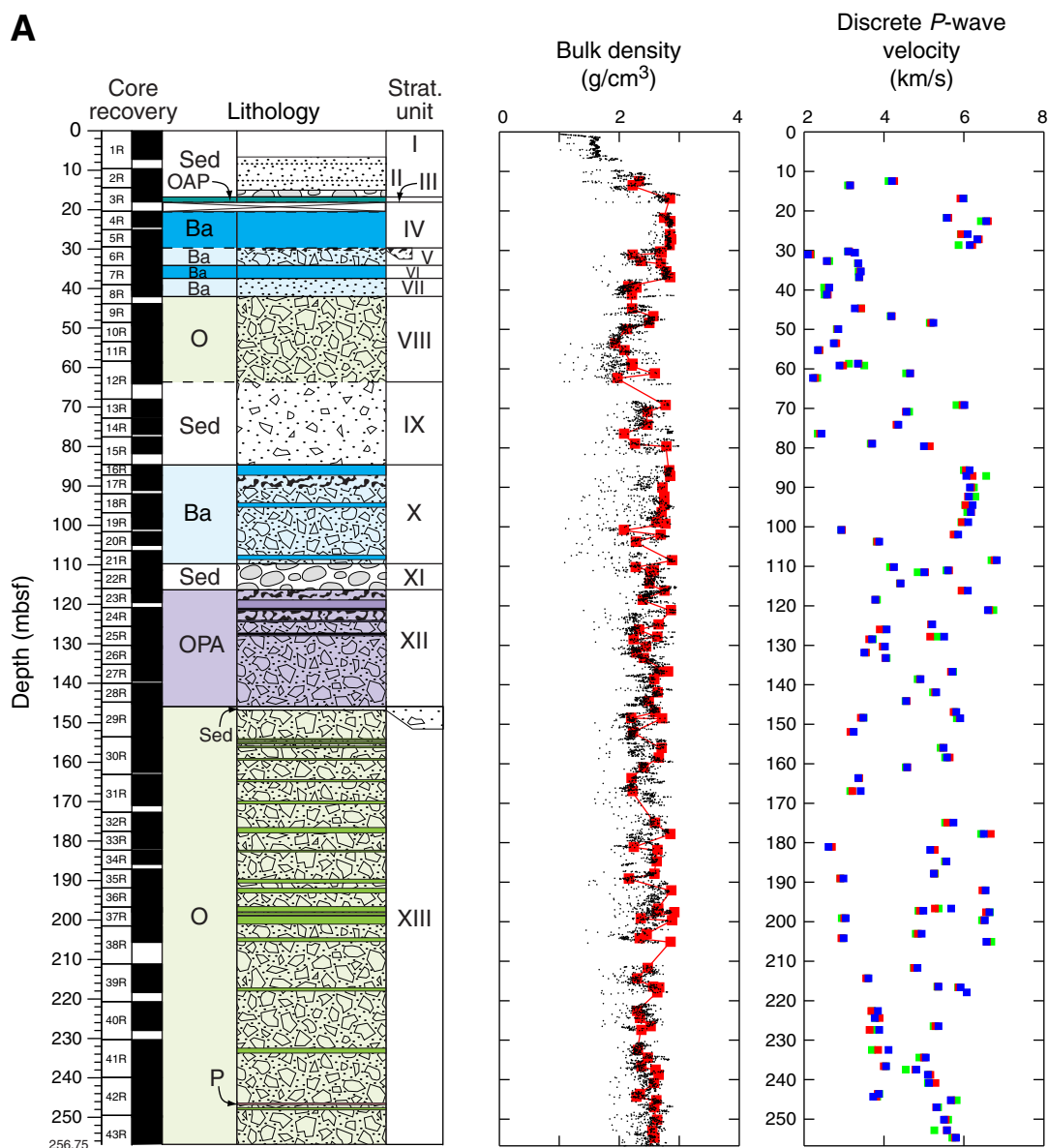


Figure F66 (continued). B. Stratigraphic Units XIV–XIX (256.75–522 mbsf).

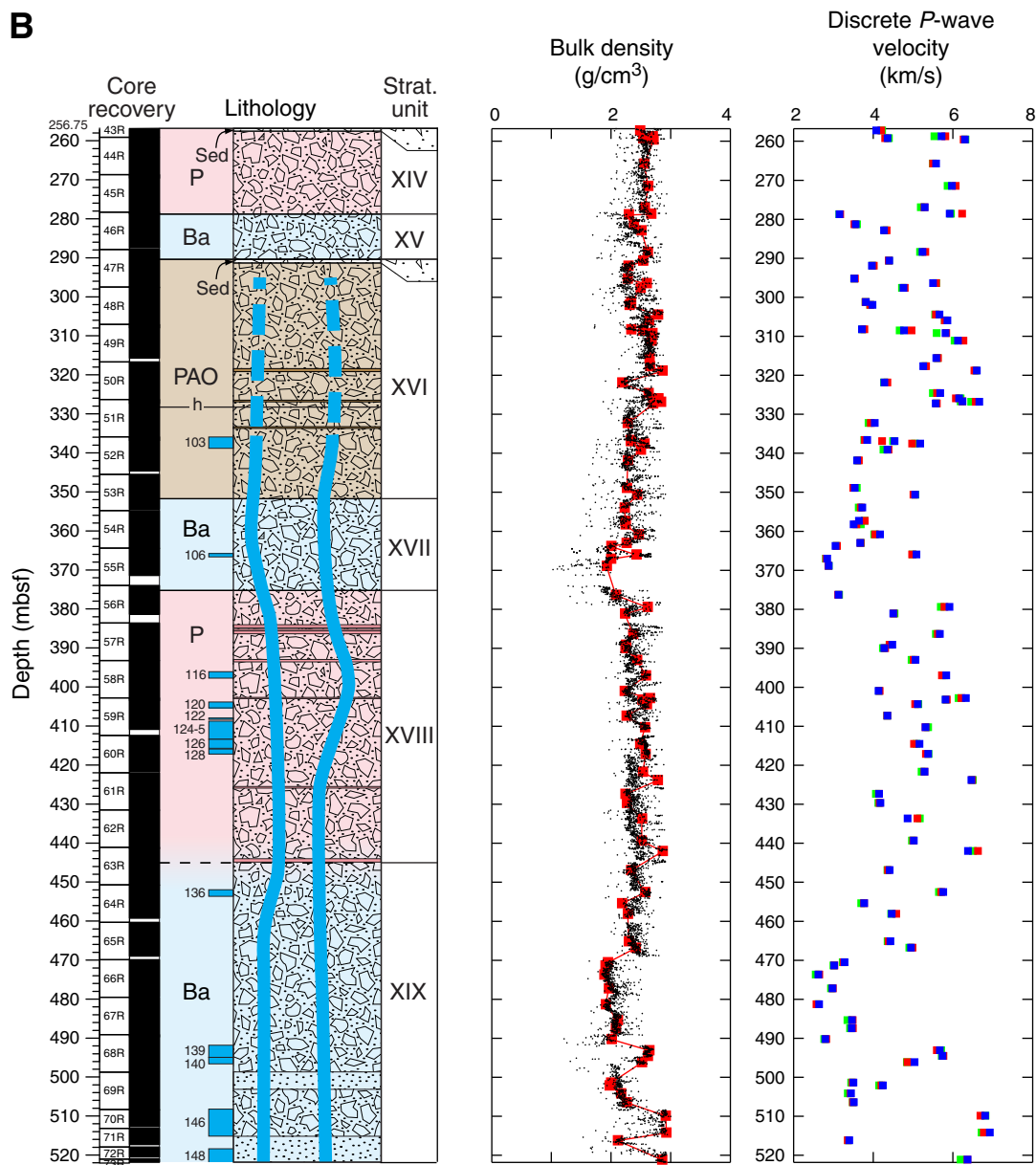




Figure F67. Depth profile of natural gamma radiation (NGR), Hole U1374A. Gray band delimits values between 13 and 21 cps. Stratigraphic column is shown for reference. For explanation of stratigraphy, see Figure F18.

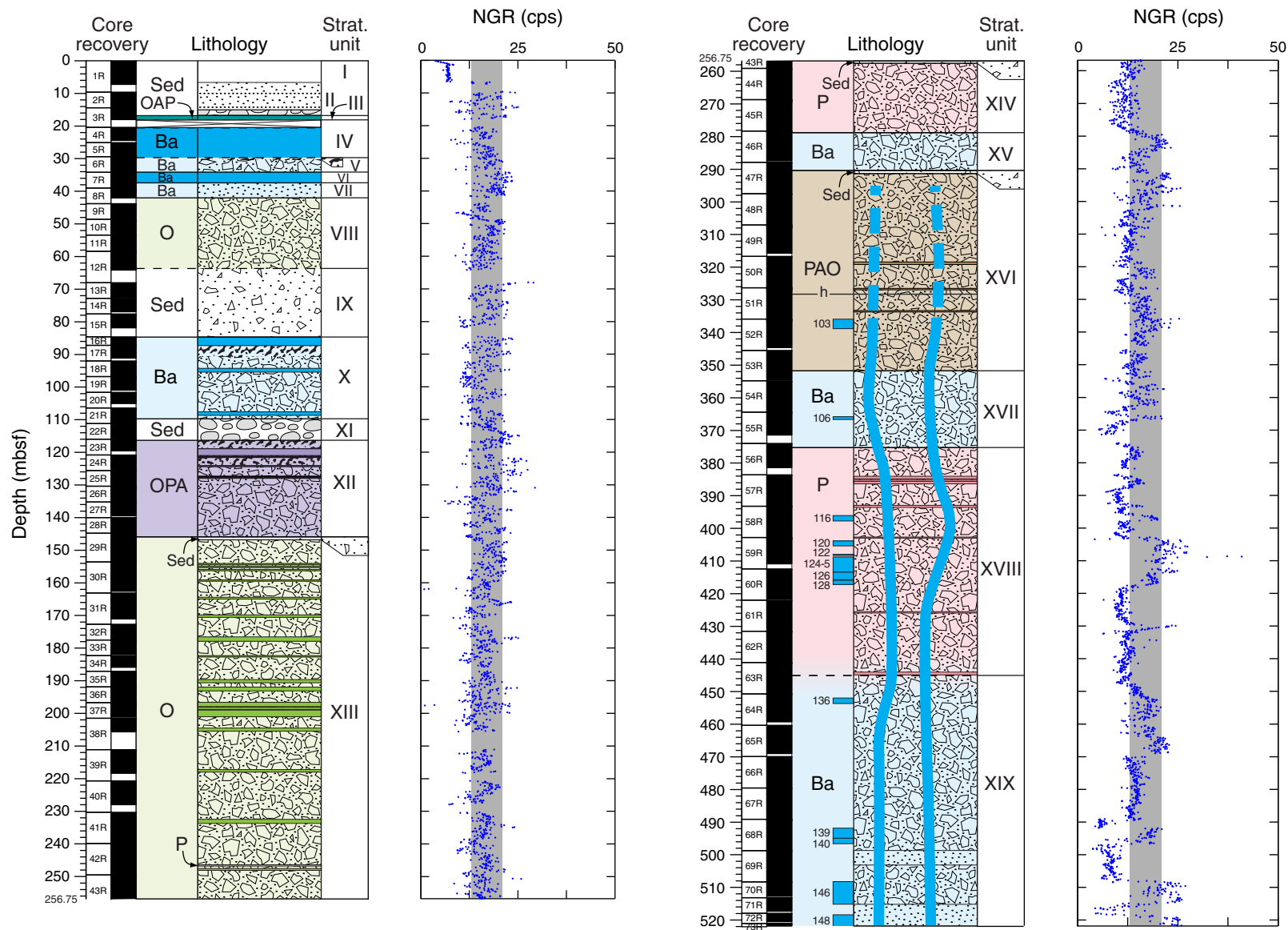


Figure F68. Plot of moisture and density Method C (MAD-C) bulk density vs. porosity of discrete samples, Hole U1374A. Results show an approximately linear negative correlation.

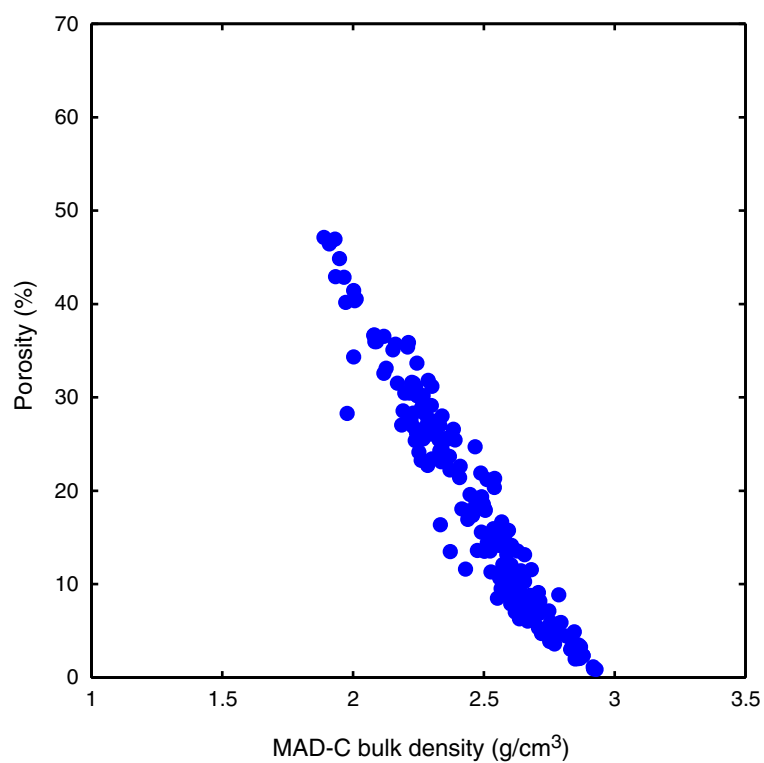


Figure F69. Plot of whole-round gamma ray attenuation (GRA) bulk density vs. moisture and density Method C (MAD-C) bulk density from discrete samples, Hole U1374A. Results show a nearly one-to-one linear relationship, with values from GRA bulk density often slightly lower than those from discrete samples. Dark red squares = outlying values.

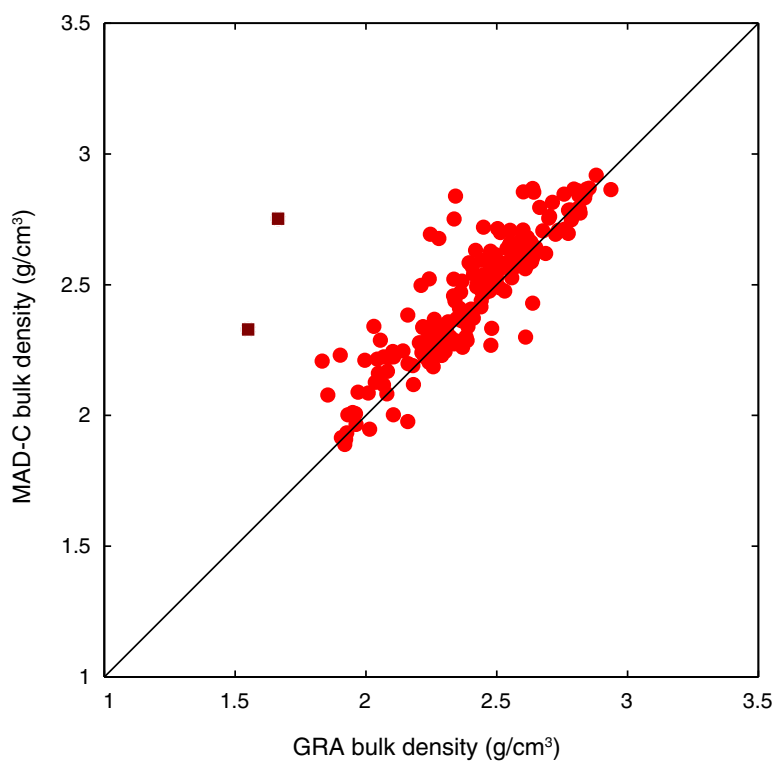




Figure F70. Depth profile of porosity from measurements on discrete samples, Hole U1374A, shown in relation to stratigraphic column. For explanation of stratigraphy, see Figure F18.

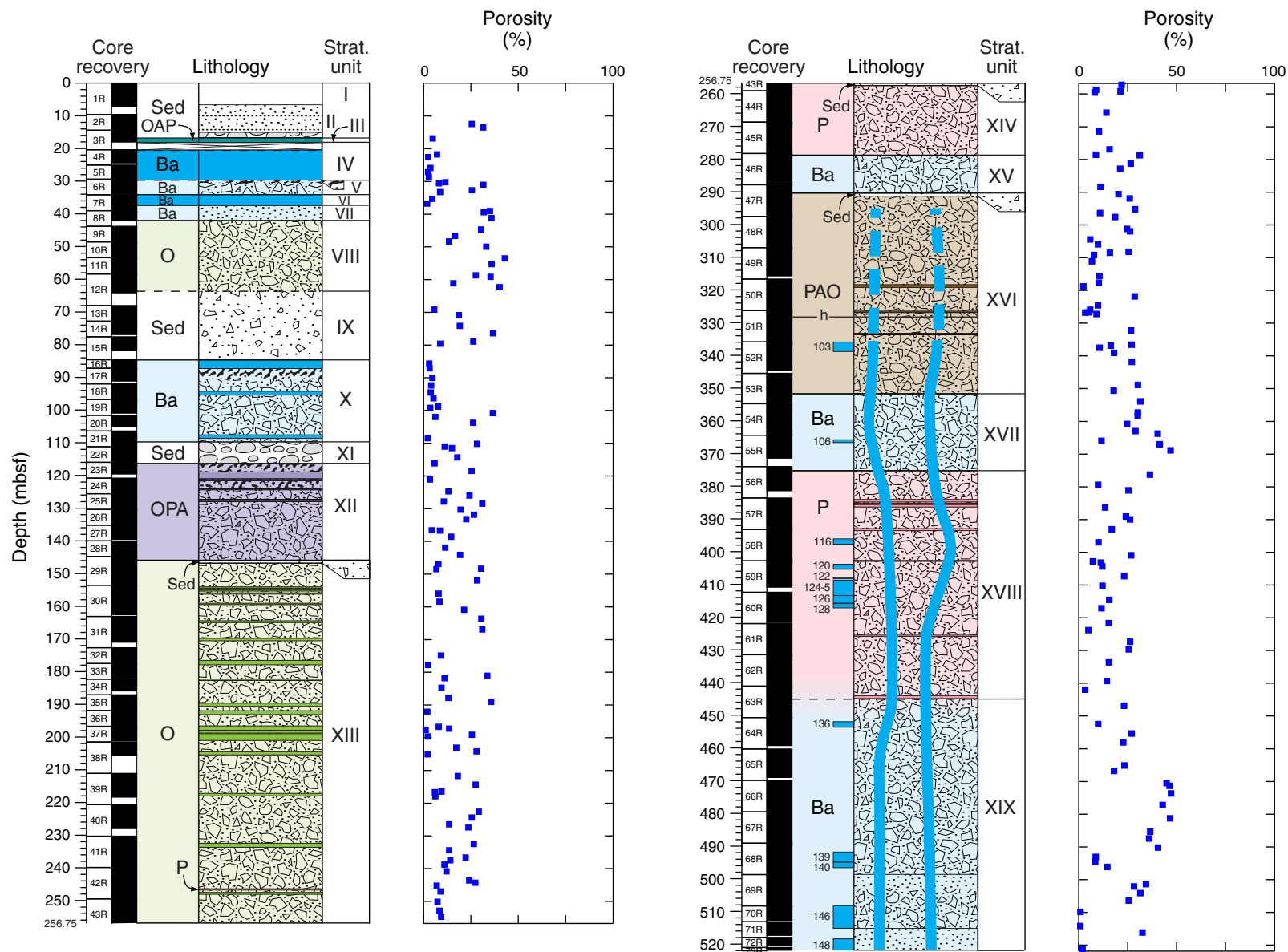


Figure F71. Plot of moisture and density Method C (MAD-C) bulk density values from discrete samples vs. discrete P -wave velocity, Hole U1374A, showing an approximately linear relationship. Squares = results from samples that were resaturated and retested because of calibration error. Colors represent different orientations for P -wave velocity measurements: blue = x -axis (normal to the split-core surface), red = y -axis (parallel to the split-core surface), green = z -axis (downcore).

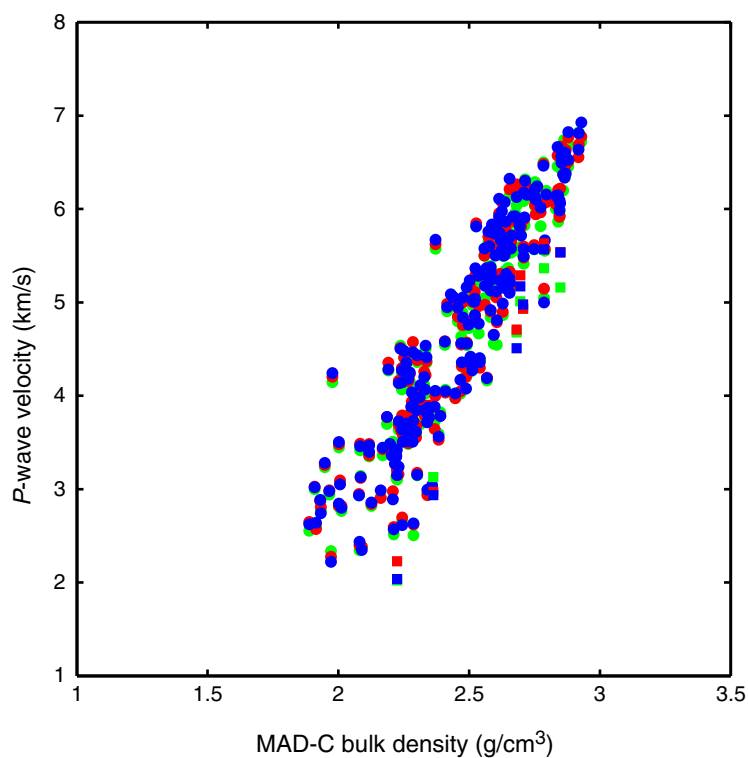


Figure F72. Plot of gamma ray attenuation (GRA) bulk density vs. thermal conductivity, Hole U1374A. Red = Hole U1374A, pink = Sites U1372 and U1373, black line = best robust linear fit to data from Sites U1372 and U1373. Squares = last two values from the damaged thermal probe in Hole U1374A; these values deviate significantly from the expected trend, demonstrating the unreliable nature of the values returned just before the thermal probe stopped working altogether.

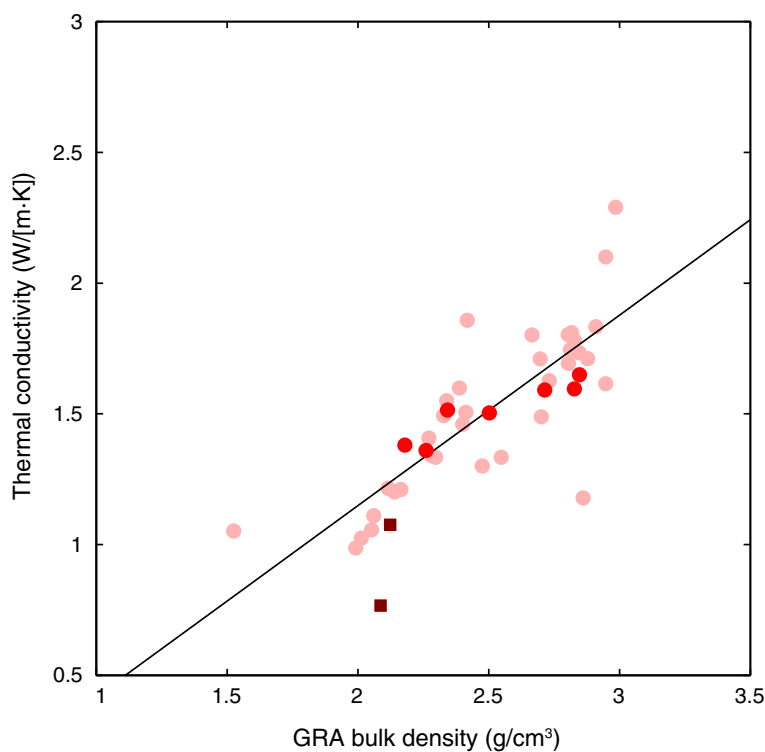


Figure F73. Downhole plots of paleomagnetic data from archive-half cores, Hole U1374A. **A.** Core recovery and observed stratigraphy (see Fig. F25 for explanation of patterns and abbreviations). **B.** Remanent intensity variations: purple = NRM intensities, black = intensities associated with principal component analysis (PCA) directions with misfits ≤ 3.42 , gray = intensities associated with PCA directions with misfits > 3.42 . **C.** WRMSL magnetic susceptibility (see “Physical properties”). **D.** Inclination: red = PCA directions with misfits ≤ 3.42 , pink = PCA directions with misfits > 3.42 . **E.** Median destructive field of the vector difference sum (MDF') for PCA directions with misfits ≤ 3.42 .

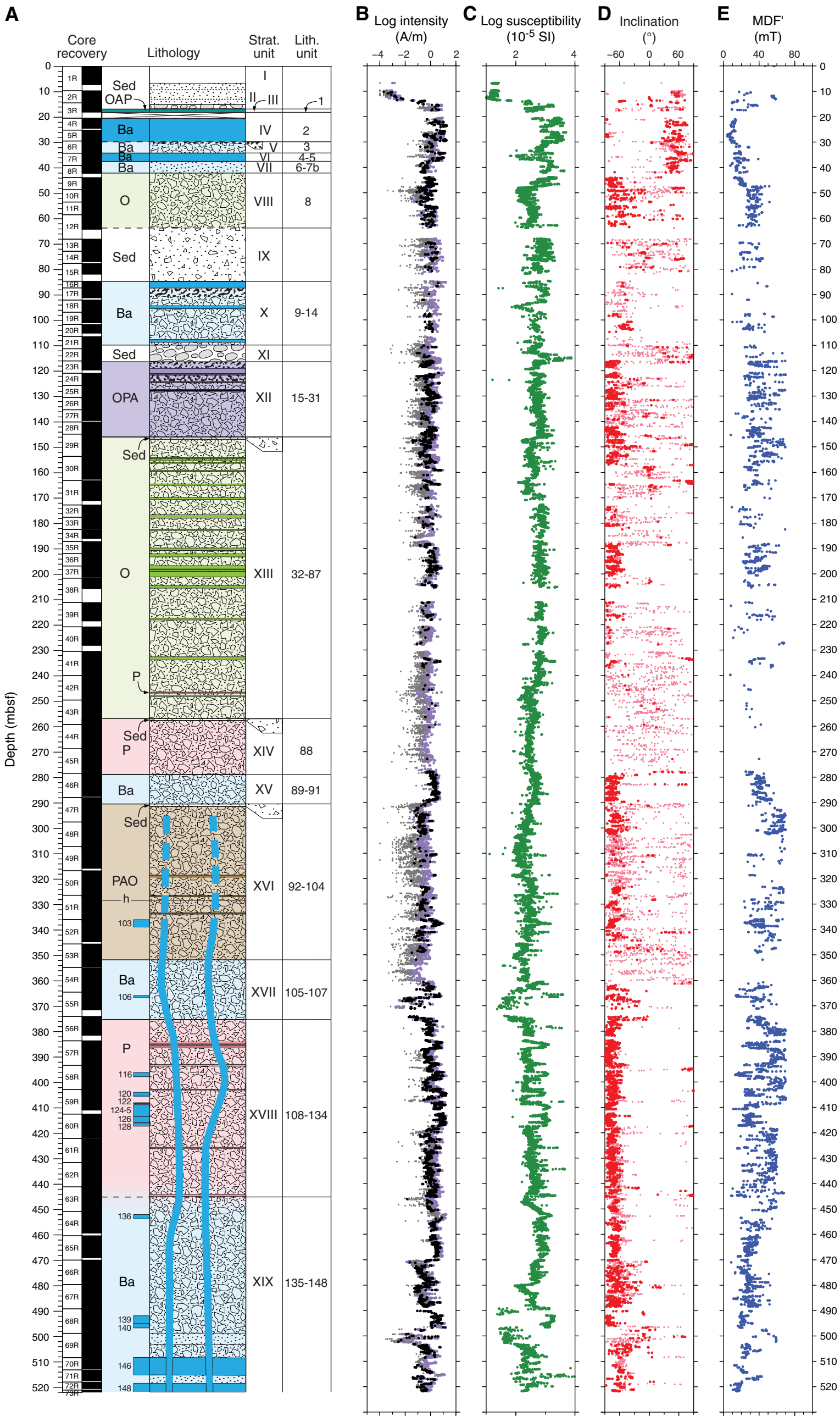


Figure F74. A–H. Representative Zijdeveld plots from archive-half cores, Hole U1374A. Solid circles = projections of vector endpoints onto the horizontal plane, open circles = projections onto the vertical plane. Red arrows = best-fitting principal component analysis (PCA) direction calculated automatically, pink arrows = rejected PCA directions (these correspond to pink symbols in Fig. F73). NRM = natural remanent magnetization. Boxes contain treatment level for PCA fit (A = anchored to origin, F = free of origin) and calculated misfit (see “Paleomagnetism” in the “Methods” chapter [Expedition 330 Scientists, 2012a]).

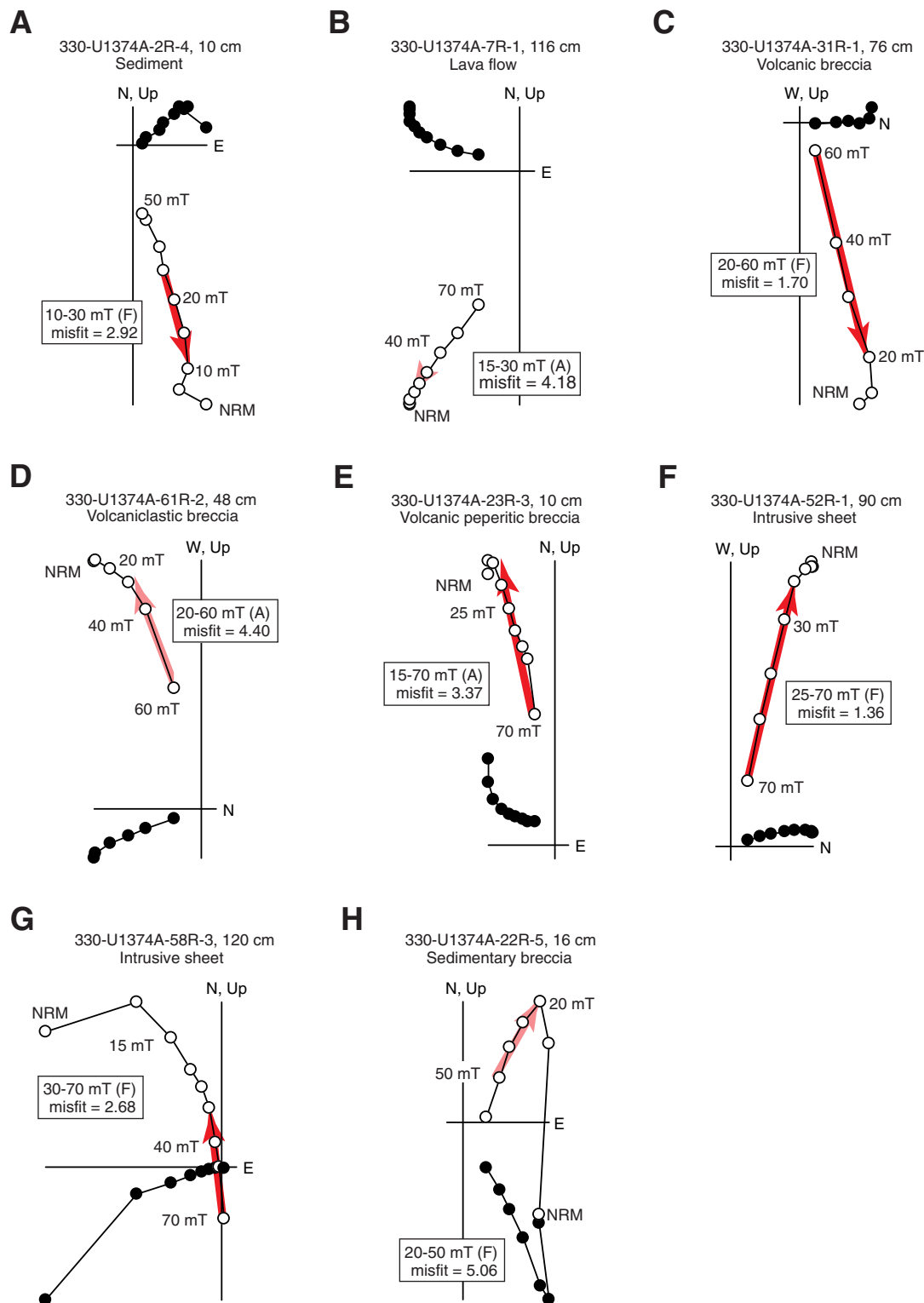


Figure F75. A, B. Histograms of natural remanent magnetization (NRM) intensities for discrete samples from different lithologies, Hole U1374A. **C.** Log-log graph of bulk magnetic susceptibility vs. Königsberger ratio (Q_n).

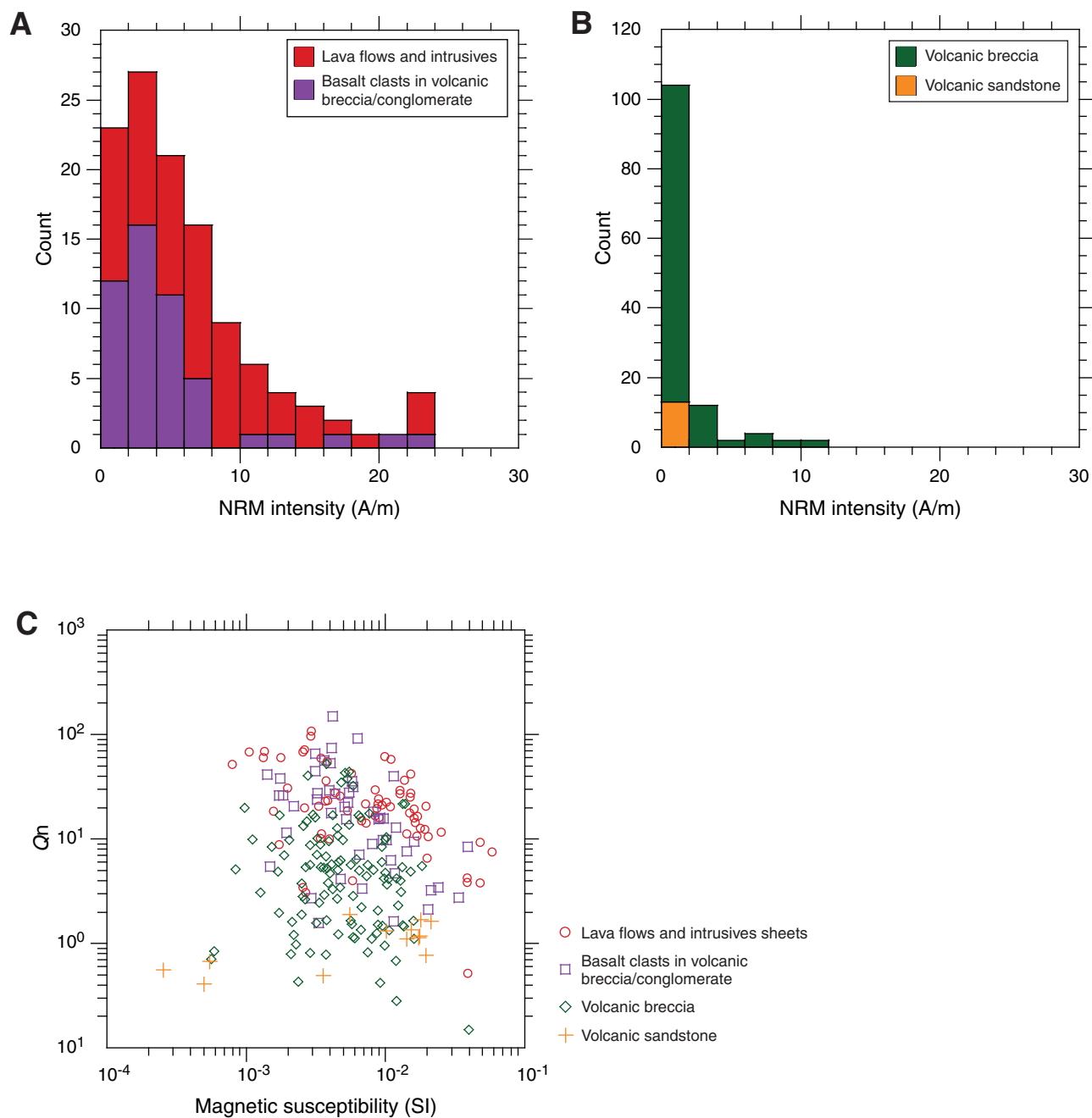


Figure F76. A–F. Representative Zijdeveld plots of AF and thermal demagnetization results from discrete samples, Hole U1374A. Solid circles = projections of vector endpoints onto horizontal plane, open circles = projections onto vertical plane. Red arrows = principal component analysis (PCA) direction, pink arrows = rejected PCA directions with maximum angular deviation $> 5^\circ$. B and E show results of thermal and AF demagnetization from adjacent samples.

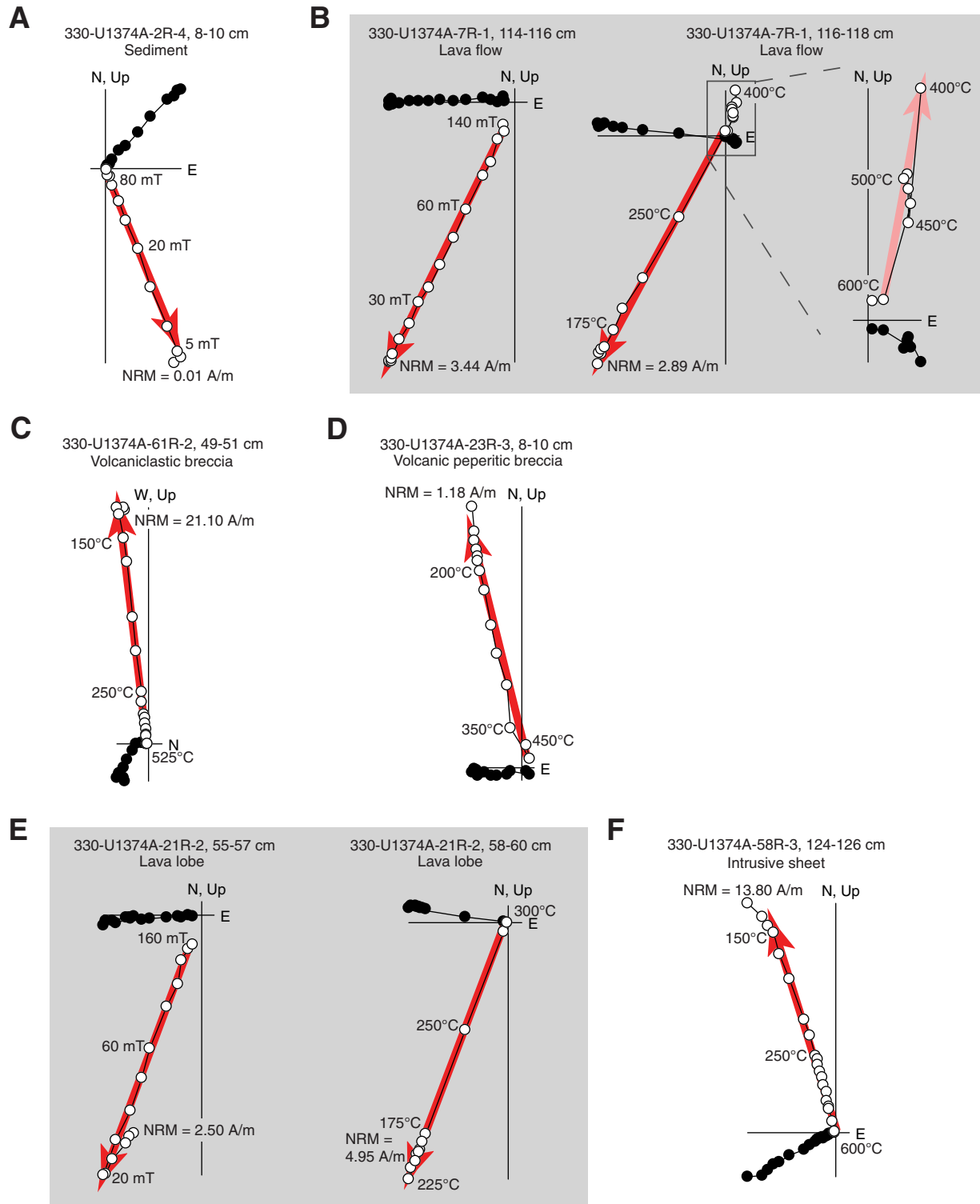


Figure F77. Lower-hemisphere equal-area projections in core coordinates showing principal axes (eigenvectors) of anisotropy of magnetic susceptibility measured on discrete samples from (A) intrusive sheets and (B) lava flows and lobes, Hole U1374A. ISCI = in situ confidence index (see “[Igneous petrology and volcanology](#)” in the “Methods” chapter [Expedition 330 Scientists, 2012a]).

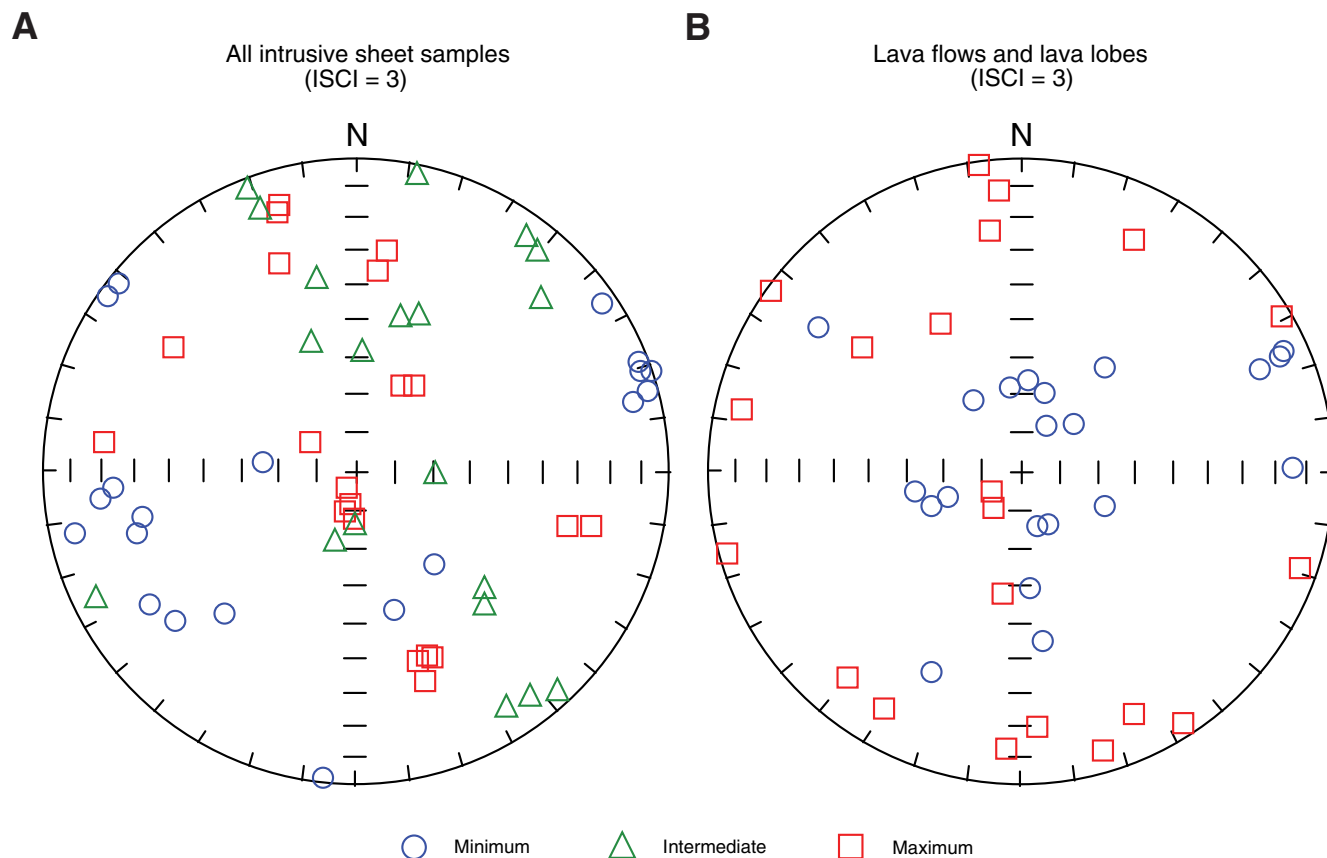


Figure F78. Downhole plots of inclination, Hole U1374A. **A.** Core recovery and observed stratigraphy (see Fig. F25 for explanation of patterns and abbreviations). **B.** All downhole inclination data measured at 2 cm intervals on archive-half cores: red = principal component analysis (PCA) directions with misfits ≤ 3.42 , pink = PCA directions with misfits > 3.42 . **C.** Average inclination for each lithologic unit (see “[Igneous petrology and volcanology](#)”), calculated using inclination-only statistics. **D.** Average inclination for each core piece longer than 9 cm, calculated using Fisher statistics. **E.** Average inclination for each lithologic unit, calculated using average piece directions displayed in D and inclination-only statistics. **F.** Characteristic remanent magnetization inclinations from discrete samples (after alternating-field [AF] or thermal demagnetization) with maximum angular deviation $\leq 5^\circ$. Shading scheme for C–F represents the ISCI for identifying distinct lava flow units, where the darkest shade of blue is the most confident and green is not applicable (NA; i.e., deposits cannot have retained their orientation since cooling).

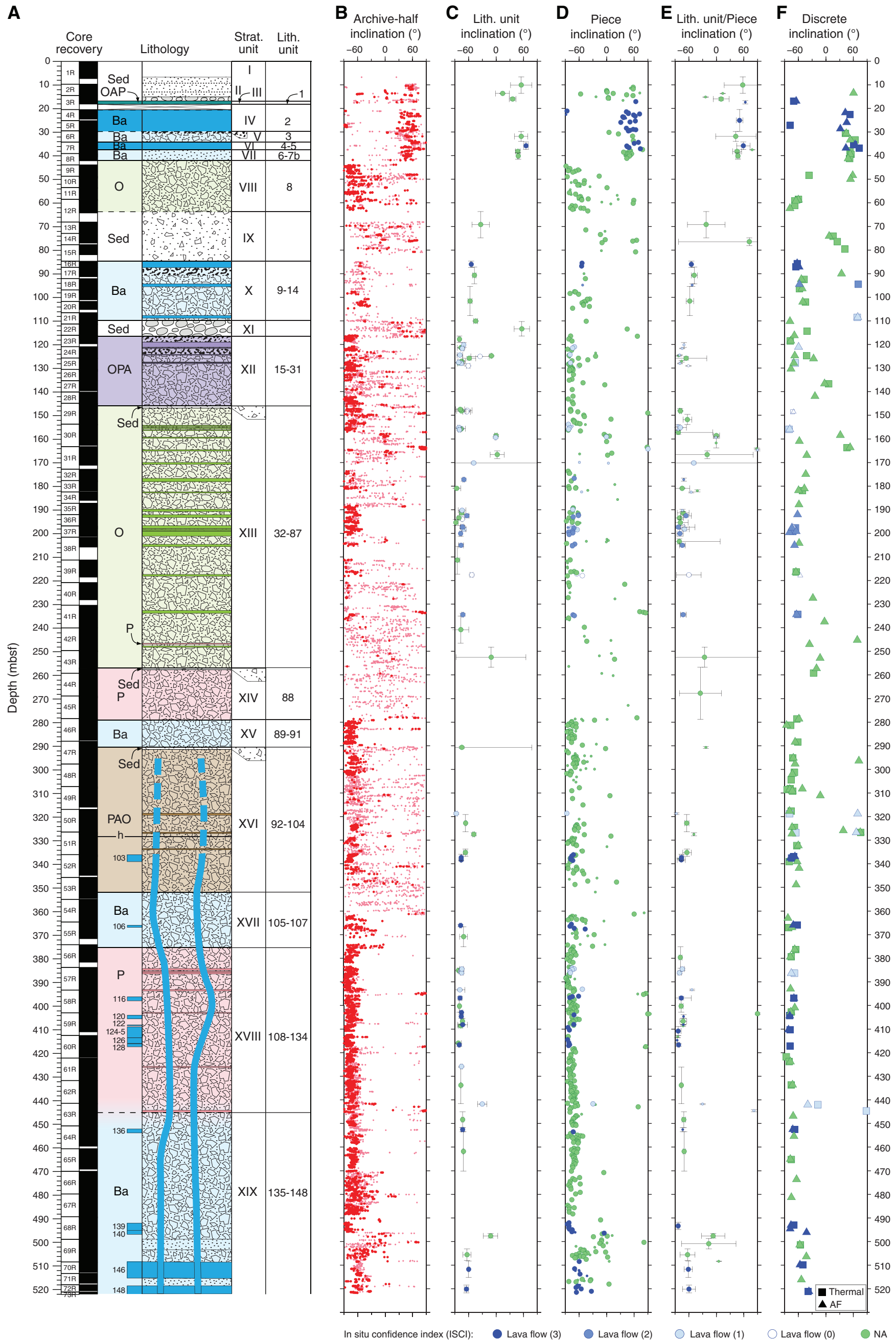


Figure F79. Histograms of Hole U1374A inclinations. **A.** All archive-half cores measured at 2 cm intervals with misfit ≤ 3.42 . **B.** Lithologic unit averages of data in A using inclination-only statistics for units with an in situ confidence index (ISCI; see “[Igneous petrology and volcanology](#)” in the “Methods” chapter [Expedition 330 Scientists, 2012a]) of 3 or 2 and with $\alpha_{95} \leq 30^\circ$. **C.** Fisher piece-average inclinations ($\text{CSD} \leq 20^\circ$) for units assigned an ISCI of 3 or 2. **D.** Lithologic unit averages of data in C using inclination-only statistics and with $\alpha_{95} \leq 40^\circ$. **E.** Inclinations from AF or thermally demagnetized discrete samples. Dashed lines in E indicate expected geocentric axial dipole inclination ($\pm 68^\circ$) for current Louisville hotspot location. Statistics presented in inset panels are inclination-only means (α_{95}). Note different scales on y-axes and that because of the uncertainty in whether some individual units are in situ, averages by lithologic unit have not been calculated.

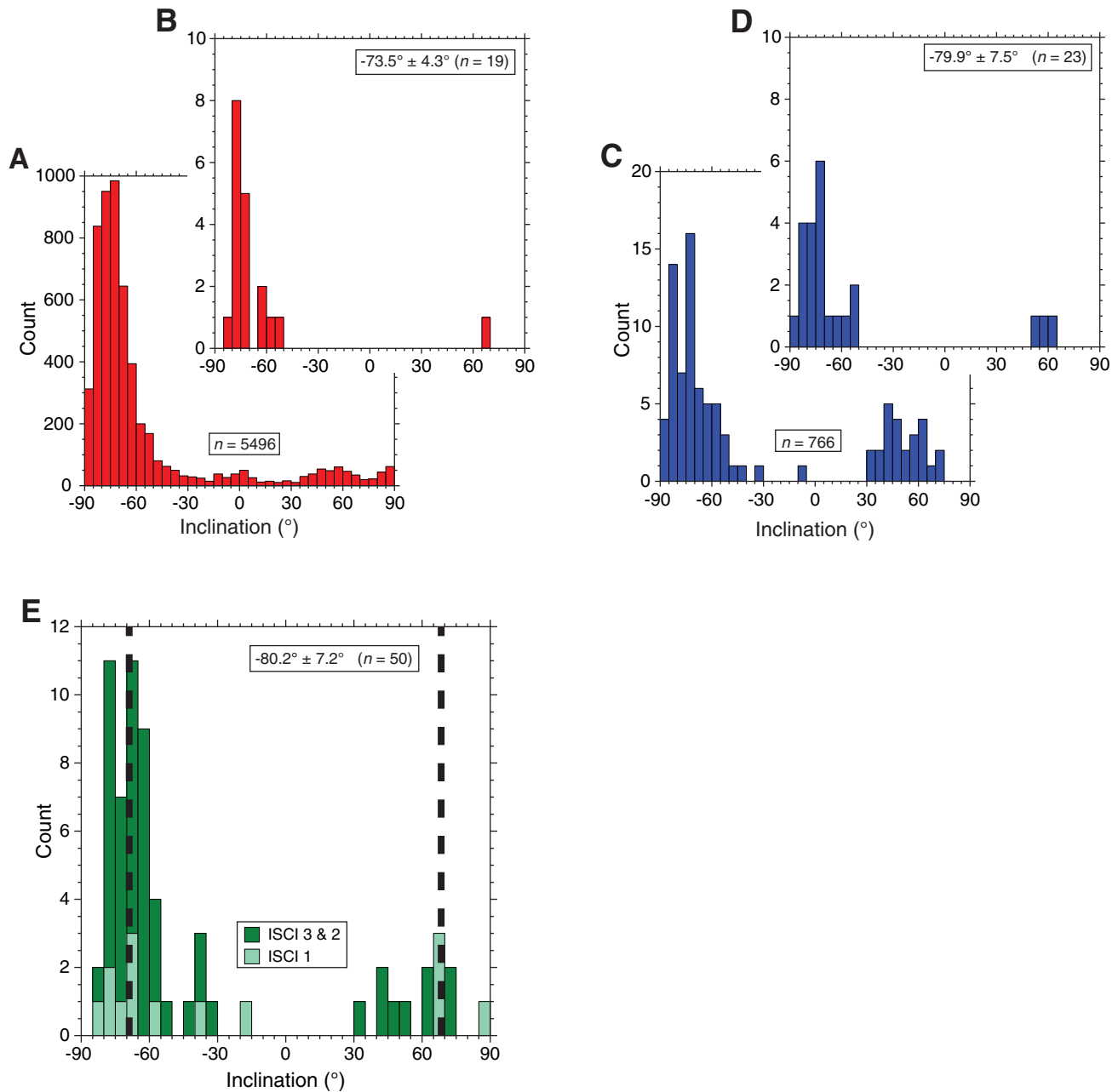


Figure F80. A. Triple combination tool string. HNGS = Hostile Environment Natural Gamma Ray Sonde, APS = Accelerator Porosity Sonde, HLDS = Hostile Environment Litho-Density Sonde, GPIT = General Purpose Inclination Tool, DIT = Dual Induction Tool. B. Schematic of Hole U1374A logging passes (one downlog, a main uplog, and a 100 m uplog repeat pass starting and ending a few meters above the end of the pipe).

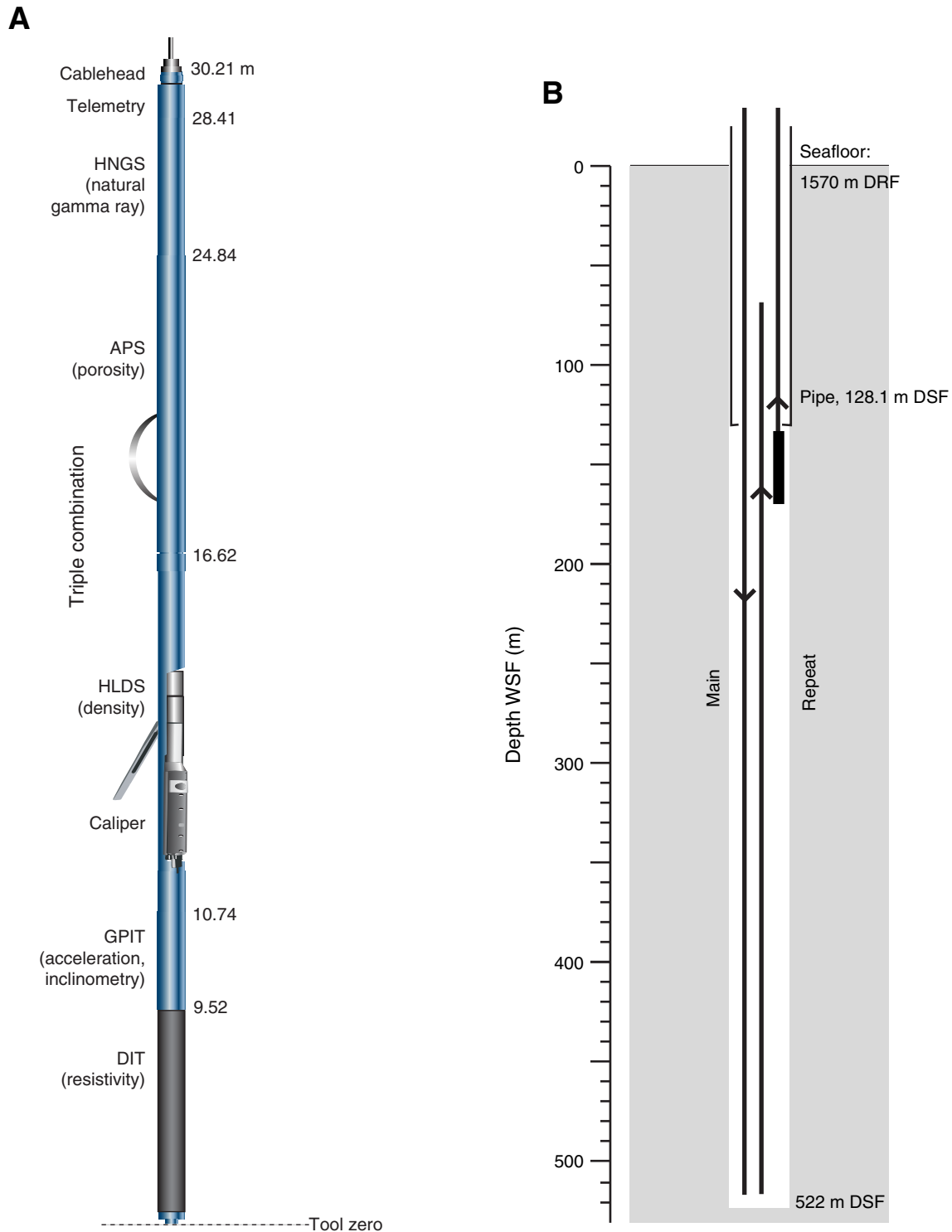


Figure F81. A. Göttingen Borehole Magnetometer (GBM) tool string. **B.** Schematic of Hole U1374A logging pass (one continuous log), which starts and ends on rig floor with a sighting of the GBM to orientate the tool before and after run.

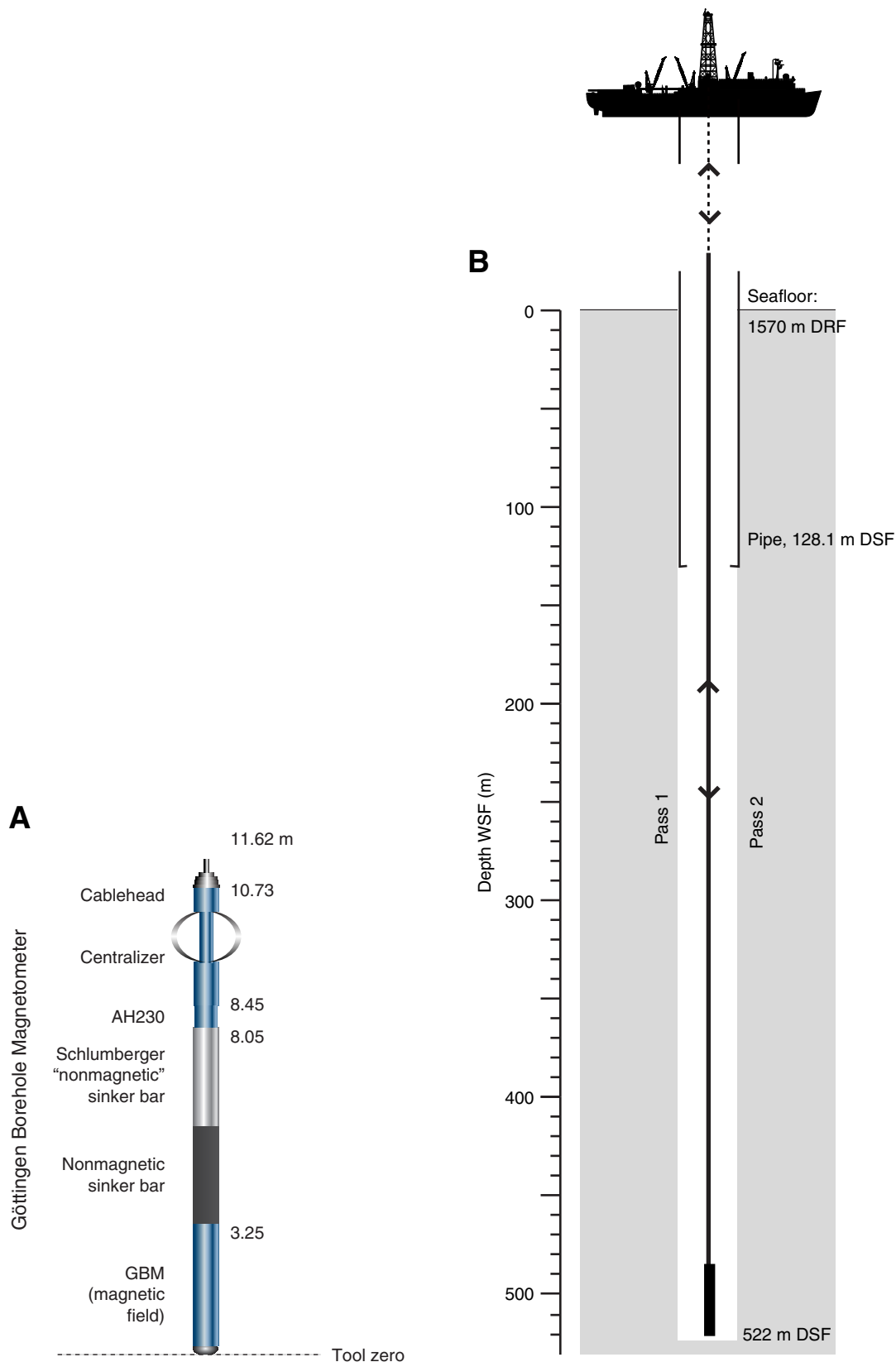


Figure F82. A. Formation MicroScanner (FMS)-sonic tool string. HNGS = Hostile Environment Natural Gamma Ray Sonde, DSI = Dipole Shear Sonic Imager, GPIT = General Purpose Inclinometry Tool. B. Schematic of Hole U1374A logging passes (two uplog passes, with image acquisition starting at bottom of hole and ending ~10 m before base of drill pipe).

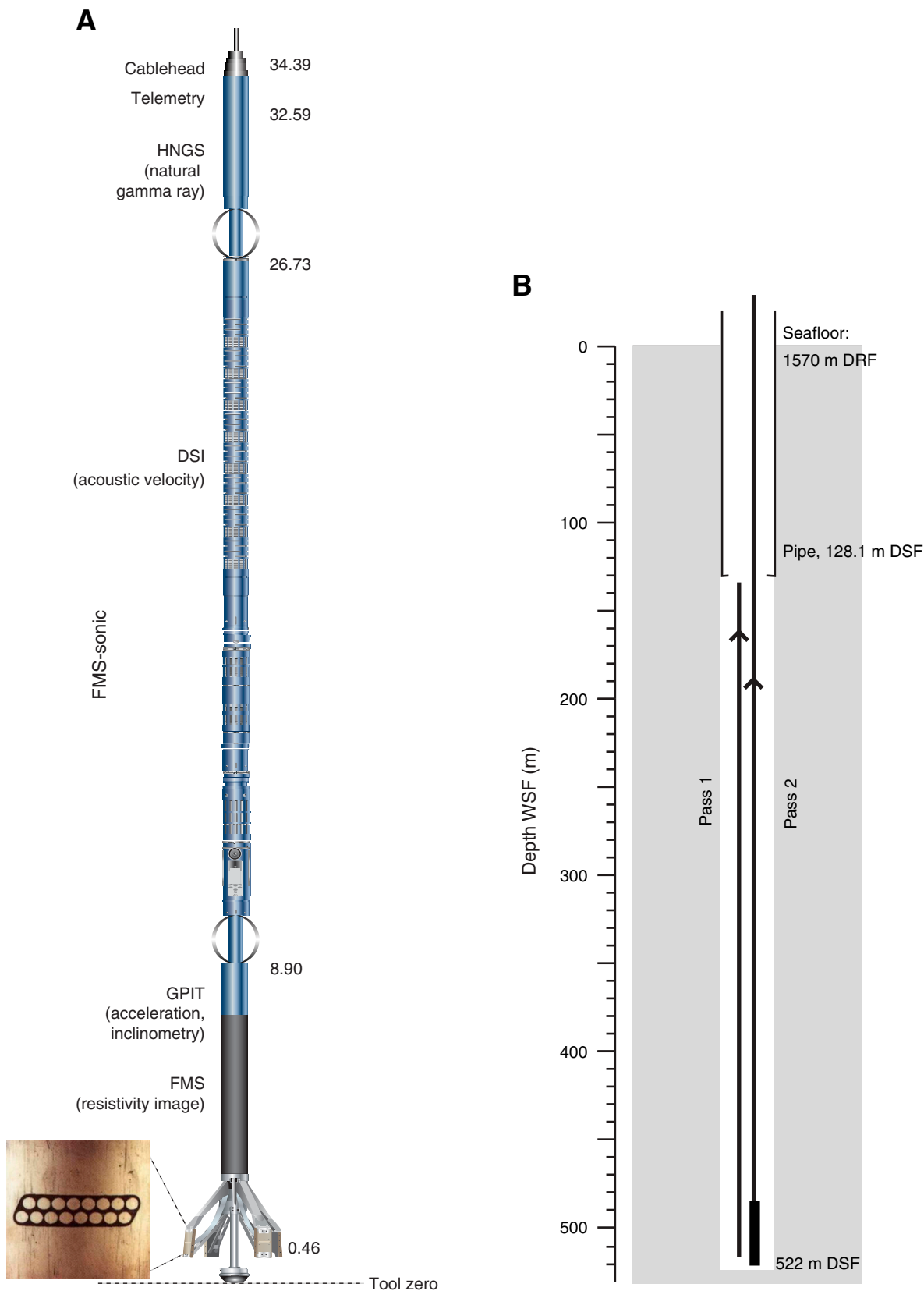


Figure F83. A. Ultrasonic Borehole Imager tool string. HNGS = Hostile Environment Natural Gamma Ray Sonde, GPIT = General Purpose Inclinometry Tool, UBI = Ultrasonic Borehole Imager Sonde and rotating sub. **B.** Schematic of Hole U1374A logging passes (five sections logged where borehole was measured to be ≤ 30 cm in diameter, starting at bottom of hole and moving upward).

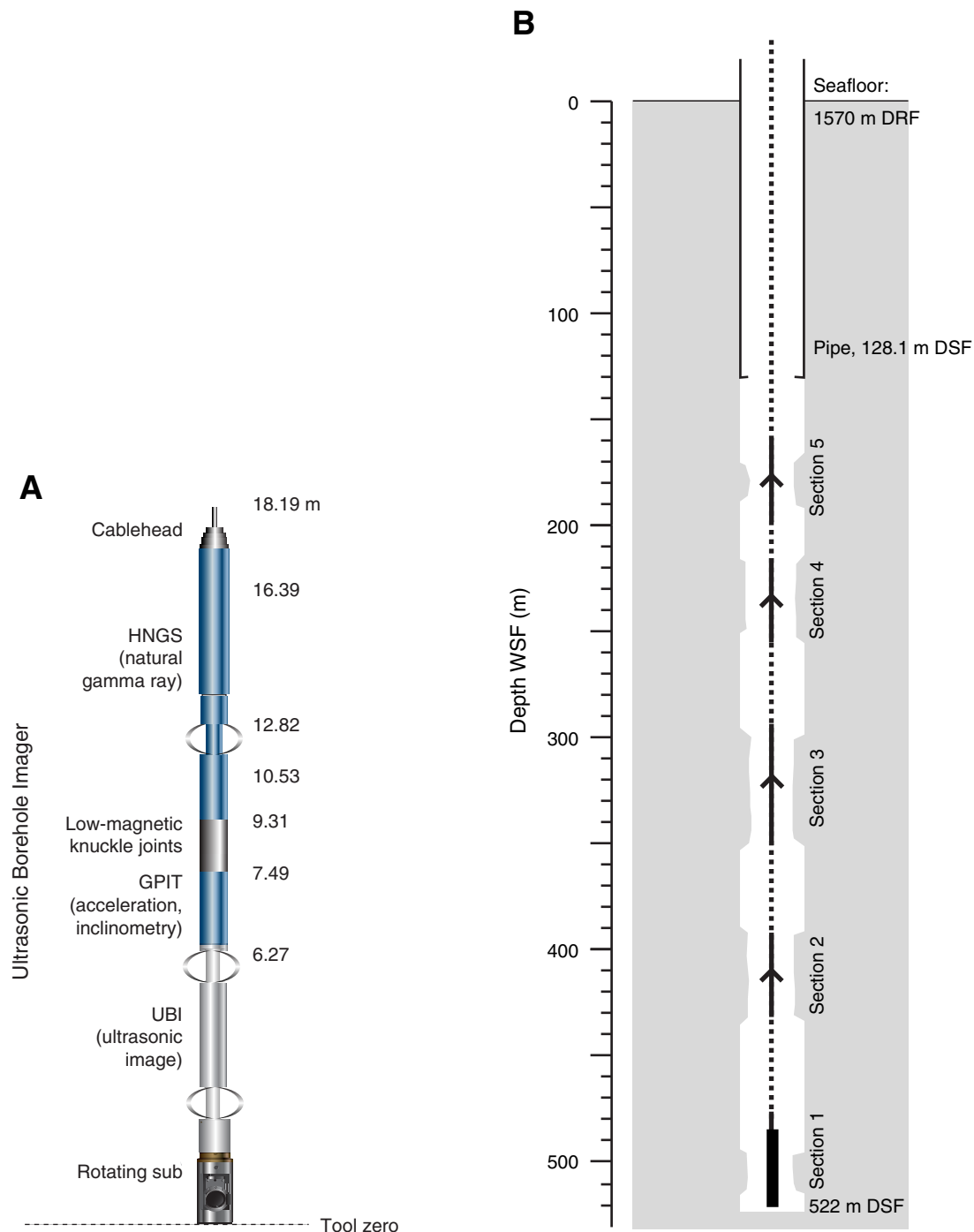


Figure F84. Summary of downhole log measurements and log unit divisions, Hole U1374A. Measurements include gamma ray (UBId = Ultrasonic Borehole Imager downlog, TCm = triple combination main log), caliper, density (MAD measurements plotted using CSF-A depth scale), resistivity (IMPH = medium induction phasor-processed resistivity, IDPH = deep induction phasor-processed resistivity), neutron porosity (APLC) and moisture and density (MAD) porosity, and *P*-wave velocity (velocity core = V_p measured on discrete core samples [CSF-A depth scale], V_p = compressional wave velocity measured with downhole sonic sonde [main and repeat runs]). A summary of core recovery and stratigraphic units is provided at far right (see Fig. F18 for explanation of abbreviations and patterns).

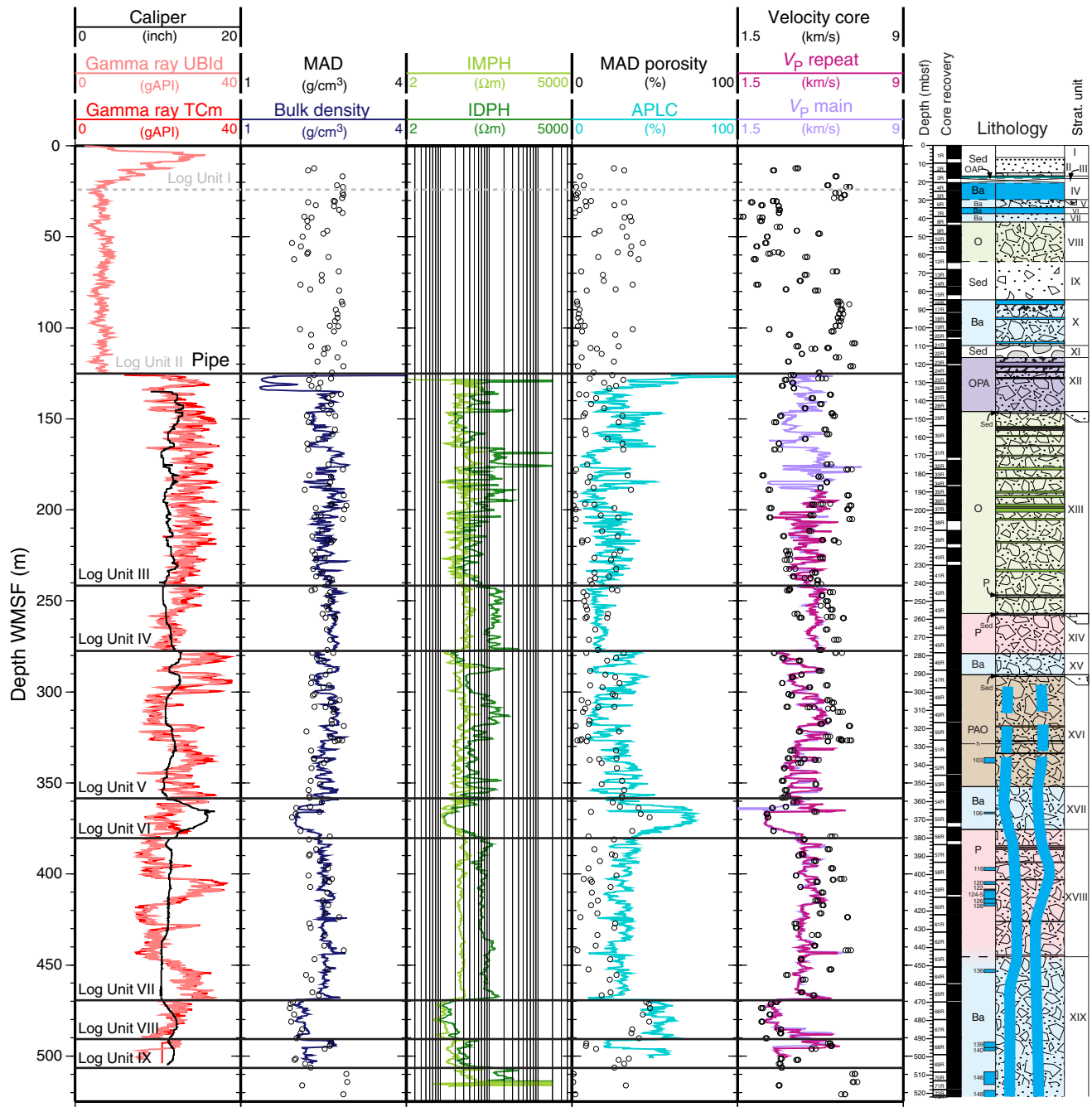


Figure F85. Summary of natural gamma ray log measurements, Hole U1374A. Note that natural gamma radiation (NGR; measured on whole-round cores) is in counts per second (cps), and all downhole measurements are in gAPI (American Petroleum Institute gamma ray units). Colored zones across the figure denote areas of massive, nonbrecciated units (purple = olivine-plagioclase-augite-phyric, green = olivine phyric, pink = plagioclase-phyric, brown = plagioclase-augite-olivine-phyric, blue = aphyric intrusions). A summary of core recovery and stratigraphic units is provided at far right (see Fig. F18 for explanation of abbreviations and patterns).

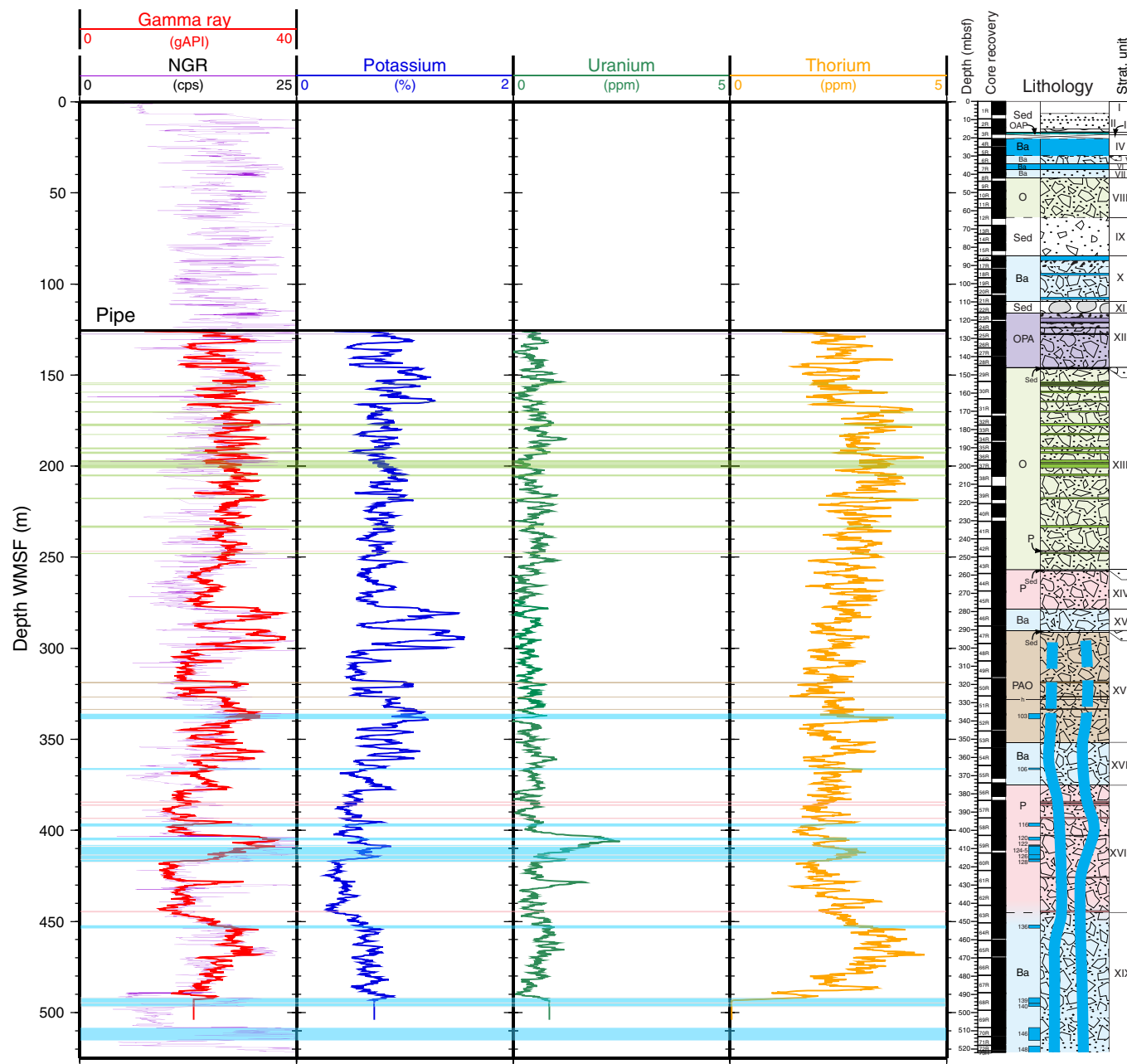


Figure F86. Borehole deviation from vertical determined during (A) Run 1 and (B) Run 2 with the Göttingen Borehole Magnetometer (GBM) (downlog and uplog) and (C) comparison with deviation determined by the General Purpose Inclineretry Tool (GPIT) in the Formation MicroScanner (FMS)-sonic and Ultrasonic Borehole Imager (UBI) tool strings, Hole U1374A. The light colors in A and B show raw GBM data, and dark colors show 16-point moving average, which is also shown in C.

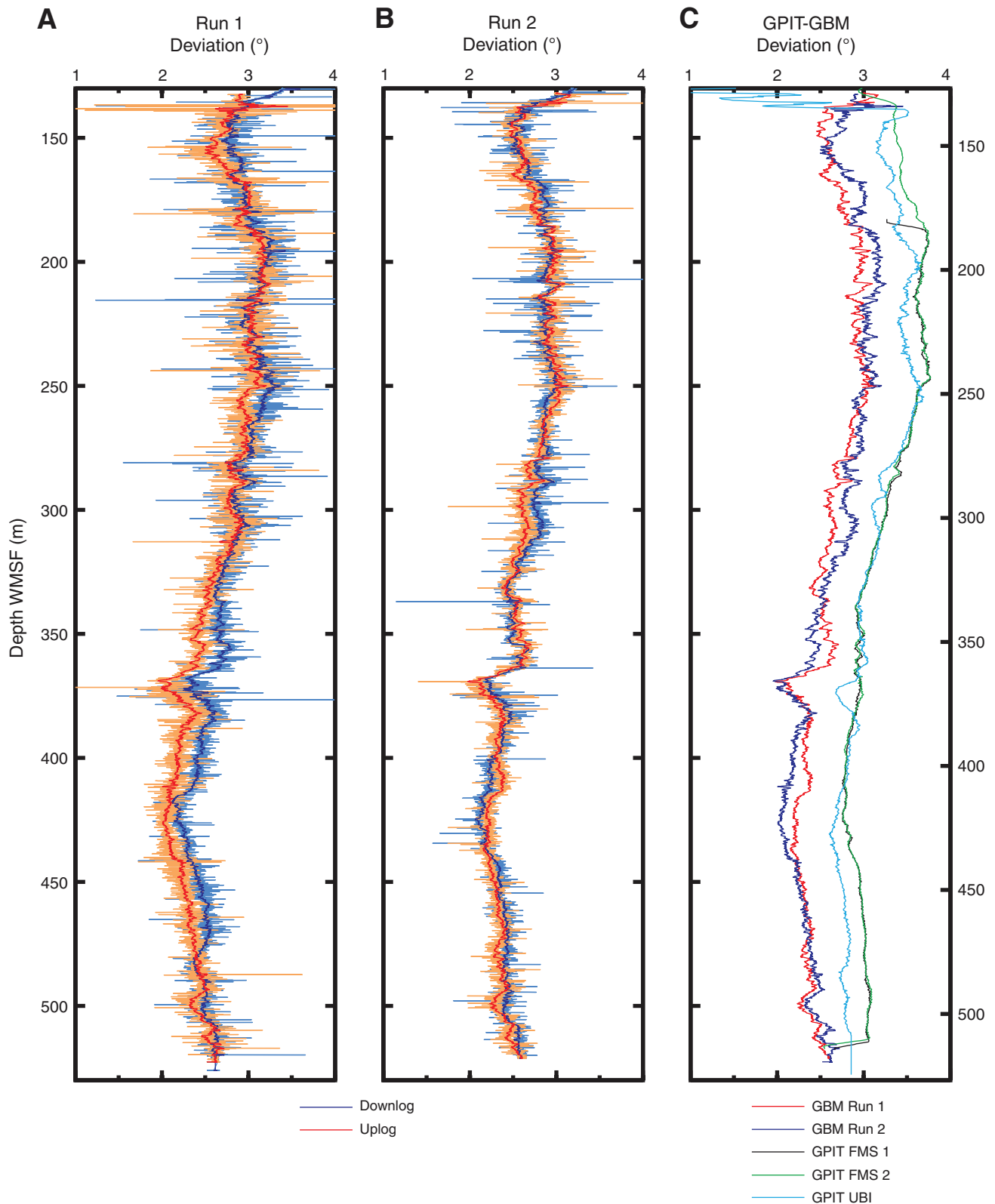


Figure F87. Raw horizontal magnetic field data for Run 1 and Run 2 with the Göttingen Borehole Magnetometer (GBM) (downlog and uplog) and comparison with horizontal magnetic field measured by the General Purpose Inclinometry Tool (GPIT) in the Formation MicroScanner (FMS)-sonic and Ultrasonic Borehole Imager (UBI) tool strings, Hole U1374A. Data are not corrected for tool inclination.

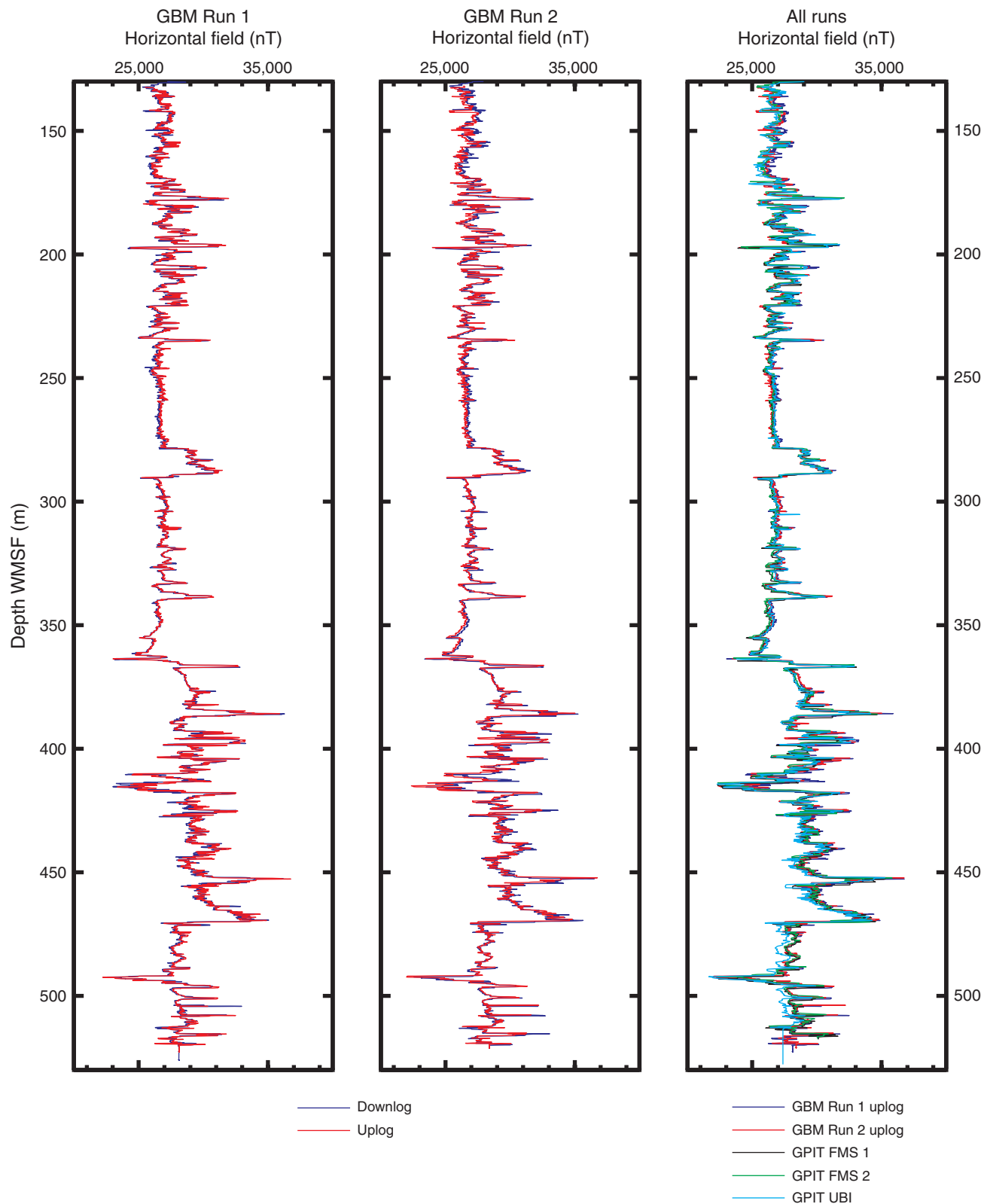


Figure F88. Raw vertical magnetic field data for Run 1 and Run 2 with the Göttingen Borehole Magnetometer (GBM) (downlog and uplog) and comparison with the vertical magnetic field measured by the General Purpose Inclineretry Tool (GPIT) in the Formation MicroScanner (FMS)-sonic and Ultrasonic Borehole Imager (UBI) tool strings, Hole U1374A. Data are not corrected for tool inclination. Offsets between logs can be explained by magnetic material present in the tool strings.

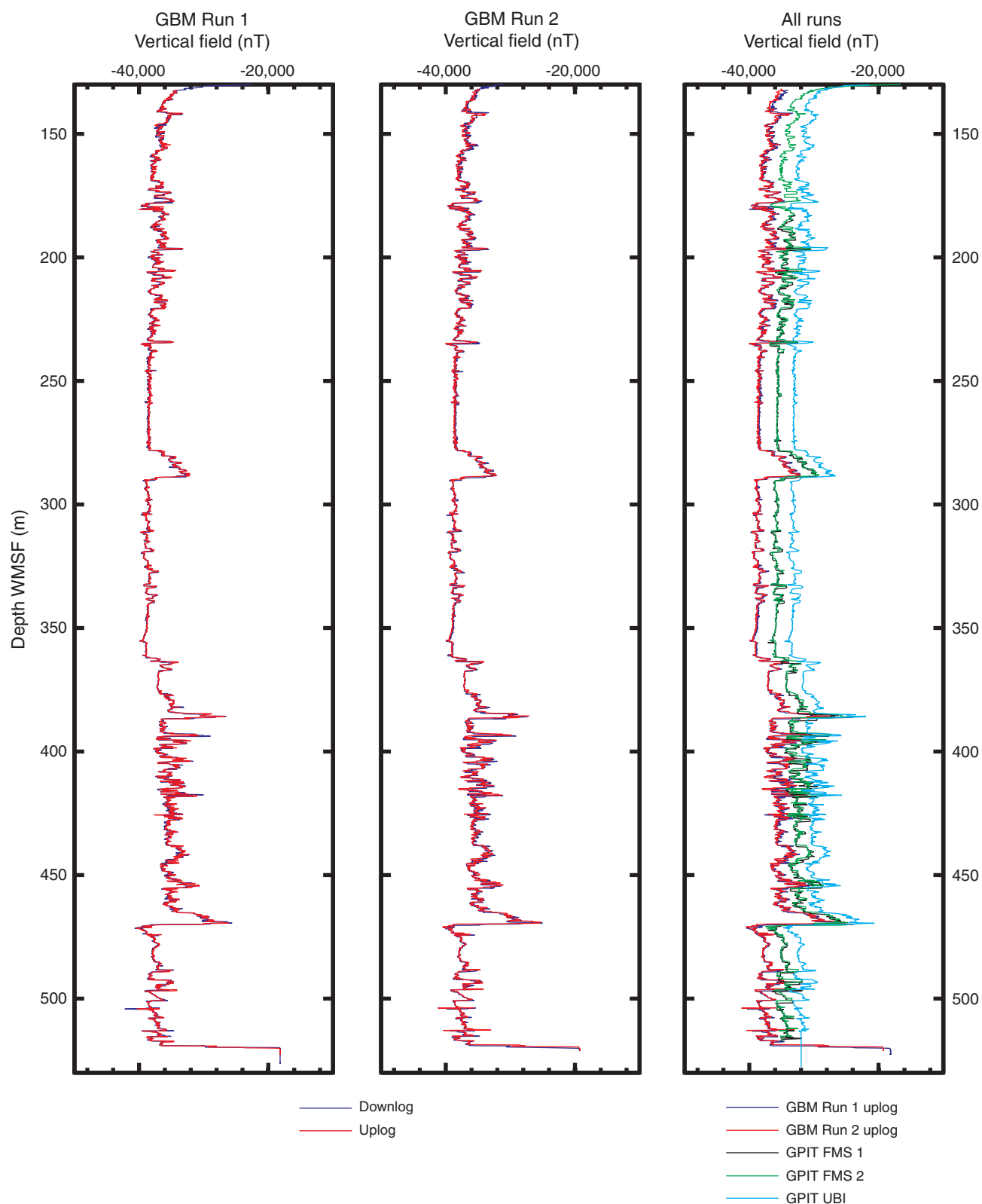


Figure F89. Magnetic field inclination determined by General Purpose Inclinometry Tool (GPIT) in the Formation MicroScanner (FMS)-sonic and Ultrasonic Borehole Imager (UBI) tool strings. Offset between different tool strings is caused by neighboring magnetized tool housings. Note that the International Geomagnetic Reference Field (IGRF11) inclination at Site U1374 is -52.2° .

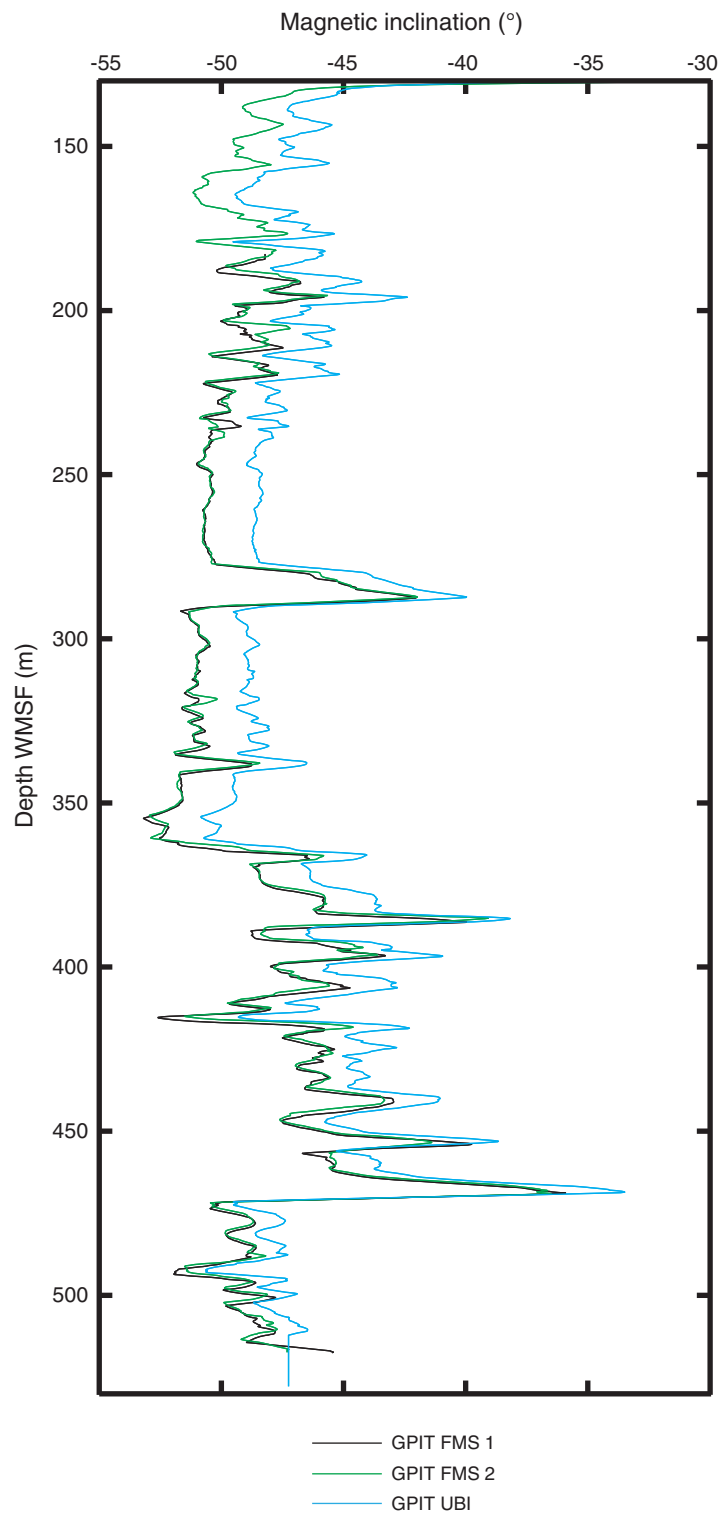


Figure F90. Accumulated angles of fiber-optic gyros for the two Göttingen Borehole Magnetometer runs. R_z is parallel to the symmetry axis of the tool, and R_x and R_y are perpendicular to R_z . In plot of R_z , green line = uplog portion of Run 1, yellow line = uplog portion of Run 2. The data are not corrected for the rotation of the Earth.

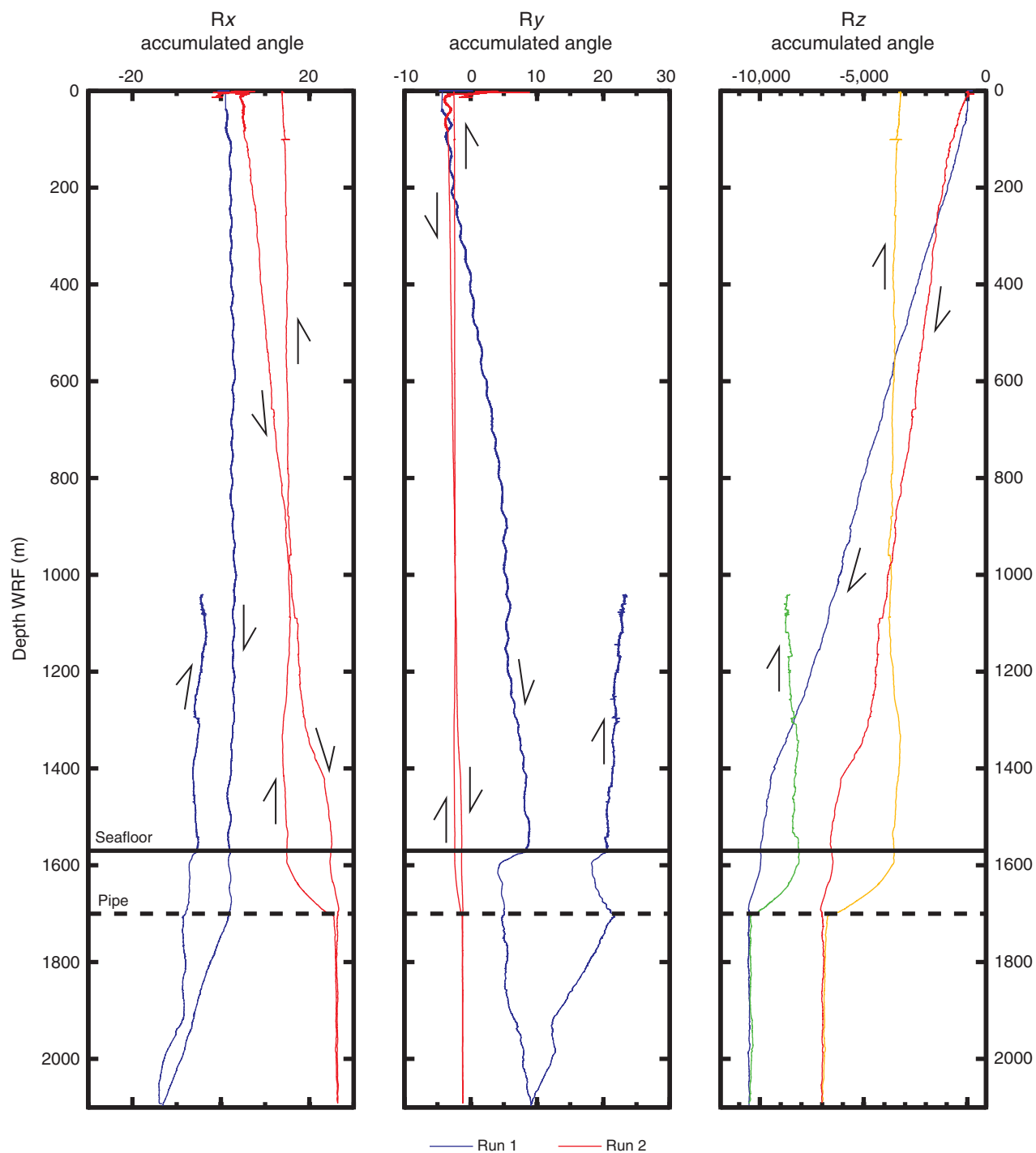


Figure F91. Comparison of raw magnetic field data (not corrected for tool inclination) of Göttingen Borehole Magnetometer Run 1 with lithology (see Fig. F18 for explanation of abbreviations and patterns). Vertical black lines indicate ambient field ($H = 28,799$ nT, $Z = -36,896$ nT; please note that these are estimations and are not corrected for borehole deviation).

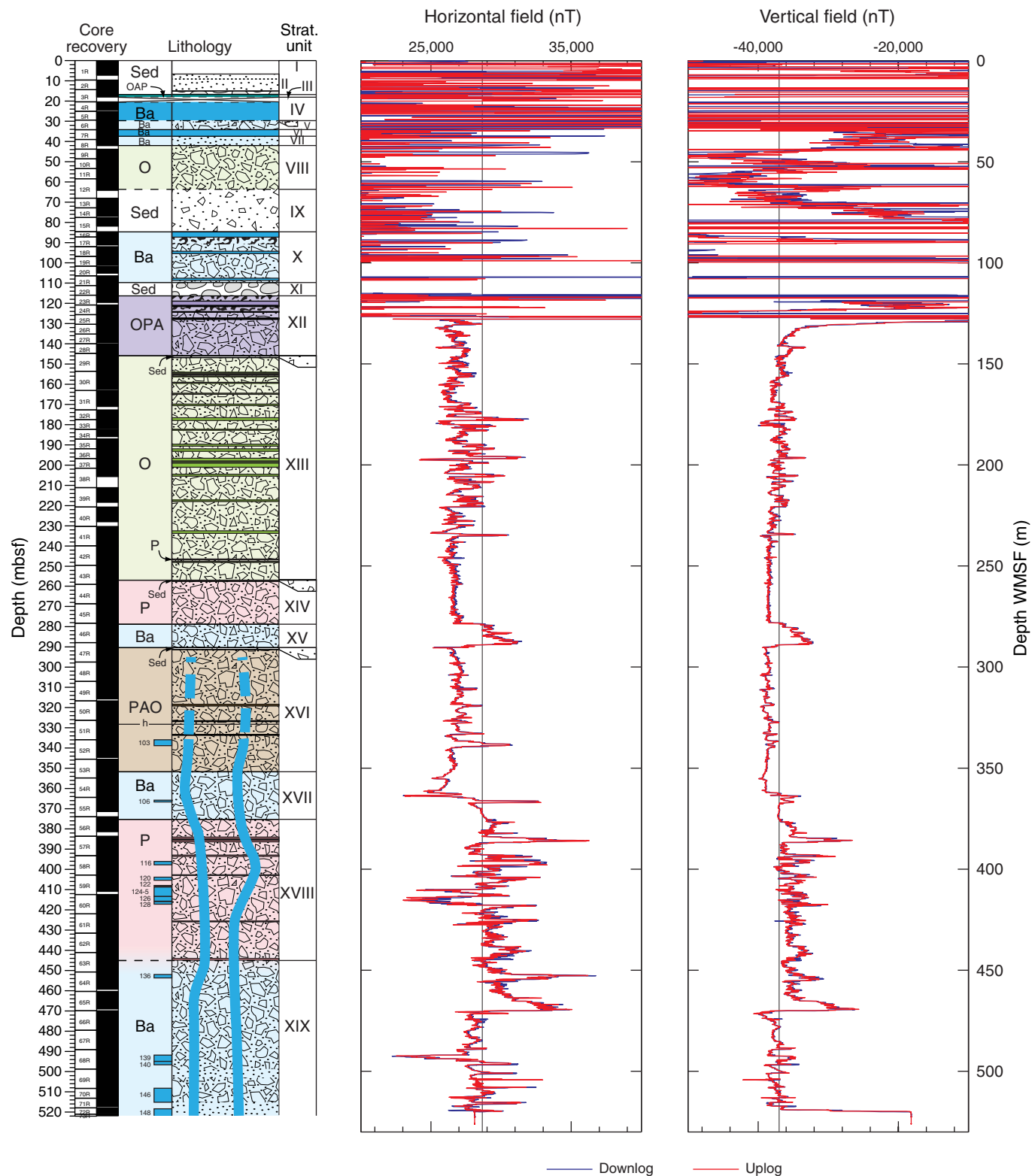


Figure F92. Composite showing several features imaged using the Formation MicroScanner (FMS), Hole U1374A. FMS images for A–E are overlain by a high-resolution bulk density curve (in red). **A.** Potential lava lobe in olivine-phyric breccia. **B.** Stratigraphic Unit XIV/XV boundary (see “[Igneous petrology and volcanology](#)” for more details). **C.** Area of large contrast showing a potential lava lobe (resistive) surrounded by much more conductive breccia. The more resistive layer also exhibits a much higher bulk density. **D.** Interbedded breccia and lava units. **E.** Lithologic Units 139 and 140. **F.** Extensive conductive fractures in lithologic Unit 146. For more details on aforementioned lithologic units, see “[Igneous petrology and volcanology](#).”

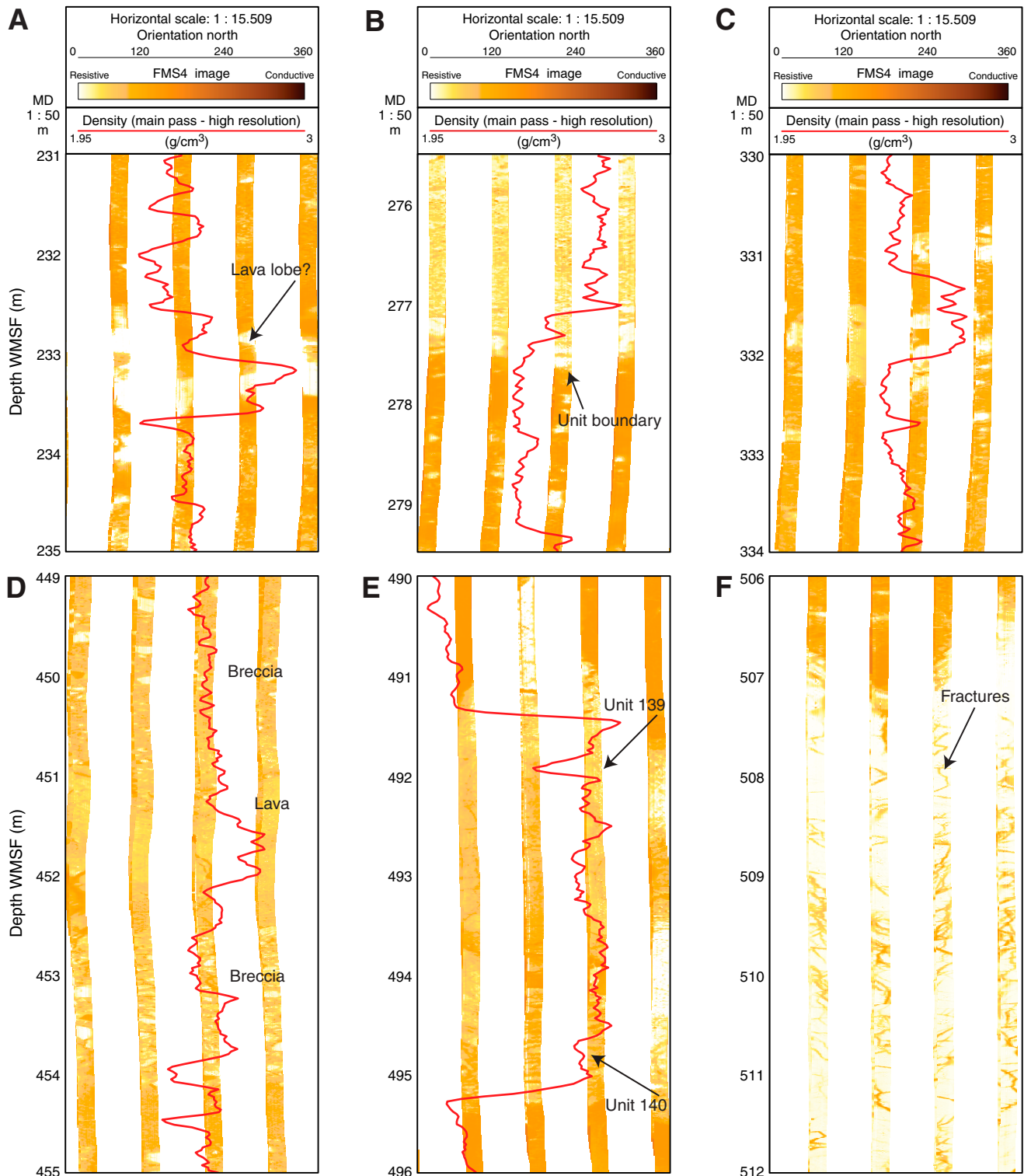


Figure F93. A–D. Summary figure of Formation MicroScanner (FMS) images showing examples of structural relationships between electrically contrasting layers, Hole U1374A. Best-fit sinusoids were picked on major features (in black), and tadpole plots of these dip angles and directions are shown next to FMS image (note that direction of tadpole tail indicates true azimuth of dip, and angle of dip is where circle is plotted). Both static- and dynamic-normalized FMS images are shown. (Figure shown on next page.)



Figure F93 (continued). (Caption shown on previous page.)

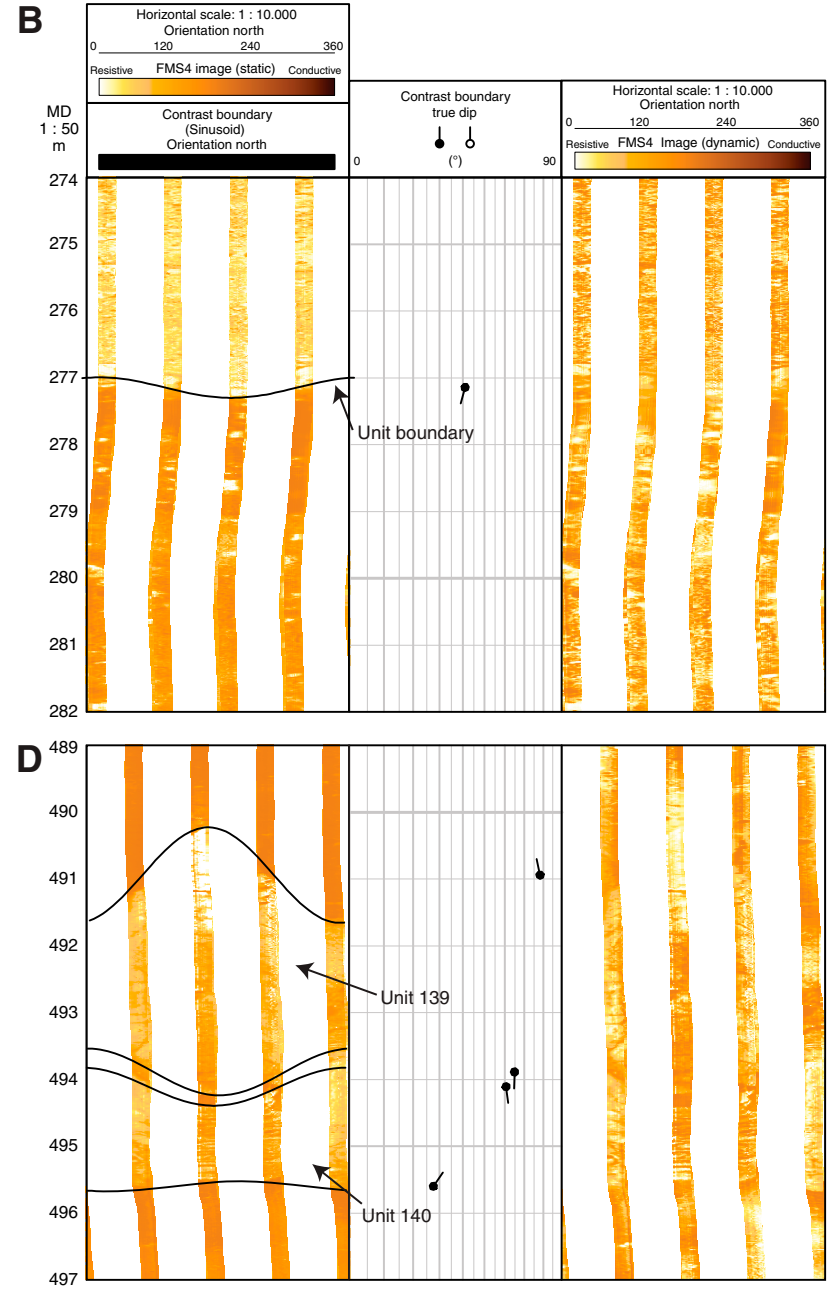
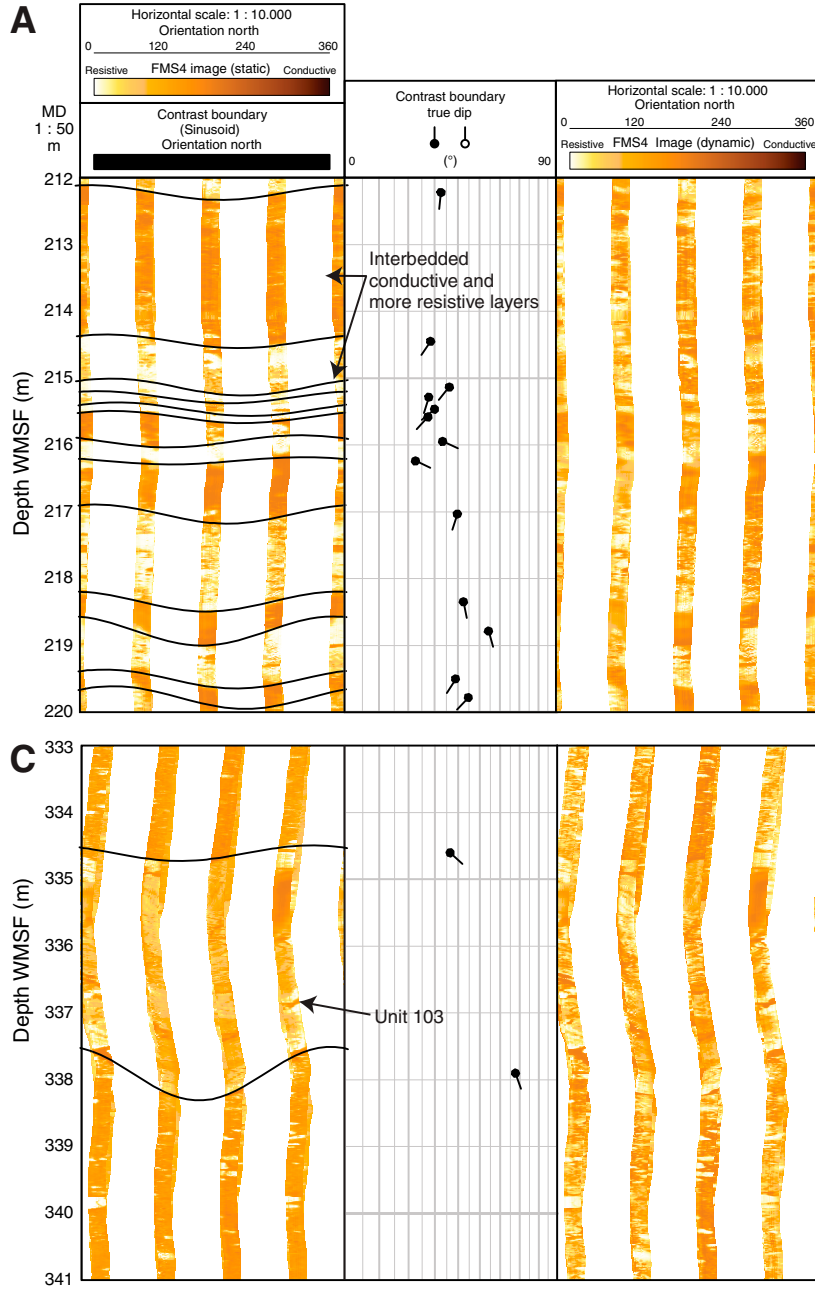


Figure F94. Summary figure of Formation MicroScanner (FMS) images showing lithologic Unit 146. Ultrasonic Borehole Imager (UBI) image is shown in gray scale, overlain by static-normalized FMS image. Top and bottom contact dip angle and direction are shown by black sinusoids and their associated tadpoles (note that direction of tadpole tail indicates true azimuth of dip, and angle of dip is where circle is plotted). FMS dynamic-normalized image is shown on right.

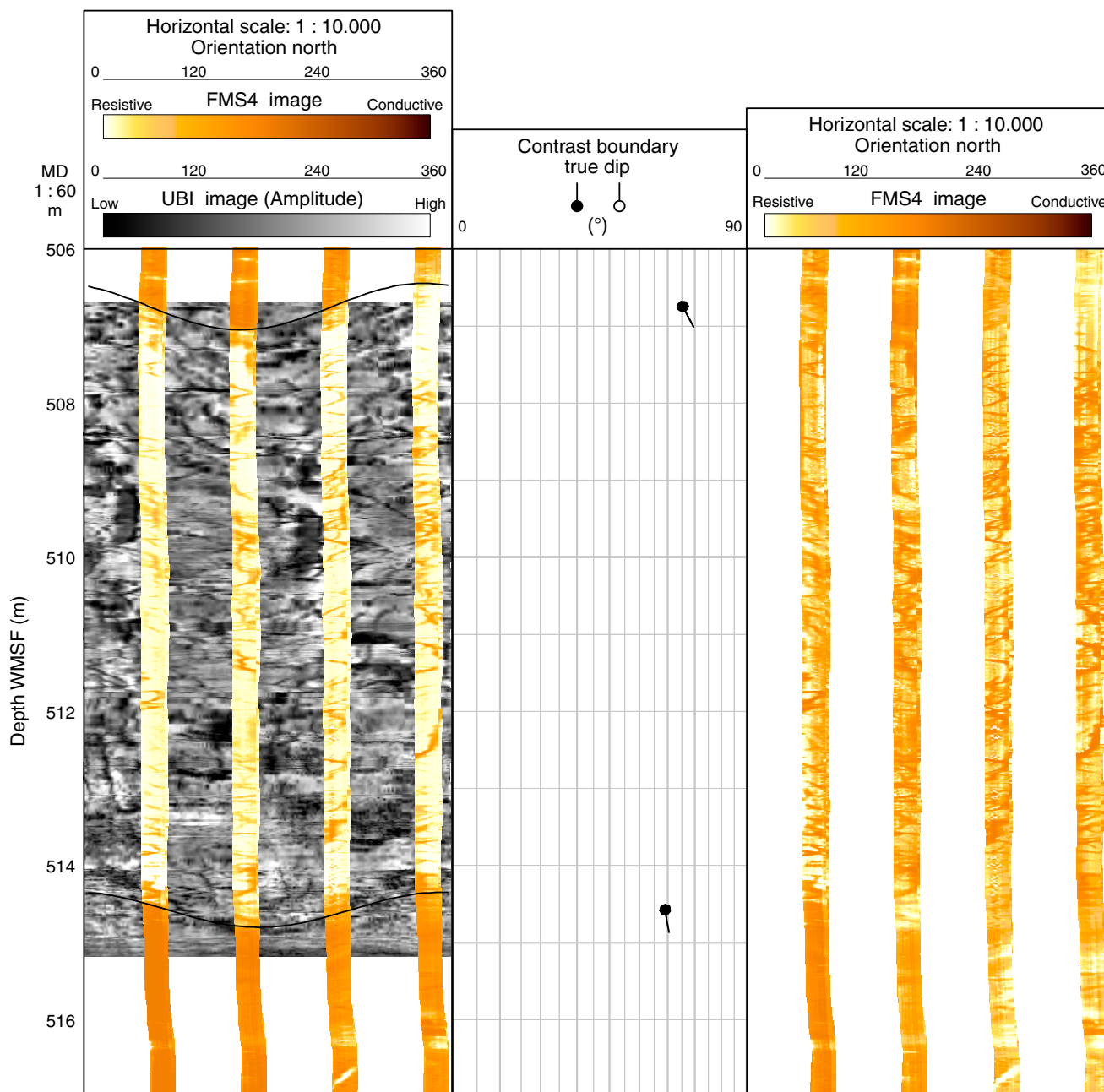




Figure F95. Schematic showing locations of microbiology (MBIO) samples, Hole U1374A.

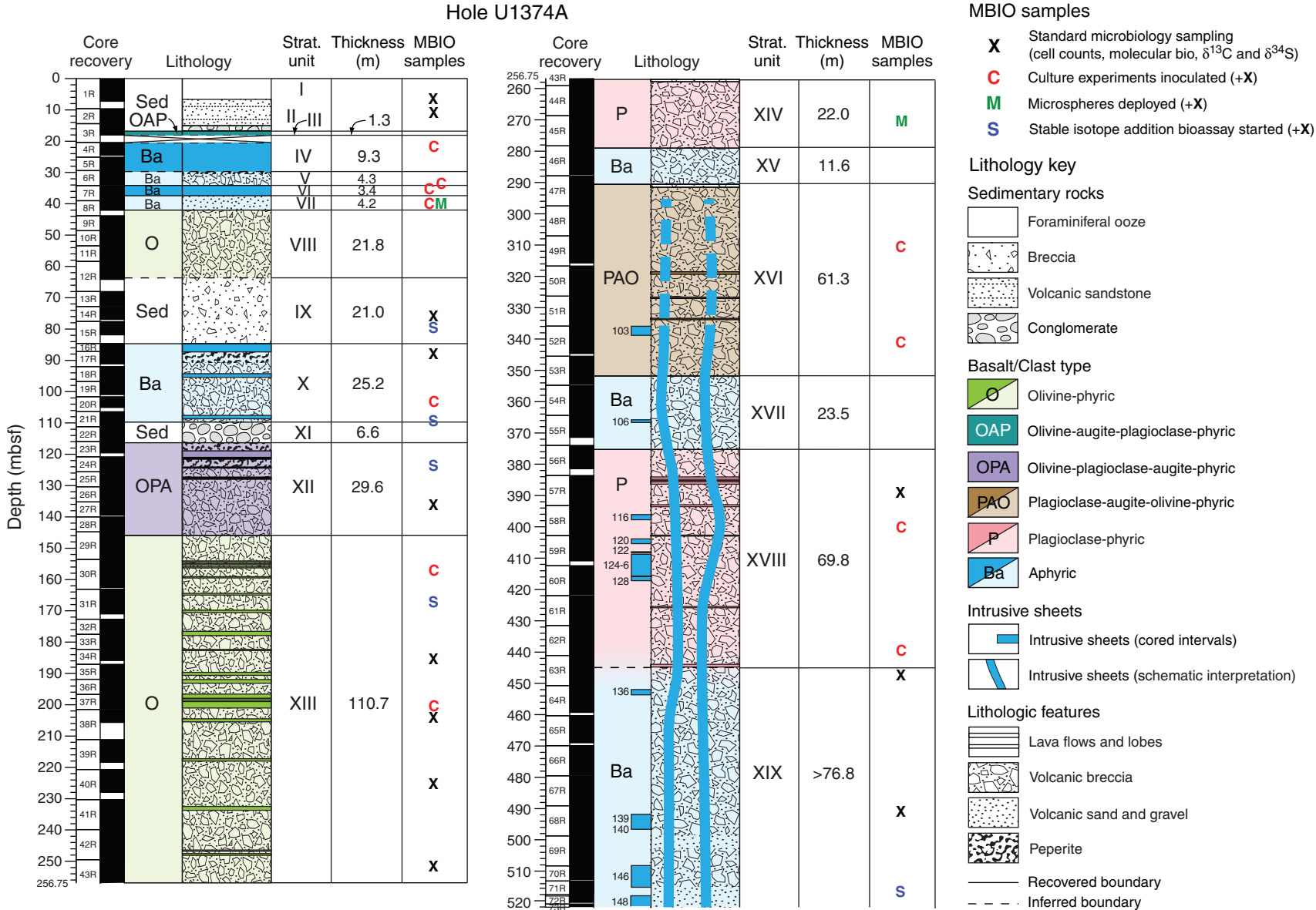


Figure F96. Whole-round samples collected for microbiology analysis, Site U1374. (Continued on next four pages.)

Core, section, interval (cm)	Depth (mbsf)	Lithology	Photograph
330-U1374A-			
1R-4, 145-150	5.95	Unconsolidated sediment	
2R-1, 99-112	10.59	Volcanic sandstone	
4R-1, 114-121	21.54	Aphyric basalt	
6R-3, 117-128	33.36	Volcanic basalt breccia	
7R-1, 120-130	35.40	Aphyric basalt	
8R-1, 60-68	39.60	Volcanic sandstone	

Figure F96 (continued). (Continued on next page.)

Core, section, interval (cm)	Depth (mbsf)	Lithology	Photograph
330-U1374A-			
14R-2, 129-140	74.95	Sedimentary breccia	
15R-2, 79-89	79.70	Sedimentary breccia	
17R-1, 40-49	87.60	Aphyric basalt	
20R-1, 128-134	102.88	Volcanic basalt breccia	
21R-2, 111-119	109.00	Volcanic basalt breccia	
24R-3, 90-101	123.58	Olivine-plagioclase-augite-phyric basalt breccia	

Figure F96 (continued). (Continued on next page.)

Core, section, interval (cm)	Depth (mbsf)	Lithology	Photograph
330-U1374A-			
27R-1, 56-70	135.76	Olivine-plagioclase-augite-phyric basalt breccia	
30R-3, 130-143	156.75	Olivine-phyric basalt breccia	
31R-3, 142-150	167.24	Olivine-phyric basalt breccia	
34R-3, 65-78	185.32	Olivine-phyric basalt breccia	
37R-4, 5-12	200.42	Olivine-phyric basalt breccia	
38R-2, 59-70	203.55	Olivine-phyric basalt breccia	

Figure F96 (continued). (Continued on next page.)

Core, section, interval (cm)	Depth (mbsf)	Lithology	Photograph
330-U1374A-			
40R-5, 9-16	225.60	Olivine-phyric basalt breccia	
43R-2, 107-116	251.85	Olivine-phyric basalt breccia	
45R-2, 20-27	270.24	Plagioclase-phyric basalt breccia	
49R-3, 60-70	310.23	Plagioclase-augite-olivine-phyric basalt breccia	
52R-4, 95-108	340.80	Plagioclase-augite-olivine-phyric basalt breccia	
57R-4, 95-106	388.77	Plagioclase-phyric basalt breccia	

Figure F96 (continued).






Core, section, interval (cm)	Depth (mbsf)	Lithology	Photograph
330-U1374A-			
58R-6, 50-62	400.22	Plagioclase-phyric basalt breccia	
62R-6, 80-91	439.30	Plagioclase-phyric basalt breccia	
64R-5, 114-126	457.34	Aphyric basalt breccia	
68R-2, 71-83	491.24	Aphyric basalt breccia	
71R-3, 47-55	516.37	Aphyric basalt sandstone	

Figure F97. Top: Photographs of five rock sections cut and counted for microsphere intrusion in Samples 330-U1374A-8R-1, 60–68 cm, and 45R-2, 20–27 cm. Subsamples for microsphere counts were taken from area between dashed yellow lines. Bottom: Photograph of rig floor workers collecting drill fluid from Core 330-U1374A-45R in a beaker for microsphere counts.



Table T1. Coring summary, Site U1374. (Continued on next page.)

Hole U1374A

Latitude: 28°35.7513'S
 Longitude: 173°22.8294'W
 Water depth (m): 1559.0
 Date started (UTC): 0330 h, 5 January 2011
 Date finished (UTC): 0645 h, 23 January 2011
 Time on hole (days): 18.1
 Seafloor depth DRF (m): 1570.0
 Seafloor depth estimation method: Tag
 Rig floor to sea level (m): 11.0
 Penetration DSF (m): 522.0
 Cored interval (m): 522.0
 Recovered length (m): 457.89
 Recovery (%): 88
 Drilled interval (m): NA
 Number of drilled interval: 0
 Total number of cores: 73
 Number of APC cores: 0
 Number of XCB cores: 0
 Number of RCB cores: 73
 Number of other cores: 0

Core	Date (2011)	Time UTC (h)	Depth drilled (m DSF)		Advanced (m)	Recovered length (m)	Curated length (m)	Depth cored (m CSF)		Recovery (%)
			Top	Bottom				Top	Bottom	
330-U1374A-										
1R	5 Jan	1100	0.0	9.6	9.6	7.22	7.26	0.0	7.3	75
2R	5 Jan	1705	9.6	14.4	4.8	4.37	4.75	9.6	14.6	91
3R	6 Jan	0235	14.4	20.4	6.0	3.23	3.64	14.4	18.0	54
4R	6 Jan	1005	20.4	25.1	4.7	3.58	4.01	20.4	24.4	76
5R	6 Jan	1850	25.1	29.4	4.3	4.47	4.82	25.1	29.9	104
6R	6 Jan	2235	29.4	34.2	4.8	4.27	4.58	29.4	34.0	89
7R	7 Jan	0405	34.2	39.0	4.8	5.77	6.26	34.2	40.5	120
8R	7 Jan	0700	39.0	43.8	4.8	2.95	3.04	39.0	42.0	61
9R	7 Jan	0955	43.8	48.6	4.8	5.58	5.69	43.8	49.5	116
10R	7 Jan	1125	48.6	53.4	4.8	4.85	5.16	48.6	53.8	101
11R	7 Jan	1300	53.4	58.4	5.0	4.97	5.65	53.4	59.0	99
12R	7 Jan	1545	58.4	68.0	9.6	4.91	5.77	58.4	64.2	51
13R	7 Jan	1805	68.0	72.8	4.8	4.21	4.62	68.0	72.6	88
14R	7 Jan	2040	72.8	77.6	4.8	3.85	4.13	72.8	76.9	80
15R	8 Jan	0140	77.6	84.6	7.0	3.70	4.27	77.6	81.9	53
16R	8 Jan	0705	84.6	87.2	2.6	2.48	2.81	84.6	87.49	95
17R	8 Jan	1110	87.2	92.0	4.8	3.49	3.95	87.2	91.2	73
18R	8 Jan	1600	92.0	96.8	4.8	5.07	5.95	92.0	98.0	106
19R	8 Jan	1925	96.8	101.6	4.8	3.43	4.15	96.8	101.0	71
20R	8 Jan	2130	101.6	106.4	4.8	3.07	3.44	101.6	105.0	64
21R	9 Jan	0140	106.4	111.2	4.8	4.51	5.12	106.4	111.5	94
22R	9 Jan	0600	111.2	116.0	4.8	5.76	6.10	111.2	117.3	120
23R	9 Jan	0850	116.0	120.8	4.8	3.49	3.56	116.0	119.6	73
24R	9 Jan	1130	120.8	125.6	4.8	4.97	5.11	120.8	125.9	104
25R	9 Jan	1435	125.6	130.4	4.8	5.46	5.68	125.6	131.3	114
26R	10 Jan	0835	130.4	135.2	4.8	4.66	4.86	130.4	135.3	97
27R	10 Jan	1125	135.2	140.0	4.8	4.27	4.27	135.2	139.5	89
28R	10 Jan	1415	140.0	144.8	4.8	5.29	5.33	140.0	145.3	110
29R	10 Jan	1820	144.8	153.6	8.8	8.93	9.22	144.8	154.0	101
30R	10 Jan	2230	153.6	163.1	9.5	8.74	8.97	153.6	162.6	92
31R	11 Jan	0405	163.1	172.7	9.6	7.29	7.90	163.1	171.0	76
32R	11 Jan	0735	172.7	177.5	4.8	4.48	5.30	172.7	178.0	93
33R	11 Jan	1030	177.5	182.3	4.8	4.07	4.48	177.5	182.0	85
34R	11 Jan	1220	182.3	187.1	4.8	3.14	3.56	182.3	185.9	65
35R	11 Jan	1520	187.1	191.9	4.8	4.47	4.87	187.1	192.0	93
36R	11 Jan	1930	191.9	196.7	4.8	5.55	6.14	191.9	198.0	116
37R	11 Jan	2230	196.7	201.5	4.8	4.14	4.47	196.7	201.2	86
38R	12 Jan	0320	201.5	211.1	9.6	3.55	4.16	201.5	205.7	37
39R	12 Jan	0655	211.1	220.7	9.6	6.46	7.26	211.1	218.4	67
40R	12 Jan	1040	220.7	230.3	9.6	6.72	7.28	220.7	228.0	70
41R	12 Jan	1350	230.3	239.9	9.6	8.93	9.62	230.3	239.9	93
42R	12 Jan	1855	239.9	249.5	9.6	9	10.13	239.9	250.0	94
43R	12 Jan	2335	249.5	259.1	9.6	8.5	9.57	249.5	259.1	89
44R	13 Jan	0335	259.1	268.7	9.6	9.15	10.53	259.1	269.6	95
45R	13 Jan	0740	268.7	278.3	9.6	8.46	10.14	268.7	278.8	88

Table T1 (continued).

Core	Date (2011)	Time UTC (h)	Depth drilled (m DSF)		Advanced (m)	Recovered length (m)	Curated length (m)	Depth cored (m CSF)		Recovery (%)
			Top	Bottom				Top	Bottom	
46R	13 Jan	1130	278.3	287.9	9.6	8.15	9.13	278.3	287.4	85
47R	13 Jan	1525	287.9	297.5	9.6	9.12	9.80	287.9	297.7	95
48R	13 Jan	1920	297.5	307.1	9.6	9.95	10.48	297.5	308.0	104
49R	13 Jan	2345	307.1	316.7	9.6	8.41	8.61	307.1	315.7	88
50R	14 Jan	0410	316.7	326.3	9.6	10.00	10.66	316.7	327.4	104
51R	14 Jan	0755	326.3	335.9	9.6	9.86	10.55	326.3	336.9	103
52R	14 Jan	1140	335.9	345.5	9.6	8.16	8.72	335.9	344.6	85
53R	14 Jan	1600	345.5	354.8	9.3	8.32	8.90	345.5	354.4	89
54R	14 Jan	1930	354.8	364.4	9.6	8.68	9.69	354.8	364.5	90
55R	14 Jan	2220	364.4	374.0	9.6	5.91	7.04	364.4	371.4	62
56R	15 Jan	0135	374.0	383.6	9.6	7.47	7.84	374.0	381.8	78
57R	15 Jan	0525	383.6	393.2	9.6	9.17	9.65	383.6	393.3	96
58R	15 Jan	0940	393.2	402.8	9.6	9.92	10.31	393.2	403.5	103
59R	15 Jan	1345	402.8	412.4	9.6	7.85	8.05	402.8	410.9	82
60R	15 Jan	1815	412.4	422.0	9.6	9.06	9.33	412.4	421.7	94
61R	15 Jan	2210	422.0	431.5	9.5	9.99	10.38	422.0	432.4	105
62R	16 Jan	0150	431.5	441.1	9.6	9.39	9.99	431.5	441.5	98
63R	16 Jan	0600	441.1	450.7	9.6	9.18	9.73	441.1	450.8	96
64R	16 Jan	1005	450.7	460.3	9.6	7.97	8.56	450.7	459.3	83
65R	16 Jan	1340	460.3	469.9	9.6	8.37	8.69	460.3	469.0	87
66R	16 Jan	1635	469.9	479.5	9.6	9.35	9.42	469.9	479.3	97
67R	16 Jan	1955	479.5	489.1	9.6	10.27	10.23	479.5	489.7	107
68R	16 Jan	2320	489.1	498.7	9.6	8.10	9.57	489.1	498.7	84
69R	17 Jan	0235	498.7	508.3	9.6	8.86	9.78	498.7	508.5	92
70R	17 Jan	0845	508.3	513.1	4.8	3.91	4.40	508.3	512.7	81
71R	17 Jan	1200	513.1	517.9	4.8	3.81	4.16	513.1	517.3	79
72R	17 Jan	1435	517.9	521.0	3.1	2.32	2.59	517.9	520.5	75
73R	17 Jan	1620	521.0	522.0	1.0	0.88	0.81	521.0	521.8	88
Hole U1374A totals:					522	457.89	494.66			

NA = not applicable. UTC = universal time coordinated. DRF = drilling depth below rig floor, DSF = drilling depth below seafloor, CSF = core depth below seafloor. APC = advanced piston corer (core type H), XCB = extended core barrel (core type X), RCB = rotary core barrel (core type R).

**Table T2.** Occurrence of basalt clast types, Site U1374.

Core, section	Strat. unit	Basalt clasts										
		Type 1	Type 2	Type 3	Type 4	Type 5	Type 6	Type 7	Type 8	Type 9	Type 10	Type 11
		Highly olivine-pyroxene-phyric basalt, 1% vesicles, medium gray	Highly olivine-phyric basalt, 0.1% vesicles, mottled gray-orange	Aphyric basalt, 2% vesicles, medium gray	Sparely olivine-phyric basalt, 10%–20% vesicles, reddish medium gray	Aphyric basalt, 15% vesicles, medium gray	Basaltic froth in small (modal size = 5 mm) angular clasts, 60% vesicles, yellow	Very highly olivine-phyric basalt, 5%–10% vesicles, mottled orange-gray	Sparely olivine-phyric basalt, 1% vesicles, medium gray	Aphyric basalt, 0.5% vesicles, medium gray	Moderately olivine-phyric basalt, 3% vesicles, medium gray	Moderately plagioclase-olivine-phyric basalt, 1% vesicles, greenish medium gray
330-U1374A-												
3R-1	II	X	X	X								
3R-2	II	X										
12R-4	IX				X				X			
13R-1	IX			X	X	X	X					
13R-2	IX	X		X	X	X	X					
13R-3	IX	X		X		X	X					
13R-4	IX			X			X	X				
14R-1	IX	X		X	X		X	X				
14R-2	IX				X	X	X	X	X			
14R-3	IX					X	X		X	X	X	
14R-4	IX				X		X					
15R-1	IX			X		X	X	X		X	X	
15R-2	IX	X	X		X	X	X	X		X		
15R-3	IX			X		X			X	X	X	
21R-3	XI					X				X		
21R-4	XI									X		
22R-1	XI									X		
22R-2	XI	X								X		X
22R-3	XI	X								X		
22R-4	XI	X										

Details on nature and occurrence of clast types are available in SEDIMENT in [“Supplementary material.”](#)

Table T3. Distribution of Cenozoic calcareous nannofossils, Hole U1374A.

Core, section, interval (cm)	Top depth (mbsf)	Bottom depth (mbsf)	Strat. unit	Zone	Age	Preservation	<i>Calcidiscus leptoporus</i>	<i>Calcidiscus macintyreii</i>	<i>Ceratolithus cristatus</i>	<i>Ceratolithus telesmus</i>	<i>Gephyrocapsa</i> sp.	<i>Helicosphaera inversa</i>	<i>Helicosphaera kamptneri</i>	<i>Helicosphaera sellii</i>	<i>Pseudoemiliania lacunosa</i>	<i>Rhabdosphaera clavigera</i>
330-U1374A-1R-1W, 99–100	0.99	1.00	I	CN13–CN15	Pleistocene–Holocene	M	F	R	A				F	C	F	
1R-2W, 99–100	2.49	2.50	I	CN13–CN15	Pleistocene–Holocene	M	F	R	R	A			F	C	F	
1R-3W, 99–100	3.99	4.00	I	CN13–CN15	Pleistocene–Holocene	M	F	R	R	A		R	F	R	C	F
1R-4W, 99–100	5.49	5.50	I	CN13–CN15	Pleistocene–Holocene	M	F	R	R	A		R		C	F	
1R-5W, 30–31	6.30	6.31	I	CN13–CN15	Pleistocene–Holocene	M	F	R	R	A			F	R	C	F

Preservation: M = moderate. Abundance: A = abundant, C = common, F = few, R = rare.

Table T4. Distribution of planktonic foraminifers, Hole U1374A.

Core, section interval (cm)	Top depth (mbsf)	Bottom depth (mbsf)	Strat. unit	Zone	Age	Preservation	Group abundance	<i>Globigerina bulloides</i>	<i>Globigerina falconensis</i>	<i>Globigerinella aequilateralis</i>	<i>Globigerinoides quadrilobatus</i>	<i>Globigerinoides ruber</i>	<i>Globigerinoides sacculifer</i>	<i>Globorotalia (Globoconella) inflata</i>	<i>Globorotalia (Globoconella) tumida tumida</i>	<i>Globorotalia (Hirsutella) hirsuta</i>	<i>Globorotalia (Hirsutella) scitula</i>	<i>Globorotalia (Truncorotalia) crassaformis</i>	<i>Globorotalia (Truncorotalia) truncatulinoides</i>	<i>Neogloboquadrina dutertrei</i>	<i>Orbulina universa</i>	<i>Pulleniatina obliquiloculata</i> (D)	<i>Sphaeroidinella dehiscens</i> s.l.
330-U1374A-1R-1W, 0–2	0.00	0.02	I	PL6–PT1b	Pleistocene–Holocene	G	A	F	R	R	F	A	R	A	P		F	F	A	P	F		
1R-2W, 0–2	1.50	1.52	I	PL6–PT1b	Pleistocene–Holocene	G	A				R	R		A			R	A	A		F		
1R-4W, 145–150	5.95	6.00	I	PL6–PT1b	Pleistocene–Holocene	G	A			P				A	R	P	P	R	A	P	P		P
1R-5W, 49–51	6.49	6.51	I	PL6–PT1b	Pleistocene–Holocene	G	A	R		R	R			A	R		R	A	A		F		P
1R-5W, 60–62	6.60	6.62	I	PL6–PT1b	Pleistocene–Holocene	M	A	R		R	R			A	R			F	A	P	R	P	
1R-6	6.78	6.78	IIA	ND	Unidentified	B																	

ND = not defined. Preservation: G = good, M = moderate. Abundance: A = abundant, F = few, R = rare, P = present, B = barren.

Table T5. Distribution of Mesozoic calcareous nannofossils, Hole U1374A.

Core, section interval (cm)	Top depth (mbsf)	Strat. unit	Zone	Age	Preservation	Abundance	<i>Arkhangelskiella</i> sp.	<i>Eiffelithus gorkae</i>	<i>Eiffelithus turrisseiffelii</i>	<i>Microrhabdulus belgicus</i>	<i>Micula concava</i>	<i>Micula decussata</i>	<i>Nephrolithus frequens</i>	<i>Prediscosphaera cretacea</i>	<i>Prediscosphaera spinosa</i>
330-U1374A-2R-4W, 32	13.75	IIC	~CC26	~late Maastrichtian	P	R									
3R-1W, 70	15.10	IIC	CC25–CC26	late Maastrichtian	P	R	R	R	R	R		R	R	R	R

Preservation: P = poor. Abundance: R = rare, B = barren.

Table T6. Distribution of macro- and microfossils observed in thin sections, Hole U1374A.

Core, section interval (cm)	Top depth (mbsf)	Bottom depth (mbsf)	Strat. unit	Zone	Age	<i>Globotruncanella</i> sp.	<i>Globotruncanella conica</i>	<i>Globotruncanella stuarti</i>	<i>Radotruncana calcarata</i>	Benthic foraminifers	Macrofossils	Planktonic foraminifers
330-U1374A-												
2R-1W, 35–38	9.95	9.98	IIA	ND	Unidentified					B	B	B
2R-2W, 106–109	11.78	11.81	IIA	ND	Unidentified					B	B	B
2R-3W, 70–73	12.78	12.81	IIB	ND	Unidentified					B	B	B
2R-4W, 10–13	13.53	13.56	IIC	ND	Unidentified					B	B	B
2R-4W, 27–32	13.70	13.75	IIB	<i>G. gansseri</i> – <i>A. mayaroensis</i>	late Campanian–Maastrichtian	P	P			P	P	P
2R-4W, 88–91	14.31	14.34	IIC	ND	Unidentified					B	P	B
3R-1W, 70–72	15.10	15.12	IID	<i>Radotruncana calcarata</i>	late Campanian	P		P		P	P	P
3R-2W, 65–68	16.48	16.51	IIE	ND	Unidentified					B	P	B
6R-1W, 32–35	29.72	29.75	V	ND	Unidentified					P	P	B
7R-4W, 26–30	38.50	38.54	VIIA	ND	Unidentified					B	P	B
7R-5W, 14–18	39.70	39.74	VIIA	ND	Unidentified					B	B	B
8R-1W, 53–57	39.53	39.57	VIIA	ND	Unidentified					B	B	B
8R-2W, 111–115	41.06	41.10	VIIA	ND	Unidentified					B	B	B
8R-3W, 19–22	41.51	41.54	VIIA	ND	Unidentified					B	P	B
13R-1W, 50–53	68.50	68.53	IXA	ND	Unidentified					B	B	B
14R-1W, 8–10	72.88	72.90	IXA	ND	Unidentified					B	B	B
14R-1W, 57–60	73.37	73.40	IXA	ND	Unidentified					B	B	B
14R-3W, 59–63	75.67	75.80	IXB	ND	Unidentified					B	B	B
17R-1W, 9–12	87.29	87.32	X	ND	Unidentified					P	P	B
17R-3W, 78–81	90.56	90.59	X	ND	Unidentified					B	P	B
19R-1W, 50–53	97.30	97.33	X	ND	Unidentified					P	P	B
21R-3W, 80–84	110.07	110.11	XIB	ND	Unidentified					B	P	B
21R-4W, 76–80	111.34	111.38	XIB	ND	Unidentified					P	P	P
22R-1W, 2–6	111.22	111.26	XIB	ND	Unidentified					P	P	P
22R-2W, 1–5	112.47	112.51	XIB	ND	Unidentified					P	P	B
22R-3W, 21–25	114.10	114.14	XIB	ND	Unidentified					B	P	B
31R-5W, 28–32	168.87	169.01	XIII	ND	Unidentified					B	B	B
43R-6W, 33–36	257.00	257.03	XIV	ND	Unidentified					P	P	P
43R-6W, 70–74	257.37	257.41	XIV	ND	Unidentified					P	P	P
44R-3W, 18–20	262.03	262.05	XIV	ND	Unidentified					B	P	B
47R-3W, 26–30	290.53	290.57	XVI	ND	Unidentified					P	P	P

ND = not defined. Abundance: P = present (number of individuals was not counted), B = barren.

Table T7. In situ confidence index (ISCI) for igneous lithologic units, Site U1374. (Continued on next two pages.)

Lith. unit	ISCI	Core, section, interval (cm)	Unit description	Strat. unit
330-U1374A-				
1	3	3R-2, 89, to 3R-3, 76	Lava flow	III
2	3	4R-1, 0, to 5R-4, 99	Lava flow	IV
3	NA	5R-4, 99, to 6R-4, 34	Volcanic breccia	V
4	3	7R-1, 0, to 7R-3, 57	Lava flow	VI
5	NA	7R-3, 57, to 7R-3, 72	Volcanic breccia	VI
6	NA	7R-3, 72, to 7R-4, 55	Lithic-vitric volcanic sand	VII
7a	NA	7R-4, 55, to 8R-3, 16	Lithic-vitric volcanic sand	VII
7b	NA	8R-3, 16, to 8R-3, 52	Volcanic breccia with sand and bioclast matrix	VII
8	NA	8R-3, 52, to 12R-4, 100	Volcanic breccia	VIII
	NA	12R-4, 100, to 16R-1, 10	Sedimentary breccia	IX
9	3	16R-1, 10, to 16R-2, 139	Lava lobe	X
10	NA	17R-1, 0, to 18R-2, 84	Volcanic breccia	X
11	2	18R-2, 84, to 18R-3, 65.5	Lava lobe	X
12	NA	18R-3, 65.5, to 21R-1, 142	Volcanic breccia	X
13	1	21R-1, 142, to 21R-2, 103	Lava lobe	X
14	NA	21R-2, 103, to 21R-3, 59	Volcanic breccia	X
	NA	21R-3, 59, to 22R-5, 24	Sedimentary conglomerate/breccia	XI
15	NA	22R-5, 24, to 23R-3, 73	Volcanic peperitic breccia	XII
16	1	23R-3, 73, to 24R-1, 44	Lava lobe	XII
17	NA	24R-1, 44, to 24R-1, 70	Volcanic breccia	XII
18	1	24R-1, 70, to 24R-1, 103	Lava flow or fragment	XII
19	NA	24R-1, 103, to 24R-4, 20	Volcanic breccia	XII
20	1	24R-4, 20, to 24R-4, 53.5	Lava flow or fragment	XII
21	NA	24R-4, 53.5, to 24R-4, 85	Volcanic breccia	XII
22	0	24R-4, 85, to 24R-4, 105	Lava flow or fragment	XII
23	0	24R-4, 105, to 25R-1, 98	Volcanic breccia	XII
24	0	25R-1, 98, to 25R-1, 115	Lava flow or fragment	XII
25	NA	25R-2, 0, to 25R-2, 77	Volcanic breccia	XII
26	1	25R-2, 77, to 25R-2, 98	Lava flow or fragment	XII
27	NA	25R-2, 98, to 25R-2, 111	Volcanic breccia	XII
28	1	25R-2, 111, to 25R-3, 11	Lava flow or fragment	XII
29	NA	25R-3, 11, to 25R-3, 84	Volcanic breccia	XII
30	0	25R-3, 84, to 25R-3, 109	Lava flow or fragment	XII
31	NA	25R-3, 109, to 29R-2, 15	Volcanic breccia	XII
32	NA	29R-2, 15, to 29R-3, 20	Volcanic breccia with sandy matrix	XIII
33	NA	29R-3, 20, to 29R-3, 86	Volcanic breccia	XIII
34	0	29R-3, 86, to 29R-3, 99	Lava fragment	XIII
35	NA	29R-3, 99, to 29R-4, 7	Volcanic breccia	XIII
36	0	29R-4, 7, to 29R-4, 27	Lava fragment	XIII
37	NA	29R-4, 27, to 29R-4, 104	Volcanic breccia	XIII
38	0	29R-4, 104, to 29R-5, 130	Lava fragment	XIII
39	NA	29R-5, 0, to 30R-1, 36.5	Volcanic breccia	XIII
40	1	30R-1, 36.5, to 30R-1, 108	Lava fragment	XIII
41	NA	30R-1, 108, to 30R-1, 143	Volcanic breccia	XIII
42	1	30R-1, 143, to 30R-2, 38	Lava fragment	XIII
43	NA	30R-2, 38, to 30R-2, 48	Volcanic breccia	XIII
44	0	30R-2, 48, to 30R-2, 67.5	Lava fragment	XIII
45	NA	30R-2, 67.5, to 30R-2, 79	Volcanic breccia	XIII
46	1	30R-2, 79, to 30R-2, 126	Lava lobe	XIII
47	NA	30R-2, 126, to 30R-4, 27	Volcanic breccia	XIII
48	NA	30R-4, 27, to 30R-4, 128	Volcanic breccia	XIII
49	1	30R-4, 128, to 30R-5, 38	Lava fragment	XIII
50	NA	30R-5, 38, to 31R-1, 66	Volcanic breccia	XIII
51	NA	31R-1, 66, to 31R-1, 129	Volcanic breccia	XIII
52	1	31R-1, 129, to 31R-2, 42	Lava lobe fragment	XIII
53	NA	31R-2, 42, to 31R-4, 116	Volcanic breccia	XIII
54	0	31R-4, 116, to 31R-4, 140	Lava lobe fragment	XIII
55	NA	31R-5, 0, to 31R-5, 122	Volcanic breccia with sandy matrix	XIII
56	1	31R-5, 122, to 31R-6, 56	Lava lobe fragment	XIII
57	NA	31R-6, 56, to 32R-3, 102	Volcanic breccia with sandy matrix	XIII
58	2	32R-3, 102, to 32R-4, 91	Lava lobe fragment	XIII
59	NA	33R-1, 0, to 33R-3, 77	Volcanic breccia	XIII
60	NA	33R-3, 77, to 33R-4, 6	Volcanic breccia	XIII
61	0	33R-4, 6, to 33R-4, 36	Lava fragment	XIII
62	NA	33R-4, 36, to 34R-1, 4.5	Volcanic breccia	XIII
63	1	34R-1, 4.5, to 34R-1, 54	Lava fragment	XIII

Table T7 (continued). (Continued on next page.)

Lith. unit	ISCI	Core, section, interval (cm)	Unit description	Strat. unit
64	NA	34R-1, 54, to 35R-2, 128	Volcanic breccia	XIII
65	1	35R-2, 128, to 35R-3, 104	Lava lobe	XIII
66	NA	35R-3, 104, to 35R-4, 94	Volcanic breccia	XIII
67	2	36R-1, 0, to 36R-1, 123	Lava lobe	XIII
68	NA	36R-1, 123, to 36R-2, 50	Volcanic breccia	XIII
69	0	36R-2, 50, to 36R-2, 79	Lava fragment	XIII
70	NA	36R-2, 79, to 36R-4, 65	Volcanic breccia	XIII
71	2	36R-4, 65, to 36R-5, 62	Lava lobe	XIII
72	0	37R-1, 0, to 37R-1, 102	Autobrecciated lava lobe	XIII
73	1	37R-1, 102, to 37R-2, 84	Autobrecciated lava lobe; sandy matrix at top	XIII
74	2	37R-2, 84, to 37R-4, 80	Autobrecciated lava lobe; sandy matrix at top	XIII
75	NA	38R-1, 0, to 38R-1, 42	Volcanic breccia	XIII
76	0	38R-1, 42, to 38R-1, 80	Lava fragment	XIII
77	NA	38R-1, 80, to 38R-3, 42	Volcanic breccia	XIII
78	2	38R-3, 42, to 38R-3, 135	Lava lobe	XIII
79	NA	38R-3, 135, to 39R-5, 38.5	Volcanic breccia	XIII
80	0	39R-5, 38.5, to 39R-5, 117	Lava lobe or fragment	XIII
81	NA	39R-5, 117, to 41R-3, 79	Volcanic breccia	XIII
82	2	41R-3, 79, to 41R-4, 75	Lava lobe	XIII
83	NA	41R-4, 75, to 42R-5, 99	Volcanic breccia	XIII
84	0	42R-5, 99, to 42R-5, 138.5	Lava lobe or fragment	XIII
85	NA	42R-5, 138.5, to 42R-6, 68	Volcanic breccia	XIII
86	1	42R-6, 68, to 42R-6, 124.5	Lava lobe or fragment	XIII
87	NA	42R-6, 124.5, to 43R-6, 7.5	Volcanic breccia	XIII
88	NA	43R-6, 7.5, to 45R-8, 10	Volcanic breccia	XIV
89	NA	45R-8, 10, to 46R-7, 68	Volcanic breccia	XV
90	0	46R-7, 68, to 46R-7, 88	Aphyric basalt	XV
91	NA	46R-7, 88, to 47R-3, 5	Volcanic breccia	XV
92	NA	47R-3, 5, to 47R-3, 88	Volcanic breccia with sandy matrix	XVI
93	NA	47R-3, 88, to 48R-7, 81	Volcanic breccia	XVI
94	0	48R-8, 0, to 48R-8, 28	Lava fragment	XVI
95	NA	48R-8, 28, to 50R-2, 15	Volcanic breccia	XVI
96	1	50R-2, 15, to 50R-2, 94	Pillow or lava lobe?	XVI
97	NA	50R-2, 94, to 51R-1, 11	Volcanic breccia	XVI
98	1	51R-1, 11, to 51R-1, 54	Pillow or lava lobe?	XVI
99	NA	51R-1, 54, to 51R-2, 63	Volcanic breccia	XVI
100	NA	51R-2, 63, to 51R-6, 12	Volcanic breccia	XVI
101	1	51R-6, 12, to 51R-6, 56	Pillow or lava lobe?	XVI
102	NA	51R-6, 56, to 51R-8, 90	Volcanic breccia	XVI
103	3	52R-1, 0, to 52R-2, 48	Intrusive sheet	
102b	NA	52R-2, 48, to 52R-2, 64.5	Volcanic breccia	XVI
103b	3	52R-2, 64.5, to 52R-3, 45	Intrusive sheet	
104	NA	52R-3, 45, to 53R-5, 87	Volcanic breccia	XVI
105	NA	53R-5, 87, to 55R-1, 134	Volcanic breccia	XVII
106	3	55R-1, 134, to 55R-2, 80	Intrusive sheet	
107	NA	55R-2, 80, to 56R-1, 118.5	Volcanic breccia	XVII
108	NA	56R-1, 118.5, to 57R-1, 62	Volcanic breccia	XVIII
109	1	57R-1, 62, to 57R-1, 138	Lava lobe or fragment	XVIII
110	NA	57R-2, 0, to 57R-2, 38	Volcanic breccia	XVIII
111	1	57R-2, 38, to 57R-2, 82	Brecciated lava lobe or fragment	XVIII
112	1	57R-2, 82, to 57R-3, 15	Lava lobe or fragment (massive base to Unit 111)	XVIII
113	NA	57R-3, 15, to 57R-8, 58	Volcanic breccia	XVIII
114	1	57R-8, 58, to 58R-1, 54	Lava lobe or fragment	XVIII
115	NA	58R-1, 54, to 58R-3, 33	Volcanic breccia	XVIII
116	3	58R-3, 33, to 58R-4, 73	Intrusive sheet	
117	NA	58R-4, 73, to 59R-1, 3	Volcanic breccia	XVIII
118	1	59R-1, 3, to 59R-1, 35	Lava lobe or fragment	XVIII
119	NA	59R-1, 35, to 59R-1, 108	Volcanic breccia	XVIII
120	3	59R-1, 108, to 59R-2, 121	Intrusive sheet	
121	NA	59R-2, 121, to 59R-4, 100	Volcanic breccia	XVIII
122	3	59R-4, 100, to 59R-5, 10	Intrusive sheet	
123	NA	59R-5, 10, to 59R-6, 25	Volcanic breccia	XVIII
124	3	59R-6, 25, to 60R-1, 34	Intrusive sheet	
125	NA	60R-1, 34, to 60R-1, 123	Brecciated margin of intrusive sheet	
126	3	60R-1, 123, to 60R-3, 73	Intrusive sheet	
127	NA	60R-3, 73, to 60R-3, 90	Volcanic breccia	XVIII
128	3	60R-3, 90, to 60R-4, 93.5	Intrusive sheet	
129	NA	60R-4, 93.5, to 61R-3, 87	Volcanic breccia	XVIII
130	1	61R-3, 87, to 61R-3, 130	Brecciated lava lobe or fragment	XVIII

Table T7 (continued).

Lith. unit	ISCI	Core, section, interval (cm)	Unit description	Strat. unit
131	NA	61R-3, 130, to 63R-1, 45	Volcaniclastic breccia	XVIII
132	0	63R-1, 45, to 63R-1, 91	Lava lobe or fragment	XVIII
133	NA	63R-1, 91, to 63R-3, 54	Volcaniclastic breccia	XVIII
134	1	63R-3, 54, to 63R-3, 140	Lava lobe or fragment	XVIII
135	NA	63R-4, 0, to 64R-2, 1	Volcaniclastic breccia	XIX
136	3	64R-2, 1, to 64R-3, 33	Intrusive sheet	
137	NA	64R-3, 33, to 66R-1, 21.5	Volcaniclastic breccia	XIX
138	NA	66R-1, 21.5, to 68R-2, 135	Volcaniclastic breccia	XIX
139	3	68R-2, 135, to 68R-5, 47	Intrusive sheet	
140	3	68R-5, 47, to 68R-6, 72	Intrusive sheet	
141	NA	68R-6, 72, to 68R-7, 122	Volcaniclastic breccia	XIX
142	NA	69R-1, 0, to 69R-4, 28	Vitric-lithic volcanic sand and gravel	XIX
143	NA	69R-4, 28, to 69R-7, 95	Volcaniclastic breccia	XIX
144	0	69R-7, 95, to 69R-7, 127	Basalt fragment	XIX
145	NA	69R-7, 127, to 69R-7, 145	Volcaniclastic breccia	XIX
146	3	70R-1, 0, to 71R-2, 71	Intrusive sheet?	XIX
147	NA	71R-2, 71, to 72R-1, 55	Vitric-lithic volcanic gravel	XIX
148	3	72R-1, 55, to 73R-1, 81	Intrusive sheet?	XIX

ISCI: 0 = unlikely to be in situ, 1 = could be in situ, 2 = probably in situ, 3 = highly likely to be in situ, NA = not applicable. See “Igneous petrology and volcanology” in the “Methods” chapter (Expedition 330 Scientists, 2012a) for a full explanation of the ISCI.

Table T8. Occurrence of fresh or nearly fresh olivine and volcanic glass in thin section, Hole U1374A.

Core, section	Thin section	Depth (mbsf)	Rocks	Olivine freshness (%)	Glass freshness (%)
330-U1374A-					
3R-1	114	15.54	Clast in sediment	65	—
3R-2	115	15.90	Lava flow	80	—
3R-2	116	16.36	Lava flow	60	—
3R-2	118	16.91	Clast in sediment	85	35
7R-4	126	39.36	Clast in sediment	—	50
13R-1	136	68.03	Clast in sediment	5	—
16R-1	141	85.85	Lava lobe	5	—
17R-3	143	87.85	Lava flow	20	—
21R-2	149	108.12	Lava lobe	—	5
24R-1	157	121.07	Lava lobe	60	—
24R-1	158	121.57	Lava flow or fragment	10	—
24R-4	159	124.45	Lava flow or fragment	50	—
25R-1	161	126.72	Lava flow or fragment	10	—
25R-2	163	128.03	Lava flow or fragment	10	—
25R-3	164	129.15	Lava lobe	20	—
27R-2	166	137.05	Volcanic breccia	10	—
29R-4	170	149.42	Lava fragment	—	35
30R-1	172	154.10	Lava fragment	40	—
30R-5	173	159.39	Lava fragment	60	—
32R-4	176	177.02	Lava lobe fragment	60	—
33R-1	177	178.32	Volcanic breccia	10	—
34R-1	178	182.42	Lava fragment	20	—
34R-2	179	184.38	Volcanic breccia	10	10
35R-3	180	190.33	Lava lobe	40	—
36R-1	181	192.88	Lava lobe	20	—
36R-4	182	196.84	Lava lobe	20	—
37R-3	183	199.64	Autobrecciated lava lobe	60	—
38R-3	184	205.06	Lava lobe	60	—
39R-2	185	213.11	Volcanic breccia	1	15
40R-4	187	225.37	Volcanic breccia	20	—
41R-4	188	234.71	Lava lobe	60	—
41R-6	189	238.09	Volcanic breccia	40	—
43R-2	192	251.52	Volcanic breccia	90	—
58R-4	215	397.70	Intrusive sheet	—	50
72R-1	222	518.43	Vitric-lithic volcanic gravel	—	10

— = no data.

Table T9. Geopetal structures, Hole U1374A.

Core, section, interval (cm)	Depth (mbsf)	Angle on core face (°)
330-U1374A-		
3R-2A, 94	16.8	0
4R-2A, 9	21.9	0
4R-2A, 29	22.1	-0
4R-2A, 63	22.5	-0
6R-1A, 3	29.4	0
6R-1A, 16	29.6	-8
5R-4A, 103	29.7	-1
5R-4A, 110	29.8	0
6R-1A, 46	29.9	-1
7R-3A, 61	37.5	0
7R-3A, 71.5	37.6	0
8R-3A, 29	41.6	2
8R-3A, 45	41.8	0
11R-3A, 5.5	56.3	0
13R-1A, 131	69.3	0
13R-1A, 143	69.4	0
13R-2A, 49	70.0	0
16R-1A, 17.5	84.8	0
16R-2A, 132	87.3	0
17R-1A, 17	87.4	0
17R-1A, 21	87.4	0
17R-1A, 98.5	88.2	0
17R-3A, 33.0–34.0	90.1	0
18R-1A, 103	93.0	0
18R-1A, 106.5	93.1	0
21R-3A, 22	109.5	0
21R-3A, 54	109.8	0
21R-3A, 59.5	109.9	0
21R-3A, 128	110.6	0
22R-2A, 84.5	113.3	0
27R-4A, 50	139.3	0

All geopetals are within 2° from horizontal as viewed on the archive-half core face, except at 29.6 mbsf, where the underlying 6 cm of sediment has clearly slumped. Because of >100% recovery in Core 330-U1374A-5R, the geopetals in Section 330-U1374A-5R-4 appear at greater depths below seafloor than those in Section 330-U1374A-6R-1.

Table T10. Rocks with flow alignment textures, Hole U1374A.

Core, section, interval (cm)	Depth (mbsf)	Flow interval (cm)	Flow/Clast/ Intrusion	Direction*	Strength	Thin section number (where present)
330-U1374A-						
3R-2W, 7–9	15.9	7–9	Clast	NA	Weak	115
4R-1	21.0	25–138	Flow	Horizontal	Moderate–strong	
4R-2W, 38–41	22.5	15–132	Flow	Horizontal to subhorizontal	Moderate–strong	119
4R-3	23.8	5–102	Flow	Horizontal	Moderate	
5R-1	25.5	7–84	Flow	Horizontal to subhorizontal	Moderate–strong	
5R-2W, 137–139	26.4	1–97	Flow	Horizontal to subhorizontal	Moderate–strong	120
5R-3	28.3	1–127	Flow	Horizontal	Moderate–strong	
6R-1W, 114–116	30.5	114–116	Flow	Horizontal to subhorizontal	Moderate	123
7R-1W, 136–138	34.5	0–59	Flow	Horizontal	Weak	124
7R-2	36.5	70–123	Flow	Horizontal	Moderate	
7R-3	37.1	0–38	Flow	Horizontal	Moderate	
15R-1	78.0	41–42	Flow	Subhorizontal	Weak	
15R-3	80.8	40–49	Clast	NA	Weak	
16R-1W, 125–127	85.6	39–131	Flow	Horizontal	Moderate	141
16R-2	86.7	28–116	Flow	Horizontal to subhorizontal	Moderate–strong	
17R-1W, 65–67	87.9	65–67	Flow	Subhorizontal	Weak	143
18R-2	94.6	109–125	Flow	Subhorizontal	Weak	
18R-3W, 23–25	95.3	54–63	Flow	Horizontal	Strong	146
19R-1W, 50–53	97.3	50–53	Clast	NA	Weak	147
19R-2W, 41–43	98.7	41–43	Clast	NA	Weak	148
21R-2W, 23–25	108.1	23–25	Flow	Subvertical	Moderate–strong	149
30R-5W, 12–15	159.4	12–15	Flow	Subvertical	Moderate	173
32R-4W, 3–5	177.2	1–40	Flow	Horizontal	Moderate	176
33R-1W, 82–84	178.3	82–84	Clast	NA	Weak	177
34R-1W, 12–14	182.4	12–14	Flow	NA (TS-nonoriented)	Weak	178
34R-2W, 63–65	184.4	63–65	Clast	NA	Weak	179
35R-3W, 61–63	190.3	61–63	Flow	NA (TS-nonoriented)	Weak	180
36R-1W, 98–100	192.8	82–94	Flow	Subhorizontal	Moderate	181
36R-4W, 76–78	197.3	118–133	Flow	Subhorizontal	Weak	182
37R-3W, 20–22	199.6	20–22	Flow	Horizontal	Moderate	183
38R-3W, 86–88	205.1	86–88	Flow	Subhorizontal	Moderate	184
39R-5W, 66–68	217.7	66–68	Flow	Horizontal	Moderate	186
40R-4W, 130–132	225.4	130–132	Clast	NA	Weak	187
41R-4W, 36–38	234.9	37–70	Flow	Subhorizontal	Moderate–strong	188
41R-6W, 103–105	237.9	72–102	Flow	Subhorizontal	Moderate	189
42R-5W, 114–117	246.7	114–117	Flow	NA	Moderate	190
42R-6W, 119–121	248.2	119–121	Flow	Subvertical	Weak–moderate	191
42R-7	248.6	7–15	Clast	NA	Moderate	
43R-7W, 83–85	258.8	83–85	Clast	NA	Moderate	195
46R-6W, 140–142	286.4	140–142	Clast	NA	Moderate	199
54R-4W, 38–40	259.3	38–40	Clast	NA	Moderate	210
55R-1	365.7	129–136	Flow	Subhorizontal	Strong	
55R-2	366.2	0–80	Flow	Subhorizontal	Moderate–strong	
56R-4W, 13–15	378.4	13–15	Flow	Horizontal	Weak	213
61R-1	422.7	65–75	Flow	Horizontal	Strong	
61R-3	425.9	85–127	Flow	Subhorizontal to subvertical	Moderate–strong	
62R-7	440.4	75–80	Clast	NA	Strong	
63R-2	443.2	52–78	Clast	NA	Strong	
63R-8	450.3	6–8	Clast	NA	Moderate	
64R-6W, 129–132	459.1	129–132	Clast	NA	Strong	219
67R-1	479.9	34–38	Clast	NA	Moderate	
70R-3	511.7	22–130	Intrusion or flow	Subvertical	Moderate–strong	
70R-4	512.4	1–31	Intrusion or flow	Subvertical	Strong	
71R-1	513.7	3–130	Intrusion or flow	Subvertical	Weak–moderate	
71R-2	514.6	0–22	Intrusion or flow	Subvertical	Weak–moderate	
72R-1W, 53–55	518.4	53–55	Intrusion or flow	Vertical	Weak–moderate	222
72R-2W, 32–35	519.9	59–82	Intrusion or flow	Subvertical	Weak–moderate	223
73R-1	521.4	0–80	Intrusion or flow	Subvertical to subhorizontal	Moderate	

* = not applicable (NA) in clasts. TS = thin section.

**Table T11.** Whole-rock major and trace element compositions, Hole U1374A. (Continued on next page.)

Hole:	330-U1374A-																
Core, section:	3R-2	4R-2	7R-1	12R-4	13R-1	16R-1	17R-1	18R-1	18R-3	19R-2	21R-2	22R-4	24R-1	27R-2	30R-5	32R-4	36R-1
Piece:	4D	2A	7	12	1	10	5	3	2	6	4	2	1C	1A	1	1	9
Interval (cm):	108–110	36–38	138–140	113–115	5–6	130–132	63–65	33–35	21–23	39–41	25–27	51–53	25–27	49–51	15–17	5–7	100–102
Top depth (mbsf):	16.91	22.18	35.58	63.8	68.05	85.9	87.83	92.33	94.95	98.63	108.14	115.52	121.05	137.05	159.42	177.04	192.9
Strat. unit:	III	IV	VI	IX	IX	X	X	X	X	X	X	XI	XII	XII	XIII	XIII	XIII
Major element oxide (wt%):																	
SiO ₂	45.00	45.84	45.52	45.88	45.93	44.79	44.43	44.19	43.83	44.16	44.66	45.71	46.09	44.64	44.40	47.10	44.57
TiO ₂	2.55	3.30	3.37	2.95	3.01	3.61	3.63	3.76	3.53	3.64	3.65	2.90	2.79	2.85	2.74	3.07	3.11
Al ₂ O ₃	14.74	16.02	16.11	15.96	17.22	17.43	17.34	17.82	16.87	17.46	17.30	15.22	15.57	15.17	14.64	16.16	16.22
Fe ₂ O ₃ ^T	12.00	14.89	14.24	10.27	12.02	14.26	14.97	15.50	15.18	15.17	15.09	13.55	13.29	12.56	12.66	12.64	12.90
MnO	0.19	0.19	0.20	0.15	0.15	0.19	0.20	0.18	0.17	0.19	0.18	0.17	0.17	0.17	0.18	0.16	0.18
MgO	9.92	5.39	4.85	4.10	2.79	5.27	5.52	4.12	5.39	5.29	4.96	7.40	8.66	7.32	8.15	6.14	5.54
CaO	8.55	9.23	9.51	15.56	12.30	10.22	8.98	8.39	9.17	8.75	9.36	12.25	10.59	10.89	10.04	9.03	9.16
Na ₂ O	3.17	3.63	3.69	3.18	4.34	3.39	3.47	3.81	3.38	3.62	3.61	3.47	2.87	2.80	3.07	3.65	3.57
K ₂ O	1.04	0.94	1.01	1.14	1.87	0.87	1.05	1.13	1.03	1.07	1.08	1.03	0.81	0.75	0.94	0.97	0.96
P ₂ O ₅	0.63	0.48	0.49	0.39	0.71	0.64	0.62	0.65	0.61	0.63	0.67	0.50	0.49	0.39	0.40	0.48	0.49
Totals:	97.78	99.91	99.00	99.57	100.35	100.69	100.22	99.55	99.17	99.98	100.56	102.20	101.32	97.54	97.21	99.39	96.70
LOI	3.3	2.3	2.2	4.0	5.0	4.3	2.1	2.3	2.3	2.1	2.0	3.2	2.2	3.0	1.1	1.0	2.0
Major element oxide (wt%) normalized to 100 wt%:																	
SiO ₂	46.02	45.88	45.98	46.08	45.77	44.49	44.33	44.39	44.20	44.17	44.42	44.72	45.48	45.77	45.67	47.39	46.09
TiO ₂	2.60	3.31	3.41	2.96	3.00	3.58	3.62	3.78	3.56	3.65	3.63	2.84	2.75	2.92	2.81	3.09	3.22
Al ₂ O ₃	15.07	16.03	16.27	16.03	17.16	17.31	17.31	17.90	17.01	17.47	17.20	14.89	15.37	15.55	15.06	16.26	16.77
Fe ₂ O ₃ ^T	12.28	14.90	14.39	10.31	11.98	14.17	14.94	15.56	15.30	15.17	15.00	13.26	13.12	12.88	13.02	12.72	13.34
MnO	0.19	0.19	0.20	0.15	0.15	0.19	0.19	0.18	0.17	0.19	0.17	0.16	0.17	0.17	0.19	0.17	0.18
MgO	10.15	5.39	4.90	4.11	2.78	5.24	5.51	4.14	5.44	5.29	4.93	7.24	8.54	7.50	8.38	6.18	5.73
CaO	8.74	9.24	9.61	15.63	12.26	10.15	8.96	8.43	9.25	8.75	9.31	11.98	10.45	11.17	10.32	9.08	9.48
Na ₂ O	3.24	3.63	3.73	3.19	4.33	3.37	3.46	3.82	3.41	3.62	3.59	3.40	2.83	2.87	3.16	3.67	3.69
K ₂ O	1.06	0.94	1.03	1.15	1.87	0.87	1.05	1.14	1.04	1.07	1.08	1.01	0.80	0.77	0.97	0.97	1.00
P ₂ O ₅	0.64	0.48	0.49	0.39	0.70	0.64	0.62	0.65	0.61	0.63	0.66	0.49	0.48	0.40	0.41	0.48	0.51
Totals:	100.00	100.00	100.00	100.00	100.00	100.00	100.00	100.00	100.00	100.00	100.00	100.00	100.00	100.00	100.00	100.00	100.00
Mg#	65.8	45.7	44.2	48.2	35.1	46.2	46.2	38.2	45.3	44.8	43.3	56.0	60.2	57.5	60.0	53.1	50.0
Trace element (ppm):																	
Ba	236	173	179	163	252	212	212	213	220	202	213	191	173	162	183	220	214
Sr	607	477	483	495	581	718	690	739	675	696	683	532	531	553	524	626	638
Zr	255	217	220	173	305	257	248	250	242	246	247	227	217	239	252	320	303
Y	32	35	36	30	36	34	34	35	33	35	34	31	30	32	32	34	34
V	190	357	357	342	336	289	283	305	278	296	294	280	265	263	245	226	245
Sc	6	19	19	31	13	8	9	10	9	10	9	16	17	25	21	16	13
Cu	41	38	47	77	65	51	45	26	31	26	27	49	52	35	32	15	12
Zn	96	113	116	107	91	110	104	98	95	97	100	99	96	104	107	107	109
Co	67	67	72	67	55	62	66	66	81	72	81	62	67	64	62	63	64
Cr	438	23	32	82	94	3	6	16	9	15	15	317	313	271	331	112	130
Ni	215	39	42	67	69	39	44	51	45	45	47	138	150	147	158	78	83

* = intrusive sheet. All analyses were conducted on samples ignited to 960°C. Fe₂O₃^T = total iron expressed as Fe₂O₃. LOI = weight loss on ignition. Mg# = $100 \times \text{Mg}^{2+}/(\text{Mg}^{2+} + \text{Fe}^{2+})$, assuming that Fe₂O₃/FeO = 0.15.



Table T11 (continued).

Hole:	330-U1374A-															
Core, section:	37R-3	39R-5	41R-4	42R-5	43R-7	46R-6	47R-7	51R-6	52R-2	54R-4	55R-2	56R-4	58R-4	64R-2	64R-6	72R-2
Piece:	2	13	2a	8	9b	10c	5	3	3	3	1	1	1	2b	13	1
Interval (cm):	20–22	86–88	36–38	117–120	85–87	135–137	104–106	47–49	35–37	38–40	6–8	10–12	64–66	37–39	138–140	28–31
Top depth (mbsf):	199.64	217.74	234.71	246.72	258.86	286.36	296.48	333.6	337.62	359.26	365.87	378.33	397.64	452.46	459.15	519.49
Strat. unit:	XIII	XIII	XIII	XIII	XIII	XV	XVI	XVI	XVI*	XVII	XVII*	XVIII	XVIII*	XIX*	XIX	XIX
Major element oxides (wt%):																
SiO ₂	45.01	44.97	44.53	42.73	42.54	44.52	43.45	43.19	41.98	43.48	46.87	44.84	42.60	46.14	44.67	45.50
TiO ₂	3.03	3.13	3.09	3.31	3.40	3.60	2.84	2.76	3.27	3.17	3.05	3.16	3.18	3.03	3.89	3.66
Al ₂ O ₃	15.65	16.18	15.84	15.56	16.07	14.88	15.95	15.25	12.79	13.63	14.43	14.95	14.30	14.83	15.29	16.96
Fe ₂ O ₃ ^T	12.71	13.38	13.14	12.46	12.46	14.68	11.26	12.01	14.90	13.14	13.19	13.59	12.83	12.91	14.79	14.03
MnO	0.17	0.16	0.17	0.17	0.16	0.19	0.20	0.15	0.20	0.18	0.20	0.17	0.17	0.16	0.18	0.17
MgO	6.46	5.39	6.46	5.73	4.86	4.94	5.54	4.96	6.13	4.60	5.65	5.72	5.90	6.33	5.41	5.48
CaO	8.84	9.48	8.73	12.18	12.88	11.60	12.78	12.43	8.57	10.85	9.81	12.78	13.41	11.03	11.39	9.22
Na ₂ O	3.48	3.61	3.68	2.74	2.58	2.94	2.38	2.42	3.17	2.63	3.23	2.35	2.67	3.09	2.86	3.44
K ₂ O	1.10	1.10	1.02	0.81	0.84	0.92	0.70	0.76	0.95	0.85	1.18	0.35	0.45	1.01	0.52	1.00
P ₂ O ₅	0.46	0.47	0.44	0.42	0.42	0.46	0.33	0.33	0.33	0.38	0.36	0.32	0.38	0.36	0.42	0.45
Totals:	96.91	97.87	97.10	96.11	96.22	98.72	95.42	94.25	92.29	92.91	97.96	98.23	95.89	98.89	99.42	99.91
LOI	1.8	2.3	1.3	1.8	1.8	3.4	2.3	1.6	3.7	2.2	3.1	1.8	3.7	4.1	1.9	0.6
Major element oxides (wt%) normalized to 100 wt%:																
SiO ₂	46.44	45.95	45.86	44.46	44.21	45.09	45.54	45.82	45.48	46.80	47.84	45.65	44.42	46.66	44.93	45.54
TiO ₂	3.13	3.19	3.19	3.44	3.53	3.64	2.97	2.92	3.54	3.42	3.11	3.22	3.32	3.07	3.91	3.67
Al ₂ O ₃	16.15	16.53	16.31	16.19	16.70	15.08	16.71	16.18	13.86	14.67	14.73	15.22	14.91	15.00	15.38	16.98
Fe ₂ O ₃ ^T	13.11	13.68	13.53	12.97	12.95	14.87	11.80	12.74	16.15	14.14	13.46	13.83	13.38	13.05	14.88	14.04
MnO	0.17	0.17	0.18	0.17	0.17	0.20	0.21	0.16	0.21	0.19	0.20	0.17	0.18	0.16	0.18	0.17
MgO	6.66	5.51	6.65	5.96	5.05	5.00	5.80	5.26	6.64	4.95	5.77	5.83	6.15	6.40	5.44	5.49
CaO	9.12	9.68	8.99	12.68	13.39	11.75	13.39	13.19	9.29	11.67	10.01	13.01	13.99	11.15	11.46	9.22
Na ₂ O	3.59	3.69	3.79	2.86	2.68	2.98	2.49	2.56	3.44	2.83	3.29	2.39	2.78	3.13	2.87	3.44
K ₂ O	1.14	1.12	1.05	0.84	0.88	0.93	0.73	0.81	1.03	0.91	1.20	0.35	0.47	1.02	0.53	1.00
P ₂ O ₅	0.48	0.48	0.46	0.43	0.44	0.46	0.35	0.35	0.35	0.41	0.37	0.33	0.40	0.37	0.42	0.45
Totals:	100.00	100.00	100.00	100.00	100.00	100.00	100.00	100.00	100.00	100.00	100.00	100.00	100.00	100.00	100.00	100.00
Mg#	54.2	48.4	53.4	51.7	47.6	43.9	53.4	49.0	48.9	44.9	49.9	49.5	51.7	53.3	46.0	47.6
Trace elements (ppm):																
Ba	208	215	216	197	190	186	122	137	156	140	190	152	193	199	207	221
Sr	613	655	631	652	659	579	524	529	412	500	402	535	569	914	646	719
Zr	296	297	289	236	240	257	196	195	202	241	220	212	231	227	261	284
Y	33	34	36	31	33	36	28	27	34	32	32	30	29	29	33	35
V	220	234	234	313	333	367	307	298	403	343	344	380	335	313	387	271
Sc	11	6	5	13	14	14	20	18	15	14	13	24	17	21	15	7
Cu	13	13	13	75	73	30	60	49	92	42	20	100	30	37	46	11
Zn	109	107	103	106	106	125	97	99	124	112	112	115	112	108	123	107
Co	64	66	68	63	73	71	54	55	71	63	60	69	59	62	74	68
Cr	141	121	137	95	118	9	194	174	35	89	24	92	26	31	38	14
Ni	117	97	102	66	65	40	69	66	53	61	45	79	48	53	46	40

Table T12. Moisture and density measurements, Site U1374. (Continued on next three pages.)

Core, section, interval (cm)	Top depth (mbsf)	Density (g/cm ³)			Void ratio	Water content (%)	Porosity (%)
		Bulk	Dry	Grain			
330-U1374A-							
2R-3, 37–39	12.45	2.328	2.068	2.774	0.342	11.20	25.47
2R-4, 8–10	13.51	2.224	1.902	2.776	0.460	14.50	31.49
3R-2, 100–102	16.83	2.846	2.796	2.940	0.052	1.76	4.90
4R-1, 133–134	21.73	2.748	2.675	2.881	0.077	2.67	7.15
4R-2, 74–76	22.56	2.852	2.826	2.900	0.026	0.93	2.58
5R-1, 79–81	25.89	2.846	2.808	2.916	0.039	1.34	3.71
5R-2, 118–120	27.18	2.865	2.840	2.913	0.026	0.90	2.51
5R-3, 121–123	28.64	2.841	2.811	2.895	0.030	1.05	2.90
6R-1, 85–87	30.25	2.682	2.564	2.898	0.130	4.41	11.54
6R-1, 116–118	30.56	2.706	2.622	2.856	0.089	3.10	8.20
6R-2, 35–37	31.04	2.225	1.901	2.779	0.462	14.55	31.61
6R-3, 50–52	32.69	2.363	2.101	2.823	0.343	11.08	25.57
6R-3, 105–107	33.24	2.696	2.606	2.858	0.097	3.36	8.83
7R-1, 114–116	35.34	2.786	2.738	2.873	0.049	1.72	4.68
7R-2, 112–114	36.76	2.849	2.829	2.886	0.020	0.72	1.99
7R-4, 77–79	39.01	2.153	1.793	2.762	0.540	16.69	35.08
8R-1, 39–41	39.39	2.288	1.962	2.878	0.467	14.24	31.83
8R-2, 126–128	41.21	2.211	1.844	2.876	0.560	16.62	35.88
9R-1, 87–89	44.67	2.215	1.904	2.737	0.438	14.07	30.45
9R-3, 42–44	46.66	2.569	2.398	2.878	0.200	6.64	16.67
9R-4, 100–102	48.33	2.502	2.364	2.733	0.156	5.53	13.51
10R-2, 112–114	49.93	2.126	1.787	2.672	0.495	15.95	33.12
10R-5, 42–44	53.49	1.933	1.494	2.618	0.753	22.74	42.94
11R-2, 43–45	55.25	2.090	1.721	2.688	0.562	17.62	35.96
11R-4, 93–95	58.67	2.221	1.938	2.678	0.381	12.73	27.61
12R-1, 75–77	59.15	2.208	1.846	2.857	0.548	16.41	35.39
12R-2, 128–130	61.10	2.594	2.433	2.888	0.187	6.22	15.77
12R-3, 113–115	62.30	1.972	1.560	2.608	0.671	20.86	40.17
13R-1, 117–119	69.17	2.774	2.715	2.879	0.060	2.10	5.68
13R-2, 134–136	70.83	2.470	2.279	2.801	0.229	7.74	18.66
14R-2, 47–49	74.13	2.472	2.275	2.816	0.237	7.95	19.19
14R-3, 130–132	76.38	2.081	1.705	2.694	0.580	18.06	36.71
15R-2, 2–4	78.93	2.261	1.992	2.703	0.357	11.92	26.31
15R-2, 70–72	79.61	2.787	2.696	2.958	0.097	3.25	8.86
16R-1, 104–106	85.64	2.832	2.801	2.889	0.031	1.09	3.02
16R-2, 107–109	87.09	2.849	2.814	2.911	0.034	1.19	3.32
17R-3, 25–27	90.03	2.720	2.672	2.804	0.049	1.77	4.71
18R-1, 35–37	92.35	2.751	2.709	2.826	0.043	1.54	4.14
18R-2, 108–110	94.49	2.752	2.712	2.821	0.040	1.44	3.87
18R-4, 16–18	96.28	2.709	2.654	2.803	0.056	2.01	5.33
19R-2, 59–61	98.83	2.614	2.535	2.749	0.084	3.05	7.78
19R-2, 95–97	99.19	2.770	2.733	2.836	0.037	1.34	3.61
19R-3, 110–112	100.77	2.079	1.704	2.688	0.578	18.05	36.63
20R-1, 37–39	101.97	2.693	2.628	2.805	0.067	2.39	6.28
20R-2, 83–85	103.77	2.279	2.010	2.725	0.356	11.80	26.25
21R-2, 55–57	108.44	2.880	2.855	2.924	0.024	0.84	2.35
21R-3, 91–93	110.18	2.274	1.984	2.766	0.394	12.73	28.27
21R-4, 47–49	111.05	2.577	2.462	2.774	0.127	4.47	11.24
22R-1, 29–31	111.49	2.521	2.367	2.785	0.177	6.10	15.01
22R-3, 41–43	114.30	2.505	2.322	2.828	0.218	7.32	17.90
23R-1, 16–18	116.16	2.755	2.694	2.863	0.063	2.19	5.89
23R-3, 5–7	118.48	2.390	2.129	2.856	0.341	10.90	25.44
24R-1, 31–33	121.11	2.863	2.827	2.930	0.036	1.25	3.48
24R-4, 60–62	124.71	2.656	2.521	2.903	0.151	5.07	13.15
25R-1, 40–42	126.00	2.332	2.083	2.752	0.321	10.67	24.30
25R-2, 108–110	127.83	2.636	2.526	2.830	0.121	4.18	10.76
25R-3, 38–40	128.49	2.240	1.922	2.787	0.450	14.19	31.04
25R-4, 86–88	130.30	2.447	2.246	2.794	0.244	8.21	19.61
26R-2, 81–83	131.85	2.284	2.011	2.743	0.364	11.96	26.68
26R-4, 13–15	133.21	2.410	2.178	2.815	0.292	9.61	22.62
27R-2, 5–7	136.61	2.815	2.770	2.899	0.047	1.62	4.45
27R-2, 13–15	136.69	2.662	2.574	2.818	0.095	3.34	8.68
27R-3, 100–102	138.56	2.583	2.433	2.849	0.171	5.79	14.61
28R-2, 51–53	141.89	2.641	2.524	2.850	0.129	4.44	11.44
28R-4, 45–47	144.14	2.492	2.294	2.844	0.240	7.96	19.36
29R-2, 100–102	146.91	2.603	2.522	2.738	0.086	3.11	7.89
29R-4, 2–4	148.37	2.198	1.886	2.712	0.438	14.19	30.47

Table T12 (continued). (Continued on next page.)

Core, section, interval (cm)	Top depth (mbsf)	Density (g/cm ³)			Void ratio	Water content (%)	Porosity (%)
		Bulk	Dry	Grain			
29R-4, 16–18	148.51	2.712	2.642	2.836	0.074	2.59	6.86
29R-6, 79–81	151.94	2.230	1.940	2.706	0.395	13.01	28.32
30R-2, 88–90	155.97	2.708	2.626	2.855	0.087	3.03	8.01
30R-4, 56–58	158.40	2.660	2.573	2.811	0.092	3.26	8.46
30R-6, 44–46	160.92	2.407	2.187	2.784	0.273	9.12	21.43
31R-1, 52–54	163.62	2.204	1.891	2.722	0.439	14.18	30.51
31R-3, 110–112	166.92	2.224	1.906	2.763	0.450	14.28	31.01
32R-2, 75–77	174.91	2.595	2.501	2.754	0.101	3.63	9.19
32R-4, 80–82	177.79	2.854	2.829	2.900	0.025	0.89	2.47
33R-3, 122–124	181.06	2.244	1.899	2.864	0.508	15.36	33.67
33R-4, 64–66	181.80	2.638	2.524	2.840	0.125	4.32	11.13
34R-3, 6–8	184.73	2.625	2.527	2.794	0.105	3.72	9.52
35R-1, 71–73	187.81	2.588	2.453	2.826	0.152	5.22	13.19
35R-2, 83–85	189.06	2.162	1.796	2.793	0.555	16.90	35.69
36R-1, 17–19	192.07	2.867	2.846	2.906	0.021	0.74	2.07
36R-4, 56–58	196.64	2.650	2.567	2.792	0.087	3.11	8.04
37R-1, 55–57	197.25	2.628	2.489	2.880	0.157	5.28	13.56
36R-5, 19–21	197.61	2.919	2.907	2.941	0.012	0.40	1.15
37R-2, 94–96	199.11	2.358	2.096	2.818	0.345	11.13	25.63
37R-3, 20–22	199.64	2.879	2.855	2.924	0.024	0.84	2.35
38R-2, 11–13	203.07	2.457	2.280	2.758	0.210	7.23	17.36
38R-2, 120–122	204.16	2.340	2.054	2.852	0.389	12.25	28.01
38R-3, 89–91	205.09	2.855	2.832	2.897	0.023	0.80	2.22
39R-1, 59–61	211.69	2.476	2.291	2.798	0.221	7.49	18.12
39R-3, 47–49	214.34	2.297	2.015	2.782	0.381	12.29	27.57
39R-4, 110–112	216.47	2.566	2.468	2.728	0.105	3.80	9.52
39R-4, 129–131	216.66	2.667	2.605	2.773	0.064	2.32	6.05
39R-5, 105–107	217.91	2.636	2.572	2.744	0.067	2.44	6.28
40R-2, 67–69	222.61	2.299	2.001	2.823	0.411	12.97	29.12
40R-4, 33–35	224.41	2.347	2.085	2.800	0.343	11.14	25.54
40R-5, 94–96	226.45	2.524	2.385	2.759	0.157	5.50	13.55
40R-6, 40–42	227.41	2.368	2.125	2.785	0.310	10.24	23.68
41R-2, 83–85	232.46	2.313	2.041	2.779	0.362	11.76	26.57
41R-4, 7–9	234.42	2.476	2.336	2.704	0.157	5.63	13.61
41R-5, 90–92	236.63	2.370	2.142	2.755	0.286	9.61	22.24
41R-6, 40–42	237.46	2.606	2.461	2.867	0.165	5.56	14.15
41R-7, 35–37	238.78	2.655	2.542	2.858	0.125	4.27	11.08
42R-1, 93–95	240.83	2.582	2.457	2.798	0.138	4.82	12.16
42R-3, 78–80	243.60	2.344	2.096	2.763	0.318	10.55	24.14
42R-4, 3–5	244.34	2.286	2.006	2.762	0.377	12.26	27.37
42R-4, 88–90	245.19	2.620	2.548	2.740	0.076	2.75	7.02
42R-6, 2–4	246.99	2.584	2.491	2.739	0.100	3.59	9.06
43R-1, 65–67	250.15	2.631	2.555	2.760	0.080	2.90	7.44
43R-3, 54–56	252.86	2.552	2.465	2.694	0.093	3.41	8.50
43R-4, 96–98	254.72	2.587	2.491	2.748	0.103	3.69	9.33
43R-6, 54–56	257.21	2.488	2.264	2.899	0.281	9.02	21.91
43R-7, 70–72	258.71	2.699	2.609	2.862	0.097	3.36	8.85
44R-1, 8–10	259.18	2.541	2.323	2.952	0.271	8.60	21.33
44R-1, 43–45	259.53	2.714	2.630	2.865	0.089	3.09	8.19
44R-5, 103–105	265.71	2.559	2.414	2.811	0.165	5.66	14.15
45R-2, 138–140	271.42	2.626	2.520	2.810	0.115	4.03	10.33
45R-6, 112–114	276.90	2.567	2.406	2.855	0.187	6.28	15.74
45R-7, 137–139	278.56	2.677	2.586	2.836	0.097	3.37	8.80
46R-1, 41–43	278.71	2.301	1.982	2.880	0.453	13.88	31.20
46R-3, 28–30	281.30	2.384	2.111	2.877	0.362	11.43	26.60
46R-4, 52–54	282.81	2.512	2.295	2.913	0.269	8.64	21.20
47R-1, 46–48	288.36	2.618	2.504	2.817	0.125	4.35	11.12
47R-3, 34–36	290.61	2.540	2.332	2.927	0.256	8.20	20.35
47R-4, 55–57	291.88	2.294	2.027	2.742	0.353	11.64	26.08
47R-6, 100–102	295.18	2.280	1.986	2.787	0.404	12.92	28.76
47R-7, 95–97	296.39	2.601	2.488	2.794	0.123	4.31	10.94
47R-8, 73–75	297.60	2.498	2.307	2.834	0.228	7.62	18.58
48R-3, 103–105	301.24	2.339	2.088	2.768	0.326	10.76	24.58
48R-4, 47–49	301.93	2.311	2.043	2.768	0.355	11.62	26.22
48R-6, 56–58	304.41	2.790	2.730	2.900	0.062	2.15	5.85
48R-7, 65–67	305.90	2.639	2.538	2.816	0.109	3.82	9.86
49R-1, 111–113	308.21	2.339	2.078	2.790	0.343	11.18	25.53
49R-2, 4–6	308.50	2.537	2.374	2.824	0.190	6.43	15.94

Table T12 (continued). (Continued on next page.)

Core, section, interval (cm)	Top depth (mbsf)	Density (g/cm ³)			Void ratio	Water content (%)	Porosity (%)
		Bulk	Dry	Grain			
49R-2, 72–74	309.18	2.693	2.613	2.835	0.085	2.99	7.85
49R-4, 25–27	311.10	2.681	2.612	2.802	0.073	2.58	6.76
49R-7, 140–142	315.59	2.648	2.540	2.841	0.118	4.09	10.58
50R-1, 98–100	317.68	2.656	2.550	2.843	0.115	3.97	10.28
50R-2, 58–60	318.78	2.866	2.842	2.911	0.024	0.85	2.38
50R-4, 92–94	321.86	2.191	1.898	2.658	0.400	13.35	28.56
50R-6, 94–96	324.56	2.632	2.531	2.807	0.109	3.83	9.84
50R-7, 99–101	325.93	2.795	2.735	2.906	0.063	2.16	5.90
50R-8, 33–35	326.70	2.760	2.707	2.856	0.055	1.93	5.21
51R-1, 48–50	326.78	2.839	2.804	2.902	0.035	1.22	3.38
51R-1, 94–96	327.24	2.708	2.615	2.877	0.100	3.44	9.10
51R-5, 54–56	332.24	2.280	2.006	2.739	0.365	12.02	26.76
51R-8, 63–65	336.58	2.332	2.055	2.817	0.370	11.87	27.03
52R-1, 98–100	336.88	2.334	2.166	2.590	0.196	7.18	16.37
52R-2, 24–26	337.51	2.561	2.452	2.744	0.119	4.26	10.65
52R-3, 68–70	339.04	2.504	2.319	2.829	0.220	7.38	18.05
52R-5, 52–54	341.81	2.284	2.007	2.753	0.372	12.14	27.09
53R-3, 86–88	348.85	2.268	1.959	2.806	0.432	13.62	30.18
53R-4, 121–123	350.60	2.439	2.256	2.746	0.217	7.50	17.85
53R-7, 35–37	353.89	2.231	1.908	2.787	0.460	14.47	31.52
54R-2, 129–131	357.32	2.244	1.935	2.773	0.433	13.79	30.22
54R-3, 76–78	358.22	2.246	1.937	2.774	0.432	13.75	30.17
54R-5, 52–54	360.79	2.467	2.214	2.941	0.328	10.26	24.71
54R-6, 127–129	362.97	2.262	1.966	2.767	0.408	13.11	28.95
54R-7, 62–64	363.77	2.007	1.593	2.671	0.677	20.59	40.35
55R-2, 11–13	365.92	2.430	2.311	2.614	0.131	4.89	11.61
55R-2, 118–120	366.99	2.003	1.578	2.695	0.708	21.19	41.44
55R-4, 25–27	368.87	1.931	1.450	2.734	0.885	24.90	46.96
56R-2, 87–89	376.27	2.085	1.712	2.693	0.572	17.88	36.41
56R-4, 116–118	379.39	2.615	2.513	2.790	0.110	3.88	9.92
56R-6, 25–27	381.07	2.237	1.977	2.650	0.340	11.62	25.39
57R-2, 135–137	386.33	2.372	2.233	2.582	0.156	5.83	13.50
57R-4, 127–129	389.09	2.251	2.004	2.642	0.318	10.98	24.13
57R-5, 82–84	389.95	2.242	1.974	2.675	0.355	11.96	26.20
57R-8, 42–44	392.95	2.438	2.265	2.727	0.204	7.12	16.95
58R-3, 121–123	396.95	2.588	2.485	2.763	0.112	3.99	10.09
58R-6, 121–123	400.93	2.231	1.956	2.674	0.367	12.32	26.84
58R-8, 19–21	402.75	2.654	2.580	2.782	0.079	2.81	7.28
58R-8, 61–63	403.17	2.527	2.411	2.719	0.127	4.58	11.30
59R-2, 12–14	404.31	2.604	2.480	2.821	0.137	4.75	12.08
59R-4, 28–30	407.27	2.261	2.023	2.635	0.303	10.53	23.26
59R-7, 22–24	410.26	2.573	2.449	2.786	0.138	4.81	12.10
60R-2, 64–66	414.52	2.491	2.331	2.762	0.185	6.41	15.59
60R-4, 68–70	417.09	2.582	2.463	2.787	0.131	4.60	11.60
60R-7, 113–115	421.62	2.536	2.379	2.810	0.181	6.20	15.35
61R-2, 47–49	423.77	2.785	2.733	2.878	0.053	1.85	5.03
61R-4, 103–105	427.34	2.243	1.974	2.676	0.355	11.97	26.22
61R-6, 63–65	429.65	2.268	2.007	2.696	0.343	11.54	25.56
62R-2, 83–85	433.62	2.522	2.364	2.795	0.182	6.27	15.43
62R-6, 95–97	439.28	2.513	2.366	2.764	0.169	5.88	14.43
63R-1, 88–90	441.98	2.869	2.835	2.932	0.034	1.18	3.31
63R-5, 35–37	446.87	2.337	2.100	2.732	0.301	10.13	23.12
64R-2, 43–45	452.52	2.573	2.471	2.744	0.110	3.96	9.95
64R-4, 48–50	455.37	2.186	1.909	2.617	0.371	12.66	27.04
64R-6, 33–35	458.10	2.285	2.053	2.656	0.294	10.18	22.72
65R-4, 93–95	465.13	2.301	2.061	2.692	0.306	10.42	23.42
65R-6, 38–40	466.76	2.415	2.231	2.722	0.220	7.65	18.05
66R-1, 59–61	470.49	1.948	1.488	2.700	0.814	23.59	44.88
66R-2, 37–39	471.34	1.909	1.433	2.676	0.867	24.91	46.44
66R-4, 52–54	473.64	1.889	1.406	2.661	0.892	25.55	47.14
66R-7, 64–66	477.18	1.966	1.527	2.672	0.750	22.33	42.86
67R-2, 105–107	481.25	1.915	1.437	2.694	0.875	24.97	46.68
67R-5, 103–105	485.34	2.117	1.743	2.747	0.576	17.67	36.53
67R-7, 38–40	487.42	2.083	1.714	2.677	0.562	17.68	35.97
68R-1, 109–111	490.19	2.012	1.597	2.685	0.681	20.63	40.53
68R-3, 109–111	493.05	2.642	2.553	2.797	0.096	3.38	8.73
68R-4, 142–144	494.54	2.618	2.531	2.766	0.093	3.33	8.51
68R-6, 10–12	496.10	2.522	2.372	2.780	0.172	5.95	14.65

Table T12 (continued).

Core, section, interval (cm)	Top depth (mbsf)	Density (g/cm ³)			Void ratio	Water content (%)	Porosity (%)
		Bulk	Dry	Grain			
69R-2, 137–139	501.35	2.003	1.651	2.514	0.523	17.56	34.33
69R-3, 65–67	502.08	1.977	1.688	2.353	0.394	14.65	28.28
69R-4, 125–127	504.13	2.169	1.846	2.696	0.460	14.88	31.52
69R-6, 75–77	506.39	2.266	2.004	2.694	0.344	11.57	25.60
70R-2, 24–26	509.84	2.919	2.909	2.937	0.010	0.33	0.95
71R-1, 107–109	514.17	2.929	2.920	2.946	0.009	0.30	0.87
71R-3, 25–27	516.15	2.118	1.784	2.647	0.483	15.76	32.59
73R-1, 13–15	521.13	2.860	2.839	2.898	0.021	0.73	2.03

Water content is relative to wet mass.

Table T13. Compressional wave velocity measurements, Site U1374. (Continued on next three pages.)

Core, section, interval (cm)	Top depth (mbsf)	Velocity (km/s)			
		x	y	z	Average
330-U1374A-					
2R-3, 37–39	12.45	4.200	4.258	4.115	4.191
2R-4, 8–10	13.51	3.152	3.152	3.102	3.135
3R-2, 100–102	16.83	5.986	5.915	5.988	5.963
4R-1, 133–134	21.73	5.571	5.612	5.567	5.584
4R-2, 74–76	22.56	6.560	6.600	6.423	6.527
5R-1, 79–81	25.89	6.092	5.935	5.926	5.984
5R-2, 118–120	27.18	6.336	6.375	6.336	6.349
5R-3, 121–123	28.64	6.145	6.207	5.865	6.072
6R-1, 85–87	30.25	4.510	4.710	4.678	4.633
6R-1, 116–118	30.56	4.978	4.931	4.934	4.948
6R-2, 35–37	31.04	2.037	2.228	2.021	2.095
6R-3, 50–52	32.69	2.936	2.969	3.130	3.012
6R-3, 105–107	33.24	5.171	5.291	5.011	5.158
7R-1, 114–116	35.34	5.567	5.632	5.366	5.522
7R-2, 112–114	36.76	5.533	5.538	5.158	5.410
8R-1, 39–41	39.39	2.634	2.620	2.506	2.587
8R-2, 126–128	41.21	2.570	2.595	2.516	2.560
9R-1, 87–89	44.67	3.273	3.430	3.422	3.375
9R-3, 42–44	46.66	4.188	4.193	4.165	4.182
9R-4, 100–102	48.33	5.236	5.181	5.147	5.188
10R-2, 112–114	49.93	2.857	2.842	2.821	2.840
10R-5, 42–44	53.49	2.744	2.808	2.775	2.776
11R-2, 43–45	55.25	2.349	2.386	2.381	2.372
11R-4, 93–95	58.67	3.348	3.366	3.126	3.280
12R-1, 75–77	59.15	2.890	2.979	3.506	3.125
12R-2, 128–130	61.10	4.653	4.655	4.557	4.621
12R-3, 113–115	62.30	2.223	2.278	2.336	2.279
13R-1, 117–119	69.17	6.014	5.964	5.816	5.931
13R-2, 134–136	70.83	4.563	4.548	4.632	4.581
14R-2, 47–49	74.13	4.358	4.315	4.329	4.334
14R-3, 130–132	76.38	2.437	2.398	2.345	2.394
15R-2, 2–4	78.93	3.705	3.695	3.668	3.689
15R-2, 70–72	79.61	4.999	5.148	5.048	5.065
16R-1, 104–106	85.64	6.141	6.051	6.001	6.064
16R-2, 107–109	87.09	6.062	6.217	6.558	6.279
17R-3, 25–27	90.03	6.153	6.185	6.252	6.196
18R-1, 35–37	92.35	6.127	6.101	6.288	6.172
18R-2, 108–110	94.49	6.216	6.043	6.031	6.097
18R-4, 16–18	96.28	6.176	6.178	6.084	6.146
19R-2, 59–61	98.83	6.110	5.951	5.939	6.000
19R-3, 110–112	100.77	2.932	2.949	2.936	2.939
20R-1, 37–39	101.97	5.855	5.745	5.778	5.793
20R-2, 83–85	103.77	3.882	3.833	3.818	3.844
21R-2, 55–57	108.44	6.824	6.766	6.689	6.760
21R-3, 91–93	110.18	4.250	4.233	4.153	4.212
21R-4, 47–49	111.05	5.601	5.628	5.562	5.597
22R-1, 29–31	111.49	5.009	5.028	4.845	4.961
22R-3, 41–43	114.30	4.419	4.406	4.397	4.407
23R-1, 16–18	116.16	6.099	5.943	5.955	5.999
23R-3, 5–7	118.48	3.783	3.786	3.824	3.798
24R-1, 31–33	121.11	6.600	6.634	6.740	6.658
24R-4, 60–62	124.71	5.210	5.181	5.188	5.193
25R-1, 40–42	126.00	4.066	3.895	4.022	3.994
25R-2, 108–110	127.83	5.507	5.158	5.336	5.334
25R-3, 38–40	128.49	3.701	3.631	3.719	3.684
25R-4, 86–88	130.30	4.025	3.975	3.977	3.992
26R-2, 81–83	131.85	3.506	3.548	3.551	3.535
26R-4, 13–15	133.21	4.048	4.035	4.066	4.050
27R-2, 13–15	136.69	5.716	5.677	5.727	5.707
27R-3, 100–102	138.56	4.917	4.902	4.842	4.887
28R-2, 51–53	141.89	5.306	5.281	5.229	5.272
28R-4, 45–47	144.14	4.556	4.571	4.541	4.556
29R-2, 100–102	146.91	5.809	5.745	5.771	5.775
29R-4, 2–4	148.37	3.482	3.424	3.489	3.465
29R-4, 16–18	148.51	5.909	5.896	5.826	5.877
29R-6, 79–81	151.94	3.242	3.161	3.234	3.212
30R-2, 88–90	155.97	5.493	5.480	5.415	5.463

Table T13 (continued). (Continued on next page.)

Core, section, interval (cm)	Top depth (mbsf)	Velocity (km/s)			
		x	y	z	Average
30R-4, 56–58	158.40	5.576	5.645	5.530	5.583
30R-6, 44–46	160.92	4.580	4.585	4.546	4.570
31R-1, 52–54	163.62	3.359	3.382	3.369	3.370
31R-3, 110–112	166.92	3.420	3.208	3.158	3.262
32R-2, 75–77	174.91	5.739	5.582	5.529	5.617
32R-4, 80–82	177.79	6.494	6.670	6.430	6.531
33R-3, 122–124	181.06	2.614	2.696	2.658	2.656
33R-4, 64–66	181.80	5.155	5.270	5.179	5.201
34R-3, 6–8	184.73	5.565	5.554	5.526	5.549
35R-1, 71–73	187.81	5.247	5.259	5.275	5.260
35R-2, 83–85	189.06	2.988	2.906	2.913	2.936
36R-1, 17–19	192.07	6.545	6.465	6.527	6.512
36R-4, 56–58	196.64	5.684	5.276	5.369	5.443
37R-1, 55–57	197.25	4.988	4.900	4.864	4.917
36R-5, 19–21	197.61	6.637	6.555	6.648	6.613
37R-2, 94–96	199.11	3.043	3.006	2.947	2.999
37R-3, 20–22	199.64	6.526	6.508	6.454	6.496
38R-2, 11–13	203.07	4.944	4.849	4.797	4.863
38R-2, 120–122	204.16	2.994	2.937	2.957	2.963
38R-3, 89–91	205.09	6.565	6.577	6.686	6.609
39R-1, 59–61	211.69	4.840	4.757	4.742	4.780
39R-3, 47–49	214.34	3.613	3.554	3.591	3.586
39R-4, 110–112	216.47	5.364	5.353	5.334	5.350
39R-4, 129–131	216.66	5.918	5.874	5.855	5.882
39R-5, 105–107*	217.91	6.072	ND	ND	6.072
40R-2, 67–69	222.61	3.848	3.685	3.703	3.745
40R-4, 33–35	224.41	3.769	3.894	3.794	3.819
40R-5, 94–96	226.45	5.365	5.290	5.240	5.298
40R-6, 40–42	227.41	3.883	3.643	3.722	3.749
41R-2, 83–85	232.46	4.114	3.853	3.697	3.888
41R-4, 7–9	234.42	5.049	4.998	4.887	4.978
41R-5, 90–92	236.63	4.053	3.998	4.043	4.032
41R-6, 40–42	237.46	4.809	4.788	4.547	4.714
41R-7, 35–37	238.78	5.102	5.162	5.118	5.127
42R-1, 93–95	240.83	5.127	5.290	5.098	5.172
42R-3, 78–80	243.60	3.873	3.845	3.880	3.866
42R-4, 3–5	244.34	3.732	3.806	3.829	3.789
42R-4, 88–90	245.19	5.672	5.685	5.819	5.726
42R-6, 2–4	246.99	5.317	5.310	5.356	5.328
43R-1, 65–67	250.15	5.500	5.546	5.605	5.550
43R-3, 54–56	252.81	5.580	5.575	5.261	5.472
43R-4, 96–98	254.72	5.803	5.775	5.710	5.763
43R-6, 54–56	257.21	4.075	4.201	4.222	4.166
43R-7, 70–72	258.71	5.717	5.812	5.536	5.688
44R-1, 8–10	259.18	4.361	4.300	4.396	4.352
44R-1, 43–45	259.53	6.303	6.268	6.317	6.296
44R-5, 103–105	265.71	5.576	5.502	5.498	5.526
45R-2, 138–140	271.42	5.978	6.073	5.866	5.972
45R-6, 112–114	276.90	5.296	5.284	5.194	5.258
45R-7, 137–139	278.56	5.921	6.232	5.954	6.036
46R-1, 41–43	278.71	3.153	3.174	3.149	3.159
46R-3, 28–30	281.30	3.562	3.527	3.592	3.560
46R-4, 52–54	282.81	4.272	4.337	4.295	4.302
47R-1, 46–48	288.36	5.235	5.306	5.177	5.239
47R-3, 34–36	290.61	4.405	4.387	4.393	4.395
47R-4, 55–57	291.88	3.969	4.016	3.981	3.988
47R-6, 100–102	295.18	3.521	3.542	3.521	3.528
47R-7, 95–97	296.39	5.500	5.577	5.584	5.554
47R-8, 73–75	297.60	4.760	4.792	4.722	4.758
48R-3, 103–105	301.24	3.814	3.808	3.808	3.810
48R-4, 47–49	301.93	3.982	3.924	3.927	3.944
48R-6, 56–58	304.41	5.664	5.575	5.552	5.597
48R-7, 65–67	305.90	5.863	5.796	5.798	5.819
49R-1, 111–113	308.21	3.718	3.780	3.733	3.744
49R-2, 4–6	308.50	4.773	4.961	4.665	4.800
49R-2, 72–74	309.18	5.813	5.832	5.591	5.745
49R-4, 25–27	311.10	6.127	6.265	6.041	6.144
49R-7, 140–142	315.59	5.582	5.626	5.617	5.608

Table T13 (continued). (Continued on next page.)

Core, section, interval (cm)	Top depth (mbsf)	Velocity (km/s)			
		x	y	z	Average
50R-1, 98–100	317.68	5.254	5.327	5.289	5.290
50R-2, 58–60	318.78	6.601	6.538	6.577	6.572
50R-4, 92–94	321.86	4.282	4.354	4.269	4.302
50R-6, 94–96	324.56	5.684	5.600	5.496	5.593
50R-7, 99–101	325.93	6.155	6.074	6.195	6.141
50R-8, 33–35	326.70	6.242	6.237	6.195	6.225
51R-1, 48–50	326.78	6.662	6.571	6.457	6.563
51R-1, 94–96	327.24	5.570	5.597	5.588	5.585
51R-5, 54–56	332.24	4.038	3.938	3.883	3.953
51R-8, 63–65	336.58	3.850	3.787	3.773	3.803
52R-1, 98–100	336.88	4.536	4.223	4.499	4.419
52R-2, 24–26	337.51	5.179	4.975	5.046	5.067
52R-3, 68–70	339.04	4.354	4.387	4.255	4.332
52R-5, 52–54	341.81	3.593	3.641	3.614	3.616
53R-3, 86–88	348.85	3.537	3.499	3.588	3.541
53R-4, 121–123	350.60	5.053	5.010	5.055	5.039
53R-7, 35–37	353.89	3.728	3.686	3.634	3.683
54R-2, 129–131	357.32	3.639	3.788	3.785	3.737
54R-3, 76–78	358.22	3.509	3.581	3.689	3.593
54R-5, 52–54	360.79	4.171	4.047	4.022	4.080
54R-6, 127–129	362.97	3.673	3.684	3.686	3.681
54R-7, 62–64	363.77	3.051	3.094	3.076	3.074
55R-2, 11–13	365.92	5.086	4.977	4.990	5.018
55R-2, 118–120	366.99	2.845	2.820	2.813	2.826
55R-4, 25–27	368.87	2.885	2.873	2.882	2.880
56R-2, 87–89	376.27	3.129	3.120	3.141	3.130
56R-4, 116–118	379.39	5.915	5.786	5.695	5.799
56R-6, 25–27	381.07	4.503	4.513	4.537	4.518
57R-2, 135–137	386.33	5.671	5.621	5.574	5.622
57R-4, 127–129	389.09	4.478	4.411	4.407	4.432
57R-5, 82–84	389.95	4.274	4.297	4.243	4.272
57R-8, 42–44	392.95	5.060	5.014	4.962	5.012
58R-3, 121–123	396.95	5.833	5.725	5.778	5.779
58R-6, 121–123	400.93	4.133	4.161	4.147	4.147
58R-8, 19–21	402.75	6.324	6.211	6.142	6.226
58R-8, 61–63	403.17	5.813	5.845	5.822	5.827
59R-2, 12–14	404.31	5.118	5.052	5.130	5.100
59R-4, 28–30	407.27	4.354	4.351	4.350	4.352
59R-7, 22–24	410.26	5.314	5.312	5.381	5.336
60R-2, 64–66	414.52	5.162	5.023	5.087	5.091
60R-4, 68–70	417.09	5.377	5.322	5.389	5.363
60R-7, 113–115	421.62	5.287	5.285	5.214	5.262
61R-2, 47–49	423.77	6.464	6.483	6.499	6.482
61R-4, 103–105	427.34	4.146	4.144	4.069	4.119
61R-6, 63–65	429.65	4.183	4.159	4.127	4.156
62R-2, 83–85	433.62	4.862	5.111	5.169	5.047
62R-6, 95–97	439.28	5.019	5.005	4.970	4.998
63R-1, 88–90	441.98	6.379	6.630	6.502	6.503
63R-5, 35–37	446.87	4.411	4.371	4.354	4.379
64R-2, 43–45	452.52	5.760	5.704	5.647	5.703
64R-4, 48–50	455.37	3.775	3.771	3.699	3.748
64R-6, 33–35	458.10	4.466	4.577	4.452	4.498
65R-4, 93–95	465.13	4.434	4.383	4.362	4.393
65R-6, 38–40	466.76	4.949	4.983	4.904	4.945
66R-1, 59–61	470.49	3.281	3.259	3.235	3.258
66R-2, 37–39	471.34	3.021	3.027	3.000	3.016
66R-4, 52–54	473.64	2.625	2.648	2.554	2.609
66R-7, 64–66	477.18	2.980	2.986	2.942	2.969
67R-2, 105–107	481.25	2.640	2.574	2.602	2.605
67R-5, 103–105	485.34	3.467	3.483	3.350	3.433
67R-7, 38–40	487.42	3.461	3.488	3.418	3.455
68R-1, 109–111	490.19	2.799	2.820	2.768	2.796
68R-3, 109–111	493.05	5.670	5.597	5.705	5.658
68R-4, 142–144	494.54	5.740	5.762	5.718	5.740
68R-6, 10–12	496.10	5.039	4.859	4.843	4.913
69R-2, 137–139	501.35	3.505	3.480	3.447	3.477
69R-3, 65–67	502.08	4.243	4.203	4.147	4.198
69R-4, 125–127	504.13	3.444	3.429	3.363	3.412

Table T13 (continued).

Core, section, interval (cm)	Top depth (mbsf)	Velocity (km/s)			
		x	y	z	Average
69R-6, 75–77	506.39	3.515	3.491	3.483	3.497
70R-2, 24–26	509.84	6.811	6.689	6.820	6.773
71R-1, 107–109	514.17	6.926	6.775	6.719	6.807
71R-3, 25–27	516.15	3.398	3.362	3.370	3.377
73R-1, 13–15	521.13	6.369	6.366	6.196	6.310

Values are accurate to ± 20 m/s. ND = no data (shape of discrete Sample 330-U1374A-39R-5, 105–107 cm, did not allow *P*-wave velocity measurements for the *y*- and *z*-axes).

Table T14. Thermal conductivity measurements, Site U1374.

Core, section, interval (cm)	Top depth (mbsf)	Thermal conductivity (W/[m·K])	Standard deviation (W/[m·K])	Space	Material
330-U1374A-					
2R-1, 73	10.33	1.380	0.005	Half	Sandstone
3R-3, 33	17.61	1.591	0.008	Half	Basalt
4R-1, 83	21.23	1.346	0.010	Half	Basalt
5R-4, 38	29.08	1.649	0.010	Half	Basalt
6R-2, 144	32.13	1.504	0.010	Half	Basalt
7R-1, 138	35.58	1.595	0.029	Half	Basalt
7R-3, 109	37.97	1.360	0.373	Half	Basalt
8R-1, 81	39.81	1.076	0.007	Half	Basalt
7R-5, 83	40.39	0.767	0.048	Half	Basalt
9R-3, 39	46.63	1.515	0.009	Half	Basalt

Table T15. Magnetic properties and demagnetization results for discrete samples, Hole U1374A. This table is available in an [oversized format](#).

Table T16. Anisotropy of magnetic susceptibility results for discrete samples, Hole U1374A. This table is available in an [oversized format](#).



Table T17. Summary of inclination-only averages for lithologic units, Hole U1374A. (Continued on next three pages.)

Strat. unit	Lith. unit	ISCI	Lithology	Lith. unit depth (mbsf)		Averages from 2 cm archive-half core data					Averages from Fisher piece averages				
						n	Inclination (°)		α_{63}	α_{95}	n	Inclination (°)		α_{63}	α_{95}
				Top	Bottom		Arithmetic mean	Maximum likelihood				Arithmetic mean	Maximum likelihood		
I	—	NA	Sediment	0.00	6.64										
IIA	—	NA	Sediment	6.64	13.59	25	34.3	54.7	52.5	23.4	10	34.8	57.5	53.8	40.3
IIB	—	NA	Sediment	13.59	13.78	3	13.8	13.9	9.8	15.0	1	13.9			
IIC	—	NA	Sediment	13.78	15.05	21 [†]					3 [†]				
IID	—	NA	Sediment	15.05	15.31	1	−23.4				1	−23.4			
IIE	—	NA	Sediment	15.31	16.72	11	6.6	35.9	12.8	7.3	5	10.3	10.5	17.8	17.2
III	1	3	Lava flow	16.72	18.04	9 [†]					1	63.1			
IV	2	3	Lava flow	20.40	29.69	130 [†]					18(20)*	49.1	50.5	15.9	6.9
V	3	NA	Volcanic breccia	29.69	33.98	21	45.5	54.5	33.9	14.4	4	36.2	42.4	35.4	43.8
VI	4	3	Lava flow	34.20	37.45	49	60.7	65.0	20.2	5.2	6	56.5	58.8	17.3	14.6
VI	5	NA	Volcanic breccia	37.45	37.60						1	78.2			
VIIA	6	NA	Lithic-vitric volcanic sand	37.60	38.79	13	46.7	47.2	9.3	4.8	4	45.2	45.5	8.4	9.6
VIIIB	7	NA	Lithic-vitric volcanic sand	38.79	41.48	35	48.0	48.1	5.9	1.8	9	46.8	47.0	6.4	4.1
VIIIC	7b	NA	Volcanic breccia with sand and bioclast matrix	41.48	41.84	2 [†]									
VIII	8	NA	Volcanic breccia	41.84	63.67	318 [†]					49 [†]				
IXA	—	NA	Sedimentary breccia	63.67	74.78	37	−23.3	−33.8	52.3	18.9	3	−21.0	−22.1	25.7	41.0
IXB	—	NA	Sedimentary breccia	74.78	78.20	20 [†]					4	27.0	71.8	70.5	154.2
IXC	—	NA	Sedimentary breccia	78.20	84.70	10 [†]					2 [†]				
X	9	3	Lava lobe	84.70	87.41	4	−54.3	−54.3	1.6	1.8	2	−54.3	−54.3	0.4	1.3
X	10	NA	Volcanic breccia	87.20	94.25	3	−47.5	−47.5	2.8	4.3	2	−48.1	−48.1	2.2	6.8
X	11	2	Lava lobe	94.25	95.40	1	−52.4				1	−52.4			
X	12	NA	Volcanic breccia	95.40	107.82	49	−54.6	−56.7	17.6	4.5	17	−55.4	−57.9	18.2	8.2
X	13	1	Lava lobe	107.82	108.92										
X	14	NA	Volcanic breccia	108.92	109.86										
XIA	—	NA	Sedimentary conglomerate/breccia	109.87	110.28	2	−44.6	−44.6	1.4	4.4					
XIB	—	NA	Sedimentary conglomerate/breccia	110.28	116.45	17	47.5	55.9	34.9	16.7	4 [†]				
XII	15	NA	Volcanic peperitic breccia	116.45	119.16	77(84)*	−76.6	−80.1	11.2	2.3	4 [†]				
XII	16	1	Lava lobe	119.16	121.24	7	−70.6	−70.7	2.6	2.0	1	−70.6			
XII	17	NA	Volcanic breccia	121.24	121.50	4	−75.9	−76.9	7.1	8.1					
XII	18	1	Lava flow or fragment	121.50	121.83	11	−73.4	−74.0	6.2	3.5	1	−74.5			
XII	19	NA	Volcanic breccia	121.83	124.31	34 [†]					3 [†]				
XII	20	1	Lava flow or fragment	124.31	124.65	4	−78.5	−79.2	5.4	6.2	1	−79.9			
XII	21	NA	Volcanic breccia	124.65	124.96	3	−10.2	−10.2	0.7	1.0	1	−82.2			
XII	22	0	Lava flow or fragment	124.96	125.16	4	−34.0	−35.0	17.3	20.0					
XII	23	NA	Volcanic breccia	125.16	126.58	9	−55.0	−58.8	21.8	14.3	4	−52.2	−65.8	36.3	45.0
XII	24	0	Lava flow or fragment	126.58	126.75										
XII	25	NA	Volcanic breccia	126.75	127.52	5	−73.7	−75.0	8.4	8.0	1	−75.7			
XII	26	1	Lava flow or fragment	127.52	127.73	7	−81.4	−81.6	2.8	2.1					
XII	27	NA	Volcanic breccia	127.73	127.86	4	−79.1	−81.2	8.3	9.5					
XII	28	1	Lava flow or fragment	127.86	128.22	5	−74.8	−76.0	7.9	7.5	1	−79.3			
XII	29	NA	Volcanic breccia	128.22	128.95	19 [†]					4 [†]				
XII	30	0	Lava flow or fragment	128.95	129.20	7	−60.6	−60.8	5.0	3.7	1	−60.8			
XII	31	NA	Volcanic breccia	129.20	146.06	250 [†]					25 [†]				
XIII	32	NA	Volcanic breccia with sandy matrix	146.06	147.18	11 [†]									
XIII	33	NA	Volcanic breccia	147.18	147.84	15	−69.7	−78.2	19.8	9.6	1	−78.9			
XIII	34	0	Lava fragment	147.84	147.97	3	−62.4	−62.8	6.6	10.2					
XIII	35	NA	Volcanic breccia	147.97	148.42	5	−73.5	−75.7	10.6	10.2	2	−78.1	−78.1	0.7	2.2



Table T17 (continued). (Continued on next page.)

Strat. unit	Lith. unit	ISCI	Lithology	Lith. unit depth (mbsf)		Averages from 2 cm archive-half core data					Averages from Fisher piece averages				
						n	Inclination (°)		α_{63}	α_{95}	n	Inclination (°)		α_{63}	α_{95}
				Top	Bottom		Arithmetic mean	Maximum likelihood				Arithmetic mean	Maximum likelihood		
XIII	36	0	Lava fragment	148.42	148.62	6	−63.2	−64.1	10.3	8.6					
XIII	37	NA	Volcanic breccia	148.62	149.39	11 [†]					2 [†]				
XIII	38	0	Lava fragment	149.39	149.65	3 [†]									
XIII	39	NA	Volcanic breccia	149.65	153.97	76(79)*	−60.0	−73.4	29.0	6.2	9(10)*	−61.0	−62.9	14.6	9.4
XIII	40	1	Lava fragment	153.97	154.68	1	−75.1				1	−83.6			
XIII	41	NA	Volcanic breccia	154.68	155.03										
XIII	42	1	Lava fragment	155.03	155.47	10	−80.7	−81.3	4.6	2.7	2	−78.1	−78.4	4.2	13.1
XIII	43	NA	Volcanic breccia	155.47	155.57	3	−80.8	−80.8	0.6	1.0					
XIII	44	0	Lava fragment	155.57	155.77	8	−72.8	−75.8	12.6	8.7					
XIII	45	NA	Volcanic breccia	155.77	155.88	3	−76.4	−76.5	0.8	1.2					
XIII	46	1	Lava lobe	155.88	156.35	12	−79.2	−79.9	5.2	2.8	1	−83.2			
XIII	47	NA	Volcanic breccia	156.35	158.11	18 [†]					2	−70.6	−82.8	22.2	74.8
XIII	48	NA	Volcanic breccia	158.11	159.12	12	−0.2	−0.2	5.7	3.1	4	0.4	0.4	6.1	6.9
XIII	49	1	Lava fragment	159.12	159.65	6	−1.2	−1.2	1.4	1.2	1	−0.9			
XIII	50	NA	Volcanic breccia	159.65	163.76	25 [†]					1	−0.3			
XIII	51	NA	Volcanic breccia	163.76	164.39	28 [†]					1	88.0			
XIII	52	1	Lava lobe fragment	164.39	165.01	9 [†]					1	89.7			
XIII	53	NA	Volcanic breccia	165.01	168.35	12	1.3	2.3	26.9	15.1	3	−15.5	−19.8	51.3	100.2
XIII	54	0	Lava lobe fragment	168.35	168.59										
XIII	55	NA	Volcanic breccia with sandy matrix	168.59	169.81										
XIII	56	1	Lava lobe fragment	169.81	170.64	2	−28.0	−49.2	59.4	154.2	2	−28.0	−49.2	59.4	154.2
XIII	57	NA	Volcanic breccia with sandy matrix	170.64	176.59	10 [†]					4 [†]				
XIII	58	2	Lava lobe fragment	176.59	177.90	2	−70.6	−70.6	0.6	1.7	1	−70.7			
XIII	59	NA	Volcanic breccia	177.50	180.61	14 [†]					4 [†]				
XIII	60	NA	Volcanic breccia	180.61	181.22	14	−73.7	−86.0	18.3	9.2	3	−72.3	−74.1	10.5	16.1
XIII	61	0	Lava fragment	181.22	181.52										
XIII	62	NA	Volcanic breccia	181.52	182.35	1	−41.2				1	−41.2			
XIII	63	1	Lava fragment	182.35	182.84	1	−54.6				1	−54.6			
XIII	64	NA	Volcanic breccia	182.84	189.72	28 [†]					4 [†]				
XIII	65	1	Lava lobe	189.72	190.76	5	−72.9	−74.2	8.7	8.2	1	−73.9			
XIII	66	NA	Volcanic breccia	190.76	191.97	20	−72.3	−75.0	12.1	4.9	4	−70.4	−72.2	11.2	12.8
XIII	67	2	Lava lobe	191.97	193.13	14	−63.1	−63.7	8.1	4.0	3	−65.5	−66.1	7.8	11.9
XIII	68	NA	Volcanic breccia	193.13	193.85	7	80.9	−81.4	4.1	3.1	2	−80.0	−80.2	2.9	9.1
XIII	69	0	Lava fragment	193.85	194.14	2	−73.7	−73.7	0.4	1.3					
XIII	70	NA	Volcanic breccia	194.14	196.73	34	−75.3	−87.7	16.9	5.2	5	−72.0	−78.3	17.1	16.5
XIII	71	2	Lava lobe	196.73	198.04	9	−72.9	−73.6	6.8	4.3	2	−77.9	−82.4	11.4	35.9
XIII	72	0	Autobrecciated lava lobe	196.70	197.72	26	−72.9	−73.8	7.6	2.7	3	−73.4	−73.5	2.7	4.2
XIII	73	1	Autobrecciated lava lobe; sandy matrix at top	197.42	199.01	29	−68.3	−70.2	12.1	4.1	3	−69.0	−69.5	6.9	10.5
XIII	74	2	Autobrecciated lava lobe; sandy matrix at top	199.01	201.17	29	−76.5	−77.2	6.0	2.0	4	−78.4	−79.3	6.1	6.9
XIII	75	NA	Volcanic breccia	201.17	201.50										
XIII	76	0	Lava fragment	201.50	202.30										
XIII	77	NA	Volcanic breccia	202.30	204.62	13 [†]					6	−35.7	−80.6	66.4	88.9
XIII	78	2	Lava lobe	204.62	205.55	5	−75.7	−76.3	5.7	5.4	3	−73.6	−73.9	4.0	6.2
XIII	79	NA	Volcanic breccia	205.55	217.25	29	−74.1	−84.5	17.7	6.0	11 [†]				
XIII	80	0	Lava lobe or fragment	217.25	218.03	2	−53.1	−53.1	1.1	3.3	2	−59.2	−59.7	8.6	27.0
XIII	81	NA	Volcanic breccia	218.03	233.86	32 [†]					12 [†]				
XIII	82	2	Lava lobe	233.86	235.10	16	−72.3	−72.5	4.0	1.9	2	−72.0	−72.0	2.1	6.3



Table T17 (continued). (Continued on next page.)

Strat. unit	Lith. unit	ISCI	Lithology	Averages from 2 cm archive-half core data						Averages from Fisher piece averages					
				Lith. unit depth (mbsf)		n	Inclination (°)		α_{63}	α_{95}	n	Inclination (°)		α_{63}	α_{95}
				Top	Bottom		Arithmetic mean	Maximum likelihood				Arithmetic mean	Maximum likelihood		
XIII	83	NA	Volcanic breccia	235.10	246.54	11(12)*	-63.2	-77.1	29.6	17.7	8†				
XIII	84	0	Lava lobe or fragment	246.54	246.94										
XIII	85	NA	Volcanic breccia	246.94	247.65										
XIII	86	1	Lava lobe or fragment	247.65	248.22										
XIII	87	NA	Volcanic breccia	248.22	256.75	5	-10.9	-10.9	59.1	75.9	4	-17.9	-25.4	64.7	118.2
XIV	88	NA	Volcanic breccia	256.75	278.73	14†					5	27.9	-34.7	42.7	45.8
XV	89	NA	Volcanic breccia	278.73	287.11	166†					30†				
XV	90	0	Aphyric basalt	287.11	287.31										
XV	91	NA	Volcanic breccia	287.31	290.32	64†					4†				
XVI	92	NA	Volcanic breccia with sandy matrix	290.32	291.15	2	-57.5	-74.9	34.9	153.1	1	-22.7			
XVI	93	NA	Volcanic breccia	291.15	306.06	169†					33†				
XVI	94	0	Lava fragment	306.06	306.34										
XVI	95	NA	Volcanic breccia	306.34	318.35	29†					7†				
XVI	96	1	Pillow or lava lobe?	318.35	319.14	4	-86.5	-86.8	1.8	2.1	1	-86.8			
XVI	97	NA	Volcanic breccia	319.14	326.41	68	-65.8	-66.5	8.4	1.8	10	-63.6	-64.3	8.3	5.0
XVI	98	1	Pillow or lava lobe?	326.41	326.84										
XVI	99	NA	Volcanic breccia	326.84	328.23	3	-48.7	-48.7	1.5	2.3	1	-48.7			
XVI	100	NA	Volcanic breccia	328.23	333.25	49†					14†				
XVI	101	1	Pillow or lava lobe?	333.25	333.69										
XVI	102	NA	Volcanic breccia	333.69	336.85	20	-65.8	-66.8	9.7	4.0	5	-62.9	-63.8	9.9	9.4
XVI	103	3	Intrusive sheet	335.90	338.81	61	-75.1	-75.9	6.5	1.5	3	-75.4	-75.5	3.1	4.7
XVI	102b	NA	Volcanic breccia	337.75	337.92						1	-79.6			
XVI	103b	3	Intrusive sheet	337.92	338.81	42	-75.9	-76.3	4.7	1.3	2	-76.1	-76.3	2.8	8.8
XVI	104	NA	Volcaniclastic breccia	338.81	351.66	78†					18†				
XVII	105	NA	Volcaniclastic breccia	351.66	365.74	60†					15†				
XVII	106	3	Intrusive sheet	365.74	366.61	37	-76.9	-77.6	5.7	1.7	4†				
XVII	107	NA	Volcaniclastic breccia	366.61	375.19	68	-53.9	-71.0	36.3	8.5	12†				
XVIII	108	NA	Volcaniclastic breccia	375.19	384.22	190†					18	-76.6	-78.0	8.0	3.4
XVIII	109	1	Lava lobe or fragment	384.22	384.98	23	-72.7	-74.8	11.0	4.2	3	-73.8	-74.0	2.9	4.5
XVIII	110	NA	Volcaniclastic breccia	384.98	385.36	16	-81.5	-82.0	4.1	1.9					
XVIII	111	1	Brecciated lava lobe or fragment	385.36	385.80	18	-75.9	-77.3	8.1	3.5					
XVIII	112	1	Lava lobe or fragment (massive base to Unit 111)	385.80	386.54	18	-74.1	-75.1	7.6	3.2	2	-79.8	-79.8	1.2	3.7
XVIII	113	NA	Volcaniclastic breccia	386.54	393.11	150†					17†				
XVIII	114	1	Lava lobe or fragment	393.11	393.74	16	-67.6	-79.0	23.4	11.0	1	-52.8			
XVIII	115	NA	Volcaniclastic breccia	393.74	396.07	42†					6†				
XVIII	116	3	Intrusive sheet	396.07	397.73	66	-72.9	-78.5	15.0	3.3	3	-72.1	-76.3	14.0	21.7
XVIII	117	NA	Volcaniclastic breccia	397.73	402.83	123	-74.9	-80.1	13.6	2.2	18	-75.0	-76.4	8.6	3.7
XVIII	118	3	Lava lobe or fragment	402.83	403.15	11	-75.1	-75.8	6.4	3.6					
XVIII	119	NA	Volcaniclastic breccia	403.15	403.88	3‡	89.2				2†				
XVIII	120	3	Intrusive sheet	403.88	405.40	65	-74.8	-75.9	7.7	1.7	1	-71.3			
XVIII	121	NA	Volcaniclastic breccia	405.40	407.99	43	-70.6	-73.2	12.6	3.4	7	-70.8	-72.2	9.6	7.2
XVIII	122	3	Intrusive sheet	407.99	408.35	4	-71.7	-73.0	9.4	10.7	1	-71.9			
XVIII	123	NA	Volcaniclastic breccia	408.35	408.91	17	-75.4	-77.6	10.0	4.4	1	-72.3			
XVIII	124	3	Intrusive sheet	408.91	412.74	102†					2	-82.9	-83.0	1.9	6.0
XVIII	125	NA	Brecciated margin of intrusive sheet	412.74	413.63	30†					1	-83.7			
XVIII	126	3	Intrusive sheet	413.63	415.89	98†					1	-85.1			
XVIII	127	NA	Volcaniclastic breccia	415.89	416.06	7	-80.1	-82.7	8.7	6.5					
XVIII	128	3	Intrusive sheet	416.06	417.35	54	-79.2	-80.4	6.5	1.6	3	-82.2	-82.2	1.2	1.8



Table T17 (continued).

Strat. unit	Lith. unit	ISCI	Lithology	Lith. unit depth (mbsf)		Averages from 2 cm archive-half core data					Averages from Fisher piece averages				
						n	Inclination (°)		α_{63}	α_{95}	n	Inclination (°)		α_{63}	α_{95}
				Top	Bottom		Arithmetic mean	Maximum likelihood				Arithmetic mean	Maximum likelihood		
XVIII	129	NA	Volcaniclastic breccia	417.35	425.66	120(124)*	-75.5	-77.6	9.8	1.6	17†				
XVIII	130	1	Brecciated lava lobe or fragment	425.66	426.09	7	-75.3	-75.4	2.6	2.0					
XVIII	131	NA	Volcaniclastic breccia	426.09	441.55	258	-74.4	-76.8	10.7	1.2	42	-75.2	-76.3	7.6	2.1
XVIII	132	1	Lava lobe or fragment	441.55	442.01	5	-29.9	-30.2	10.6	10.1	1	-29.9			
XVIII	133	NA	Volcaniclastic breccia	442.01	444.16	27†					7†				
XVIII	134	1	Lava lobe or fragment	444.16	445.02	20†					1	82.0			
XIX	135	NA	Volcaniclastic breccia	445.02	451.71	59	-71.7	-72.9	9.1	2.1	17	-69.7	-70.7	8.6	3.8
XIX	136	3	Intrusive sheet	451.71	453.53	3	-73.0	-73.0	2.0	3.1	1	-73.0			
XIX	137	NA	Volcaniclastic breccia	453.53	470.12	318	-70.4	-71.3	8.3	0.8	37	-68.8	-69.9	9.2	2.7
XIX	138	NA	Volcaniclastic breccia	470.12	491.85	397					31†				
XIX	139	3	Intrusive sheet	491.85	494.97	109					5	-82.9	-83.1	2.5	2.4
XIX	140	3	Intrusive sheet	494.97	496.64	12					5†				
XIX	141	NA	Volcaniclastic breccia	496.64	498.59	8	-11.6	-12.1	22.1	15.6	4	-6.6	-6.7	21.5	25.1
XIX	142	NA	Vitric-lithic volcanic sand and gravel	498.70	503.16	20†					8	-7.1	-16.5	61.2	59.2
XIX	143	NA	Volcaniclastic breccia	503.16	507.98	61	-50.3	-63.6	35.5	8.7	20	-48.3	-62.7	37.1	16.4
XIX	144	0	Basalt fragment	507.98	508.30										
XIX	145	NA	Volcaniclastic breccia	508.30	508.48	1	5.5				1	5.5			
XIX	146	3	Lava flow or intrusive sheet?	508.30	515.19	76	-59.3	-59.8	7.4	1.5	7	-59.9	-61.0	11.8	8.9
XIX	147	NA	Vitric-lithic volcanic gravel	515.19	518.45	25†					8†				
XIX	148	3	Lava flow or intrusive sheet?	518.45	521.81	57	-60.6	-64.8	19.9	4.8	6	-57.2	-59.6	16.8	14.2

* = no solution possible with initial distribution (initial n in parentheses); results are reported for dominant polarity. † = no solution possible. ‡ = inclination consistently steep but did not converge. — = no lithologic unit. ISCI = in situ confidence index (see “[Igneous petrology and volcanology](#)” in the “Methods” chapter [Expedition 330 Scientists, 2012a]). NA = not applicable. The method of Arason and Levi (2010) was used to calculate inclination-only mean and associated statistics. α_{63} = circular standard deviation, α_{95} = 95% confidence angle.

Table T18. Culturing efforts, Hole U1374A.

Core, section, interval (cm)	Media	Vials inoculated (N)	Growth
330-U1374A-			
4R-1, 114–121	Autotrophic S oxidizers	2	–
	Heterotrophic S oxidizers	2	–
	Autotrophic Fe reducers	2	ND
	Heterotrophic Fe reducers	2	ND
	Autotrophic Fe oxidizers	2	ND
	Heterotrophs; 1% marine broth (low oxygen)	2	–
	Heterotrophs; 10% marine broth (saturated oxygen)	2	–
6R-3, 117–128	Autotrophic S oxidizers	2	++
	Heterotrophic S oxidizers	2	++
	Autotrophic Fe reducers	2	ND
	Heterotrophic Fe reducers	2	ND
	Autotrophic Fe oxidizers	2	ND
	Heterotrophs; 1% marine broth (low oxygen)	2	Maybe
	Heterotrophs; 10% marine broth (saturated oxygen)	2	+
7R-1, 120–130	Autotrophic S oxidizers	2	+
	Heterotrophic S oxidizers	2	+
	Autotrophic Fe reducers	2	ND
	Heterotrophic Fe reducers	2	ND
	Autotrophic Fe oxidizers	2	ND
	Heterotrophs; 1% marine broth (low oxygen)	2	++
	Heterotrophs; 10% marine broth (saturated oxygen)	2	++
8R-1, 60–68	Heterotrophs; 1% marine broth (low oxygen)	2	–
	Heterotrophs; 10% marine broth (saturated oxygen)	2	Maybe
20R-1, 128–134	Autotrophic S oxidizers	2	–
	Heterotrophic S oxidizers	2	–
	Autotrophic Fe reducers	2	ND
	Heterotrophic Fe reducers	2	ND
	Autotrophic Fe oxidizers	2	ND
	Heterotrophs; 1% marine broth (low oxygen)	2	–
	Heterotrophs; 10% marine broth (saturated oxygen)	2	–
30R-3, 130–143	Autotrophic S oxidizers	2	Maybe
	Heterotrophic S oxidizers	2	–
	Autotrophic Fe reducers	2	ND
	Heterotrophic Fe reducers	2	ND
	Autotrophic Fe oxidizers	2	ND
	Heterotrophs; 1% marine broth (low oxygen)	2	Maybe
	Heterotrophs; 10% marine broth (saturated oxygen)	2	–
37R-4, 5–12	Heterotrophic methanogens	2	–
	Heterotrophic S oxidizers	2	–
	Heterotrophs; 1% marine broth (low oxygen)	1	Maybe
	Heterotrophs; 10% marine broth (saturated oxygen)	1	–
49R-3, 60–70	Heterotrophic sulfate-reducing bacteria	2	–
	Heterotrophs; 1% marine broth (low oxygen)	2	+
	Heterotrophs; 10% marine broth (low oxygen)	2	+
52R-4, 95–108	Heterotrophic sulfate-reducing bacteria	2	–
	Heterotrophs; 1% marine broth (low oxygen)	2	–
	Heterotrophs; 10% marine broth (low oxygen)	2	++
58R-6, 50–62	Heterotrophs; 1% marine broth (low oxygen)	2	++
	Heterotrophs; 10% marine broth (low oxygen)	2	++
	Heterotrophs; 1% marine broth (saturated oxygen)	2	++
	Heterotrophs; 10% marine broth (saturated oxygen)	2	++
62R-6, 80–91	Heterotrophs; 1% marine broth (low oxygen)	2	Maybe
	Heterotrophs; 10% marine broth (low oxygen)	2	Maybe

Analysis of growth was determined by shaking the vials. If turbidity was greater than in the initial sample, growth was considered positive. ++ = both vials were positive, + = one vial was positive, – = no growth. ND = not determined (media targeting iron reducers and iron oxidizers contain particulates, and therefore a change in turbidity was impossible to detect).

Table T19. Samples used for stable isotope addition bioassays, Hole U1374A.

Core, section, interval (cm)	Treatment	Vials (N)	Approximate volume of rocks per vial (cm ³)
330-U1374A- 15R-2, 79–89	+2.71 mM ¹³ C bicarbonate +300 μM ³⁴ S elemental S	3	15
21R-2, 111–119	+2.71 mM ¹³ C bicarbonate +300 μM ³⁴ S elemental S	3	25
	+10 mM ¹³ C glucose +10 mM ¹³ C acetate +300 μM ³⁴ S elemental S	3	25
24R-3, 90–101	+2.71 mM ¹³ C bicarbonate +300 μM ³⁴ S elemental S +0.5 mM ¹⁵ N ammonia	5	30
	+10 mM ¹³ C glucose +10 mM ¹³ C acetate +300 μM ³⁴ S elemental S +1.0 mM ¹⁵ N nitrate	5	30
31R-3, 142–150	+2.71 mM ¹³ C bicarbonate +300 μM ³⁴ S elemental S +0.5 mM ¹⁵ N ammonia	6 (live)	30
	+2.71 mM ¹³ C bicarbonate +300 μM ³⁴ S elemental S +0.5 mM ¹⁵ N ammonia	2 (dead)	30
71R-3, 47–55	+2.71 mM ¹³ C bicarbonate +300 μM ³⁴ S elemental S +0.5 μM ¹⁵ N ammonia	5 (live)	25
	+2.71 mM ¹³ C bicarbonate +300 μM ³⁴ S elemental S +0.5 μM ¹⁵ N ammonia	2 (dead)	25
	+10 mM ¹³ C acetate +300 μM ³⁴ S elemental S +1.0 μM ¹⁵ N nitrate	3	30

Table T20. Quantification of microspheres in collected samples, Site U1374.

Sample	Microspheres	
	Number/g rock	Number/mL fluid
330-U1374A-8R-1, 60–68 cm		
Drill fluid		3.7×10^5
First rock rinse		8.0×10^3
Second rock rinse		1.2×10^4
Third rock rinse		0.00
Section 1 cut	0	
Section 2 cut	0	
Section 3 cut	0	
Section 4 cut	0	
Section 5 cut	0	
Outside top	0	
Center	0	
Outside bottom	0	
Between outside and center	0	
330-U1374A-45R-2, 20–27 cm		
Drill fluid		1.2×10^4
First rock rinse		0.00
Second rock rinse		0.00
Third rock rinse		0.00
Section 1 cut	0	
Section 2 cut	0	
Section 3 cut	0	
Section 4 cut	0	
Section 5 cut	0	
Center	0	